Advanced control functions of automotive brake systems for the optimisation of braking performance, brake wear and particle emissions

Dissertation zur Erlangung des
akademischen Grades Doktor-Ingenieur (Dr.-Ing.)

vorgelegt der Fakultät für Maschinenbau
der Technischen Universität Ilmenau

von M.Sc. Vincenzo Ricciardi

1. Gutachter: Prof. Dr.-Ing. Klaus Augsburg
2. Gutachter: PD Dr.-Ing. Stephan Schmidt
3. Gutachter: Dr.-Ing. Sebastian Gramstat

Tag der Einreichung: 30.10.2020
Tag der wissenschaftlichen Aussprache: 01.07.2021

DOI: 10.22032/dbt.49391
URN: urn:nbn:de:gbv:ilm1-2021000211

Zusammenfassung

In den letzten Jahrzehnten wurden Fahrzeuge einem tiefgreifenden Einfluss auf die Anforderungen an Sicherheit, Komfort und Umweltfreundlichkeit ausgesetzt. Heutzutage hat der starke Trend zur Umwandlung traditioneller Fahrzeuge in komplexe Systeme und die ständig steigende Anzahl von Elektro- und Elektronikkomponenten die Industrie dazu gezwungen, neue Regelmethoden und deren Entwicklungsprozesse zu entwerfen. Die Optimierung der Bremsverteilung in elektrischen Antrieben mit Brake-by-Wire-Systemen erfordert die Entwicklung fortgeschrittener Schätzfunktionen. Darüber hinaus fördern die Trends zu strengeren Abgasvorschriften und das nachgewiesene Wachstum der Fahrzeugzulassungen den Bedarf an neuen Anwendungen, die die Hersteller über die Umweltfreundlichkeit ihrer Fahrzeugflotte informieren.

In diesem Rahmen werden in der vorliegenden Arbeit Steuerungs- und Schätzlösungen für emissionsarme, multi-aktuierte Fahrzeuge vorgestellt, um die Bremsleistung bei gleichzeitiger Überwachung des Bremsverschleißes und der bremsbedingten Partikelemissionen zu verbessern. Die Erreichung dieses Ziels führt zu interdisziplinären Methoden, die von Fortschritten bei numerischen Modellierungs- und Simulationswerkzeugen über die Anwendung innovativer experimenteller und sensorischer Fusionstechniken bis hin zur Entwicklung und Verifizierung neuartiger Algorithmen zur Zustandsschätzung und -steuerung reichen. Die Entwicklung von Steuerungs- und Schätzfunktionen wird durch Modell-, Software- und Hardware-in-the-Loop-Techniken unterstützt, die durch ein neuartiges, an der Technischen Universität Ilmenau entwickeltes Scheibenbremsmodell verbessert werden.

Auf dem Prüfgelände durchgeführte Experimente zeigen, dass die Bremsleistung in Brake-by-Wire-Systemen durch Kompensation unerwünschter Schwankungen des Bremsreibungskoeffizienten verbessert werden kann. Die Kompensationsfunktion bietet dem Fahrer eine Bremsservounterstützung, wenn die erforderliche Verzögerung nicht zu erreichen ist. In Hybrid- und Vollelektrofahrzeugen verbessert die Bremsreibungskompensation das Blending mit Elektromotoren, indem eine bessere Verfolgung der Referenzverzögerung sichergestellt wird. Außerdem ermöglicht die Schätzung des Bremsreibungskoeffizienten zusätzliche Bremsüberwachungsfunktionen. Durch neuartige Design-of-Experiments und Data-Mining-Verfahren werden die relevanten Einflüsse auf den Bremsverschleiß und die Partikelbildung erfasst. Die experimentellen Beweise treiben die Implementierung und Identifizierung fortschrittlicher Schätzverfahren voran, die früheren Schätzverfahren überlegen sind. Die vorgeschlagenen Kontroll- und Schätzfunktionen weisen im Vergleich zu anderen Ansätzen nach dem jüngsten Stand der Technik eine höhere Leistung unter realen Fahrbedingungen aus.

Abstract

During the past decades, on-road vehicles have undergone profound restrictions in safety, comfort and environmental friendliness requirements. Nowadays, the strong trend towards the transformation of traditional on-road vehicles to complex systems interconnected with the environment and users and the constantly increasing number of electric and electronics components has forced the industry to devise new control functions and development processes thereof. Advanced estimation functions are necessary to optimise the control demand distribution in brake-by-wire systems also in the event of blended operation with electric motors. Moreover, the trends in stricter tailpipe emissions standards and the proven growth in vehicle registrations motivate the need for new tools that inform the original equipment manufacturers about the environmental friendliness of their vehicle fleet.

Under this framework, the present work introduces control and estimation solutions for low-emission multi-actuated ground vehicles to improve braking performance with simultaneous monitoring of brake-related wear and particle emissions. The achievement of this goal brings up interdisciplinary methods ranging among advancements in numerical modelling and simulation tools, application of innovative experimental and sensors fusion techniques and development and verification of novel state estimation and control algorithms. The development of control and estimation functions is supported by model-, software- and hardware-in-the-loop techniques enhanced by means of a novel disc brake model developed at Technische Universität Ilmenau.

Experiments performed on the proving ground shows that braking performance can be improved in brake-by-wire systems through compensation of undesired variations in the brake lining coefficient of friction. The compensation function provides the driver with brake servo assistance when the required deceleration cannot be achieved. In the case of hybrid and full electric vehicles, the brake lining friction compensation improves the control of brake blending with electric motors by ensuring a better tracking of the driver's reference deceleration. Moreover, the availability of an estimate of the brake lining coefficient of friction enables additional brake monitoring functions. Clever design of experiments and advanced data mining techniques allow identifying the relevant factors influencing brake-related wear and the process of particle formation. The experimental evidence drives the implementation and identification of advanced estimation techniques never dealt with in the past. The proposed control and estimation functions exhibit superior performance when compared to state-of-the-art approaches under real driving conditions.

Acknowledgements

This work is the result of five years of continuous research and development as research associate at Technische Universität Ilmenau. During these years I have had the opportunity to meet wonderful people who have contributed to the achievement of my PhD. I would like to thank my *Doktorvater*, Prof. Dr. Ing. Klaus Augsburg, for giving me the opportunity to pursue a PhD research in innovative fields of engineering and use cutting-edge testing facilities. I would also like to thank Dr. Valentin Ivanov for guiding me through the Marie Curie ITEAM Project, which granted me with a top-notch technical training in automotive technologies.

The realisation of this research was only possible thanks to a close collaboration with the colleagues of ThIMo and participation in numerous conferences, summer schools and workshops. In this regard, I would like to thank my colleagues Viktor, David, Peter, Sebastiaan and Cyrano, who helped with the instrumentation of the test benches and vehicle demonstrators, and Ludwig, who was always available to address IT issues. Special thanks also go to my friends Eugenia, Manuel, Andrei, Toni, Alessandro and Cassio for the precious time spent together.

The support of my family was essential to dealing with the challenges of living abroad. I will always be grateful to my wife Olena for the role she played in my professional development. Without her, I would have never achieved this result.

Contents

List of Abbreviations and Symbols

Abbreviations

ABS	Anti-Lock Braking System
ADAS	Advanced Driver Assistance Systems
AMS	Auto Motor und Sport
ANN	Artificial Neural Networks
BBC	Base Brake Control
BLCF	Brake lining coefficient of friction
CAN	Controller Area Network
CPC	Constant Pressure Cycle
DoF	Degree-of-Freedom
DOE	Design of Experiments
DS	dSPACE
EBD	Electronic Brake Force Distribution
ECE	Economic Commission for Europe
EF	Emission Factor
EHB	Electrohydraulic Brake
EHCU	Electrohydraulic Control Unit
EKF	Extended Kalman Filter
EM	Electric Motor
HIL	Hardware-in-the-Loop
ICE	Internal Combustion Engine
ILVO	Ilmenau Volvo Brake Model
ISO	International Organisation for Standardisation
KF	Kalman Filter
KPI	Key Performance Index
MIL	Model-in-the-Loop
MSE	Mean Square Error
NVH	Noise-Vibration-Harshness
OBS	Observer

PC	Principal Component
PCA	Principal Component Analysis
PCU	Powertrain Control Unit
PEMS	Portable Emissions Measurement System
PM	Particulate Matter
PNC	Particle Number Concentration
PSNR	Peak Signal-to-Noise ratio
RDE	Real Driving Emissions
RLS	Recursive Least Square
nRMSE	(Normal) Root Mean Square Error
SAE	Society of Automotive Engineers
SCB	Slip Control Boost
SIL	Software-in-the-Loop
SUV	Sport Utility Vehicle
TM	Tyre Model
VCU	Vehicle Control Unit
VS	Virtual Sensor
WLTP	Worldwide harmonized Light vehicles Test Procedure

Nomenclature

Symbol	Quantity	Unit
A_k	Brake calliper piston(s) area	m^2
A_{eff}	Effective brake disc convective area	m^2
A_{pad}	Real pad-disc contact area	m^2
A_{real}	Geometrical pad-disc contact area	m^2
a_x	Longitudinal vehicle deceleration	m/s^2
a_x^{dem}	Demanded longitudinal vehicle deceleration	m/s^2
b	Vehicle wheel track	m
Bi	Biot number	[/]
c_p	Disc specific heat capacity	$J\ kg^{-1}\ K^{-1}$
c_s	Equivalent suspensions damping	$N\ s\ m^{-1}$
C_L	Tyre longitudinal slip stiffness	N
C_S	Tyre lateral slip stiffness	N
d_p	Calliper piston(s) diameter	m
E_b	Dissipated brake energy	J
EF	Brake particle number emission factor	[/]
f	Brake blending factor	[/]
F_L	Wheel longitudinal contact force[1]	N

F_S	Wheel lateral contact force[1]	N
F_X	Wheel longitudinal contact force[2]	N
F_Y	Wheel lateral contact force[2]	N
F_Z	Wheel vertical force	N
F_V	Suspensions reaction forces	N
$F_{X,drag}$	Frontal air drag resistance	N
$F_{Y,drag}$	Lateral air drag resistance	N
F_n	Calliper clamping force	N
h_{CoG}	Vehicle center of gravity	m
h_{ht}	Brake convective heat transfer coefficient	$W\,m^{-2}\,K^{-1}$
I_{xx}	Vehicle roll inertia	$kg\,m^2$
I_{yy}	Vehicle pitch inertia	$kg\,m^2$
I_{zz}	Vehicle yaw inertia	$kg\,m^2$
I_ω	Wheel rotational inertia	$kg\,m^2$
J_f	Equivalent vehicle inertia on a front wheel	$kg\,m^2$
k_b	Specific brake pad wear	$g\,J^{-1}$
k_{ht}	Brake disc conductivity	$W\,m^{-1}\,K^{-1}$
k_s	Equivalent suspensions stiffness	$N\,m^{-1}$
K_f	Force allocation factor	[/]
K_L	Longitudinal tyre stiffness	$N\,m^{-1}$
K_S	Lateral tyre stiffness	$N\,m^{-1}$
K_Z	Vertical tyre stiffness	$N\,m^{-1}$
l_f	Vehicle front semi wheel base	m
l_r	Vehicle rear semi wheel base	m
m_b	Brake pad wear mass	g
m_{disc}	Brake disc mass	g
m_v	Vehicle mass	kg
m_s	Vehicle sprung mass	kg
m_{us}	Vehicle unsprung mass	kg
n_p	Number of pistons per side per calliper	[/]
l_f	Front semi wheelbase	m
l_r	Rear semi wheelbase	m
p_0	Brake calliper push-out pressure	bar
p_b	Brake calliper pressure	bar
p_b^{dem}	Required brake calliper pressure	bar
PN	Number of brake emitted particles	s^{-1}
PNC	Brake particle number concentration	cm^{-3}
$\dot{Q}_{conv,air}$	Convective heat	W
$\dot{Q}_{fric}$	Heat converted friction power	W

$\dot{Q}_{rad}$	Radiated heat	W
r_ω	Tyre effective radius	m
r_0	Tyre undeformed radius	m
r_{eff}	Brake disc effective radius	m
r_{in}	Brake pad inner radius	m
r_{out}	Brake pad outer radius	m
R_L	Wheel rolling resistance	Nm
s_{ped}	Brake pedal position	[/]
t	Time	s
T_b	Brake torque at wheel	Nm
T_b^{dem}	Demanded brake torque at wheel	Nm
T_d	Drive torque at wheel	Nm
T_{EHB}	Foundation brake torque	Nm
T_{EHB}^{dem}	Demanded foundation brake torque	Nm
T_{EM}	Electric motor torque	Nm
T_{EM}^{dem}	Demanded electric motor torque	Nm
T_w	Wheel applied torque	Nm
T_R	Residual brake dynamometer torque	Nm
v_{in}	Initial vehicle speed	$m\,s^{-1}$
v_t	Target vehicle speed	$m\,s^{-1}$
v_x	Vehicle longitudinal velocity	$m\,s^{-1}$
v_y	Vehicle lateral velocity	$m\,s^{-1}$
v_z	Vehicle body vertical velocity	$m\,s^{-1}$
v_{CoG}	Vehicle velocity resultant at CoG	$m\,s^{-1}$
v_L	Wheel longitudinal velocity	$m\,s^{-1}$
α	Wheels side slip angle	rad
α_b	Pad-disc adimensional real contact area	[/]
β	Vehicle side slip angle at CoG	rad
δ_{ht}	Brake disc cooling coefficient	s^{-1}
δ	Steering angle	rad
Δt	Integration time step	s
Δt_b	Brake application duration	s
θ	Vehicle pitch angle	rad
θ_f	Brake pad circumferential angle	rad
κ	Brake lining adhesion coefficient	[/]
λ	Longitudinal tyre slip	[/]
μ_b	Brake lining coeff. of friction (BLCF)	[/]
μ_{b0}	Previous μ_b estimate	[/]
μ_{road}	Maximum road grip potential	[/]

ν	Disc infinitesimal element sliding speed	$m\,s^{-1}$
ξ	Normalised braking power to heat fraction	$K\,N^{-1}\,m^{-1}$
σ	Braking power to heat fraction	[/]
$\sigma_{z\theta}$	Disc infinitesimal element tangential stress component	$N\,m^{-2}$
σ_{zz}	Disc infinitesimal element normal stress component	$N\,m^{-2}$
ΣPN	Emitted brake particle number per km	km^{-1}
τ	Brake disc temperature	K
τ_{env}	Ambient temperature	K
τ_{in}	Initial brake disc temperature	K
$\tau_{rl,L}$	Longitudinal tyre relaxation constant	s
$\tau_{rl,S}$	Lateral tyre relaxation constant	s
ϕ	Vehicle roll angle	rad
χ_{road}	Road slope	%
ψ	Vehicle yaw angle	rad
ω	Wheel rotational velocity	$rad\,s^{-1}$

---

[1] Wheel Reference Frame

[2] Vehicle Reference Frame

Chapter 1

Introduction

1.1 Research background

During the past decades, on-road vehicles have been subject to a profound impact on safety, comfort and environmental friendliness requirements [1]. Nowadays, the strong trend towards the transformation of traditional on-road vehicles to complex systems interconnected with the environment, infrastructures and users and the constantly increasing number of electric and electronics components has forced the industry to devise new development processes and/or conform to best practices, which allow for a standard compliant product or service. New technologies such as hybrid and electric powertrains, advanced driver assistance systems (ADAS) and x-by-wire systems have become focus of great research effort and noticeable industrial investments. Moreover, the trends in stricter tailpipe emissions standards and the proven growth in vehicle registrations suggest that brake and tyre wear and road resuspension have gained a remarkable impact over the global vehicle emissions. Under this framework, the present work introduces control and estimation solutions for low-emission multi-actuated ground vehicles to improve braking performance with simultaneous monitoring of brake-related wear and particle emissions. The achievement of a low-emission paradigm is made possible due to the presence of several chassis actuators (i.e. electric motors and brake-by-wire), which coexist on the vehicle and can cooperate to enhance driving performance and improve the vehicle environmental friendliness. The concept of low-emission multi-actuated ground vehicle includes:

- novel vehicle subsystems featuring fast-dynamics actuators;
- advanced control algorithms robust against external disturbances;
- advanced estimation functions monitoring the actuators operation.

This work brings up interdisciplinary methods ranging among advancements in numerical modelling and simulation tools, application of innovative experimental and sensors fusion techniques and development and verification of novel state estimation and control algorithms.

1.2 Transport-related emissions

Transport related emissions are associated with adverse health effects and environmental hazards [2]. Among the main pollutants, fine particulate matter ($PM_{2.5}$) and ultra-fine particles ($PM_{0.1}$) show the greatest impact on human health. The ultrafine particles are proven to pass the alveoli, placental and brain barriers to generate serious health impacts [3]. Motor vehicle emissions, which represent the main source of urban pollutant emissions, can be divided into two main categories according to their source: engine exhaust emissions and non-exhaust emissions. Engine exhaust emissions result from fuel combustion and lubricant volatilisation that occur during the combustion process. Non-exhaust emissions are generated through the resuspension of road dust or road surface wear as the vehicle travels over the road surface, corrosion of vehicle components or during the mechanical processes associated with driving. Particularly, several studies underline the significance of brake-related non-exhaust emissions and the need for legislation and abatement strategies to reduce their contribution to ambient PM concentrations [4].

The European Monitoring and Evaluation Programme stresses the importance of reviewing and maintaining the emission inventory guidebook by reporting the emissions by year, pollutant and country [5]. Among others, the current source categorisation includes exhaust emissions for different vehicle classes (e.g. 1.A.3.b.i for passenger cars, 1.A.3.b.ii for light duty vehicles and 1.A.3.b.iii for heavy duty vehicles), tyre and brake wear as one source category (1.A.3.b.vi), road surface abrasion emissions without considering the resuspension effect (1.A.3.b.vii), railways exhaust-related emissions (1.A.3.c) and non-road mobile machinery associated emissions (1.A.4.a.ii) [6]. Figure 1.1a and Figure 1.1b report the PM_{10} and $PM_{2.5}$ emission trends in the period 2000-2016 for the EU28 countries.

In Figure 1.1a and Figure 1.1b, it is noticeable that the stricter regulations have had a remarkable impact on the reduction of exhaust emissions, whereas there is a noticeable increase in non-exhaust brake emissions mainly due to greater vehicle use. Moreover, the impact of non-exhaust particulate matter is assumed to become dominant in the short-term as the exhaust particulate matter has been progressively reduced thanks to the fleet turn-over and the replacement of non-DPF diesels [7]. This proves that the increasingly stringent policies on traffic related emissions, promulgated during the past years, succeeded in reducing the exhaust related emissions but did not address adequately the non-exhaust component such as the brake wear, tyre wear and road dust resuspension [7]. The contribution of non-exhaust particulate matter is reported to be significant in big cities and urban environments because of the frequent occurrence of braking events [8].

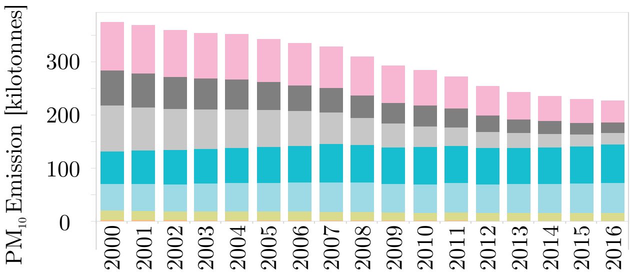

(a) *Emissions of PM$_{10}$ in kilotonnes in EU28 countries.*

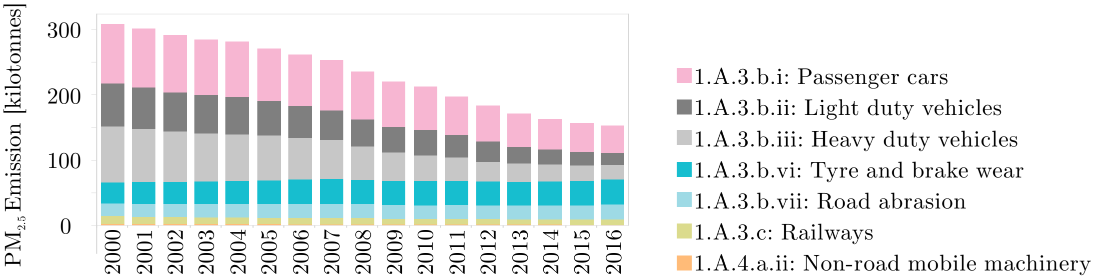

(b) *Emissions of PM$_{2.5}$ in kilotonnes in EU28 countries.*

Figure 1.1: *PM$_{10}$ and PM$_{2.5}$ emissions in EU28 countries for different sources. Road non-exhaust emissions are predominant, whilst railways and non-road mobile machinery represent only a tiny fraction.*

The achievement of the low-emission multi-actuated ground vehicle paradigm requires extensive effort towards the development of low-emission vehicle technologies and advanced control functions capable of exploiting their full potential. Figure 1.2 reports a typical urban scenario where, among all road participants, a low-emission multi-actuated full electric vehicle (in green color) achieves a reduction in brake-related emissions with simultaneous fulfilment of the velocity constraints by blended operation of electric motors and friction brakes. This is made possible by brake-by-wire technologies such as the decoupled electrohydraulic brake system (EHB), aimed at providing additional flexibility to the distinctive functions of brake blending and regeneration. To achieve a smooth and coordinated control of regenerative and conventional friction brakes, the brake lining coefficient of friction (BLCF) shall be estimated. The availability of a reliable BLCF estimate may enable advanced control functions of brake systems for the optimisation of braking performance [9], brake-related wear and particle emissions [10].

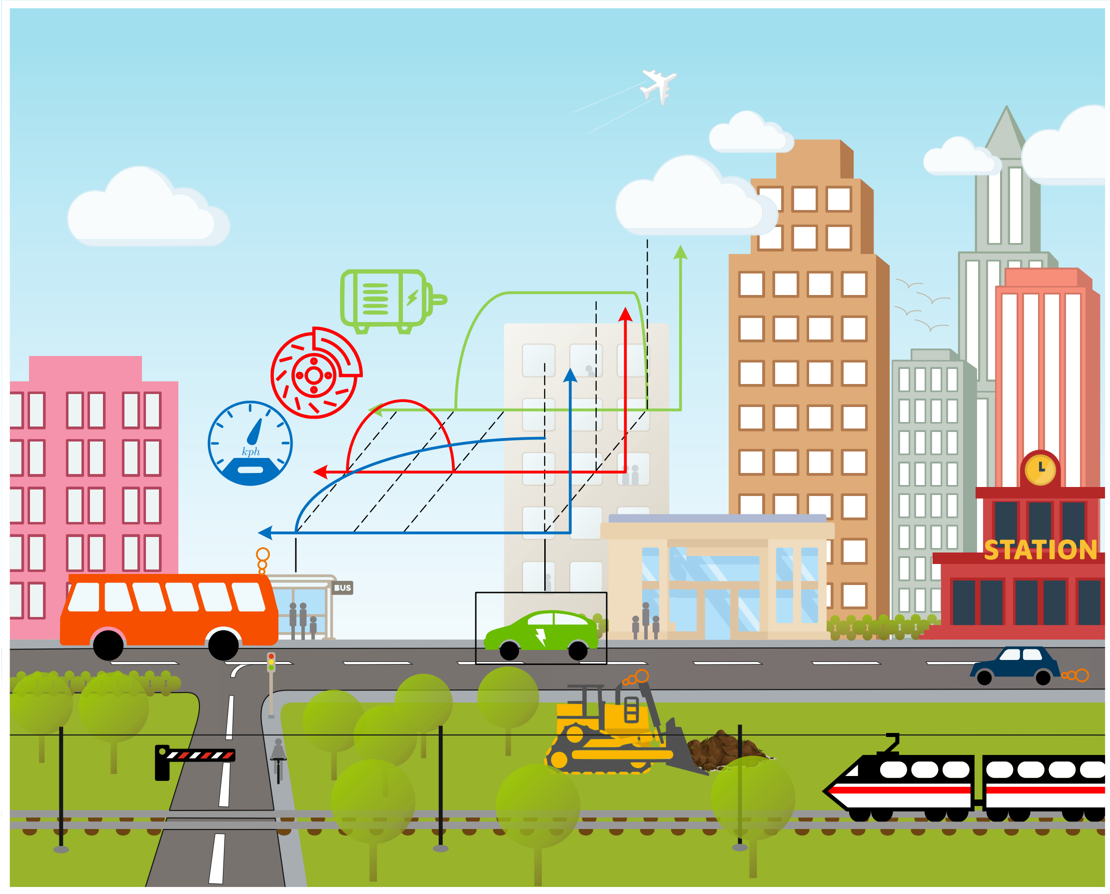

Figure 1.2: *Typical urban scenario featuring several road participants where the low-emission multi-actuated full electric vehicle brakes with blended control of electric motors.*

1.3 Real driving conditions

On May 3rd, 2018, the EU member states adopted the latest amendment to regulation EU 2017/1151 [11]. This latter introduced the real driving emissions (RDE) tests as a mandatory part of the type-approval procedure for new passenger cars and light-commercial vehicles in Europe. The on-road RDE test complements the laboratory test and is intended to ensure that the emission levels of vehicles under real-world driving conditions stay within the not-to-exceed limits. Under the new type-approval system, manufacturers must demonstrate that new vehicle models pass the RDE test to obtain a certificate of conformity with Euro 6 standards. The directive establishes air quality objectives for improving human health and environmental quality up to 2020; however, the directive does not account for the non-exhaust emission sources, which, at the time of writing, are being investigated to understand whether regulatory actions need to be taken [12].

RDE-compliant driving cycles must fulfil a series of requirements in accordance with EU 2016/427 [13] and conveniently reported in Table 1.1. RDE-compliant cycles are becoming the standard in real world conditions testing and complement the Worldwide harmonised Light vehicle Test Procedure (WLTP) in use for emissions measurement on chassis dynamometers in controlled laboratory conditions [13]. During RDE, the vehicle is being tested under various driving and external conditions, which include driving style, road slopes and banking, varying weather conditions and varying traffic conditions. The RDE-compliant driving cycle developed at Technische Universität Ilmenau, namely Ilmenau cycle [12], is used as a basis for validating the solutions herein proposed. In accordance with the RDE requirements of Table 1.1, Ilmenau cycle is characterised by urban, rural and motorway sections with a total length of 87 km, which occur on public roads in the vicinity of Technische Universität Ilmenau. Compared to WLTP, the RDE-compliant Ilmenau cycle replicates real driving conditions, resulting in greater speed and deceleration values [14]. Moreover, the driving style, weather conditions and traffic characteristics determine the cycle-to-cycle repeatability. Based on more than 200 cycles, the experiments show that the Ilmenau cycle features an average duration of 100 min with a standard deviation of 15 min.

TABLE 1.1: RDE requirements and Ilmenau cycle compliance (after Commission Regulation EU 2016/427 and EU 2017/1154).

RDE-conformity	Requirement	RDE-Ilmenau
Duration	$90\ min < t < 120\ min$	$\approx 100\ min$
Urban trip distance	$s > 16\ km$	$\approx 32\ km$
Rural trip distance	$s > 16\ km$	$\approx 31\ km$
Motorway trip distance	$s > 16\ km$	$\approx 24\ km$
Share of urban window	$29\% < p < 44\%$	$\approx 37\%$
Share of rural window	$23\% < p < 43\%$	$\approx 35\%$
Share of motorway window	$23\% < p < 43\%$	$\approx 27\%$
Share of stop time	$t > 10\%$	$\approx 12\%$
Time on motorway	$t > 5\ min$	$\approx 12\ min$
Average veh. speed (urban sec.)	$15\ km/h < v_x < 40\ km/h$	$\approx 28\ km/h$
Maximum speed	$v_x < 145\ km/h$	$\approx 120\ km/h$
Positive altitude gain	$< 1200\ m/100\ km$	$= 1062\ m/100\ km$

The RDE-compliant Ilmenau cycle is used in this thesis to infer driving features under real conditions. Experiments demonstrate that BLCF is not constant. BLCF is subject to dynamics at various time scales, caused by complex processes taking place in the pad-disc contact layer. Figure 1.3 reports an inference analysis of three Ilmenau cycles performed by three different drivers on the sedan of Appendix D, with special focus on braking events. The deceleration and BLCF values for each brake application are computed in accordance with ECE R90 and SAE J2522, respectively. The mean and standard deviation of deceleration and BLCF values are reported for each trip in Table 1.2.

It is worth noticing that the average deceleration lays for each trip around $1.7 m/s^2$ and

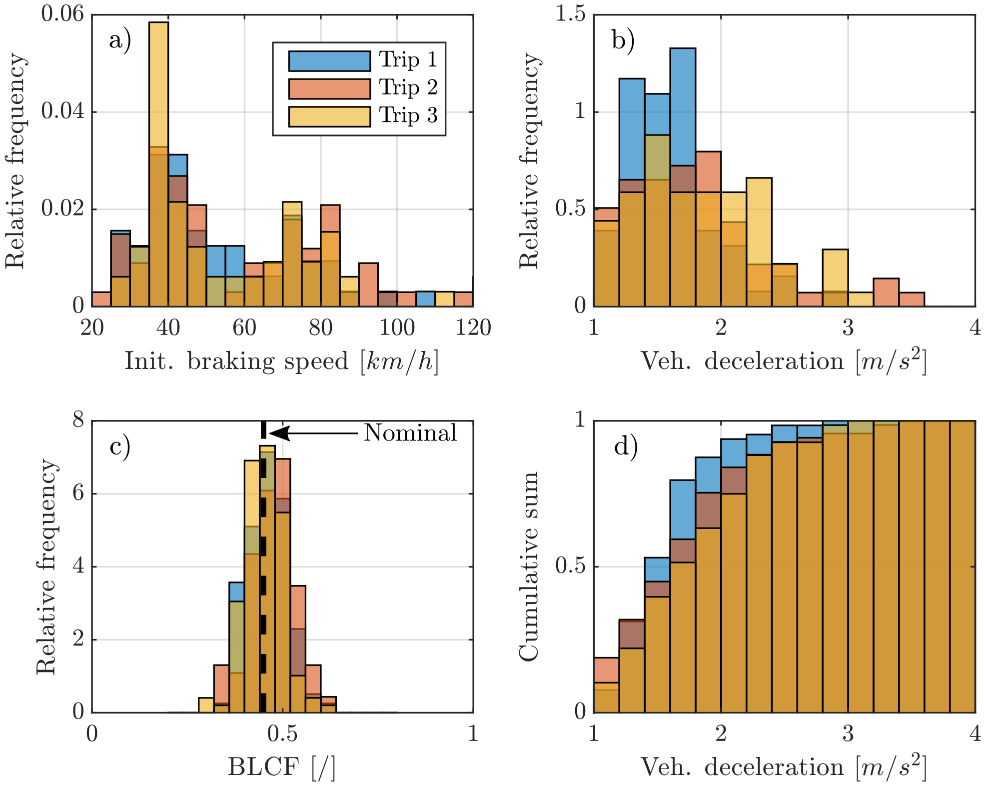

Figure 1.3: *Statistical inference of RDE-compliant Ilmenau cycle during brake applications. The upper figure a) reports the initial vehicle speed upon braking occurrence. The right figures, b) and d), report the probability density function of the vehicle deceleration values and its cumulative. Figure c) reports the probability density function of the observed BLCF. The dashed line in c) represents the nominal BLCF value, in accordance with SAE J2522.*

Table 1.2: Statistical inference for three RDE-compliant Ilmenau cycles.

	Vehicle deceleration		BLCF	
	Mean	Standard deviation	Mean	Standard deviation
Trip 1	1.59 m/s^2	0.35 m/s^2	0.46	0.05
Trip 2	1.70 m/s^2	0.61 m/s^2	0.47	0.06
Trip 3	1.82 m/s^2	0.51 m/s^2	0.45	0.05

it often reaches peaks up to 2 m/s^2. From experimental data, the following conclusions can be drawn:

- deceleration values that lay between 1 m/s^2 and 2 m/s^2, identified herein as gentle braking manoeuvres, occur between 60% and 80% of the time;
- between 10% and 30% of the deceleration values reach an intensity of up to 3 m/s^2;
- very rarely higher deceleration values can be recorded under real driving conditions.

This analysis shows that clear variations in BLCF occur during real driving conditions. Therefore, treating BLCF as a steady-state parameter, or even as a constant, represents a major reduction [15]. Although this topic will be addressed with more details later in the thesis, the knowledge of BLCF plays a crucial role in the performance of base brake control algorithms in brake-by-wire systems. Figure 1.4 reports a simplified brake control scheme of an electric vehicle equipped with an electrohydraulic brake-by-wire. This architecture provides additional flexibility to the base brake functionality as the brake torque request can be allocated between braking axles and blended with the regenerative torque from the powertrain control unit (PCU) without the driver noticing. However, large BLCF deviations from the reference value employed in the controller lead to undesirable deterioration of the brake control functions [16]. In fact, the individual pressure control done by the electrohydraulic control unit (EHCU) requires the provision of BLCF.

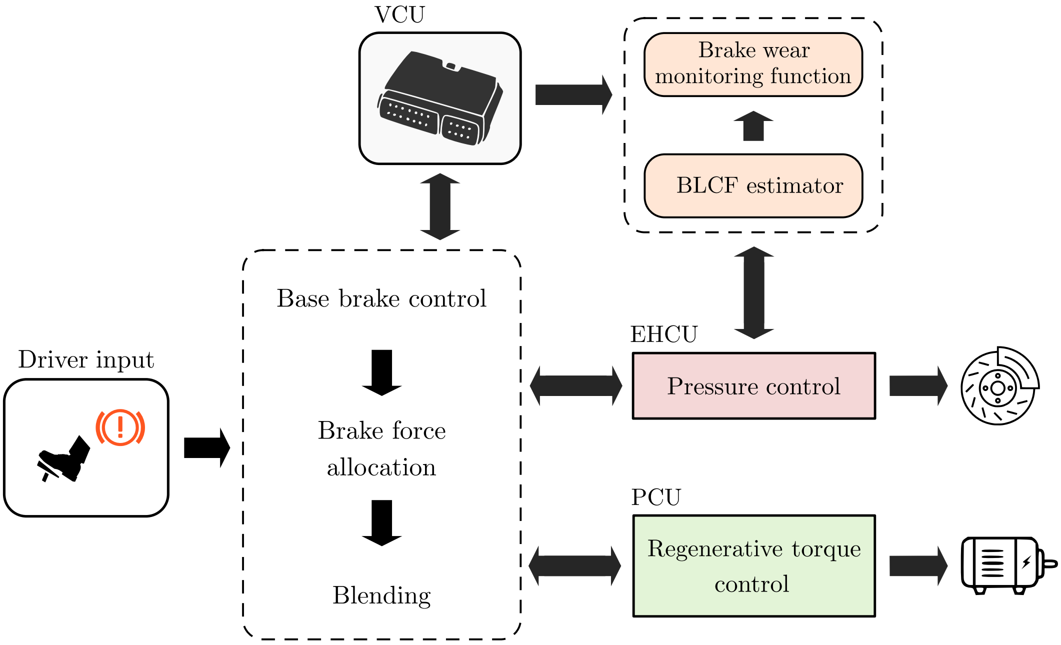

Figure 1.4: *Schematics of in-vehicle communication network with respect to base brake functions. A BLCF estimator allows compensating undesired BLCF variations, improving braking performance and enabling brake-related wear monitoring functions.*

For a pure friction brakes deceleration, Figure 1.5 shows that a wrong BLCF estimate has a direct impact on the achieved deceleration level. Depending on the BLCF estimation error $\Delta\mu_b$, the vehicle might exhibit overbraking, when the actual deceleration is larger than the requested, or underbraking, when the actual deceleration is smaller than the requested. In both cases, in absence of any BLCF compensation function, the driver him-/herself shall compensate for undesired BLCF variations. Hence, an on-board, real-time capable BLCF estimator could be used to compensate the individual calliper pressure control in the EHCU, also in presence of blending with electric motors. The

BLCF estimator along with signals from the vehicle control unit (VCU) allows for novel brake monitoring functions, which provide information on brake-related wear and particle emissions.

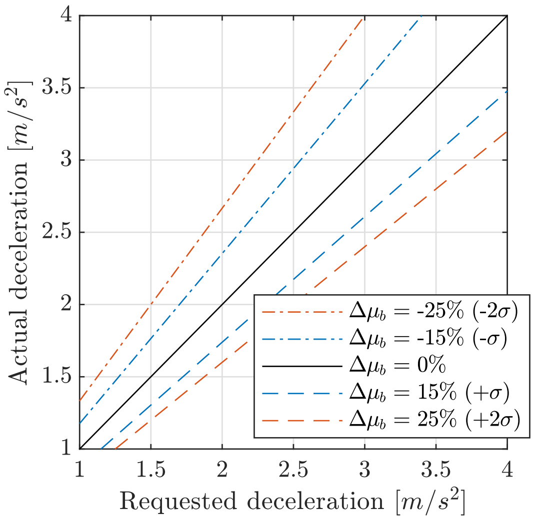

Figure 1.5: *Effect of the BLCF estimation error ($\Delta\mu_b$) on the base brake functionality. A negative error represents underestimated BLCF; a positive error stands for overestimated BLCF.*

1.4 Standards and terminology

The adopted nomenclature is reported at the beginning of this work. The unit of measurements follow the SI reference, unless otherwise stated in the text. Vectors and matrices are differentiated from scalar variables by using bold characters and capital bold characters, respectively. As an example, x may represent a scalar variable, whilst $\mathbf{x}$ and $\mathbf{X}$ represent its vector and matrix variants, respectively. Time-discrete variables feature the subscript k (e.g. the discrete state vector $\mathbf{x}_k$). The adopted engineering vocabulary refers to the following standards:

- ISO 8855 and SAE J670 for the vehicle dynamics;
- ECE R90 for the brake system and components thereof;
- ECE R13H for the brake system architecture and control solutions;
- SAE J2522 for the brake performance characterisation and dynamometer tests.

Chapter 2

Brake friction coefficient estimation in automotive applications

2.1 Introduction

In recent decades, phenomenological and empirical approaches, along with experimental techniques, have evolved compared to the first friction studies of Coulomb more than 200 years ago. Friction estimation has undergone consistent development in industrial applications involving small displacements and velocities where the static friction and pre-sliding displacement play crucial roles. On the contrary, friction estimation in automotive application involving large displacements and high speeds has been rarely addressed.

Upon providing an overview of automotive disc brakes and basic mechanisms ruling the friction phenomena, this chapter surveys and examines existing brake friction coefficient estimation techniques. Thereafter, a benchmark analysis demonstrates that the instances established in the literature do not exhibit satisfactory performance and a novel approach enabling real-time, on-board, inexpensive and robust estimation of the brake friction coefficient is required.

2.2 Construction of disc brakes

A vehicle requires a brake system to stop or adjust its speed. The basic principle used in a brake system is to convert the kinetic energy of the vehicle into other forms of energy, including but not limited to thermal energy and wear. Although two types of brakes can be generally identified, namely drum brakes and disc brakes, these latter have become the popular solution in passenger cars thanks to their superior performance. In a disc brake system, the braking action is achieved by pressing a set of brake pads against a rotating disc. A friction force arises at the pad-disc interface. The produced work is converted into heat and this latter transferred to the environment. The brake calliper represents the fundamental element of a brake system as it is the component where the control actuation is realised. The brake calliper houses the brake pads and provides the channel for the brake fluid, which actuates the pistons.

A schematic representation of typical brake system architectures is reported in Figure 2.1. It is worth mentioning that a floating calliper houses the piston only on the inboard side of the disc (Figure 2.1a). When the pressure is exerted, the piston acts on the inboard pad. The force reaction brought about in the calliper pushes the outer pad against the outer disc surface. Fixed brake calliper does not move relative to the brake disc and houses the pistons on both sides of the disc (Figure 2.1b). The brake fluid must therefore reach both pistons to perform the required brake actuation. In a system with fixed callipers, not only is the mounting much more rigid but the stiffness of the calliper itself is greatly increased. This results in enhanced braking performance and pedal feel. Since the fixed calliper is more suited for a multi-piston configuration, the improved pressure distribution also guarantees more uniform pad wear. The fixed calliper architecture is generally used on high performance vehicles where its higher costs are justified.

Independently of the calliper architecture, it is possible to distinguish characteristic elements. When the brake fluid pressure is increased in the master cylinder, perfect seal between the piston-calliper crevices must be ensured. Typical configurations include the use of one or more o-ring seal(s) rated for the specific maximum calliper pressure. In order to prevent outer dust from entering the fluid chamber, a dust seal is employed. The fluid acts on the calliper piston(s), which in turn lead the pads to move toward the disc. The brake discs are generally made of grey cast iron because it provides good castability and machinability, high thermal conductivity, heat capacity and resistance to brake fade. Nonetheless, the aluminium has been recently discovered as an innovative light-weight material with good NVH properties and reduced wear [17]. Although it cannot guarantee the same fading resistance of the grey cast iron, it contributes to dramatically abate the unsprung mass of the vehicle.

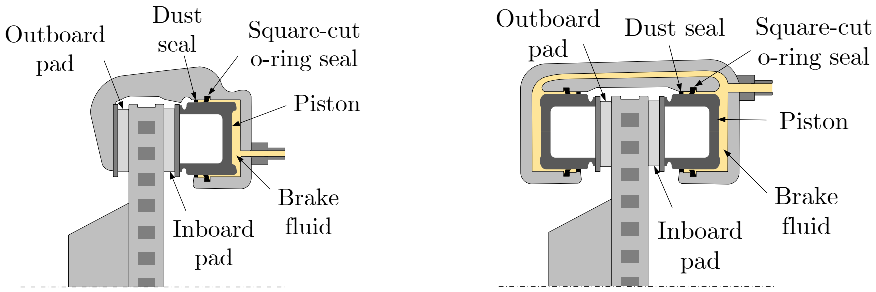

(a) *Schematic of a floating calliper brake system.*

(b) *Schematic of a fixed calliper brake system.*

Figure 2.1: *Schematics of brake systems architecture typically used in passenger cars.*

A brake pad consists of a friction material, also referred to as brake lining, attached to a stiff backing plate (Figure 2.2). A brake pad can incorporate one or more slots on its surface and chamfers in correspondence of the leading edge (tip of the pad coming into contact with a point of the disc surface first) and trailing edge (tail of the pad coming into contact with the same point last). Slots and chamfers are realised to reduce NVH and to improve the removal of wear material [18]. Moreover, the slots allow the pad to bend, reducing the risk of cracks formation. Very often, an additional layer of material, called underlayer, is placed between friction material and backing plate (Figure 2.2). Its main purpose is to damp vibrations originating at the pad-disc interface [19]. The backing plate is solidly bounded to the friction material, either by adhesive bonding or mechanical retention, and transmit the actuation force. The shim is a viscoelastic laminate attached mechanically to the backing plate. During the brake operation it is in contact with the calliper piston or calliper housing, depending on the calliper architecture. The shim dampens vibrations arising from unstable dynamics at the pad-disc interface [20].

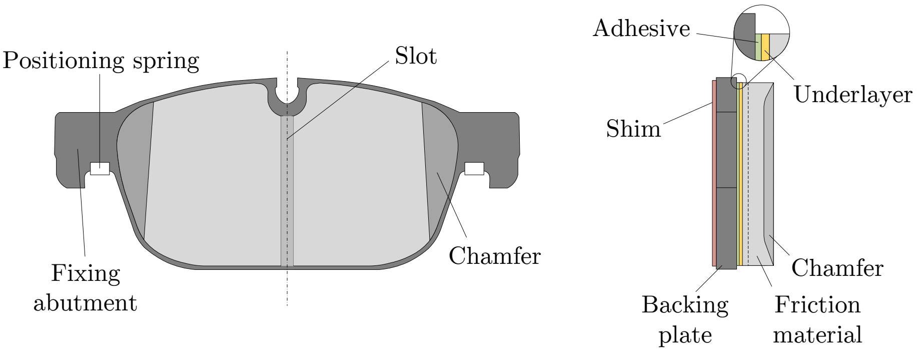

Figure 2.2: *Schematic of a brake pad.*

After the ban of asbestos was officially promoted due to its widespread acknowledgement as a carcinogenic [21], the brake lining manufacturers began to produce a multitude of different brake pads, each with their own special composition. The main components constituting the brake linings are: (i) the binder, often composed of phenolic resins, holds the components of the lining together; (ii) the reinforcing fibres provide mechanical strength and can be made of metal, carbon, glass, aramid or ceramic material; (iii) the filler, commonly constituted of mica, vermiculite or barium sulphate, is used to improve the machinability of the lining; (iv) the additives, mainly represented by graphite or metal sulphides, are used to improve the thermal stability and to control the wear rate. In particular, the reinforcing fibres provide mechanical strength to the friction material; in fact, the braking load is carried by tiny plateaus of reinforcing material, which make up only a fraction of the total pad surface [22]. The binder maintains the brake lining structural integrity under mechanical and thermal stresses: it must exhibit a high heat resistance because it has to remain structurally intact during the braking operations [22].

The fillers are used to improve the lining manufacturability and to reduce the entire cost of the pad itself. The additives represent another ingredient and are used to modify the friction coefficient and the brake behaviour during transient operations [22]. The additive is responsible for the enhancement of the lubricant or the abrasive behaviour of the brake lining.

It is worth reporting that friction material manufacturers currently use more than one hundred different components for the production of a brake lining. The brake lining composition is set in order to match safety, noise and wear requirements such as short running-in period, stability of friction coefficient under combined high speed-load, stability of the friction under high temperature, stability of friction under wet conditions. Regardless, the brake pads can be classified under three main categories: (i) low-steel linings are generally referred to as ECE linings in Europe, whose reinforcing fibers are mainly made of steel and copper, where the latter acts as a lubricant; (ii) non-asbestos organic, also known as NAO linings, are composed of mineral fibres or other composition modifiers such as rubber and graphite and used in USA, China, Japan; (iii) semi-metallic linings represent a mixture of metallic and organic materials.

2.3 Tribology of disc brakes

The BLCF value is linked to the number and size of contact patches involved in the pad-disc interface [23]. The plateaus can grow or decay in relation to processes of agglomeration, compaction and disintegration of the wear debris. As described by Gramstat in [24], this dynamics is not only dependent on the lining chemical composition but also on the brake operating conditions.

With reference to the pad-disc tribological contact, two main theories have been proposed to describe the processes taking place at the pad-disc interface. The first approach is based on the studies of Eriksson in [25, 22], which relate the brake performance to the formation, growth and degradation of contact plateaus. The second approach is based on the studies of Österle in [26], which relate the brake performance to the third body layers formed during a brake application. In accordance with this latter, the pad and disc are separated by a layer of third body material that consists of load-bearing patches and fine grained wear debris, whose thickness is function of the temperature. Based on *in-situ* investigations conducted at Technische Universität Ilmenau, the two mechanisms coexist under the same braking event [24]. Particularly, wear debris motion in the third body layer is responsible for the compaction, formation and destruction of load-bearing locations, which constitute the real area of contact. The stability of the third body layer hinges upon the pad and disc surface characteristics, which are improved after the bedding-in has taken place. During this phase, the average BLCF is not stable because its value is a function of the tribo-layer thickness [24].

The general consensus among the brake community is that the real contact area consists of primary and secondary plateaus [25]. The primary plateaus are made of structural components of the friction materials (e.g. metal fibres) and principally form during the initial run-in of a green (unused) pad, thus causing a large increase in BLCF during the first stops. The secondary plateaus are composed of wear debris, compacted and agglomerated in front of the more stable primary plateaus (their constituents may differ from the lining chemical components). The debris are composed of less wear resistant pad constituents and might agglomerate and compact to form new secondary plateaus.

As depicted in Figure 2.3, the area of real contact is confined within the plateaus that generally constitute a fraction of the geometric surface area of the pad [25].

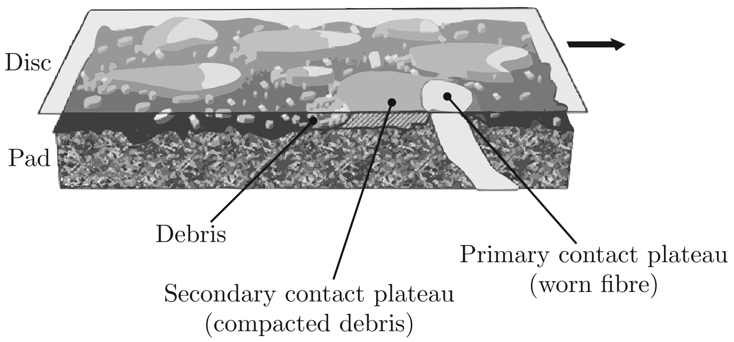

Figure 2.3: *Schematic of the contact situation at the interface between an organic brake pad and a grey cast iron disc, involving plateaus of primary and secondary type (after [25]).*

In-situ analysis performed at Technische Universität Ilmenau on a brake dynamometer equipped with transparent borosilicate brake disc enables optical investigation of the friction mechanisms at the pad-disc interface. By means of a high speed camera, a section of approximately 10 mm^2 on the pad surface can be visualized with up to 100X magnification [27]. The pad surface topography at successive time steps for a drag brake test with 8 bar brake pressure and a disc rotation of 35 min^{-1} is reported in Figure 2.4. With reference to this latter, the speed vector indicates the disc direction of rotation relative to the pad. The test is performed on a bedded-in brake pad. The secondary plateau in Figure 2.4a has already formed and constitute the base of agglomeration and compaction of additional debris. The experimental test demonstrates that upon pressure application at $t = 0$ s, a flow of wear debris is generated. Thereafter, the agglomeration and compaction of wear debris leads to the enlargement of the secondary plateau and thus to a widening of the real contact area (Figure 2.4b and Figure 2.4c). Upon reaching a critical size at $t = 25$ s, the small area of real contact experiences plastic deformation and is disintegrated by wear (Figure 2.4d and Figure 2.4e). The process might stop or, as in this case, proceed until complete destruction of the secondary plateau (Figure 2.4f). It is worth pointing out that this *in-situ* analysis only focuses on an area corresponding to approximately 0.2% of the pad area. Hence, the same phenomenon occurs simultaneously at microscopic scales in other locations of the pad surface.

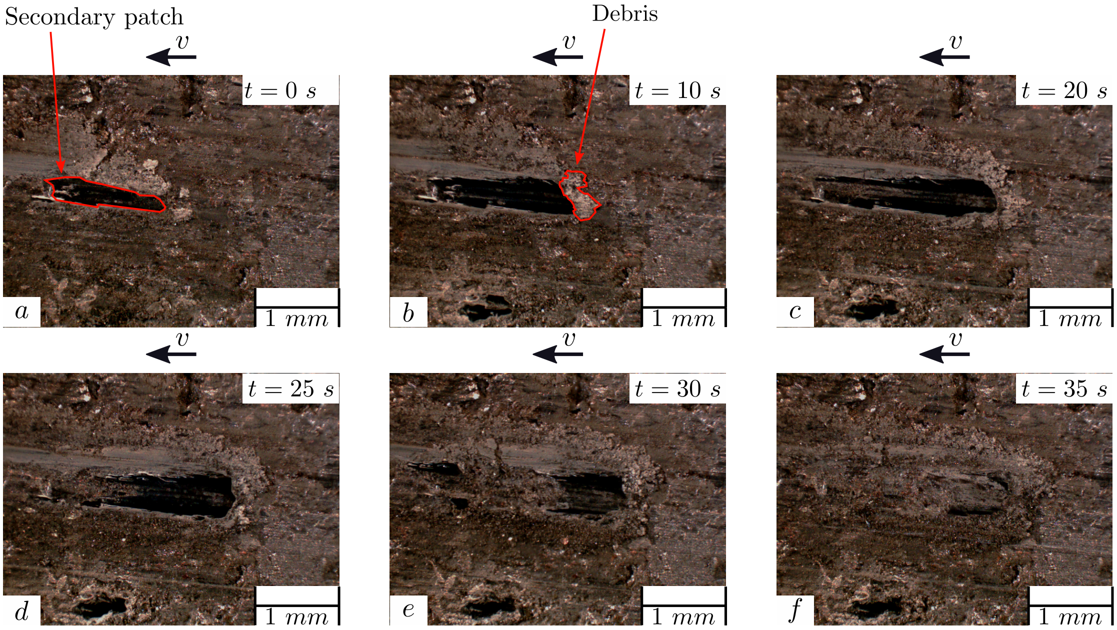

Figure 2.4: *Phenomena interaction at the pad-disc contact interface for ECE lining and borosilicate brake disc. Graph a) to c) report the wear debris agglomeration and compaction dynamics on a secondary patch. Graph d) to f) show the destruction dynamics due to plastic deformation, taking place upon achieving a critical patch size (after [24]).*

The agglomeration - compaction - disintegration dynamics of the secondary plateaus rules well-known mechanisms such as brake fading [28, 29], brake bedding-in [22], brake wear [30, 31]. Other instances demonstrate that the contact patch formation is also influenced by humidity [32] and local pressure [25]. In relation to the plateaus birth-growth-destruction dynamics, the coefficient of friction can range between 0.3 and 0.7 [24, 33].

2.4 Estimation of the friction coefficient of disc brakes

Only few literature instances address the estimation of the brake lining coefficient of friction in automotive applications. The proposed solutions have been mainly developed for simulation and design purposes [15], the majority of which has not undergone experimental assessment but only simulation tasks. Moreover, many of the proposed approaches stem from experiments conducted on pin-on-disc tribometers under controlled laboratory environment where real braking conditions are hardly reproducible [34, 35]. Studying the BLCF dynamics is certainly a challenging task as it is the result of several mechanisms taking place at the pad-disc interface, such as bedding-in [22], fading [28] and stick-and-slip [36]. The BLCF dynamics not only depends on the brake operating conditions but also on the environmental conditions [37], brake ageing [22] and brake lining material composition [33]. In this section, a literature review of state-of-the-art BLCF estimation methods is provided. Thereafter, the most popular solutions are compared under real driving conditions.

2.4.1 Literature review

The sought literature instances suggest that BLCF estimation techniques can be classified into three main categories, namely look-up-tables, static and dynamic models and neural networks [15].

Look-up-tables are widely used in the automotive industry for control purposes. They demand an accurate design of experiments on the brake dynamometer and usually do not include more than two inputs because of the data curse of dimensionality. In [38, 39], the authors propose a look-up-table linking the brake disc speed and brake pressure to BLCF. An illustration is reported in Figure 2.6. This approach cannot account for the combination of thermal and mechanical behaviour of the pad-disc contact since the temperature does not appear as an influencing factor.

Static and dynamic models correlate BLCF with system inputs, such as the brake pressure, and with system states, such as the disc temperature and speed. Static models imply an algebraic dependence between the friction force and input and state variables, whilst dynamic models describe the memory effect by means of a complementary differential equation ruling the dynamics of the friction forces. Model based approaches require an *ad-hoc* parameters calibration with respect to the specific plant. The experimental burden necessary to the model identification depends strongly on the number of parameters and on the analytical dependencies. In general, strong non-linearities and differential equations lead to an increased experimental burden [40]. In [41], a static formulation based on the stick and slip dynamics is proposed by considering a rate-dependent damping term for the Stribeck effect and an elastic term for the pre-sliding modelling [42]. In [43], a simple quadratic model in the velocity state is used. In [44], an analytical formulation considering only the friction dependence against the speed is proposed. A very simple analytical formulation based on steady-state experimental tests that correlates pressure, speed and temperature with friction and wear is also assessed in [45]. In [46], an alternative algebraic formulation is put forth that, in addition to the sliding speed, involves thermal effects due to the increase in temperature of the friction materials. In [47, 48], a simplified static LuGre model is used to determine the friction force between disc and pad. The authors in [49] propose a novel static friction formulation as a function of the brake disc temperature, brake pressure and braking speed. In [50], Ostermeyer proposes a dynamic model that relies on two differential equations in the BLCF and brake disc temperature states, respectively. This dynamic model tries to capture the transient behaviour of the friction and its dependence against the temperature during braking occurrence. The frame of the model dwells on the assumption that the friction coefficient is the result of the equilibrium between the flow of formation and destruction of contact patches, as presented in Figure 2.4. The model is as follows:

$$\begin{cases} \dot{\mu_b} = -p_1 \left[\left(F_n \, \omega \, r_{eff} + p_2 \right) \, \mu_b - p_3 \, \tau \right], & \text{(2.1a)} \\ \dot{\tau} = \xi \, \left\| 2 \, n_p \, F_n \, \mu_b \, \omega \, r_{eff} \right\| - \delta_{ht} \, (\tau - \tau_{env}), & \text{(2.1b)} \end{cases}$$

where, the normal clamping force F_n is defined as,

$$F_n = p_b \, A_k, \tag{2.2}$$

and p_b is the applied brake pressure, n_p is the number of calliper pistons per side and A_k is the calliper piston(s) area. Equation (2.1a) is the dynamic equation in the BLCF state μ_b. Equation (2.1b) is better known as lumped capacitance model [29] and describes the thermal dynamics of the brake rotor, where τ represents the lumped disc temperature and τ_{env} is the ambient temperature. In Equation (2.1a), the term in round brackets describes the destroying effect linked to the friction power and the extent of the patches area supposed proportional to BLCF itself, where ω is the disc angular speed and r_{eff} is the brake effective radius. The parameter p_1 is a time constant ruling the growth/destruction rate of the contact area and its current value; p_2 is a correlation parameter between the change rate of the contact area and its current value; the parameter p_3 correlates the change rate of the contact area and temperature. The strictly positive sign of the parameters is driven by stability consideration, although this might not reflect the real nature of the friction process. As shown by the author of the present thesis in [40], the parameters introduced by Ostermeyer cannot be considered constant during a braking manoeuvre and further dependencies shall be explored. Moreover, Equation (2.1) derives from experimental results conducted on the pin-on-disc where the temperature dynamics is much different from a real brake system.

Artificial neural networks, herein referred to as ANN, have found extensive application for the estimation of BLCF as a function of braking pressure, sliding velocity and disc temperature [51]. ANN differ from traditional modelling approaches since they are trained to learn the right solutions rather than being designed to model specific phenomena. Modelling non-linear relationships using ANN is generally simpler in comparison with other non-linear regression approaches as they offer high adaptability and do not require knowledge of the friction mechanisms. The literature examples show that ANN can predict with sufficient accuracy the effect of braking conditions on tribological performance, provided that a demanding experimental campaign is a justified mean. The explanatory Figure 2.5 shows that ANN are composed of nodes (or neurons), responsible for the processing of information through the layer and branches (i.e. synapses), responsible for the transmission of signals between layers. The neurons between the input and the output layers constitute hidden layers that add non-linearity to the system and ramify the interactions among the variables of the previous layer. It is obvious that the network performance depends on its structure in terms of both number of neurons per each layer and number of hidden layers. The transmission of the signals is performed in analogy with the way biological neural systems operate. The signals are generated in the neurons when the information coming from the previous layer exceeds a certain threshold (bias). Once the signal is generated, it is transmitted through the synapses to the next layer; the synapses modulate the relative importance of the signals flowing between two layers. Drawing on the analytical representation, the threshold crossing is modelled through an activation function, generally a sigmoid function; the transmission across the layer is realised through a weighted summation of the signals coming from the previous layer. The choice of activation function is particularly important to capture the non-linearities of the modelled mechanisms.

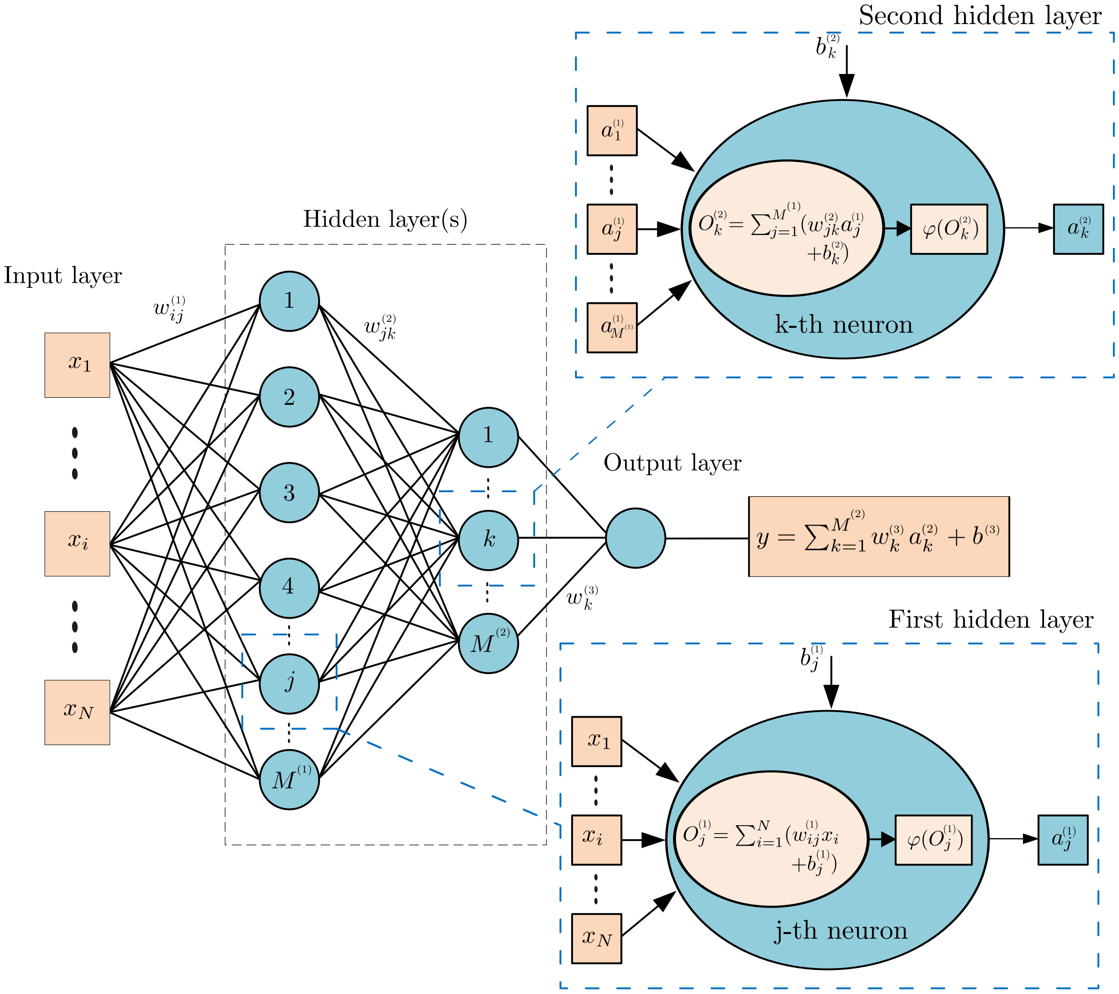

Figure 2.5: *Schematic of a fully-connected two-hidden layer neural network. It is worth noticing that the subscripts i, j and k refer to the connections between adjacent layers.*

ANN exist in several shapes and architectures. ANN usually employed by the tribology community feature a two-layered structure, as per Figure 2.5. In this case, the input layer has N inputs, the two hidden layers have $M^{(1)}$ and $M^{(2)}$ neurons, respectively, and the output layer provides the estimated BLCF. As mentioned above, the activation function in the hidden layers is generally represented by the sigmoid functions of Equations (2.3b) and (2.3d), while linear functions are used for the output layers:

$$O_j^{(1)} = \sum_{i=1}^{N} w_{ij}^{(1)}\, x_i + b_j^{(1)}, \tag{2.3a}$$

$$a_j = \varphi(O_j^{(1)}) = \frac{1}{1+e^{-O_j^{(1)}}}, \tag{2.3b}$$

$$O_k^{(2)} = \sum_{i=1}^{M^{(1)}} w_{jk}^{(2)}\, a_j^{(1)} + b_k^{(2)}, \tag{2.3c}$$

$$a_k = \varphi(O_k^{(2)}) = \frac{1}{1+e^{-O_k^{(2)}}}, \tag{2.3d}$$

$$y = \sum_{i=1}^{M^{(2)}} w_k^{(3)}\, a_k^{(2)} + b^{(3)}. \tag{2.3e}$$

The output of each $j-th$ neuron to the first hidden layer, Equation (2.3a), stems from a weighted summation that passes through the activation function of Equation (2.3b), where a_j is the output of the neurons of the previous layer, N_u is the number of inputs to the neuron and $w_{ij}^{(1)}$ is the weight between input $i-th$ and neuron $j-th$. The sum in Equation (2.3a) is biased by the factor $b_j^{(1)}$. The same algorithm holds for the output of the second hidden layer, where, this time, the previous layer of $M^{(1)}$ is weighted by the factors $w_{jk}^{(2)}$. The sum in Equation (2.3c) is biased by the factor $b_k^{(2)}$. Finally, the output layer performs an algebraic summation, where the outputs of the $M^{(2)}$ neurons are weighted by the factors $w_k^{(3)}$ and biased by $b^{(3)}$, as per Equation (2.3e). ANN output is represented by the variable y (Figure 2.5).

ANN must be trained on a set of experimental data defining the relationships among the friction material behaviour and different formulations, environmental conditions and operating conditions. In other words, before its direct application, it is required to teach the network analytical relations between input and output to ensure results with the lowest error possible. The number of training data pairs has a significant influence on the networks generalisation capability. ANN require that the training examples span the domain of interest completely; indeed, as a general rule of thumb, the operation of interpolation is always preferred to extrapolation. The non-linearity of ANN also implies the existence of many sub-optimal solutions, which correspond to local minima of the associated error function. Therefore, depending on the initial choice of the networks parameters, namely weights and biases, multiple solutions are allowed. One of the most common approaches for the training of a network is based on the back propagation method, whose basic principle is to reduce the square error between the expected and measured output of the network by modifying the weight and bias vectors [52]. Hence, the squared error between the measured and the estimated output is differentiated against the weights and biases in order to define the direction of error reduction. After the training procedure has completed, two additional steps must be performed for the achievement of good estimation performance, namely validation and testing. A validation dataset is used to exit the ANN training process by criteria of estimation accuracy. A test dataset is used to examine the final quality of the developed ANN and to evaluate their generalisation and prediction capabilities.

In [53], the author focuses on the analysis of the influence of the ANN architectures on its generalisation capability and conclude that an insufficient number of neurons in the hidden layers leads to inability to solve the problem. On the other hand, too many neurons lead to over-fitting and consequently to a worsening of the generalisation capability. In [54], ANN are proposed to predict BLCF by using as input parameters the brake lining composition, the manufacturing process conditions and the brake operating conditions. In [45], experiments performed on a brake dynamometer are used to identify a static ANN relating pressure-speed-temperature with BLCF. In [55], the authors consider the hysteresis phenomenon by including the sliding acceleration influence. Moreover, the authors of [55] envisage applying ANN to generate $3D$ maps of BLCF for the implementation of advanced control algorithms in the brake control units. In [56], ANN are used to estimate the tribological properties of frictional materials, in particular BLCF and wear rate. The author of [57] puts forth an estimator of the BLCF mean value for non-asbestos brake linings with different compositions. In [58], ANN have been used to model BLCF by considering several influencing factors such as the friction material composition, the manufacturing parameters and the operating conditions. Further studies concern the use of dynamic ANN to sift out the influence of disc brake operating conditions and material characteristics on the generated braking torque [53, 59]. The listed literature instances require very expensive experimental campaigns for the parameters identification and may provide wrong results when the operating conditions lay far from the identification data set.

In the next section, the functionality of the most popular state-of-the-art BLCF estimation techniques is tested under real driving conditions. This analysis allows identifying the applicability limits of the surveyed methods and motivates the necessity to devise a novel estimation approach, free from *ad-hoc* parametrisations and thus robust against changing plant characteristics.

2.4.2 Benchmarking of state-of-the-art estimation algorithms

The estimation capabilities of a second-order surface response model, the Ostermeyer model and a fully-connected ANN are analysed in the present section. In this regard, real driving data from the instrumented sedan in Appendix D is used. The true BLCF reference value for the benchmark is provided by the estimation approach later addressed in Chapter 4. With reference to the inference analysis presented in Chapter 1, the surveyed approaches are identified on Trip 1 and validated on Trip 2. It is also worth noting that the second-order response surface is extracted from quasi-static braking conditions in accordance with SAE J2707, the Ostermeyer model is parametrised against the true BLCF values and ANN features a common two hidden layer architecture with eight and six neurons. Graphical representations of the second-order surface response and ANN are provided in Figures 2.6 and 2.7, respectively. The second-order surface approximation only considers vehicle speed and brake pressure as input variables. ANN, on the contrary, allows for the inclusion of multiple inputs without incurring curse of dimensionality. Moreover, Ostermeyer model and ANN require estimation of the disc temperature, which is normally not available on commercial vehicles. For this reason, the benchmark also addresses the impact that a wrong temperature estimate has on BLCF. For the sake of space, only the results corresponding to the front-left wheel of the sedan in Appendix D are reported. It is however worth noting that the methods under analysis require different parametrisations for the rear wheels.

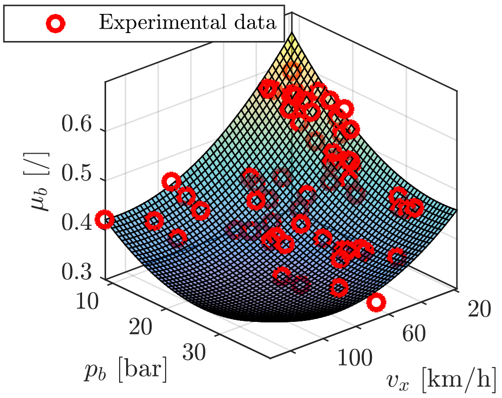

Figure 2.6: *Second-order response surface based on quasi-static braking conditions extracted from experimental data.*

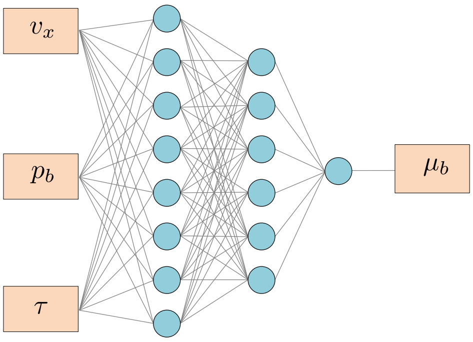

Figure 2.7: *Two-layered ANN trained against the collected data.*

Four manoeuvres extracted from RDE-compliant Trip 2 are considered: braking (A) consists of a mild deceleration at low speed; braking (B) identifies a mild deceleration at high speed; braking (C) is a gentle deceleration at low speed; braking (D) features a gentle deceleration at high speed. Figures 2.8a to 2.8d report the benchmark results with reference to the second-order response surface, Ostermeyer model and ANN. Moreover, the results also include the estimated disc temperature by means of the lumped capacitance model in Equation (2.1b). The estimation performance of the techniques under analysis are quantified in terms of normal round mean square error in Table 2.1.

The results clearly show that ANN exhibits better performance under all circumstances. Nevertheless, the results also demonstrate that ANN is more susceptible to a wrong estimate of the disc temperature, as per Figure 2.9, when compared to other approaches.

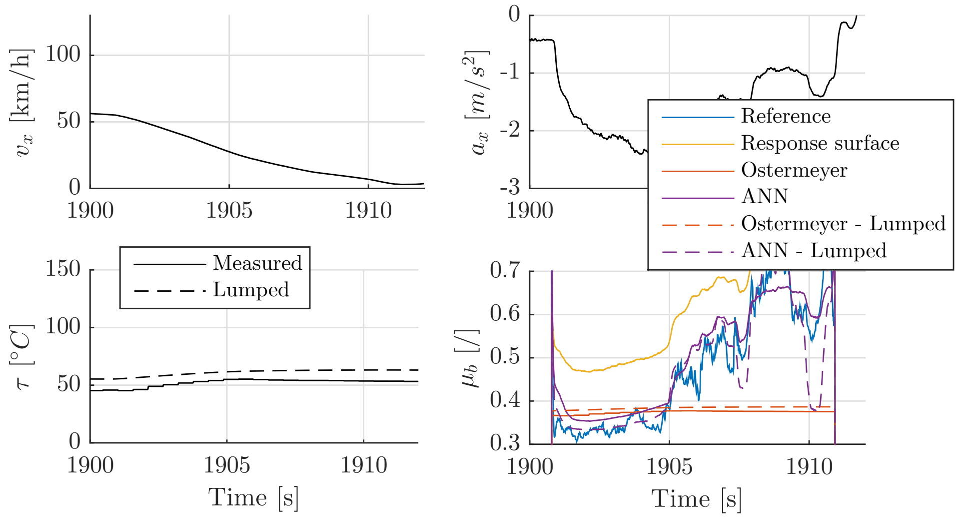

(a) *Braking manoeuvre (A) characterised by low initial vehicle speed and mild deceleration level.*

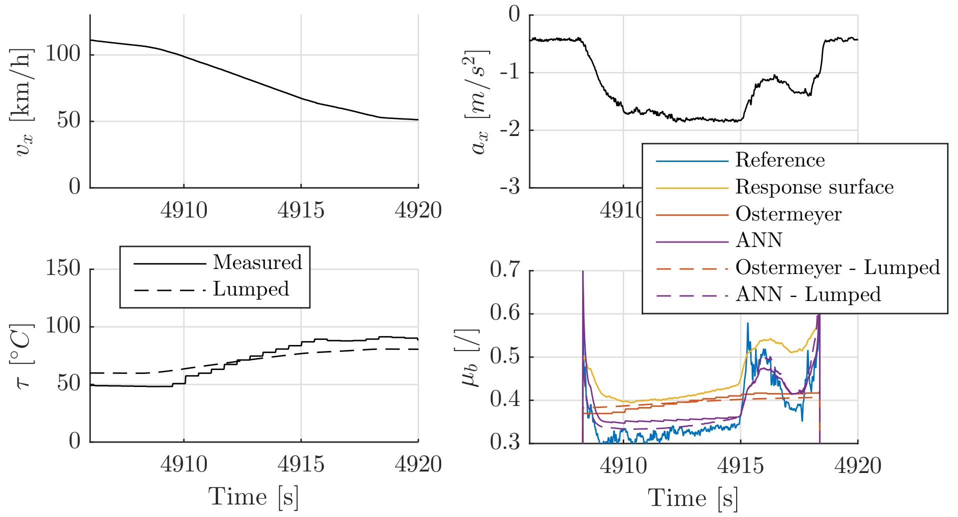

(b) *Braking manoeuvre (B) characterised by high initial vehicle speed and mild deceleration level.*

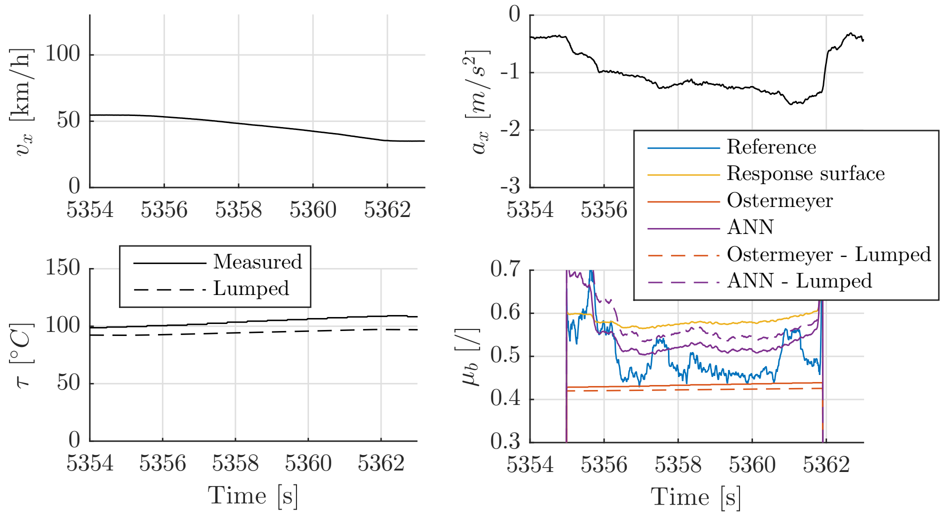

(c) *Braking manoeuvre (C) characterised by low initial vehicle speed and gentle deceleration level.*

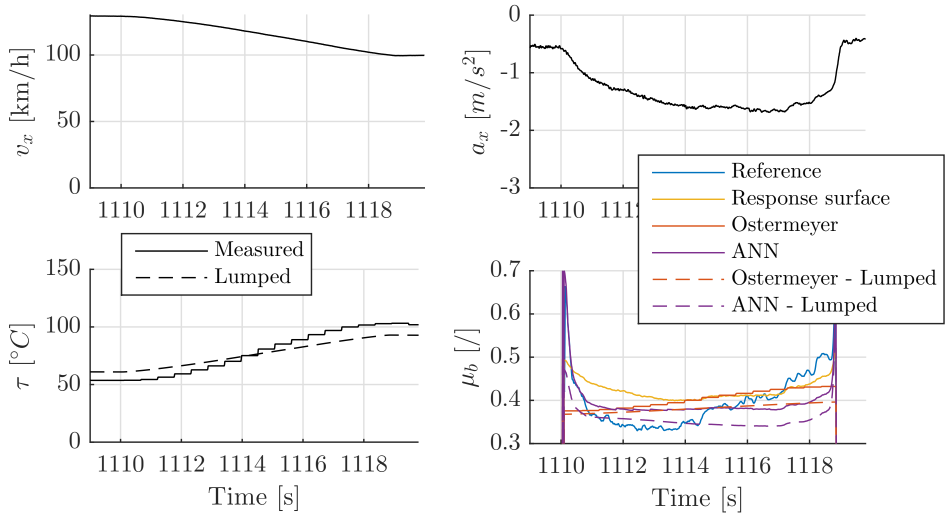

(d) *Braking manoeuvre (D) characterised by high initial vehicle speed and gentle deceleration level.*

Figure 2.8: *Braking manoeuvres extracted from Trip 2 of RDE-compliant Ilmenau cycle (please, refer to Chapter 1). The upper figures relate to the vehicle kinematics; the bottom-left figures show the measured and estimated disc temperature; the bottom-right figures report reference and estimated BLCF.*

ANN also outperforms other methods during BLCF transients. This is particularly noticeable in Figure 2.8a. In accordance with Table 2.1, the method based on the surface response does not guarantee acceptable estimation performance, being unable to capture the BLCF dynamics and featuring a relatively high estimation error. Similarly, Ostermeyer model shows poor estimation performance, particularly in the case of manoeuvre (A) characterised by a progressively decaying deceleration intensity. Although Figure 2.9 indicates that Ostermeyer model exhibits good robustness against temperature estimation errors, this latter performs poorly at tracking the BLCF dynamics.

TABLE 2.1: Normalised RMSE of the analysed BLCF estimation techniques. The estimation error is computed with respect to a true BLCF estimate.

		Response surface	Ostermeyer	ANN	Ostermeyer*	ANN*
Driving section	A	28.14%	36.99%	14.06%	35.70%	14.67%
	B	17.74%	13.19%	6.68%	13.96%	7.85%
	C	18.35%	20.03%	10.95%	21.78%	11.48%
	D	12.27%	13.52%	10.05%	14.61%	9.71%

*enhanced with lumped capacitance model for temperature estimation.

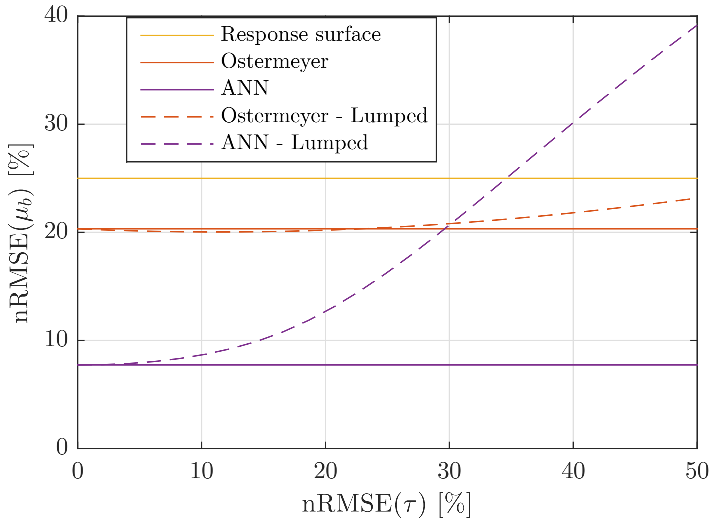

Figure 2.9: *Sensitivity of the employed estimation approaches against error in the temperature estimate. Errors refer to whole Trip 2.*

The following conclusions can be drawn from the benchmark results:

- estimation techniques based on look-up-tables and ANN do not provide rightful physical insight on the friction mechanisms but only describe the effects;
- look-up-tables are of simple interpretation; however, similarly to ANN, a high experimental effort is demanded to their implementation;

- model-based approaches may be designed to be robust against wrong temperature estimates; however, they require a high experimental burden for the parameter identification;
- ANN may exhibit high sensitivity against wrong input (e.g. wrong temperature estimate) and the associated computational burden may not comply with the hardware requirements;
- all previous methods require a plant-specific parametrisation;
- the analysed approaches become unreliable when the plant characteristics change due to brake wear itself or in case of replacement with after market brake pads;
- the analysed methods feature poor extrapolation performance and are limited by the necessity of estimating the disc temperature.

These considerations motivate the need for a novel estimation approach that is robust against external sources of error (e.g. wrong temperature estimate or noisy speed measurement) and does not require costly experimental campaigns for its parametrisation. For this purpose, the present work focuses on the development of a state observer, which provides a BLCF estimate based on information readily available from vehicle sensors without the need to model friction mechanisms. In accordance with the schematic of Figure 2.10, the observer design consists in creating a reference system model, whose state variables are to be observed. The reference system model shall be arranged so that output and input variables are known. To contain the model error with respect to the real system, the former is corrected with the error between measured and observed output variables. Depending on the observer type, the reference tracking error may be used under different shapes to correct the states estimation.

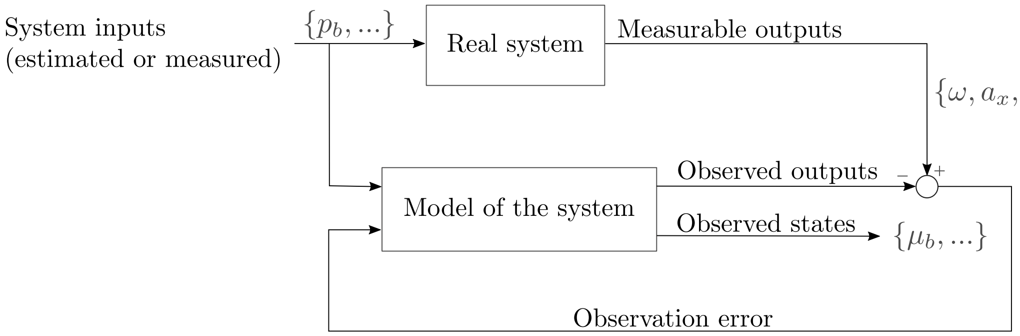

Figure 2.10: *Schematic of a state observer.*

Although this will be made clear next in Chapter 4, it is worth mentioning that the proposed observer considers the chassis and wheels rotational dynamics as reference system models, assumes the brake pressure as known system input and relies upon the wheel speed sensors and the inertia measurement unit as measurable outputs. Thanks to this scheme, unlike the above listed methods, the analytical description of non-linear phenomena occurring at the pad-disc interface is avoided. The features of a state observer can be summarised as follows:

- it uses measurements coming directly from the vehicle sensors by avoiding an analytical description of the brake phenomenology;
- it does not require high experimental burden for the parameters identification and its calibration can be directly performed on the target vehicle;
- it is easily adaptable to new or constantly changing plant characteristics (e.g. replacement with aftermarket brake pads);
- it is valid for any brake systems independently of the calliper geometry, friction material composition and brake architecture;
- it can be designed so as not to rely on temperature or friction models, which are source of errors.

2.5 Research objectives and methodology

The knowledge of BLCF plays a crucial role in the performance of base brake control algorithms in brake-by-wire systems since large deviations in the BLCF from the reference value employed in the controller could lead to undesirable deterioration of the brake control functions [16]. The main research objective of this thesis is a novel BLCF observer that enhances braking performance and enables advanced brake monitoring functions. This is achieved by compensating for undesired BLCF variations in vehicles equipped with brake-by-wire systems and monitoring thermal and wear state of the brake components. The compensation function cooperates with existing active safety systems and enhances braking performance in presence of brake blended operation with electric motors, uncertain environment and driving behaviour.

At present, there is no general norm or consensus regulating BLCF estimation accuracy requirements in vehicle dynamics control applications. Nevertheless, in accordance with the experimental results in Figure 1.3 and Table 1.2, it can be concluded that the BLCF true value falls within 25% deviation from its nominal value with 95% confidence interval (two-sigma rule). In accordance with the simulation results of Figure 1.5, if a constant BLCF estimate equal to its nominal value is used in the controller, in absence of any BLCF compensation, the driver experiences a normally distributed deviation in the actual deceleration from its requested value up to 25% with 95% confidence interval. Hence, the knowledge of BLCF is necessary to maintain the vehicle deceleration close to the desired value and to enable advanced brake monitoring functions. The estimation accuracy of the on-board, real-time capable BLCF observer shall enable the compensation function and outperform the case where a constant BLCF estimate, equal to its nominal value, is used.

The achievement of the above mentioned research objectives requires a modelling framework for the development, verification and validation of estimators and controllers. Model-in-the-loop (MIL), software-in-the-loop (SIL) and hardware-in-the-loop (HIL) are integrated in different stages of the research activity. Details of the vehicle dynamics model and subsystems thereof are reported in Appendix A. The proposed functions are developed and tested under MIL/SIL environment, whilst their functionality is verified under HIL environment. Finally, on-road tests reveal necessary to fine-tune and validate the developed functions. Under the framework of this work, the development, verification and validation of vehicle control and estimation functions follows industry compliant standards and processes that more generally relate to ISO/IEC 15504-2 (Automotive SPICE). The standard software development process specified in ISO/IEC 15504-2 is the V-cycle. This latter prescribes the activities to be performed and the results that have to be produced during the functions development. In Figure 2.11, the left side of the V-cycle represents the decomposition of requirements and creation of functional specifications for the function development. The right side of the V-cycle represents the software integration and its validation. Due to the complexity and size of the developed control functions, the V-cycle improves the overall quality of the function, increases development efficiency and eliminates systematic software errors.

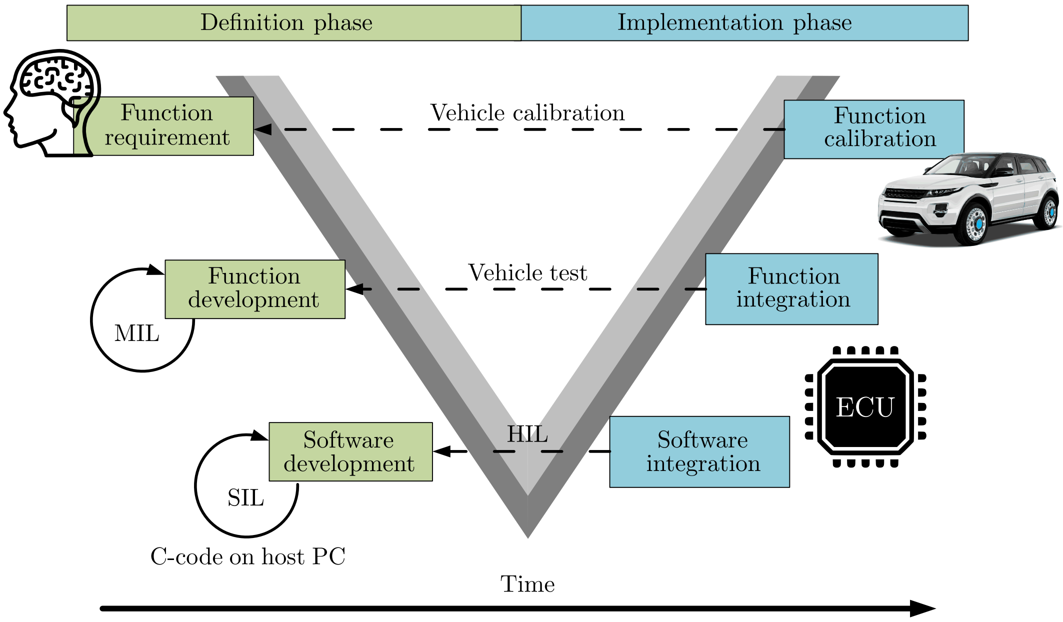

Figure 2.11: *Depiction of the function development process.*

To achieve the listed goals, this research made use of top-notch facilities at Technische

Universität Ilmenau (Ilmenau, Germany), among others a modern HIL test-rig for real-time verification of brake functions, a brake dynamometer for brake-related wear analysis, two vehicles for testing under real driving conditions. Important research contributions were provided by Volvo Cars (Göteborg, Sweden), which supported the experimental campaign on the brake dynamometer aimed at formulating and validating a novel BLCF model to enable loyal MIL/SIL/HIL simulations [40]. The University of Liverpool (Liverpool, England) supported the investigation of novel meta-models capable of predicting brake-related particle emissions under real driving conditions. Finally, tests conducted in collaboration with Flander's Make (Lommel, Belgium) at the Ford Lommel proving ground were used to test the functionality of the proposed BLCF observer. In the framework of this work, the design of experiments relevant to the development of the proposed control and estimation functions complies with SAE J2522 and SAE J2707 standards for brake dynamometer testing and ECE R13H guidelines for vehicle dynamics simulations and proving ground tests.

As basic performance index for the quantification of estimation performance, the round mean square error (RMSE) is considered. This latter is widely used in control applications because it provides a second degree loss function that incorporates the estimation bias. On the contrary, the RMSE emphasizes greater errors than smaller ones, which makes it very sensitive to outliers. For this reason, depending on the use case, additional key performance indexes such as the average absolute deviation and the variance accounted for are used.

2.6 Originality and innovative aspects of the research

The present work introduces numerous novelty elements. Relevant literature instances are brought up in each dedicated chapter and the innovative contributions specified in the introductory section of each chapter. For the sake of clarity, the distinctive research contributions are herein summarized.

The literature features inconsistent and sometimes contradictory results when it comes to the BLCF dependencies against brake operating conditions [40]. As a consequence, existing modelling frameworks fail at describing the underlying BLCF dynamics under varying operating conditions [60]. In the framework of this work, experiments are conducted on a cutting-edge brake dynamometer at Volvo Cars (Göteborg, Sweden) to study the impact of the brake operating conditions on the BLCF dynamics. A novel BLCF dynamics model that outperform state-of-the-art techniques is thus introduced to enhance the modelling fidelity of model-, software- and hardware-in-the-loop tests for the brake functions development and verification.

Existing BLCF estimation techniques are not able to correctly capture the BLCF dynamics under real driving conditions [16] or are only validated under very limited test conditions [61]. In this work, a novel BLCF observer based on a non-linear Kalman filter is developed and tested under the enhanced SIL/MIL simulation frameworks. The observer robustness against fault injection is proved.

Multiple literature instances addressing brake-related control functions assume a constant BLCF [16]. This approximation does not hold true for scenarios involving multiple braking applications, varying operating conditions and brake blending with electric motors [16]. In the present work, a novel BLCF compensation algorithm for base brake functions is presented and verified in real-time on the brake-by-wire HIL platform at Technische Universität Ilmenau (Ilmenau, Germany). The BLCF observer functionality in presence of blended braking with electric motors is demonstrated.

The few literature instances addressing BLCF estimators do not prove their functionality under real driving conditions [47, 61]. In this work, the proposed BLCF observer is calibrated by means of genetic algorithms and validated on the proving ground. Different braking manoeuvres are performed to test the observer robustness against vehicle speed, deceleration intensity and brake thermal conditions.

The literature lacks of consolidate brake wear prognosis functions, the majority of which refer to pin-on-disc studies where the BLCF dynamics and the associated wear process is far from reality [38]. This work proposes a semi-empirical wear model that makes use of the BLCF observer to predict brake-related wear. Experimental wear data collected from the brake dynamometer lead to an algebraic model, which is then validated against 30.000 km of real driving conditions.

Recent literature instances address the estimation of brake-related particle emissions from vehicle fleets by means of static maps. These latter cannot capture the epistemic uncertainty associated with the brake particle formation mechanisms [38]. The present thesis deals with advanced machine learning techniques to handle the highly stochastic process of brake-related particle emissions, which is a topic never dealt with in the past.

2.7 Thesis outline

The present Chapter 2 puts forth the basic mechanisms ruling the friction phenomena at the pad-disc interface. Experiments conducted on a special tribometer at Technische Universität Ilmenau (Ilmenau, Germany) allow for *in-situ* investigation of the contact zone. Chapter 2 also examines BLCF estimation techniques frequently employed in the literature, ranging from model-based to advanced machine learning approaches. These latter are then benchmarked under real driving conditions, showing that a BLCF observer, real-time capable and robust against real operating conditions is demanded. The rest of the thesis is organised in accordance with the flowchart of Figure 2.12.

Aiming at the creation of a high-fidelity MIL/SIL/HIL simulation framework for the development of advanced estimation functions, Chapter 3 introduces a new BLCF dynamic model stemming from a thorough experimental campaign conducted at Volvo Cars (Göteborg, Sweden). The data-driven model results in a set of three differential

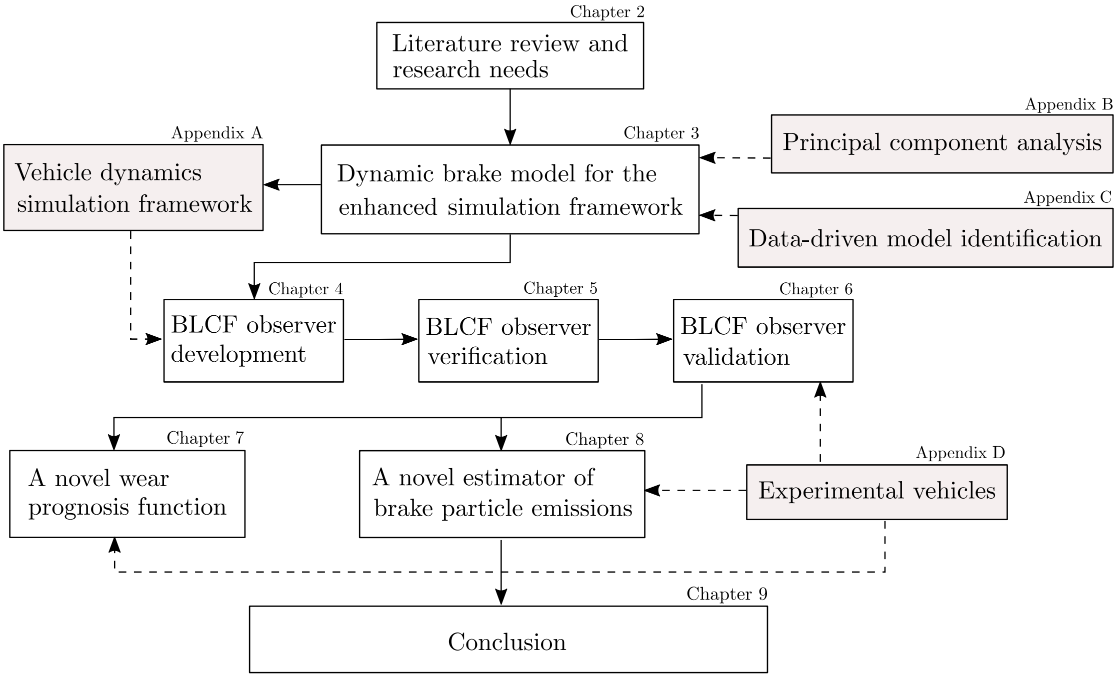

Figure 2.12: *Flowchart of the thesis outline.*

equations that are parametrised and validated against brake dynamometer data and embedded in SIL/MIL/HIL environments for successive analysis. A detailed description of the simulation framework is provided in Appendix A. The inclusion of the BLCF model in the simulation environment represents a required task to enable BLCF and disc temperature dynamics and to ensure a reliable and loyal vehicle dynamics simulation. The procedure leading to the formulation of the novel BLCF dynamic model are detailed in Appendices B and C. The modelling framework proposed in Chapter 3 outperforms state-of-the-art techniques being able to better capture the BLCF dynamics under all investigated conditions.

In Chapter 4, a novel BLCF observer is put forth and its functionality proven under different operating conditions in SIL/MIL environment. The simulation includes real sensors noise and real actuators dynamics; the signal acquisition complies typical CAN-Bus communication speeds. Chapter 5 follows with the BLCF observer real-time verification and fault injection test on the HIL platform at Technische Universität Ilmenau (Ilmenau, Germany). This chapter is dedicated to BLCF compensation for improved braking performance, also in presence of blended braking with electric motors. In Chapter 6, the developed observer is then validated with a full electric SUV at the Ford's Lommel (Lommel, Belgium) proving ground.

Thereafter, the work proves that the BLCF observer enables advanced monitoring functions of brake wear and particle emissions. In Chapter 7, a novel brake wear model is presented, whose formulation is driven by data collected on the brake dynamometer at Technische Universität Ilmenau (Ilmenau, Germany). Particularly, a new design of experiments is introduced, which consists in reproducing real driving cycles on the brake dynamometer. The functionality of the wear monitoring tool is demonstrated with respect to 30.000 km under real driving conditions.

Finally, advanced meta-modelling techniques, i.e. neural networks, are introduced in Chapter 8 for the estimation of the number of emitted brake particles. The proposed neural networks outperform state-of-the-art solutions and demonstrate to be capable of satisfactorily predicting the brake-related particle emission number. Appendix D reports the technical specifications of the experimental vehicles used in the framework of this research.

The dissertation terminates with the conclusive remarks of Chapter 9, which summarises the progress made within this work and highlights the potential industrial applications of the proposed control and estimation functions. Relevant recommendations for future investigations and associated research topics are also provided.

Chapter 3

A novel semi-empirical dynamic brake model

3.1 Introduction

This chapter reports the results of an extensive experimental campaign conducted at Volvo Cars (Göteborg, Sweden), which ultimately led to a novel model of the BLCF dynamics. The model formulation is based on state-of-the-art knowledge of the friction problem and is data driven, that is, its realisation is supported by experimental evidence. A complex design of experiments (DOE) is proposed to assess the BLCF variability with respect to brake line pressure, sliding speed and disc temperature. Principal Component Analysis (PCA) is then used to extract meaningful information from large set of experimental data. This latter allows for an intuitive understanding of the sought functional dependencies of pressure, temperature and speed with respect to BLCF.

Three passenger cars brake systems featuring different ECE lining compositions, among which two floating callipers and one fixed calliper, are tested on the brake dynamometer at Volvo Cars (Göteborg, Sweden) to generate experimental data and assess the model performance. All tests are performed under dry sliding conditions in controlled laboratory environment. The formulation of the brake pads cannot be publicly shared; however, the brakes geometrical data are reported in Table 3.1. The employed brake discs feature a base grey cast iron composition.

The proposed model, named ILVO, takes its name after the partners who contributed to its development, namely Technische Unviersität Ilmenau (Ilmenau, Germany) and Volvo Cars (Göteborg, Sweden). ILVO model outperforms the state of the art outside the investigated region of braking conditions. The integration of ILVO in the vehicle dynamics simulation software enhances the simulation fidelity of MIL/SIL/HIL frameworks by enabling the BLCF and disc temperature dynamics.

Table 3.1: Technical specification of the brakes under analysis.

	Brake A	Brake B	Brake C
Composition	ECE 1	ECE 2	ECE 3
Construction type	Floating	Floating	Fixed
Disc diameter	366 mm	340 mm	400 mm
Calliper piston(s) diameter	60 mm	42 mm	32/34/36 mm
Calliper piston(s) area	2827 mm^2	1385 mm^2	2730 mm^2
Pad area	7125 mm^2	2984 mm^2	5460 mm^2
N. of pistons	1	1	6
Effective radius	145.9 mm	144 mm	154.2 mm
Equivalent tyre radius	360 mm	360 mm	340 mm
Nominal μ_b (SAE J2522)	0.47	0.43	0.42

3.2 Experiments on the brake dynamometer

A schematic of the employed brake dynamometer is reported in Figure 3.1. The dynamometer is controlled through the manufacturer's proprietary software that ensures a seamless control of the system actuators. The compressed air hydraulic actuator increases the pressure up to 210 bar within the master cylinder. The system is equipped with a flow meter of the brake fluid and a pressure sensor that measures the actual pressure at the master cylinder. The brake torque is measured through a sensor positioned inside the inertial hub and corresponds to the output torque. The brake dynamometer allows for a maximum operating regime of 2500 rpm and features a peak power of 200 kW and a maximum torque of 6000 Nm. The temperature of the brake system is acquired in different points. Particularly, both the pad and disc temperatures are measured by means of embedded thermocouples located underneath the surfaces. The dynamometer is capable of simulating the inertia corresponding to the quarter curb vehicle mass.

To ensure repeatability of the data, the brake pads underwent a bedding-in procedure in accordance with SAE J2522 Sec. 2. The brake manoeuvres have variable duration depending on the boundary operating conditions. The signals are acquired with 200 Hz frequency. The manoeuvres exit condition may be either based on a target final temperature or a target final speed. To determine the global BLCF behaviour, a recursive least square (RLS) filter is used to post-process the raw data [62]. The experimental campaign consists of two test sessions designed together with Volvo Cars and realised for each brake system. The constant pressure cycle (CPC) is a full factorial design that allows for a thorough investigation of the influence of the control variables initial vehicle speed, initial disc temperature and brake line pressure ($5 \times 7 \times 9$). The control variables tested levels are conveniently reported in Figure 3.2 together with the average BLCF computed in accordance with SAE J2522, as the fourth dimension on the coloured bar. The modified *Auto Motor und Sport* (AMS) for dynamometer test rigs consists of consecutive full-stop braking manoeuvres from an initial speed of 100 km/h with a fixed deceleration of 1 G.

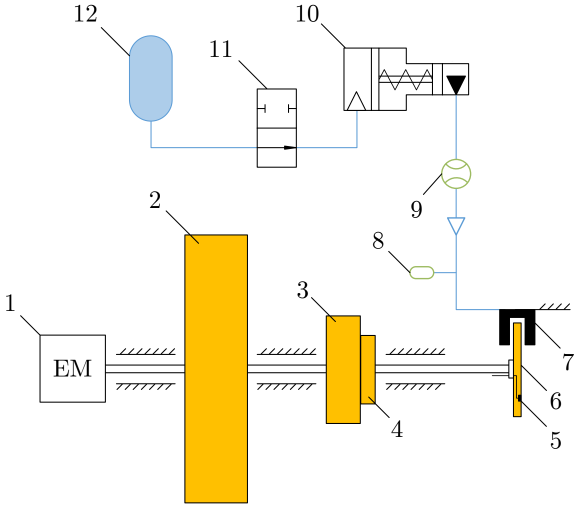

Figure 3.1: *Brake dynamometer with climatic chamber, employed for experimental tests at Volvo Cars. 1-Drive Motor, 2-Flywheels, 3-Inertial hub, 4-Torque sensor, 5-Temperature sensor, 6-Brake disc, 7-Brake calliper, 8-Brake pressure sensor, 9-Flow meter, 10-Master cylinder, 11-Compressed air hydraulic actuator, 12-Pressure accumulator.*

The first dataset is of general-purpose and is herein used to feed the data driven approach and to identify the model parameters. The second dataset is specifically used to validate the model extrapolation capability as it involves a higher brake line pressure and disc temperature.

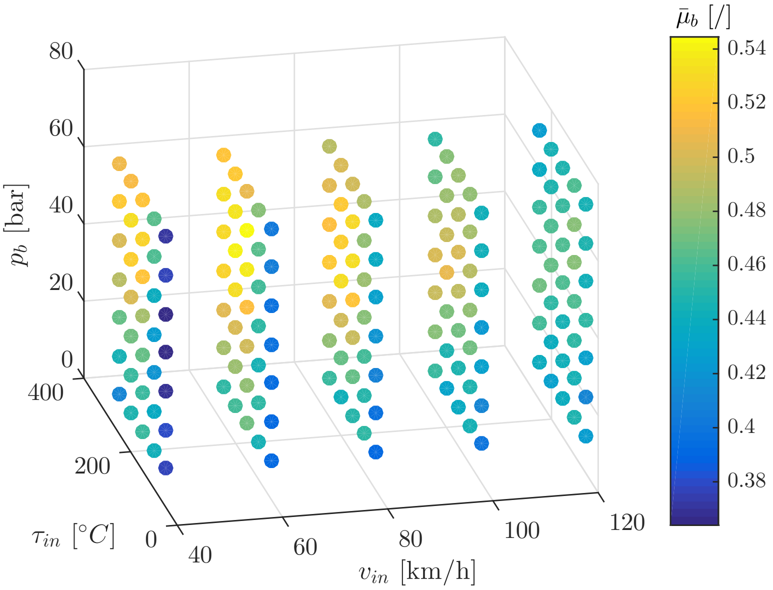

Figure 3.2: *DOE of CPC with full factorial design. The average BLCF values refer to Brake A.*

3.3 Analysis of experimental data

The patch formation and destruction dynamics is mainly confined to secondary plateaus, which, along with the primary plateaus, constitute the real are of contact. Formation and growth of the secondary plateaus depends upon temperature, normal pressure and shear forces [22]. In accordance with the in-situ experiments conducted at Technische Universität Ilmenau, the change in size and number of the secondary plateaus is the reason for BLCF variations [23, 27]. The model herein presented sets out to describe the slow increase of BLCF due to variation in the real area of contact.

The friction mechanisms entails highly stochastic processes, thus a good measurement reproducibility across consecutive measurements in hardly achievable. However, large brake dynamometer data allows identifying a general trend between BLCF and brake operating conditions. CPC data are employed to extract meaningful information about the BLCF behaviour both under steady-state and transient conditions. Figure 3.3 reports the results of the CPC test. It can be noted that average BLCF tends to increase with increasing pressure. Indeed, the increasing pressure leads to the formation of more patches and thus to a widening of the real contact area [63], [64]. The effect of initial sliding speed is not clearly reflected in the average BLCF; nevertheless, higher speed values play a detrimental role on the patch formation. The temperature contributes to the formation of more patches until a critical temperature is reached where BLCF begins to decay.

Twelve braking manoeuvres are extracted from CPC data to analyse the BLCF behaviour under transient conditions. Figure 3.4 reports the BLCF values for Brake A recorded at the target speeds (v_t) of $60\,km/h$ and $30\,km/h$ for twelve braking manoeuvres featuring three levels of initial temperature ($50°C$, $150°C$ and $200°C$), two levels of initial vehicle speed ($80\ km/h$ and $120\ km/h$) and two levels of pressure ($20\ bar$ and $60\,bar$). In accordance with SAE J2522, the braking initial condition is set as the instant at which the measured pressure achieves 90% in value of the reference pressure signal. The experimental results show that BLCF increases with a faster rate at higher pressure values. Indeed, higher pressure values correspond to higher deceleration rates and, thus, enhanced agglomeration of debris. From Figure 3.4, another important evidence is that higher speed values hinder the agglomeration of patches and, thus, lower the formation of new contact area. This effect is much more pronounced at higher pressure values [64, 65].

In addition to this analysis, the relative importance of each input variable has been quantitatively assessed by means of PCA (the reader is referred to Appendix B for details on the implemented algorithm). PCA takes high-dimensional data and represents it in a lower-dimensional form without losing too much information. This is done by identifying the directions of maximum data variation in a reduced order dimensional space. For this reason, only the first three principal components (PCs) are selected, which together account for more than 80% variation in the BLCF (Table 3.2). In this 3-dimensional

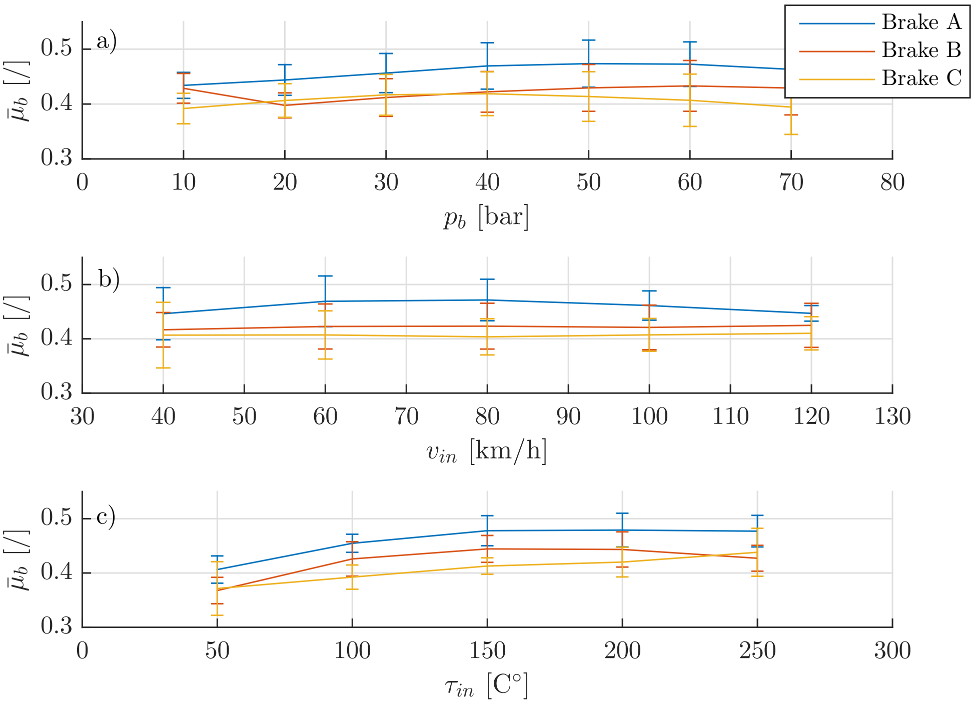

Figure 3.3: *Results of CPC test for the brake systems under analysis. From lower to top, sub-figures a), b) and c) render the dependence of the average BLCF against the brake line pressure, initial disc speed and initial disc temperature, respectively.*

space, one can identify the direction of maximum variation of each input variable initial vehicle speed, brake pressure and initial disc temperature, respectively, and the output variable average BLCF, computed in accordance with SAE J2522. The projections of the input variables onto the PCs reference system represent an orthogonal reference as the input variables are varied one at a time (refer to Figure B.3). The relative importance of each input variable can be computed by projecting the associated vector onto the average BLCF vector. The results of this procedure carried out across the CPC data demonstrate that the contact temperature accounts for more than 60% variance in the average BLCF computed for each manoeuvre, in accordance with SAE J2522. The relative importance of input variables on the average BLCF is conveniently reported in Table 3.2.

TABLE 3.2: Relative importance of the input variables resulting from PCA conducted across the CPC data set. For details, the reader is referred to Appendix B.

Variable	Relative weight		
	Brake A	Brake B	Brake C
Initial vehicle speed	-9.61%	3.46%	1.22%
Brake pressure	36.6%	35.1%	12.6%
Initial disc temperature	59.8%	61.3%	69.6%
Total variance identified by the first three PCs	92.8%	89.5%	87.7%

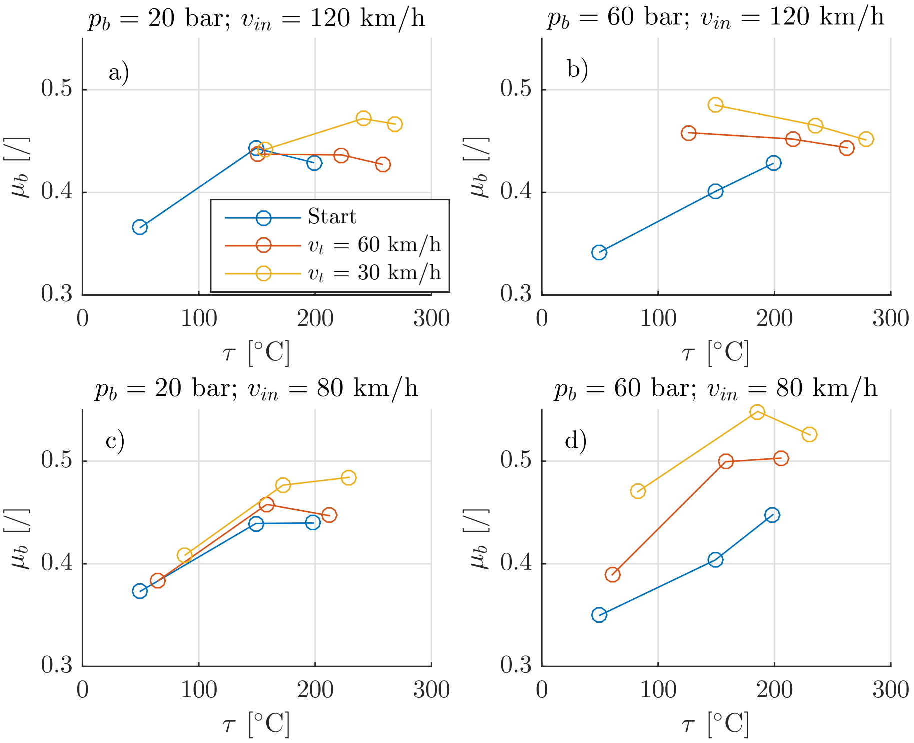

Figure 3.4: *Partial results of CPC test of Brake A allow analysing the BLCF dynamic behaviour. The upper graphs, a) and b), refer to braking from an initial vehicle velocity of* 120 *km/h. The lower graphs, c) and d), refer to an initial vehicle velocity of* 80 *km/h. The BLCF values at the initial condition, at the intermediate target speed of* 60 *km/h and at the final target speed of* 30 *km/h are identified by blue, red and yellow lines, respectively.*

Table 3.2 shall be read as follows: "the initial disc temperature is responsible for more than 60% of the variance in the measured average BLCF". It is worth noticing that PCA not only describes the absolute magnitude but also the expected direction of variation. In other words, one can conclude that for Brake A, a higher initial speed leads to a reduction in BLCF, whilst for Brake B and C the speed account just for a tiny variation in BLCF. Moreover, for Brake C, the pressure does not play an important role because of the more even pressure distribution provided by the fixed calliper architecture with multiple pistons. This analysis motivates the choice of the functional dependencies rendering the average BLCF, which is better discussed later in the text. Although the experimental evidence of Figure 3.3 demonstrates that BLCF entails stochastic phenomena, a deterministic modelling approach is herein proposed. Due to BLCF stochastic nature and the necessary plant-specific model parametrisation, the scope of ILVO is a tool to be included in MIL/SIL/HIL simulation frameworks. The experimental evidence guides the model development, which is expressed formulaically by the data driven approach of Appendix C.

3.4 Enhanced lumped capacitance model

The lumped capacitance model has been widely used in the literature to render the brake temperature dynamics [66]. The basic assumption of the lumped capacitance is that an uniform temperature field is assumed in the disc; therefore, the temperature is a function of time only. This statement is valid if the Biot number of the brake disc is smaller than 0.1 [67]. The Biot number is defined as the ratio between the convective heat transfer coefficient and the conductive heat transfer coefficient, as per Equation (3.1):

$$Bi = \frac{h_{ht}\, r_{out}}{k_{ht}}, \tag{3.1}$$

where, Bi is the Biot number, h_{ht} is the disc convective heat transfer coefficient, k_{ht} is the disc conductive heat transfer coefficient and r_{out} is the critical dimension over which conduction occurs, generally the radial disc direction across which the highest temperature gradient is measured (Figure 3.5). For the brake systems under analysis, a Biot number of 0.08 is calculated, making the lumped capacitance model applicable. If the Biot number exceeds the threshold, the temperature gradients within the disc may influence the heat transfer behaviour making the lumped capacitance model not applicable.

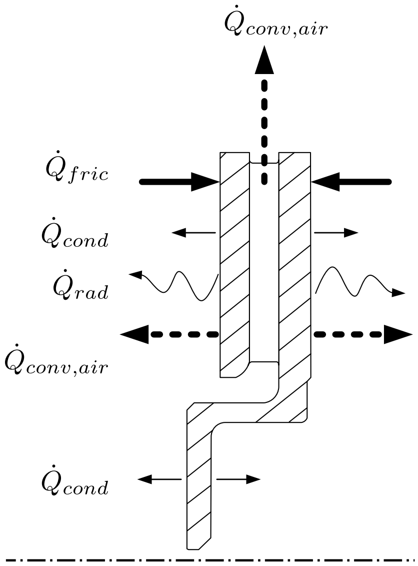

Figure 3.5: *Energy balance of a cast iron brake disc.*

The temperature dynamics of the brake system is concerned mostly with the cooling and heating of the disc as it is the primary storage for thermal energy and its temperature influences the nearby components. Due to its higher thermal conductivity if compared to the brake pads, the disc dissipates almost 96% of the generated heat [29]. The brake disc thermal dynamics accounts for the energy equilibrium between heat provided by means of frictional power and the heat removed by convection with the surrounding air. The lumped capacitance model also assumes that the heat dissipated through conduction into the wheel carrier is negligible and the radiation effect can be neglected if compared to the convection with air. Given these assumptions, the following model can be formulated:

$$c_p\, m_{disc}\, \dot{\tau} = \dot{Q}_{fric} - \dot{Q}_{out}, \tag{3.2}$$

where,

$$\dot{Q}_{fric} = \sigma\ \|T_b\, \omega\|\,, \quad \dot{Q}_{out} = \dot{Q}_{conv,air} + \dot{Q}_{cond} + \dot{Q}_{rad} \approx \dot{Q}_{conv,air}. \tag{3.3}$$

The model in Equations (3.2) and (3.3) gives rise to Equation (3.4):

$$c_p\, m_{disc}\, \dot{\tau} = \sigma\ \|T_b\, \omega\| - h_{ht}\, A_{eff}\, (\tau - \tau_{env}), \tag{3.4}$$

which can in turn be rewritten as Equation (3.5):

$$\dot{\tau} = \frac{\sigma}{c_p\, m_{disc}}\ \|T_b\, \omega\| - \frac{h_{ht}\, A_{eff}}{c_p\, m_{disc}}\, (\tau - \tau_{env}), \tag{3.5}$$

and,

$$\dot{\tau} = \xi\ \|T_b\, \omega\| - \delta_{ht}\, (\tau - \tau_{env}). \tag{3.6}$$

where, σ represents the heat portion dissipated by the disc, m_{disc} is the mass of the disc, c_p is the disc specific heat capacity (generally between $450\frac{J}{kgK}$ and $550\frac{J}{kgK}$ for normal brake disc operating conditions), h_{ht} is the convective heat transfer coefficient (usually between $1\frac{W}{m^2K}$ and $100\frac{W}{m^2K}$) [67], A_{eff} represent the effective brake disc area subject to convective heat transfer, τ and τ_{env} represent the disc and ambient temperature respectively, T_b is the brake torque and ω the disc speed. The first term in Equation (3.6) is replaced with ξ which identifies the portion of frictional power converted into disc temperature variation. The second term is defined as the characteristic disc cooling coefficient δ_{ht}.

The lumped model can well perform under a restricted temperature range corresponding to relatively modest energy inputs. At high temperatures, where the grey cast iron thermal properties change dramatically, such model tends to break down and provides an inaccurate representation of the brake thermal behaviour. With this in mind, data collected from the dynamometer at Volvo Cars are used to identify and validate an improved lumped capacitance model that accounts for variation in the disc specific heat and cooling coefficient against varying temperature and sliding speed, respectively. Experimental data shows that the relationship between disc material specific heat capacity c_p and disc temperature τ can be represented by a linear function, as in Figure 3.6a. Data collected from the proving ground at Volvo Cars show that the cooling coefficient of the disc δ_{ht} can be expressed as a linear function of the relative air speed, herein assumed equal to the vehicle linear velocity, as in Figure 3.6.

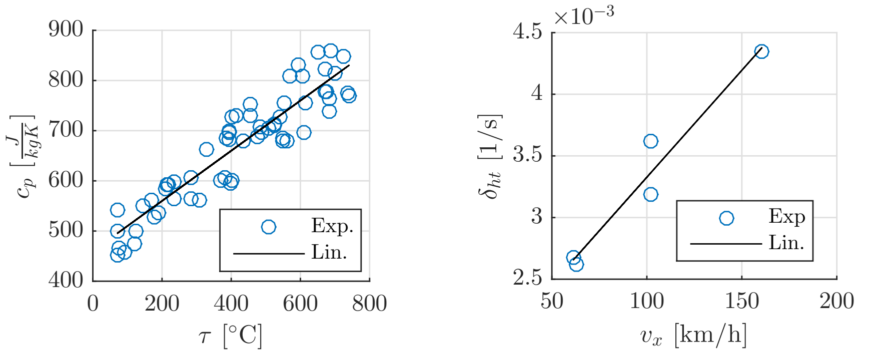

(a) *Specific heat of a cast iron disc as a function of its temperature.*

(b) *Dependence of the cooling coefficient against the relative air speed.*

Figure 3.6: *Thermal properties of the cast iron disc under analysis.*

In accordance with the experimental evidence, the lumped capacitance model is corrected as:

$$\dot{\tau} = \xi(\tau)\ \|T_b\, \omega\| - (\delta_{ht,0} + \delta_{ht,1}\, v_x)\,(\tau - \tau_{env}). \tag{3.7}$$

The performance of the corrected lumped model of Equation (3.7) are reported in Figures 3.7 and 3.8 for the disc cooling and heating case, respectively. The disc cooling data, in Figure 3.7, refer to measurements at constant cruising speed, performed on a proving ground at Volvo Cars (Göteborg, Sweden). The experimental data in Figure 3.8 refers to constant deceleration manoeuvres with a brake pressure of 30 bar, performed on the dynamometer at Volvo Cars. For the sake of space, only two sets of measurement are reported for each case, corresponding to a low and high speed braking, respectively. It is noticeable that the steady state error is reduced when the corrected lumped model is used. This is mostly valid for braking manoeuvres performed from higher speed values.

For a matter of simplicity and to ensure stability in the numerical solution, the disc specific heat coefficient is assumed almost constant, leading to the parametrisation in Appendix C. This assumption does not affect the validity of the model. Based on the results reported later in the document, the lumped capacitance model functionality is proven up to a disc temperature of 350°C.

3.5 Proposed model of the brake lining coefficient of friction

As shown in Chapter 2, dry friction stems from different mechanisms occurring at the microscale. Although the friction is a result of numerous phenomena, the extended Amonton's law well describes the friction force between dry surfaces that slide over each other in presence of adhesion [68]. The adhesion contribution is proportional to the number of bonds that are broken and reformed when the surfaces slide relatively to each other. The number of bonds is proportional to the apparent contact area only

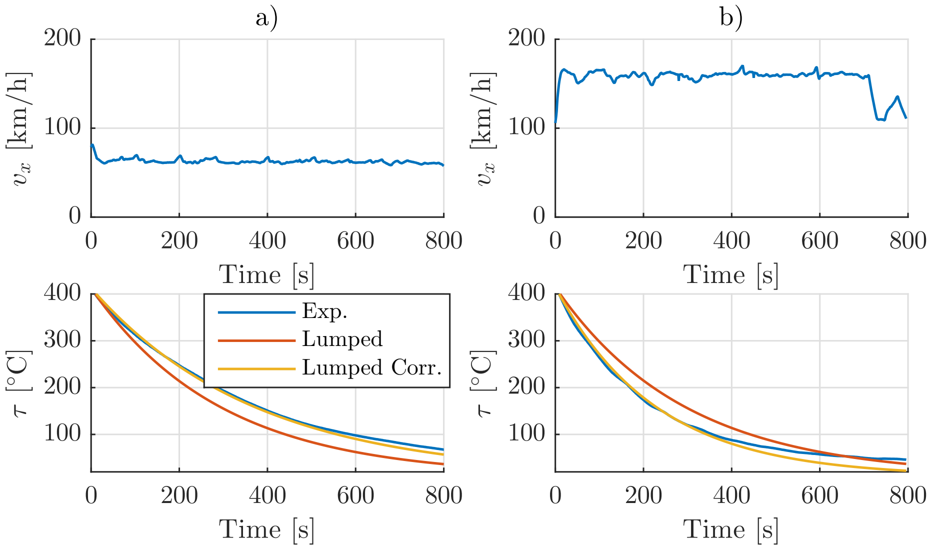

Figure 3.7: *Comparison between the modelling performance of the conventional lumped capacitance model and its corrected version from an initial disc temperature of* 400°C. *Sub-figures a) and b) refer to cruising at low and high speed, respectively.*

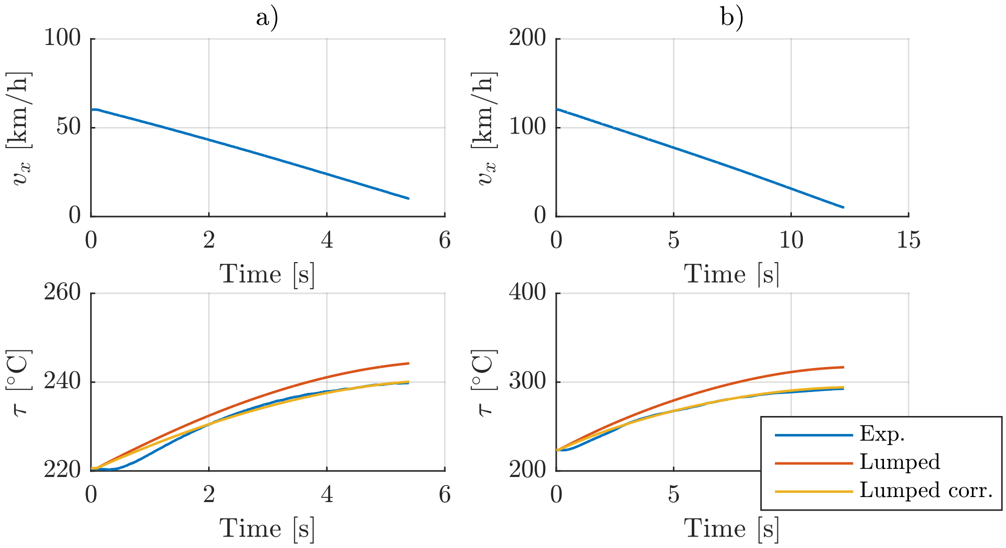

Figure 3.8: *Comparison between the conventional lumped capacitance model and its corrected version from an initial temperature of* 220°C. *Sub-figures a) and b) refer to braking from low and high speed, respectively.*

if the surfaces are completely smooth. For rough surfaces, the real contact area A_{real} differs dramatically from the apparent contact area A_{pad} as the former could be much larger or much smaller depending on the surfaces material hardness and applied normal pressure [22]. In this case, the area is referred to as the real contact area and its increase corresponds to a higher BLCF [23, 27]. Henceforth, the ratio between the real and apparent contact area is herein defined as the normalised real contact area as follows:

$$\alpha_b \propto \frac{A_{real}}{A_{pad}}. \tag{3.8}$$

An infinitesimal element lying at the pad-disc contact interface is selected and studied. A schematic of the proposed differential approach is presented in Figures 3.9a and 3.9b.

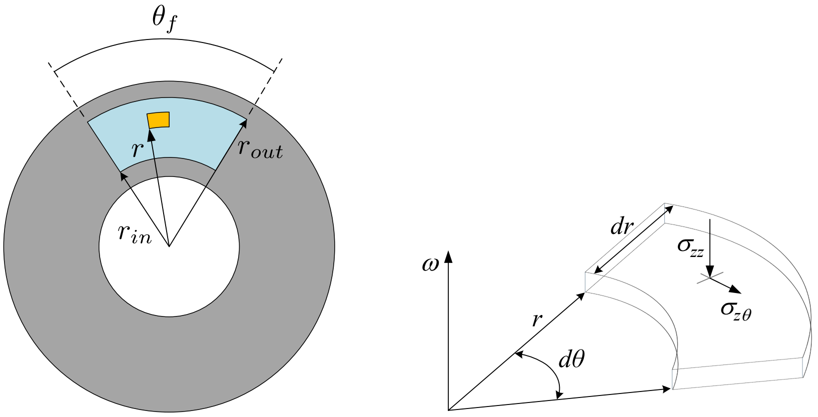

(a) *A disc brake and infinitesimal element at the pad-disc interface, in yellow.*

(b) *Depiction of the infinitesimal element at the pad-disc interface together with stress components.*

Figure 3.9: *Schematic of the proposed differential approach.*

The sought functional dependencies stem from a data driven approach, which is based on the minimisation of a cost function in accordance with criteria of both generalizability and fitting performance (please, refer to Appendix C). For the generic infinitesimal element, one can define the relation between normal and tangential stress components as follows:

$$\sigma_{z\theta} = -\mu_b(\sigma_{zz}, \tau, \nu, t)\, \sigma_{zz}\, sign(\nu), \tag{3.9}$$

where,

$$\nu = r\, \omega. \tag{3.10}$$

The stress component $\sigma_{z\theta}$ in the tangential direction is associated with the friction force experienced by the element at the contact interface; the stress component σ_{zz} in the vertical direction is caused by the pressure distribution in the contact zone when pressure is applied; τ represents the local disc temperature in correspondence of the infinitesimal element; ν represents the local sliding speed of the infinitesimal element located on the circumference of radius r, given the angular disc velocity ω. At microscopic level, the real contact area is not constant, which directly affects the friction coefficient. PCA across CPC data demonstrates that the temperature plays an important role on the adhesion friction as a varying temperature causes different levels of surface interaction. To account for the adhesion effect, BLCF is expressed as a combination of two variables, viz:

$$\mu_b(\sigma_{zz}, \tau, \nu, t) = \kappa(\tau)\, \alpha_b(\sigma_{zz}, \tau, \nu, t), \tag{3.11}$$

where, the normalised real contact area α_b is dynamically being modified by local deformation and flow of wear debris, the contact coefficient κ expresses the adhesion between pad and disc. The adhesion coefficient can be extracted from CPC by considering a unitary contact area and computing the average BLCF in accordance with SAE J2522, for a fixed initial sliding speed and initial disc temperature. The same procedure is repeated for different brake line pressure values, leading to the results in Figure 3.10.

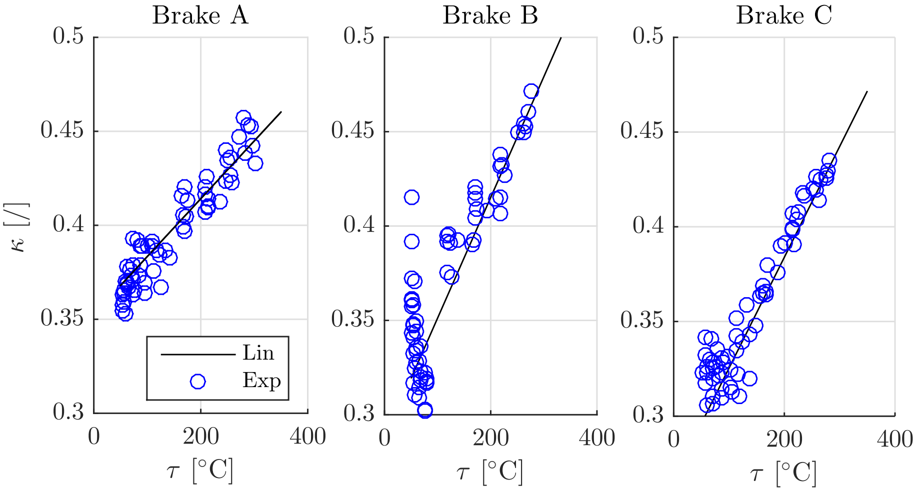

Figure 3.10: *Adhesion coefficient κ against disc temperature for the brake systems under analysis. From left to right brakes A, B, C, respectively.*

Based on the results of Figure 3.10, the adhesion coefficient is approximated as a linear function of the brake disc temperature. The analytical expression is given by Equation (3.12):

$$\kappa(\tau) = \kappa_1 \tau + \kappa_0, \tag{3.12}$$

This equation carries the inherent property of increased interactions due to higher atomic kinetic energy represented by temperature. At this point, the data driven approach of Appendix C leads to the following differential equation for the normalised real contact area dynamics:

$$\dot{\alpha}_b = a\, \sigma_{z\theta}\, \nu + b\, \dot{\nu} - g(\sigma_{zz}, \tau), \tag{3.13}$$

which can be rewritten as,

$$\dot{\alpha}_b = a\, \kappa\, \alpha_b\, \sigma_{zz}\, \nu + b\, \dot{\nu} - g(\sigma_{zz}, \tau). \tag{3.14}$$

In its preliminary version, the model also included a pressure gradient dependent term, which was then removed because the data driven approach assigned a low significance to it. This conclusion was also supported by experiments conducted on the dynamometer at Volvo Cars for varying pressure gradients and pressure levels. The results in Figure 3.11 show that the pressure gradient does not play a visible role in the average BLCF value computed in accordance with SAE J2522. Hence, its effect is neglected.

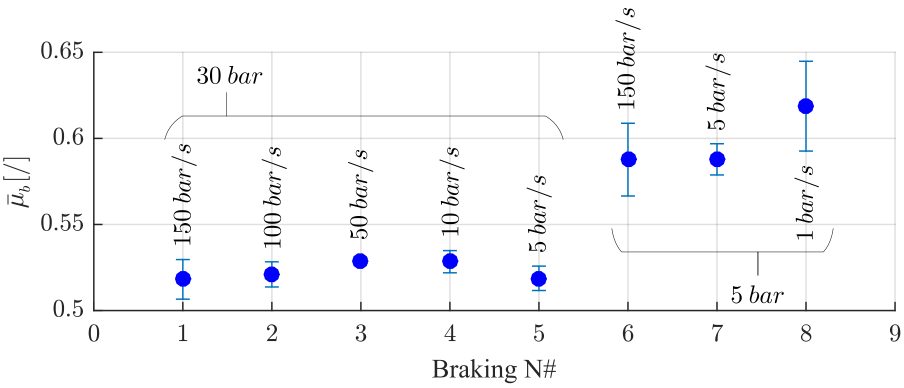

Figure 3.11: *Effect of the pressure gradient on the average BLCF. The results refer to Brake A.*

The resulting expression is composed of three terms: (i) the first one associated with the shear stress, which can contribute to the creation of new contact area; (ii) the second term is associated with the accumulation of debris in the contact area induced by the disc deceleration and contributes to increasing the effective contact area; (iii) the third term is associated with thermo-plastic effects, which lead to a reduction in the real contact area. It is worth noticing that the function $g(\sigma_{zz}, \tau)$ is specific for each brake system as it describes the frictional behaviour under steady conditions (no area growth/destruction). Based on the results of PCA, the data driven approach maximises the fitting for:

$$g(\sigma_{zz}, \tau) = c\, \sigma_{zz}\, \tau. \tag{3.15}$$

By substituting Equations (3.12) and (3.15) in Equation (3.14), the expression follows:

$$\dot{\alpha}_b = a\,(\kappa_1 \tau + \kappa_0)\, \alpha_b\, \sigma_{zz}\, \nu + b\, \dot{\nu} - c\, \sigma_{zz}\, \tau. \tag{3.16}$$

Finally, one can combine BLCF with shear stress and calculate the torque applied to each differential area elements dA of the pad, leading to the following expression:

$$dT_b = r\, \sigma_{z\theta}\, dA = -r\, \kappa(\tau)\, \alpha_b(\sigma_{zz}, \tau, \nu, t)\, \sigma_{zz}\, sign(\nu)\, dA. \tag{3.17}$$

To identify the parameter of the proposed model, Equation (3.17) shall be brought to the integral form by integrating over the pad area in polar coordinates:

$$T_b = 2 \iint\limits_{A_{pad}} \mathrm{d}T_b = 2 \int_{r_{in}}^{r_{out}} \int_0^{\theta_f} -r^2\, \kappa(\tau)\, \alpha_b(\sigma_{zz}, \tau, \nu, t)\, \sigma_{zz}(r, \theta)\, sign(\nu)\, \mathrm{d}\theta \mathrm{d}r. \tag{3.18}$$

At this stage, an important and practical simplification is to move the problem to the macroscopic scale by dismissing the radial and angular distribution of temperature, normal stress and normalised real contact area:

$$\tau(r, \theta) = \tau, \quad \sigma_{zz}(r, \theta) = \sigma_{zz}, \quad \alpha_b(\sigma_{zz}, \tau, \nu, t) = \alpha_b(\sigma_{zz}, \tau, r_{eff}\, \omega, t), \quad sign(\nu) = sign(\omega). \tag{3.19}$$

As a result, Equation (3.18) becomes:

$$T_b = -2\, sign(\omega)\, \kappa(\tau)\, \alpha_b(\sigma_{zz}, \tau, r_{eff}\omega, t)\, \sigma_{zz}\, \theta_f\, \frac{r_{out}^3 - r_{in}^3}{3}. \tag{3.20}$$

where,

$$\sigma_{zz} = \frac{p_b\, A_k}{A_{pad}}, \quad A_{pad} = \theta_f \frac{r_{out}^2 - r_{in}^2}{2}, \quad r_{eff} = \frac{2}{3} \frac{r_{out}^3 - r_{in}^3}{r_{out}^2 - r_{in}^2}. \tag{3.21}$$

Finally, a complete definition of the dynamic system is given by Equations (3.22a) to (3.22c):

$$\begin{cases} \dot{\omega} = -\dfrac{1}{I_\omega}(T_b + \sum T_{ext}), & (3.22a) \\ \dot{\tau} = \xi\, \|T_b\, \omega\| - \delta_{ht}(v_x)\, (\tau - \tau_{env}), & (3.22b) \\ \dot{\alpha}_b = a\, (\kappa_1 \tau + \kappa_0)\, \alpha_b\, \sigma_{zz}\, r_{eff}\, \omega + b\, r_{eff}\, \dot{\omega} - c\, \sigma_{zz}\, \tau. & (3.22c) \end{cases}$$

Equation (3.22a) describes the disc rotational dynamics. In accordance with the previous section, the brake temperature dynamics is rendered by Equation (3.6) and conveniently rewritten as Equation (3.22b). Equation (3.22c) is the proposed dynamics for the normalised real contact area. The model features seven parameters, which need to be identified based on the brake system under consideration: the fraction of the brake power that is converted into heat (ξ), the brake cooling coefficient (δ_{ht}), two parameters associated with the adhesion coefficient (κ_1 and κ_0) and three parameters related to the real contact area dynamics (a, b and c). The equations comprised above are a set of non-linear differential equations where line pressure is seen as an input to trigger the braking mechanism. In accordance with SAE J2522, a brake line pressure of 0.5 *bar* is set to trigger the integration start. The formulation proposed conveys that the particles flow increases the size of the contact patches due to friction power, whilst pressure and temperature modulate the wear and thus the destruction process of the contact patches [50].

3.6 Model identification and benchmarking

In [50], Ostermeyer proposes a dynamic model for BLCF that relies on two differential equations in the BLCF and temperature sate variables (please, refer to Chapter 2). The experimental evidence demonstrates that the parameters introduced by Ostermeyer cannot be considered constant during the braking manoeuvre and further dependencies shall be explored. To this effect, the authors in [69] propose a revised model based on nine parameters. Nevertheless, both models are derived from experiments conducted on the pin-on-disc where the temperature dynamics is much different from that of disc brakes. Thereafter, ILVO model is benchmarked against the Ostermeyer model and its revised version. The reader is referred to the work in [69] for more details.

During the development stage, several optimisation methods were deployed for the models identification. Herein, the set of differential equation are integrated by means of the fourth-order Runge-Kutta algorithm with a fixed step of 0.01 s, which ensures at the same time low computational burden and improved convergence stability. It is proved that both the constrained least square method (LSQ) and the unconstrained derivative-free simplex search method (DSS) [70] converge to the same global minimum. The reader is referred to Appendix C for more details.

The normalised effective area of ILVO model is initialised to the unitary value at the beginning of each braking manoeuvre. The initial brake temperature τ_0 must be specified before the simulation starts to account for the initial brake thermal state. Moreover, the Ostermeyer model and its revised variant require the knowledge of the initial BLCF to ensure convergence of the solution. This represents an important limitation of the Ostermeyer model where the initial BLCF value must be set upon integrating. In the case of ILVO, the initial BLCF condition is left to the identification of Equation (3.15) in the optimisation routine. The CPC fitting performance of the models under analysis are herein quantified by the normalised round mean square error ($nRMSE$). The results reported in Table 3.3 demonstrate ILVO superior performance. Moreover, no noticeable improvement is brought about by the revised Ostermeyer model in [69] when compared to its original version.

Table 3.3: CPC fitting performance of the models under analysis for the three brake systems.

CPC	$nRMSE(\mu_b)$		
	Brake A	Brake B	Brake C
Ostermeyer	12.91%	13.86%	15.34%
Revised Ostermeyer	12.87%	15.23%	16.56%
ILVO	4.35%	7.51%	8.70%

As an example, two CPC braking manoeuvres characterised by low and high brake pressure are reported in Figures 3.12a and 3.12b, respectively. The results show that ILVO model can reproduce well the effective contact area dynamics when compared with an estimate extracted from the experimental data. The resulting models parametrisations are reported in Tables C.2 and C.3 of Appendix C.

3.7 Model validation and results

In this section, the model validation is carried out against the AMS data set. This latter involves temperature and pressure values beyond the CPC investigated domain. Therefore, AMS also allows to assess the models extrapolation performance. For the sake of space, only the graphical results corresponding to Brake A are reported in Figure 3.13. The extended validation results are instead reported under the form of Table 3.4. In addition to $nRMSE$, capturing the transient BLCF behaviour, another performance index is considered, namely the average BLCF, computed in accordance with SAE J2522.

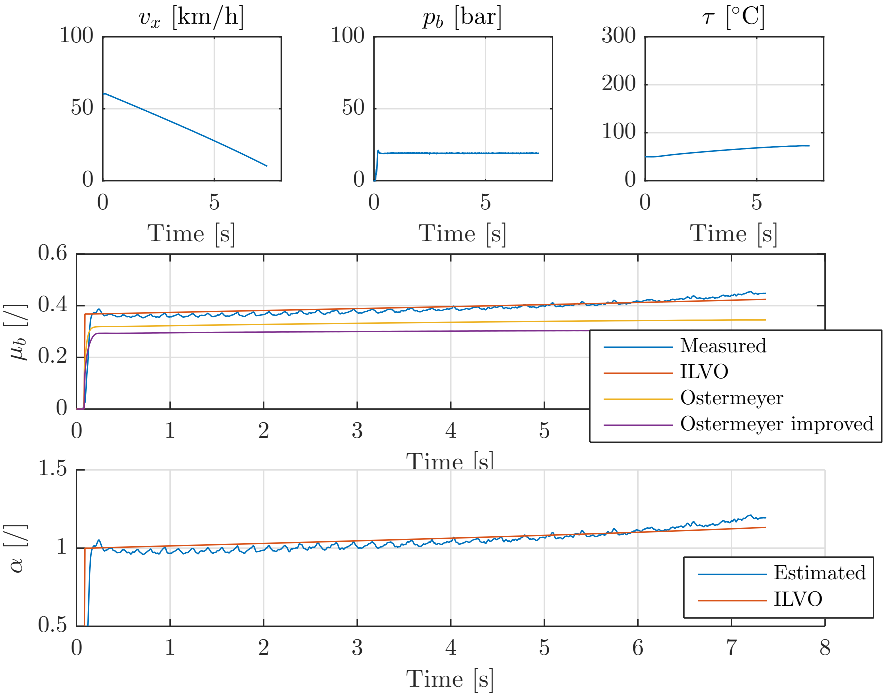

(a) *Fitting performance of the benchmarked models at low brake pressure.*

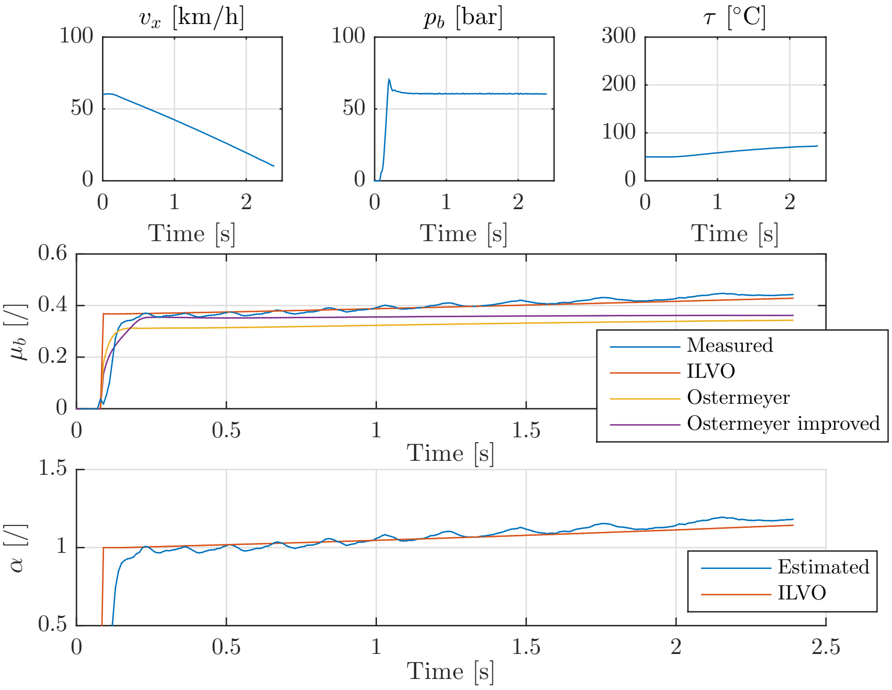

(b) *Fitting performance of the benchmarked models at high brake pressure.*

Figure 3.12: *Fitting performance of the models. Input variables BLCF and contact area dynamics are reported in the upper, middle and lower graphs, respectively.*

Figure 3.13 shows that whilst the Ostermeyer model fails upon reaching a brake disc temperature of $200°C$, ILVO model can reproduce well BLCF decay due to the increasing temperature, which is particularly evident above $250°C$.

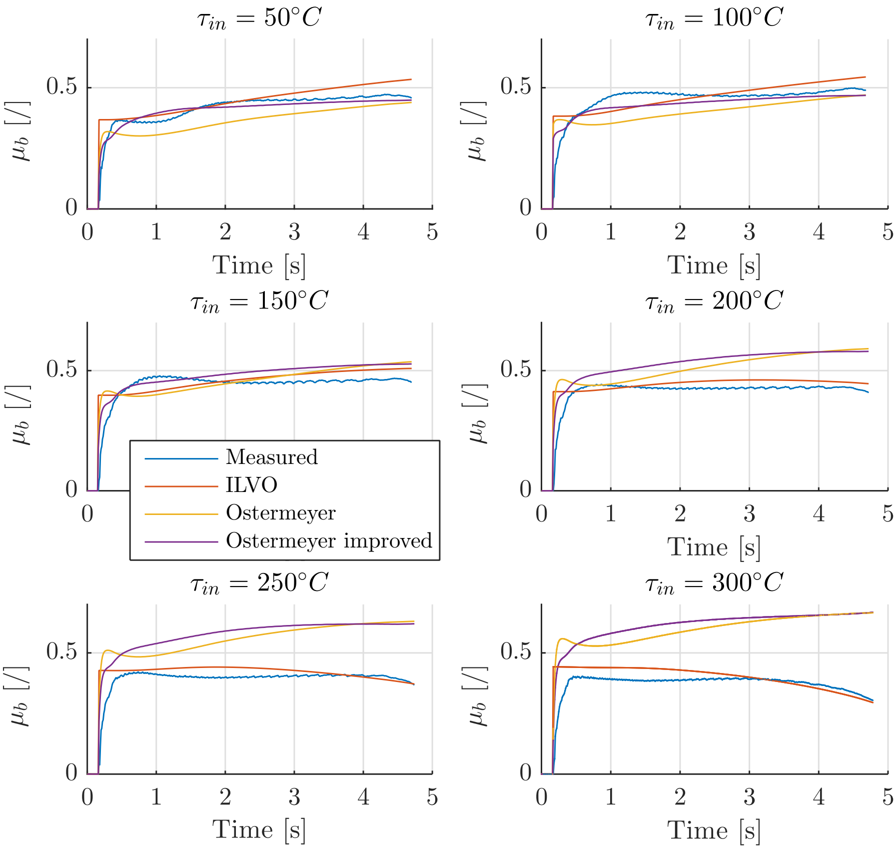

Figure 3.13: *Validation results for Brake A. ILVO model renders the friction phenomenon for a wider range of temperatures when compared with the Ostermeyer's model and its improved variant.*

In accordance with the extended results in Table 3.4, the improved Ostermeyer model shows good prediction performance for a relatively restricted temperature range, up to $150°C$. Upon reaching a brake disc temperature of $200°C$, this latter starts failing, whilst ILVO model keeps exhibiting a very low prediction error. The capability of ILVO model of capturing both the steady state friction and its dynamics is demonstrated by the low average BLCF prediction error and $nRMSE$, which are kept within 15% margin. This is particularly evident for Brake A and Brake B. The higher error values that can be noticed for Brake C suggest that a different formulation in Equation (3.15) may be necessary. The results demonstrate that ILVO model can depict decaying BLCF due to increasing disc temperature, which results in a remarkable reduction in the effective contact area [71].

Table 3.4: Validation results of the models under analysis with respect to AMS data.

AMS		$\bar{\mu}_b$				$nRMSE(\mu_b)$		
	τ_{in}	Meas.	Ost.	Ost. imp.	ILVO	Ost.	Ost. imp.	ILVO
Brake A	$50°C$	0.4338	0.3757 (-13.4%)	0.4263 (-1.73%)	0.4601 (+6.05%)	15.10%	5.34%	7.92%
	$100°C$	0.4711	0.4090 (-13.18%)	0.4436 (-5.85%)	0.4717 (+0.12%)	15.50%	7.14%	8.64%
	$150°C$	0.4584	0.4681 (+2.11%)	0.4947 (+7.91%)	0.4678 (+2.04%)	11.00%	10.91%	8.34%
	$200°C$	0.4291	0.5239 (+22.09%)	0.5478 (+27.67%)	0.4491 (+4.65%)	26.55%	30.14%	6.40%
	$250°C$	0.4030	0.5727 (+42.11%)	0.5956 (+47.80%)	0.4215 (+4.60%)	45.81%	50.41%	7.03%
	$300°C$	0.3775	0.6161 (+63.19%)	0.6378 (+68.93%)	0.3911 (+3.59%)	66.97%	71.83%	8.62%
Brake B	$50°C$	0.3929	0.3330 (-15.24%)	0.3044 (-22.53%)	0.3921 (+0.2%)	17.5%	25.86%	5.36%
	$100°C$	0.4843	0.3844 (-20.63%)	0.3375 (-30.30%)	0.4406 (-9.03%)	22.36%	33.03%	11.36%
	$150°C$	0.5424	0.4447 (-18.02)	0.3803 (-29.87%)	0.4853 (-10.52%)	19.75%	32.22%	15.36%
	$200°C$	0.5303	0.4975 (-6.19%)	0.4220 (-20.42%)	0.4997 (-5.77%)	8.75%	22.18%	11.73%
	$250°C$	0.5094	0.5429 (+6.58%)	0.4592 (-9.86%)	0.4957 (-2.7%)	8.61%	10.89%	6.36%
	$300°C$	0.4959	0.5690 (+14.73%)	0.4804 (-3.13%)	0.4917 (-0.85%)	16.68%	4.41%	4.04%
Brake C	$50°C$	0.3756	0.3217 (-14.35%)	0.3488 (-7.15%)	0.4056 (+7.98%)	18.85%	11.69%	6.38%
	$100°C$	0.4229	0.3846 (-9.05%)	0.4059 (-4.02%)	0.4304 (+1.79%)	14.40%	8.40%	5.34%
	$150°C$	0.3843	0.4190 (+9.01%)	0.4424 (+15.12%)	0.4182 (+8.82%)	14.04%	14.28%	9.50%
	$200°C$	0.3340	0.4639 (+38.89%)	0.4877 (+46.02%)	0.4013 (+20.15%)	43.55%	46.25%	19.14%
	$250°C$	0.3005	0.4982 (+65.77%)	0.5233 (+74.13%)	0.3812 (+26.85%)	73.44%	76.77%	25.12%
	$300°C$	0.2773	0.5378 (+93.97%)	0.5637 (+103.3%)	0.3589 (+29.45%)	104.6	108.3%	27.90%

3.8 Characteristics of the model-based approach

The achievement of ILVO model represents an important advancement in the field of tribology and vehicle dynamics studies. The formulation of a loyal BLCF dynamic model can not only support the brake design but also increase the simulation fidelity of vehicle dynamics simulation software. The main innovative contributions of the proposed model can be boiled down to the following statements:

- ILVO model provides a description of the effective contact area dynamics, which represents the birth-destruction dynamics of contact patches at the pad-disc interface;
- ILVO model considers a contact coefficient reproducing the adhesion property of the frictional contact, which enhances the modelling performance for a wide temperature range;
- ILVO model with fixed parametrisation is capable of capturing BLCF decay for increasing disc temperature, although this information is not provided during the model identification procedure.

In this analysis, the model operational range is limited to a brake disc temperature of around 350°C. This limit does not affect the model applicability (e.g. for HIL simulation) as the disc temperature commonly reached in service lies beneath 250°C [72]. Higher temperature values can be achieved when the brake undergoes severe braking conditions such as extended braking on a down-hill.

3.9 Chapter summary

This chapter introduces a novel BLCF model that outperforms the state of the art in capturing both the average BLCF and its dynamics. Although the BLCF dynamics entails highly stochastic phenomena, the proposed deterministic data-driven model features a good fitting of the investigated braking conditions. The results demonstrate that the proposed method outperforms state-of-the-art solutions. Particularly, the proposed model extrapolates well BLCF for brake temperature values laying far from the investigated region.

Although the proposed model does not account for high frequency phenomena, it provides a novel modelling framework, which allows for the inclusion of additional phenomena. NVH-related mechanisms may be included by adding limit-cycle oscillations terms to the effective area dynamics; the local pressure distribution shall be also taken into account for a more accurate formulation of the integral problem. The proposed model is embedded in the vehicle dynamics simulation software to enhance the modelling fidelity of SIL/MIL/HIL frameworks. The enhanced modelling framework can be therefore used for brakes controls and design purposes in Chapter 4.

Chapter 4

A novel brake friction coefficient observer

4.1 Introduction

The present chapter features a novel BLCF observer based on the extended Kalman filter. This latter encompasses the chassis and wheels rotational dynamics and relies upon the wheel speed sensors and the inertia measurement unit (IMU) by avoiding the analytical description of non-linear phenomena occurring in the pad-disc interface. The functionality of the developed estimator is proved in MIL/SIL environment by means of the vehicle dynamics simulator IPG CarMaker® with experimentally validated model of a full electric SUV equipped with four on-board motors and EHB. Information on the model implementation and subsystems thereof is reported in Appendix A. In accordance with the results of Chapter 3, ILVO model allows for improved fidelity of the MIL/SIL frameworks due to inclusion of the BLCF and disc temperature dynamics. Under this framework, straight-line braking tests as per ECE R13H [73], involving different initial braking speed and deceleration values, are used as reference test scenario to assess the functionality of the developed observer. The brake pedal actuation speed is set equal to 150 mm/s. The statistical analysis in Chapter 1 shows that the actual BLCF value might exhibit deviations up to 25% from its nominal value with 95% confidence interval under real driving conditions. To this effect, the BLCF observer shall exhibit superior performance when compared to the case where a constant BLCF estimate, equal to its nominal value, is used.

4.2 Vehicle model

The vehicle model used for MIL/SIL and also HIL investigations is the full electric SUV equipped with the decoupled electrohydraulic brake system (EHB) and four on-board electric motors (EM). Information on the model implementation and subsystems thereof is reported in Appendix A. The vehicle model parametrisation is based on experimental data collected from the full electric SUV demonstrator provided by Flander's Make. For details, the reader is referred to Appendix D. The schematics of the vehicle under study is reported in Figure 4.1. The vehicle features four on-board motors connected to the wheels by means of half shafts. Braking action can be provided both by EHCU and EM. The regenerative torque can be requested upon checking the battery availability *via* the battery management unit (BMU). The required control signals are made available by the VCU, in accordance with the description already provided in Chapter 1. The brakes are composed of grey cast iron disc and ECE linings. The on-board motors are synchronous machines of switched reluctance type.

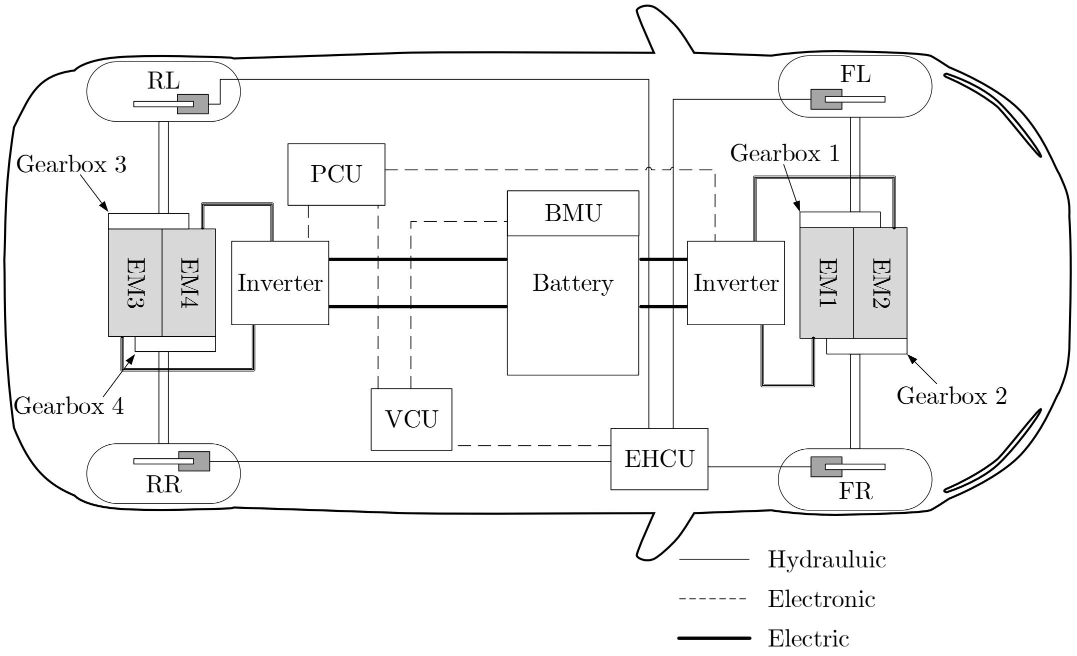

Figure 4.1: *Architecture of the full electric sport utility vehicle.*

Legal requirements demand that the braking system of road vehicles provides stable behaviour under all driving scenarios [73]. ECE R13H defines two important features, namely the adhesion utilisation and basic braking stability based on wheel-lock sequence. It is important that rear wheels do not saturate during braking occurrence as this might lead to vehicle spin-out. EHB allows the distribution between front and rear axles to be flexibly adjusted according to the driving conditions. This enables optimised vehicle handling stability under all payload conditions, even wear between front and rear axles and improved vehicle deceleration with the same pedal force. An ideal force distribution ensures equal tyre-road friction utilisation between front and rear axles (see Figure 4.2). The associated calculation stems from the quasi-static equations of pure longitudinal motion during braking occurrence [74]. Conventional electronic brake force distribution systems (EBD) feature a reduction in the rear wheel torque at higher deceleration levels so to approximate the ideal brake force distribution (see Figure 4.2).

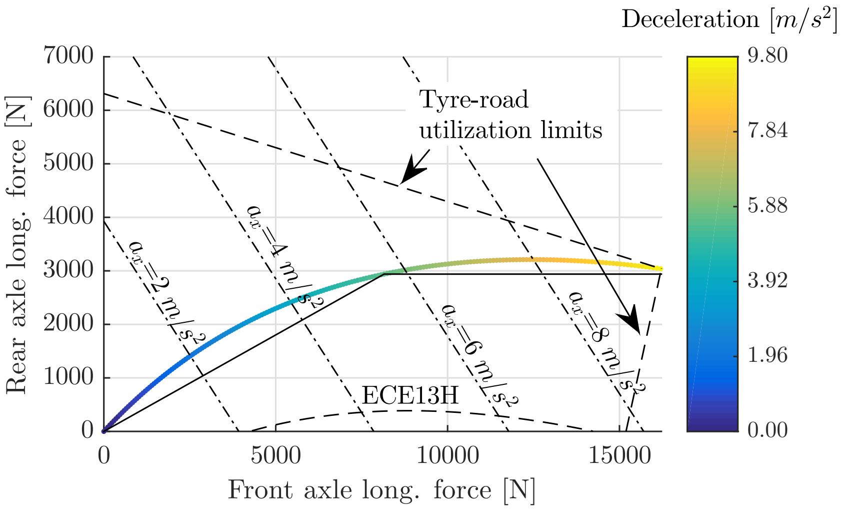

Figure 4.2: *The fixed brake distribution (conventional EBD) is reported as solid black line, whilst the ideal distribution follows the coloured bar. Stability and friction utilisation limits on dry road are reported as dashed black lines. Iso-deceleration conditions are represented by dash-dotted lines.*

Under the framework of MIL/SIL and also HIL simulations, the ideal distribution curve is implemented in the base brake controller [75]. Figure 4.2 reports the ideal brake force distribution curve spanned for different vehicle deceleration levels. Figure 4.2 also reports the vehicle stability limits set by ECE R13H [73] during braking occurrence and the tyre-road friction utilisation limits on dry conditions. These constraints set the limits to avoid rear wheels lock during braking. Other distributions are suitable for the scope of this work, provided that they comply with ECE R13H [73].

4.3 Observer of the brake lining coefficient of friction

State observers have been applied during the past years for the estimation of vehicle dynamics states in control applications [76]. However, the potential benefits of an on-line BLCF observer have very rarely been addressed by the research community and BLCF has often been assumed known and constant [16]. In [47], the author proposes a tool based on the extended Kalman filter to estimate the brake torque for the enhancement of blending between the conventional and regenerative brakes. Particularly, the author applies a linear Kalman filter to observe the temperature of each brake disc. A LuGre friction model that takes into account the speed and temperature dependence of BLCF is then used to predict the brake torque [77]. The method relies upon a friction model that cannot reproduce the underlying BLCF mechanisms. Indeed, in case of variation in the plant characteristics or environmental conditions, the model leads the linear Kalman filter to a wrong estimate. In [61], the authors propose and validate a wheel torque observer that ultimately lead to the estimation of BLCF. Although the methodology does not make use of any temperature or BLCF model, it is only valid for a fixed brake torque distribution and requires the execution of expensive experiments on the real vehicle to extract characteristic chassis kinematics curves.

The present work proposes the Kalman filter under a new shape [16]. The proposed observer encompasses the chassis and wheels rotational dynamics and relies upon the wheel speed sensors and the inertia measurement unit by avoiding the analytical description of non-linear phenomena occurring in the pad-disc interface. Unlike [47], the proposed observer does not hinge upon a brake temperature model and, unlike [61], the estimation scheme is independent of any brake torque allocation strategy. Such an estimator represents a cost-effective solution suitable for current production vehicles, provided that an accurate wheel slip estimation is available. As it will be later shown in this work, a robust estimation of BLCF leads to improved braking performance, reduced driver's workload and enables novel brake monitoring functions.

4.3.1 Kalman filter theory

In accordance with numerous literature instances, the Kalman theory has been widely used as a state observer because it ensures good robustness for tolerating differences between models and real dynamics of the vehicle, variations of model parameters and signal errors. The Kalman filter is the minimum variance state estimator for linear dynamic systems with Gaussian noise. It comprises two stages: the prediction step, based on the model of the process; the update step, based on sensor measurements. The noise on the input variables makes the model of the process less accurate; the noise of the sensors deteriorates the correction provided during the update step. For the sake of clarity, this section briefly reports an overview of the Kalman filter theory. Let be the system:

$$\mathbf{x}_{k+1} = \mathbf{A}_k \mathbf{x}_k + \mathbf{B}_k \mathbf{u}_k + \mathbf{w}_k, \tag{4.1a}$$

$$\mathbf{y}_k = \mathbf{C}_k \mathbf{x}_k + \mathbf{v}_k, \tag{4.1b}$$

where, $\mathbf{A}_k$ is the state transition matrix applied to the previous state $\mathbf{x}_k$, $\mathbf{B}_k$ defines the control-input matrix applied to the control vector $\mathbf{u}_k$, and $\mathbf{w}_k$ is the process noise assumed zero mean multivariate normal with covariance $\mathbf{Q}_k$. Moreover, $\mathbf{y}_k$ and $\mathbf{C}_k$ are the output vector and output matrix, respectively, and $\mathbf{v}_k$ is the observation noise assumed zero mean Gaussian with covariance $\mathbf{R}_k$. Thus, the Kalman filter is composed of a prediction stage defined as:

$$\hat{\mathbf{x}}_{k+1|k} = \mathbf{A}_k \hat{\mathbf{x}}_{k|k} + \mathbf{B}_k \mathbf{u}_k, \tag{4.2a}$$

$$\mathbf{P}_{k+1|k} = \mathbf{A}_k \mathbf{P}_{k|k} \mathbf{A}_k^T + \mathbf{Q}_k, \tag{4.2b}$$

where, $\hat{\mathbf{x}}_{k+1|k}$ represents the predicted state vector at time step $k+1$ from the previous best estimate; $\mathbf{P}_{k+1|k}$ is the covariance matrix of the state updated with the best previous estimate. Equations (4.2a) and (4.2b) are responsible for the information content of the "model predicted component" of the Kalman filter. This is followed by the updating stage:

$$\mathbf{S}_k = \mathbf{R}_k + \mathbf{C}_k \mathbf{P}_{k+1|k} \mathbf{C}_k^T, \tag{4.3a}$$

$$\mathbf{K}_k = \mathbf{P}_{k+1|k} \mathbf{C}_k^T \mathbf{S}_k^{-1}, \tag{4.3b}$$

$$\hat{\mathbf{x}}_{k+1|k+1} = \hat{\mathbf{x}}_{k+1|k} + \mathbf{K}_k (\mathbf{y}_{k+1} - \mathbf{C}_k \hat{\mathbf{x}}_{k+1|k}), \tag{4.3c}$$

$$\mathbf{P}_{k+1|k+1} = \mathbf{P}_{k+1|k} - \mathbf{K}_k \mathbf{S}_k \mathbf{K}_k^T, \tag{4.3d}$$

where, the new subscript means that both state vector and its covariance matrix are updated with the sensors information. $\mathbf{K}_k$ represents the Kalman gain. It is worth remarking that $\mathbf{Q}_k$ and $\mathbf{R}_k$ are the filter tuning parameters. The higher $\mathbf{Q}_k$ with respect to $\mathbf{R}_k$ is, the more the Kalman filter will rely on the sensors measurements.

In presence of non-linear processes, the linear Kalman filter cannot be directly employed. The most common solution relies on the linearisation of the associated state equations by Langrangians calculation. This is also known as the extended Kalman filter (EKF). Let be the system:

$$\mathbf{x}_{k+1} = \mathbf{f}(\mathbf{x}_k, \mathbf{u}_k) + \mathbf{w}_k, \tag{4.4a}$$

$$\mathbf{y}_k = \mathbf{h}(\mathbf{x}_k) + \mathbf{v}_k. \tag{4.4b}$$

The function $\mathbf{f}(\cdot)$ can be used to compute the predicted state from the previous estimate and, similarly, the function $\mathbf{h}(\cdot)$ can be used to compute the predicted measurement from the predicted state. These functions cannot be applied directly to the covariance matrices; thus, partial derivatives matrices for the states and outputs, are computed:

$$\mathbf{A}_k = \frac{\partial \mathbf{f}}{\partial \mathbf{x}} |_{\hat{\mathbf{x}}_{k|k}, \mathbf{u}_k}, \tag{4.5a}$$

$$\mathbf{C}_k = \frac{\partial \mathbf{h}}{\partial \mathbf{x}} |_{\hat{\mathbf{x}}_{k+1|k}}. \tag{4.5b}$$

Hence, the EKF is composed of a prediction stage:

$$\hat{\mathbf{x}}_{k+1|k} = \mathbf{f}(\hat{\mathbf{x}}_{k|k}, \mathbf{u}_k), \tag{4.6}$$

and $\mathbf{P}_{k+1|k}$ is already defined in Equation (4.3d), followed by the update stage:

$$\tilde{\mathbf{y}}_{k+1|k+1} = \mathbf{y}_{k+1} - \mathbf{h}_k(\hat{\mathbf{x}}_{k+1|k}), \tag{4.7}$$

with $\mathbf{S}_k$, $\mathbf{K}_k$, $\mathbf{P}_{k+1|k+1}$ and $\hat{\mathbf{x}}_{k+1|k+1}$ being defined as for the linear Kalman filter. It is worth noting that the Kalman filter tuning parameters shall be properly set to ensure the filter functionality. $\mathbf{R}_k$ accounts for uncertainty in the measured data, while $\mathbf{Q}_k$ is generally tuned depending on the quality of the developed model. The right selection of $\mathbf{Q}_k$ represents an awkward problem and in most cases a good state estimation can be achieved even in presence of a poor model, provided that enough uncertainty is injected into the model via the right selection of $\mathbf{Q}_k$. Although conventionally $\mathbf{R}_k$ and $\mathbf{Q}_k$ are obtained heuristically by trial and error, the present work adopts a systematic approach based on genetic algorithms, which is later discussed in Chapter 6. This latter leads the Kalman filter to a suboptimal solution by minimising the prediction error. A schematic of the embedded Kalman filter is reported in Figure 4.3.

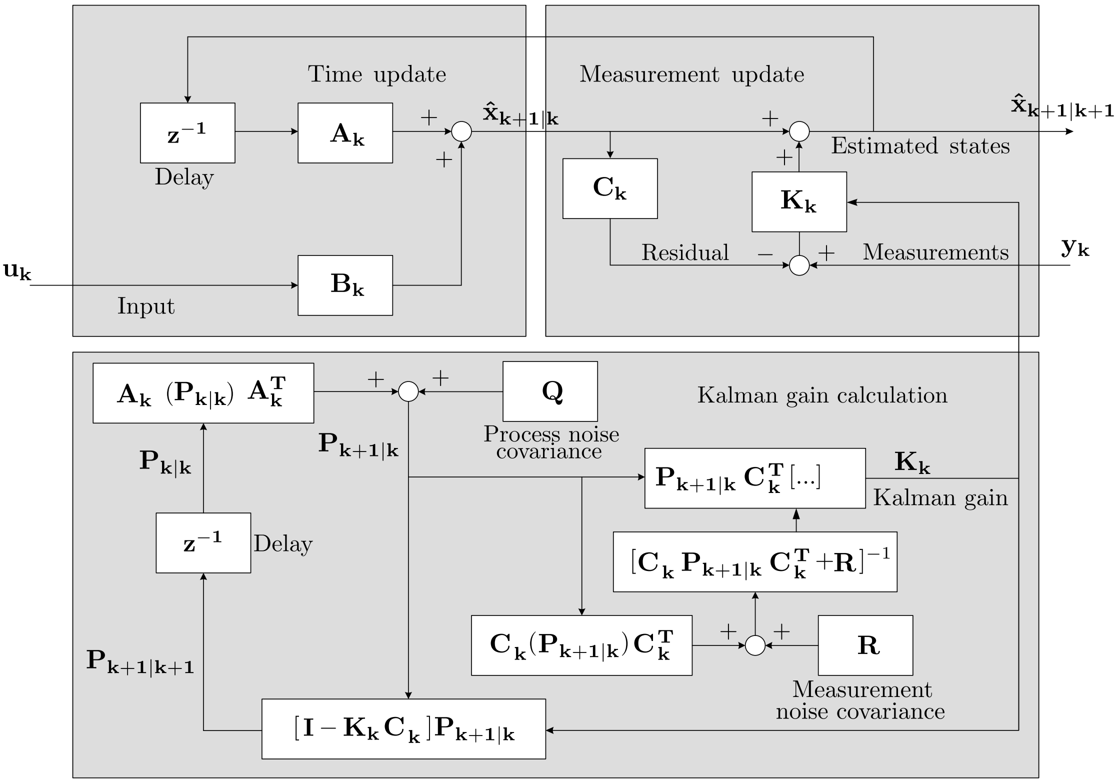

Figure 4.3: *Scheme of the Kalman filter implemented in Simulink®.*

4.3.2 Estimation variants

The state-space formulation associated with the observer stems from a quarter-car model for the vehicle longitudinal and lateral dynamics with fixed parameters. In this section, two estimation variants are proposed:

- Observer 1, direct measurement of the tyre longitudinal forces;
- Observer 2, virtual sensing of the tyre longitudinal forces;

where, the first design requires expensive wheel force transducers [78], whilst the second design relies on inexpensive commercially available sensors. For this reason, Observer 2 is further developed for successive analysis and Observer 1 is only confined to this chapter for benchmarking purposes.

A schematic of the developed observer architectures is reported in Figure 4.4. Henceforth, the hat superimposition denotes an estimated or observed quantity; the "$^{(S)}$" apex refers to a measured variable, "$^{(VS)}$" to a virtually sensed variable and "$^{(TM)}$" to a tyre-model variable. The subscripts "ij" identifies the wheel of the vehicle and "k" is the generic simulation step. In the first design, it is assumed that the tyre longitudinal forces can be measured by means of wheel force transducers or hub-force sensors [78]. Despite hub-force sensors and wheel force transducers have been continuously subject to technological enhancements during the last years, the technology is still expensive and has not been implemented in production vehicles. In Observer 2, the direct measurement of the longitudinal forces is replaced with a virtual sensor that relies on readily available measurements such as the vehicle body acceleration and estimates of the vehicle mass, tyre slip, tyre vertical load and tyre longitudinal slip stiffness.

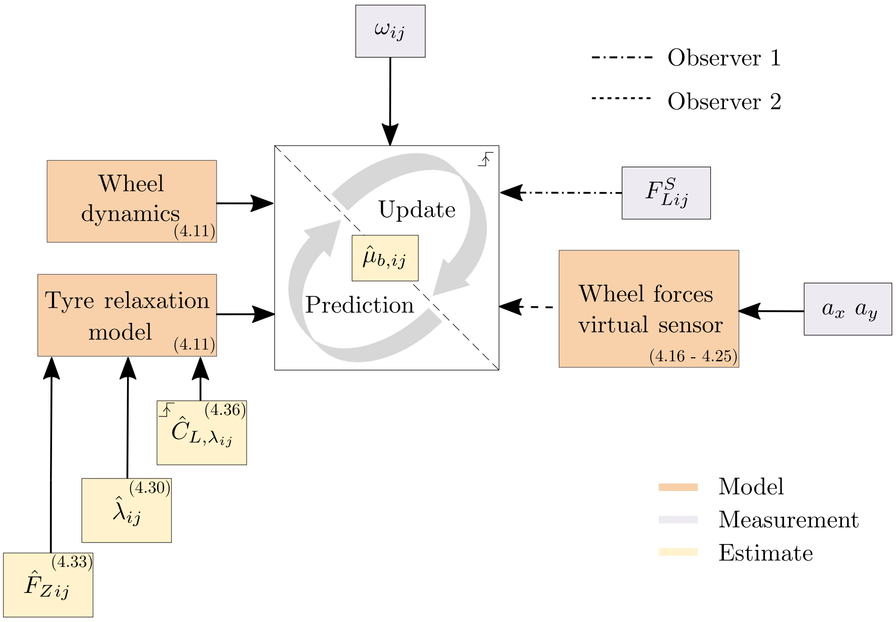

Figure 4.4: *Scheme of the developed observer architectures. Dash-dotted lines refer to Observer 1; dashed lines refer to Observer 2. The longitudinal slip stiffness estimation block and BLCF observer are triggered subsystems. The numbers in parenthesis point to the associated equations.*

The filter state, measurement and input vectors are defined in Equations (4.8) to (4.10), respectively.

$$\mathbf{x}_k = \left\{\hat{\omega}_{ij_k}, \hat{F}_{L,ij_k}, \hat{\mu}_{b,ij_k}\right\}^T, \tag{4.8}$$

$$\mathbf{y}_k = \left\{\omega^{(S)}_{ij_k}, F^{(S\ or\ VS)}_{L,ij_k}\right\}^T, \tag{4.9}$$

$$\mathbf{u}_k = \left\{p^{(S)}_{b,ij_k}, F^{(TM)}_{L,ij_k}, \hat{T}_{d,ij_k}\right\}^T, \tag{4.10}$$

where $\hat{\omega}_{ij_k}$ represents the wheel speed estimate, $\hat{F}_{Lij_k}$ is the wheel longitudinal force estimate and $\hat{\mu}_{b,ij_k}$ is the BLCF estimate. The measurements vector includes the wheel speed sensors measurements $\omega^{(S)}_{ij_k}$ and the longitudinal force, which can be either measured $F^{(S)}_{Lij_k}$ (Observer 1) or virtually sensed $F^{(VS)}_{Lij_k}$ (Observer 2). At last, the input vector contains the longitudinal force prediction $F^{(TM)}_{Lij_k}$ stemming from the quasi-static linear tyre model [79], the measured EHB calliper pressure $p^{(S)}_{b,ij_k}$ and the drive or regenerative torque component $\hat{T}_{d,ij_k}$. The state variables, in discrete time space, evolve in accordance with the dynamics described in Equations (4.11a) to (4.11c):

$$\begin{cases} \hat{\omega}_{ij_{k+1}} = \hat{\omega}_{ij_k} - \Delta t \, \dfrac{\hat{T}_{b,ij_k} - r_{\omega,ij}\hat{F}_{L,ij_k} - \hat{T}_{d,ij_k}}{I_{\omega,ij}}, & (4.11a) \\ \hat{F}_{L,ij_{k+1}} = \left(1 - \dfrac{\Delta t}{\tau_{RL}}\right)\hat{F}_{L,ij_k} + \dfrac{\Delta t}{\tau_{RL}} F^{(TM)}_{L,ij_k}(\hat{\lambda}_{ij_k}, \hat{C}_{L,ij_k}), & (4.11b) \\ \hat{\mu}_{b,ij_{k+1}} = \hat{\mu}_{b,ij_k}. & (4.11c) \end{cases}$$

The above-defined set of equations represents the observer prediction model in discrete time rendering the wheel rotational dynamics in Equation (4.11a) and the tyre relaxation model in Equation (4.11b). With reference to the adopted terminology, Δt is the simulation time step, $r_{\omega,ij}$ is the wheel radius and $I_{\omega,ij}$ represents the wheel inertia. It is worth remarking that the quasi-static tyre model $F^{(TM)}_{L,ij_k}$ is function of the estimated longitudinal slip $\hat{\lambda}_{ij,k}$ and the estimated longitudinal slip stiffness $\hat{C}_{L,ij_k}$. The tyre rolling resistance is assumed as process noise. The applied brake torque follows the definition given in Equation (A.19), whilst the presence of a drive or regenerative torque $\hat{T}_{d,ij_k}$ during braking occurrence depends upon the vehicle drivetrain architecture. When braking, $\hat{T}_{d,ij_k}$ is equal to the electric motor regenerative torque, whilst in conventional ICE vehicles it is equal to the engine drag torque. With reference to the employed tyre model, as long as the braking action occurs within the tyre linear region limits (Figure A.6) the longitudinal force can be approximated by the linear tyre model:

$$F^{(TM)}_{L,ij} = \hat{C}_{L,ij}\ \hat{\lambda}_{ij}. \tag{4.12}$$

In case excessive wheel slip or even wheel lock occurs, a non-linear tyre model shall be employed. With reference to this scenario, an example will be shown next in Chapter 5. For the sake of simplicity, the tyre relaxation coefficient is assumed inverse function of the vehicle speed, in accordance with Equation (A.14). Its identification is based on open-loop braking manoeuvres at varying deceleration levels and initial vehicle velocity values. At last, a random-walk approach is used for the BLCF state variable, whose value will be thereafter corrected in the update phase.

In order to initiate the execution of the state space in Equation (4.11), the initial states condition must be provided upon the observer activation:

$$\mathbf{x}_0 = \{\omega_{ij_0}, F_{L,ij_0}, \mu_{b,ij_0}\}, \tag{4.13}$$

where, ω_{ij_0} equals the wheel rotational speed at the beginning of a braking manoeuvre, F_{L,ij_0} is set equal to a quarter of the longitudinal vehicle body force upon braking, μ_{b,ij_0} is equal to the last BLCF estimate. In case no previous estimated value is available, μ_{b,ij_0} is set equal to the average BLCF determined by the manufacturer in accordance with SAE J2522.

In this work, it is assumed that the brake calliper pressure is available. Nonetheless, in case a direct measurement of the calliper pressure is not available, the master cylinder pressure can be used as a mean to estimate the former [80]. Due to hydraulic dynamics, this choice may results in different estimation performance and, thus, require a proper observer tuning. In accordance with the linearisation required by the extended Kalman filter, the state $\mathbf{A}_k$ and output $\mathbf{C}_k$ matrices, in discrete time, are defined as follows:

$$\mathbf{A}_{ij_k} = \begin{bmatrix} 1 & \frac{\Delta t}{I_w} r_{\omega,ij} & -2n_p\pi\frac{d_p^2}{4}p_{b,ij_k}\frac{\Delta t}{I_{\omega,ij}}r_{eff,i} \\ 0 & \left(1-\frac{\Delta t}{\tau_{RL}}\right) & 0 \\ 0 & 0 & 1 \end{bmatrix} \tag{4.14}$$

$$\mathbf{C}_{ij_k} = \begin{bmatrix} 1 & 0 & 0 \\ 0 & 1 & 0 \end{bmatrix} \tag{4.15}$$

Observer 2 relies on a global force virtual sensor that uses the measured longitudinal acceleration to compute a global tyre-road force, in accordance with Equations (4.16) and (4.17):

$$F_X^{(VS)} = \hat{m}_v a_x^{(S)} - \hat{F}_{X,drag}, \tag{4.16}$$

$$F_Y^{(VS)} = \hat{m}_v a_y^{(S)} - \hat{F}_{Y,drag}, \tag{4.17}$$

where $\hat{F}_{X,drag}$ and $\hat{F}_{Y,drag}$ represent the estimated air drag forces in the longitudinal and lateral directions and $a_x^{(S)}$ and $a_y^{(S)}$ are the measured longitudinal and lateral accelerations. It is worth remarking that the road slope and inertial effects shall not be considered in the previous equations as they are already captured by the body acceleration sensors. Moreover, the vehicle mass $\hat{m}_v$ shall be estimated upon applying Equations (4.16) and (4.17). This can be done by using a linear Kalman observer, provided that the drive torque can be estimated with less than 10% accuracy during acceleration manoeuvres [81]. Therefore, the global longitudinal and lateral body forces can be computed by subtracting the air drag resistance from the vehicle inertial forces.

It is worth noting that whilst Equations (4.16) and (4.17) provide a global value for the longitudinal and lateral forces, the output vector in Equation (4.9) requires longitudinal forces in the wheel reference $F_{L,ij_k}^{(VS)}$ for each wheel. This is addressed by introducing an allocation factor that stems from the ratio between two global chassis forces, namely the global virtually sensed force and the global modelled body force [16]:

$$K_f = \frac{\sqrt{\left(F_X^{(VS)}\right)^2 + \left(F_Y^{(VS)}\right)^2}}{\sqrt{\left(F_X^{(TM)}\right)^2 + \left(F_Y^{(TM)}\right)^2}}. \tag{4.18}$$

A filter based on the recursive least square method is applied across a finite set of time steps in order to capture the time-varying properties of the correction factor by simultaneously mitigating its rapid variations. Equation (4.18) can be rewritten in a linear fashion as follows:

$$\mathbf{y}_k = \mathbf{X}_k \cdot \theta_k, \tag{4.19}$$

where, $\mathbf{y}_k = \sqrt{\left(F_{X_k}^{(VS)}\right)^2 + \left(F_{Y_k}^{(VS)}\right)^2}$, $\mathbf{X}_k = \sqrt{\left(F_{X_k}^{(TM)}\right)^2 + \left(F_{Y_k}^{(TM)}\right)^2}$ and $\theta_k = [K_{f_k}]$. The filtered correction factor $\hat{K}_f$ is obtained by applying the recursive least square routine (RLS):

$$\hat{\theta}_k = \hat{\theta}_{k-1} + \mathbf{g}_k \cdot \left[\mathbf{y}_k - \mathbf{X}_k \cdot \hat{\theta}_{k-1}\right], \tag{4.20}$$

$$\mathbf{g}_k = \left[\lambda_{RLS} + \mathbf{X}_k^T \cdot \mathbf{P}_{k-1} \cdot \mathbf{X}_k\right]^{-1} \cdot \mathbf{P}_{k-1} \cdot \mathbf{X}_k, \tag{4.21}$$

$$\mathbf{P}_k = \frac{1}{\lambda_{RLS}} \cdot [1 - \mathbf{g}_k \cdot \mathbf{X}_k] \cdot \mathbf{P}_{k-1}. \tag{4.22}$$

The RLS estimation constant, λ_{RLS}, namely forgetting factor, produces a delay in the filtered correction factor. As a consequence, the observer adaptation time against changing road conditions depends on the RLS settings. Upon solving the optimisation problem in Equation (4.19), the virtually sensed tyre-ground forces can be estimated in accordance with Equations (4.23) and (4.24):

$$F_{X,ij}^{(VS)} = \hat{K}_f \; F_{X,ij}^{(TM)}, \tag{4.23}$$

$$F_{Y,ij}^{(VS)} = \hat{K}_f \; F_{Y,ij}^{(TM)}. \tag{4.24}$$

The estimation of the correction factor is the key element for the adaptability of the proposed observer against varying road conditions. The virtual sensor provides the observer with intrinsic fault tolerance against errors or failures that might affect the linear tyre model. This feature will be later addressed in Chapter 5. Nevertheless, excessive longitudinal load transfer and extreme variation in road conditions might still be hard to compensate by means of the correction factor. In this case, the tyre longitudinal slip stiffness needs to be newly estimated in accordance with the routine reported in Section 4.3.5. The routine for the tyre longitudinal slip stiffness estimation is only activated if the braking occurs in a straight line and the filtered correction factor exceeds a threshold. The direct proportionality in Equations (4.23) and (4.24) dictates that the modelled and virtually estimated global body forces point in the same direction.

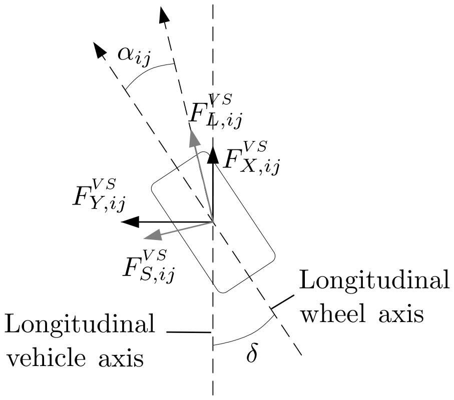

Figure 4.5: *The reference translation from the chassis $(X-Y)$ to the wheel $(L-S)$ encompasses the steering angle δ and the wheel side slip angle α_{ij}.*

However, the virtually sensed and model predicted components of tyre forces reside in two different reference systems, which are the chassis and tyre reference systems, respectively (Figure 4.5). Thus, the virtually sensed force and the Kalman filtered longitudinal components of the tyre force must be moved to the same reference to perform a correct observation. As shown in Figure 4.5, the tyre side slip angle $\hat{\alpha}_{ij}$ and the steering angle δ shall be taken into account to rotate the body virtually sensed force into the wheel reference. The translation matrix is defined as:

$$\begin{bmatrix} F_{L,fj} \\ F_{S,fj} \\ F_{L,rj} \\ F_{S,rj} \end{bmatrix} = \begin{bmatrix} cos\hat{\alpha}_{fj}\ cos\delta \pm sin\hat{\alpha}_{fj}\ sin\delta & sin\hat{\alpha}_{fj}\ cos\delta - cos\hat{\alpha}_{fj}\ sin\delta & 0 & 0 \\ -sin\hat{\alpha}_{fj}\ cos\delta + cos\hat{\alpha}_{fj}\ sin\delta & cos\hat{\alpha}_{fj}\ cos\delta + sin\hat{\alpha}_{fj}\ sin\delta & 0 & 0 \\ 0 & 0 & cos\hat{\alpha}_{rj} & sin\hat{\alpha}_{rj} \\ 0 & 0 & -sin\hat{\alpha}_{rj} & cos\hat{\alpha}_{rj} \end{bmatrix}^{-1} \begin{bmatrix} F_{X,fj} \\ F_{Y,fj} \\ F_{X,rj} \\ F_{Y,rj} \end{bmatrix}. \tag{4.25}$$

At this point, the virtual forces of Observer 2 can be used to close the loop and update the final longitudinal force estimation.

It is worth remarking that the proposed observer can only capture BLCF dynamics occurring at a larger time scale than the characteristic time constant of the filter process model. The limiting time constant in Equation (4.11) is surely represented by the tyre relaxation time τ_{RL}. Therefore, the proposed observer cannot capture BLCF dynamics associated with brake disc thickness variation [82] and creep groan vibrations [83], which are typically characterised by a time constant much smaller than the tyre relaxation time.

4.3.3 Wheel slip estimation

The wheel slip estimation relies upon a correct estimation of the vehicle velocity, which is usually done by averaging the wheel speed sensors information [84], and the correct processing of the wheel speed sensor measurements. The lack of free rolling wheels during braking makes the vehicle speed estimation from wheel speed sensors an awkward task. Therefore, the speed estimation during braking manoeuvres require an appropriate integration of the accelerometer signal. In this work, the accelerometer signal and wheel encoders are combined to estimate the vehicle speed: the estimation approach is composed of the four wheel tangential speeds at the tyre-road contact point and the longitudinal vehicle acceleration.

For limited vehicle side slip angles, the four tangential speed values at the tyre-road contact points can be corrected to the vehicle CoG by application of Equation (4.26):

$$\begin{cases} v_{\omega,fl}^{(CoG)} = v_{\omega,fl}^{(S)}\ cos\delta + \dot{\psi}^{(S)}\dfrac{b}{2}, & (4.26a)\\ v_{\omega,fr}^{(CoG)} = v_{\omega,fr}^{(S)}\ cos\delta - \dot{\psi}^{(S)}\dfrac{b}{2}, & (4.26b)\\ v_{\omega,rl}^{(CoG)} = v_{\omega,rl}^{(S)} + \dot{\psi}^{(S)}\dfrac{b}{2}, & (4.26c)\\ v_{\omega,rr}^{(CoG)} = v_{\omega,rr}^{(S)} + \dot{\psi}^{(S)}\dfrac{b}{2}, & (4.26d) \end{cases}$$

where, $v_{\omega,ij}^{(S)}$ represents the rotational equivalent wheel speed computed as $(r_{\omega,ij} \cdot \omega_{ij})$ and $\dot{\psi}^{(S)}$ represents the measured vehicle yaw rate.

With reference to the accelerometer, this latter needs to be corrected by compensating its tilted position in relation to the inertial coordinate system of the vehicle. Moreover, road banking and the inertial centripetal forces affect the acceleration measurement. Therefore, these latter are corrected in accordance with Equation (4.27):

$$a_x^{(C)} = a_x^{(S)} + g\ sin(\hat{\chi}_{road}) + \dot{\psi}^{(S)}\hat{v}_y, \tag{4.27}$$

where, the apex "$^{(C)}$" stands for the corrected signal and $\hat{\chi}_{road}$ represents the estimated road banking and $\hat{v}_y$ is the estimated lateral vehicle velocity.

The linear Kalman filter proposed in [81] is used for the data fusion. Indeed, all four corrected rotational equivalent wheel speeds are combined to provide a least variance estimation of the vehicle speed at the CoG. The filter state and measurement vectors are defined in Equations (4.28) and (4.29), respectively.

$$\mathbf{x}_k = \{\hat{a}_{x_k}, \hat{v}_{x_k}\}^T, \tag{4.28}$$

$$\mathbf{y}_k = \left\{a_{x_k}^{(C)}, v_{\omega,fl_k}^{(CoG)}, v_{\omega,fr_k}^{(CoG)}, v_{\omega,rl_k}^{(CoG)}, v_{\omega,rr_k}^{(CoG)}, v_{x_k}^{(S)}\right\}^T, \tag{4.29}$$

where, the output vector contains the corrected measured vehicle acceleration, the wheel speed values translated to the vehicle CoG and, if available, a vehicle speed sensor measurement. As it will be shown in the next chapters, $v_{x_k}^{(S)}$ can be either provided via GPS or via optical measurement sensors. The discrete state space formulation of the vehicle speed observer is as follows:

$$\begin{cases} \hat{a}_{x_{k+1}} = \hat{a}_{x_k} & (4.30a) \\ \hat{v}_{x_{k+1}} = \hat{v}_{x_k} + \Delta t \ \hat{a}_{x_k}. & (4.30b) \end{cases}$$

The associated representation for the implementation in the Kalman filter follows:

$$\mathbf{A}_k = \begin{bmatrix} 1 & 0 \\ 1 & \Delta t \end{bmatrix}, \tag{4.31}$$

$$\mathbf{C}_k = \begin{bmatrix} 1 & 0 & 0 & 0 & 0 & 0 \\ 0 & 1 & 1 & 1 & 1 & 1 \end{bmatrix}^T. \tag{4.32}$$

Once the vehicle speed v_x is observed, Equation (A.6) can be used to estimate the wheel slip. To avoid undesired oscillation in the slip estimate, this latter is low-pass filtered at 16 Hz cut-off frequency.

4.3.4 Tyre vertical forces estimation

For the estimation of the tyre vertical forces, a simple open loop scheme is adopted. Although more sophisticated methods, based on suspensions deflection sensors have been proposed during the past years [85], in the present work the tyre vertical forces are estimated by means of the quasi-static weight transfer model presented in [85]. The proposed estimation scheme draws upon the available measurements of longitudinal and lateral accelerations. During acceleration, braking and cornering, the load transfer causes varying vertical force components on the tyres. The estimation scheme neglects the suspension dynamics and disregards the pitch/roll coupling:

$$\begin{cases} \hat{F}_{Zfl} = \hat{m}_v g \dfrac{l_r}{2(l_f + l_r)} - \hat{m}_v a_x^{(S)} \dfrac{h}{2(l_f + l_r)} - \hat{m}_v a_y^{(S)} \dfrac{h l_r}{b(l_f + l_r)}, & (4.33a) \\ \hat{F}_{Zfr} = \hat{m}_v g \dfrac{l_r}{2(l_f + l_r)} - \hat{m}_v a_x^{(S)} \dfrac{h}{2(l_f + l_r)} + \hat{m}_v a_y^{(S)} \dfrac{h l_r}{b(l_f + l_r)}, & (4.33b) \\ \hat{F}_{Zrl} = \hat{m}_v g \dfrac{l_r}{2(l_f + l_r)} + \hat{m}_v a_x^{(S)} \dfrac{h}{2(l_f + l_r)} - \hat{m}_v a_y^{(S)} \dfrac{h l_r}{b(l_f + l_r)}, & (4.33c) \\ \hat{F}_{Zrr} = \hat{m}_v g \dfrac{l_r}{2(l_f + l_r)} + \hat{m}_v a_x^{(S)} \dfrac{h}{2(l_f + l_r)} + \hat{m}_v a_y^{(S)} \dfrac{h l_r}{b(l_f + l_r)}. & (4.33d) \end{cases}$$

A validation of the vertical force estimation scheme against data collected from the full electric SUV of Appendix D on the proving ground are reported in Figure 4.6. For the sake of space, only the results corresponding to the double lane change (ISO 3888) are considered in the present section.

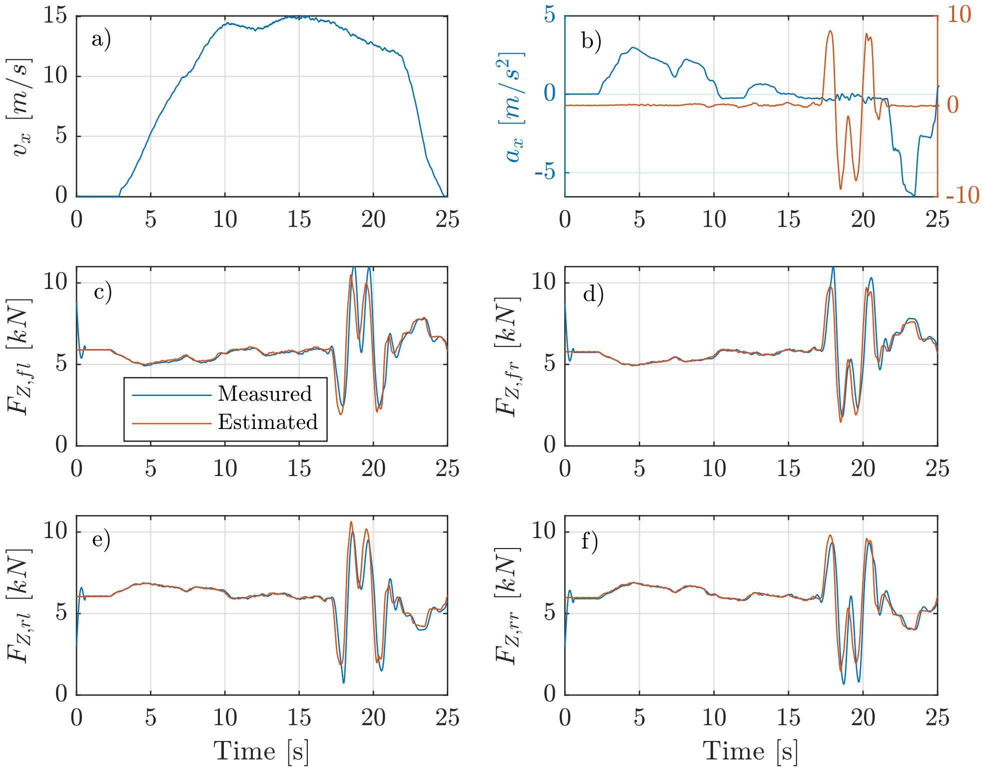

Figure 4.6: *Validation of the vertical force observer with respect to Double Lane Change (ISO 3888). a) Vehicle velocity; b) Vehicle longitudinal and lateral acceleration; c) to f) Vertical tyre forces on front-left, front-right, rear-left and rear-right corners.*

4.3.5 Estimation of the tyre longitudinal slip stiffness

The BLCF observer is initialised with a tyre longitudinal slip stiffness corresponding to a dry road at nominal vertical load and inflation pressure (Figure 4.7b). If during the estimation loop the correction factor $\hat{K}_f$ exceeds a threshold, that is, the tyre model lays too far from the information provided by the virtual sensor, the tyre longitudinal slip stiffness is newly estimated. As shown in Appendix A, the tyre longitudinal slip stiffness depends upon several variables, among others the wheel vertical force, the tyre inflation pressure, the camber angle and the road friction conditions. The analytical definition of the tyre longitudinal slip stiffness has been provided in Equation (A.15).

Under the assumption that the braking action occurs within the tyre linear limits and an uniform road surface is considered, the tyre longitudinal slip stiffness can be estimated during straight line braking from Equation (4.34):

$$F_X^{(VS)} = \hat{C}_{L,f}\hat{\lambda}_f + \hat{C}_{L,r}\hat{\lambda}_r. \tag{4.34}$$

Taking into account the load proportionality principle [85], the tyre longitudinal stiffness can be expressed as a function of the tyre vertical load ($C_{L,f} = C_{L,f0}\,\frac{F_Z}{F_{Z0}}$), where C_0 is the tyre longitudinal stiffness at the nominal load F_{Z0}. This assumption is supported by experimental data as reported in Figure 4.7.

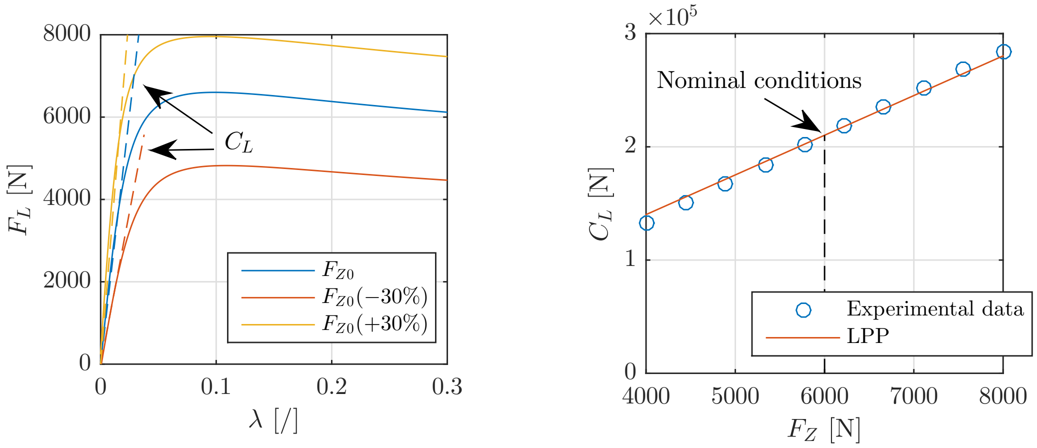

(a) *Tyre longitudinal slip stiffness with respect to varying tyre vertical load on a dry road.*

(b) *Longitudinal slip stiffness as a function of the tyre vertical load in accordance with the load proportionality principle (LPP).*

Figure 4.7: *Experimental results on a dry surface show that the tyre longitudinal slip stiffness can be approximated as a linear function of the tyre vertical load.*

By expressing the rear longitudinal stiffness as a function of the front longitudinal stiffness, the following expression can be formulated:

$$\hat{C}_{L,r} = \hat{C}_{L,f}\,\frac{\hat{F}_{Z,r}}{\hat{F}_{Z,f}}. \tag{4.35}$$

Eventually, the longitudinal stiffness can be calculated from the measured longitudinal acceleration, the estimated longitudinal slips and the estimated tyre vertical loads, as per Equation (4.36):

$$\hat{C}_{L,f} = \frac{F_X^{(VS)}}{\hat{\lambda}_f + \hat{\lambda}_r \frac{\hat{F}_{Z,f}}{\hat{F}_{Z,r}}}. \tag{4.36}$$

4.4 Observability analysis and observer tuning

To prove the observer functionality, the observability matrix and observability condition of the BLCF observers must be proved. The observability of the system holds if the observability matrix O_μ has rank equal to the number of system states. Given N the size of the state vector in Equation (4.8), the observation matrix is defined as follows:

$$O_\mu = \left[A\ AC\ AC^2\ AC^3\ ...\ AC^{N-1}\right]; \tag{4.37}$$

The full rank of O_μ can be proved for all equilibrium points where the applied pressure p_b and the resulting BLCF are non-zero. Moreover, at very low speeds, the tyre relaxation length, embedded in the observer scheme, might induce numerical instabilities (please, refer to Equation (A.14)). Hence, the observer is switched off upon reaching low driving speeds ($\approx 15\ km/h$) and at brake release. In case the filtered correction factor $\hat{K}_f$ exhibits strong variations caused by poor wheel slip estimation, the observer is switched off and a constant BLCF estimate, equal to the latest BLCF estimate, is provided. This situation occurs when the intensity of requested deceleration is not enough to produce detectable wheel slip. In case no previous BLCF estimated value is available, the nominal BLCF computed in accordance with SAE J2522 is provided.

In case of excessive wheel slip, or even wheel lock, the functionality of the proposed Observer 2 is limited. Particularly, the observability of the system cannot be proved because Equation (4.11a) does not hold. Wheel lock condition makes the system not observable, whilst excessive wheel slip excites the tyre in the non-linear region where the linear model of Equation (4.12) is not valid. A non-linear Burckhardt tyre model [81] is employed in Chapter 5 showing that the adoption of a non-linear tyre model in Observer 2 is necessary in presence of excessive wheel slip. It is also worth noting that the proposed observation scheme is designed for relatively smooth asphalt roads where the rolling resistance can be included in the process noise due to its low magnitude.

Concerning the observer tuning, $\mathbf{R}$ has been set time invariant depending on the white noise of the employed sensors. The process covariance matrix $\mathbf{Q}$ has been scheduled so to inject more uncertainty in the model of the process when the model fails at correctly predicting the states, for example at low driving speed and for deceleration requests lower than $2\ m/s^2$. The scheduling of the process covariance matrix $\mathbf{Q}$ against the requested deceleration is set so as to produce the maximum filtering effect while meeting the signal settling time requirements.

4.5 Results

The proposed BLCF observer is implemented in the IPG CarMaker® for preliminary MIL/SIL simulations. As shown in Appendix A, the powertrain, EHB and base brake controller are implemented as external Simulink® functions. A fixed time step of $1\ ms$ is set during the simulations and the signals required by the observer are acquired at $100\ Hz$. An additive noise model is employed to incorporate white Gaussian noise into the simulation signals. The standard deviation values of the noise are extracted from data-sheets of state-of-the-art instrumentation and reported in Table 4.1.

A set of straight-line braking tests, in accordance with ECE R13H [73], are performed. The braking manoeuvres start from a cruising speed of $120\ km/h$; the vehicle is then brought to a full stop by applying a constant deceleration request. The electric motors are deactivated during the whole manoeuvre. To demonstrate adaptivity of the observer to varying road conditions, braking manoeuvres are performed on dry and wet road with

Table 4.1: Sensors white noise implemented in the vehicle model.

Sensor	Measured quantity	White noise (σ)
GPS sensor	Vehicle speed	$\sigma_{v_x} = 0.027\ m/s$
Wheel encoders	Wheel speed	$\sigma_{\omega} = 0.1\ rad/s$
Wheel force transducer	Long. wheel force	$\sigma_{F_X} = 10\ N$
IMU	Vehicle long. acceleration	$\sigma_{a_x} = 0.01\ m/s^2$
Pressure sensor (EHCU)	Calliper pressure	$\sigma_p = 1.8\ bar$

$\mu = 1.2$ and $\mu = 0.7$, respectively. The catalogue of manoeuvres is reported in Table 4.2. The estimation performance is quantified in terms of normal round mean square error.

Table 4.2: Catalog of maneuvers.

Test	v_{in} $[km/h]$	Grip	a_x $[m/s^2]$
#1	120	Dry	3 - 5
#2	120	Dry	6 - 8
#3	120	Wet	3 - 5
#4	120	Wet	6 - 8

Results corresponding to the first test, mild braking on dry road, are depicted in Figure 4.8. Expectedly, the best estimation performance are achieved by the observer design based on direct measurement of the longitudinal wheel forces. BLCF is estimated accurately upon the braking manoeuvre is initiated and follows precisely the evolution dictated by the employed state space model. Nonetheless, the observer design based on virtual longitudinal forces features good estimation capability. Noise can be noticed on the rear axle estimates due to the low excitation level. Moreover, this also causes a slight delay in reaching the steady state value. The results of the second test, hard braking on a dry road, are reported in Figure 4.9. In this case, a slight offset appears on the estimate of the rear longitudinal force provided by the second observer design. The load proportionality principle is compromised in this test due to high longitudinal load transfer, thus affecting the accuracy of the rear BLCF estimate. Despite this, the error remains within reasonable values and can be considered acceptable. The results obtained in the third test, mild braking on a wet road, are omitted as significant differences with respect to the first test are not identified. Finally, the results of the hard braking input on a wet road are depicted in Figure 4.10. In this case, the performance of Observer 2 is affected by the wheel-lock occurring at the end of the test ($t \approx 4 - 5s$).

To conclude, the accuracy of the proposed observers is quantified by means of the root mean square estimation error and its outcomes are presented in Table 4.3. Overall, the error of the BLCF estimate remains within reasonable limits. Under the tested driving scenarios, important differences in terms of BLCF estimation error are not noticed between the two observers, indicating the advisability of the low-cost observer. Higher errors can be observed on the rear axle due to limited longitudinal force excitation.

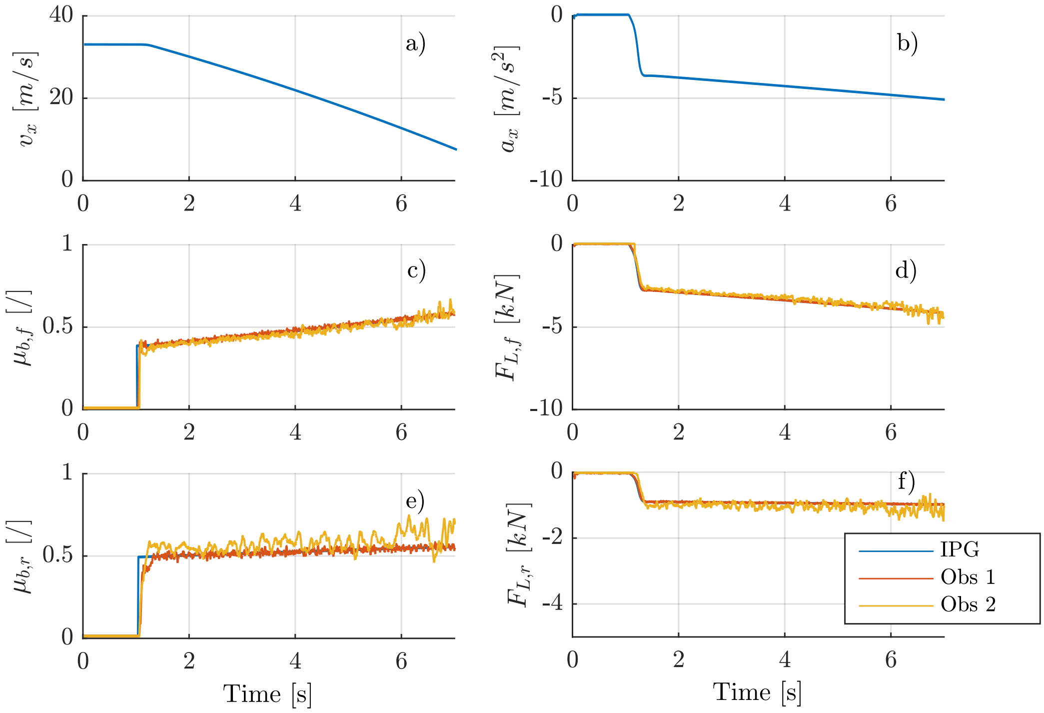

Figure 4.8: *Test #1. Mild braking on dry road: a) vehicle velocity; b) vehicle deceleration; c) and e) front and rear BLCF, respectively; d) end f) front and rear longitudinal tyre force, respectively.*

TABLE 4.3: Normalised round mean square error of the observers.

Test	Design	$nRMSE(\mu_{b,f})$	$nRMSE(\mu_{b,r})$	$nRMSE(F_{L,f})$	$nRMSE(F_{L,r})$
#1	Obs. 1	3.55%	5.68%	0.35%	0.98%
	Obs. 2	4.74%	7.23%	5.91%	14.46%
#2	Obs. 1	2.13%	4.04%	0.30%	0.54%
	Obs. 2	3.34%	6.96%	5.49%	10.75%
#3	Obs. 1	3.55%	4.68%	0.35%	0.98%
	Obs. 2	4.55%	8.51%	6.61%	16.62%
#4	Obs. 1	2.13%	4.04%	0.34%	0.54%
	Obs. 2	3.13%	7.87%	5.37%	14.12%

4.6 Fault tolerance and sensitivity analysis

In this section, Observer 2 functionality is tested in presence of fault occurrence and for a wider deceleration range involving gentle braking manoeuvres. To check Observer 2 fault tolerance capability, a simulation is performed in presence of a failure induced in the linear tyre model. The vehicle starts from an initial speed of 100 km/h, afterwards a full stop braking occurs. As from Figure 4.11, an artificial failure is induced in the tyre longitudinal slip stiffness at $(t = 4s)$, which leads to a wrong tyre model prediction. The

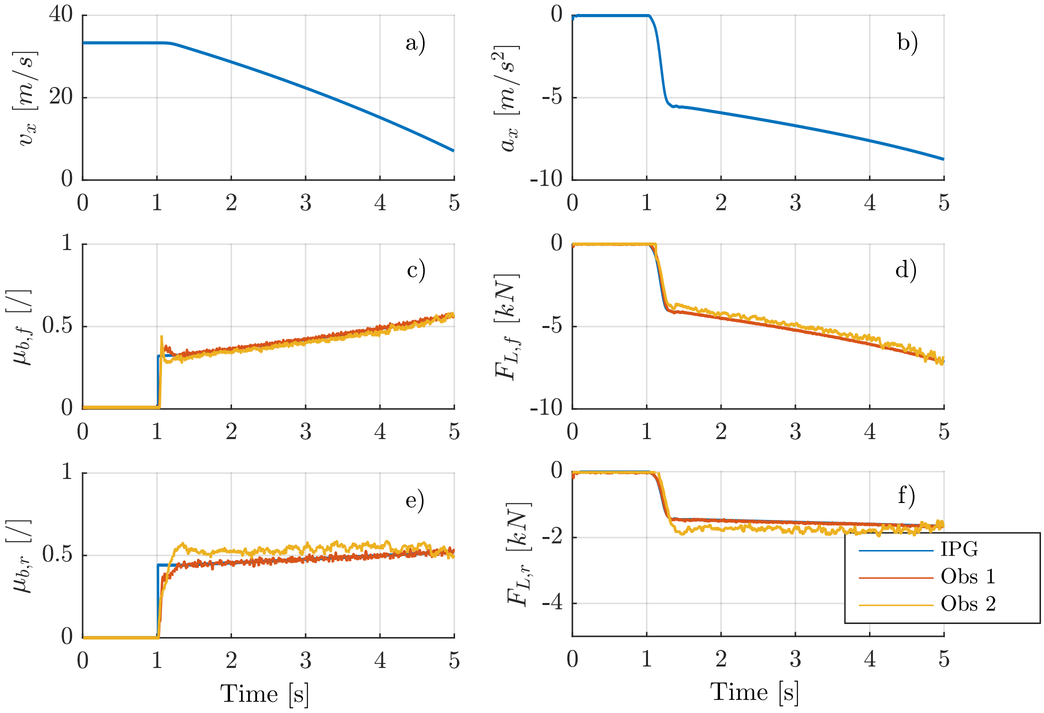

Figure 4.9: *Test #2. Hard braking on dry road: a) vehicle velocity; b) vehicle deceleration; c) and e) front and rear BLCF, respectively; d) end f) front and rear longitudinal tyre force, respectively.*

results demonstrate that the observer is capable of adapting to a wrong estimate of the tyre longitudinal slip stiffness thanks to the correction factor $\hat{K}_f$. The virtual sensor provides the right value of longitudinal body force because it relies on the accelerometer information, as per Equations (4.16) and (4.17). Hence, after an adaptation time of around 100 ms, the correct longitudinal tyre force and BLCF are estimated.

Thereafter, a sensitivity analysis with respect to the driver requested deceleration allows investigating the functionality of Observer 2 against the degree of wheel excitation. In accordance with ECE R13H [73], straight-line braking tests on a dry surface from an initial cruising speed of 100 km/h are performed. The maximum deceleration request is limited to 8 m/s^2 in order to avoid excessive wheel slip, beyond the tyre linear limits. An analysis of the required modifications to the observer in presence of excessive wheel slip will be provided in the framework of HIL verification in Chapter 5. The observer performance are quantified by means of the normalised RMSE between the reference BLCF value and the observed BLCF. The results are reported in Figure 4.12, showing that Observer 1 features overall a better estimation accuracy. The excitation induced on the axles, which is in turn proportional to the exerted friction brake force, has an effect on the BLCF estimation accuracy. This explains why the BLCF observer exhibits reduced estimation performance on the rear axle. Therefore, depending on the chosen

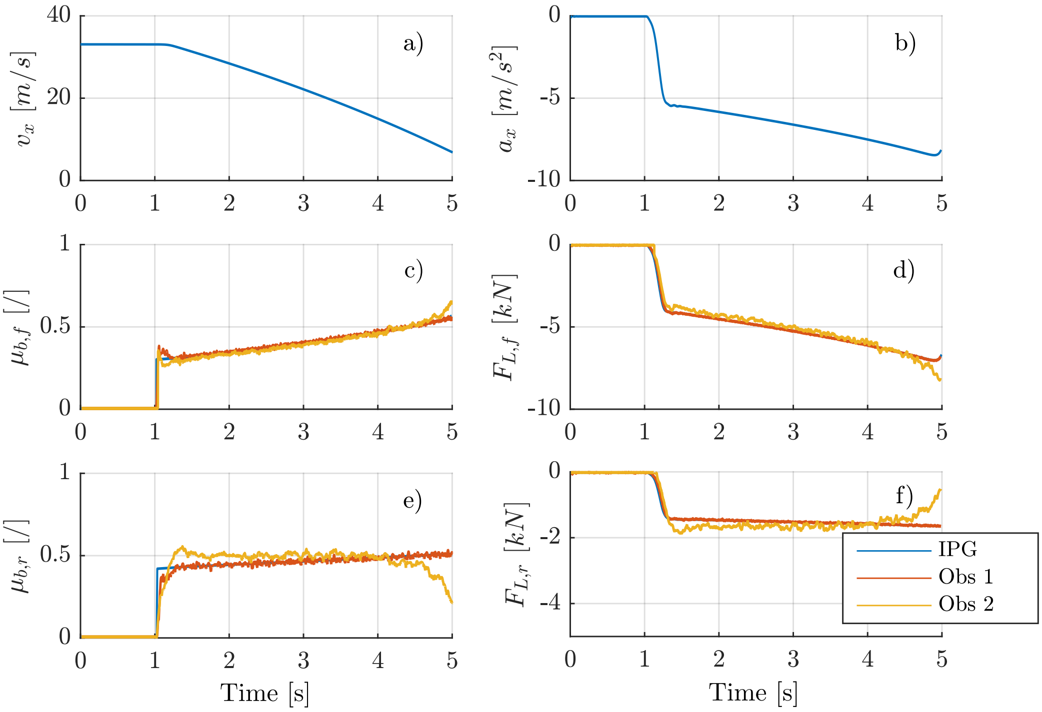

Figure 4.10: *Test #4. Hard braking on wet road: a) vehicle velocity; b) vehicle deceleration; c) and e) front and rear BLCF, respectively; d) end f) front and rear longitudinal tyre force, respectively.*

brake torque allocation strategy, different results are possible.

The analysis also reveals that, whilst for higher vehicle deceleration values Observer 2 features a prediction accuracy comparable with Observer 1, at lower deceleration requests Observer 2 provides a BLCF estimate far from the true value. The observers performance are analysed with respect to the case where the nominal BLCF computed in accordance with SAE J2522 is used. From Figure 4.12, it can be thus concluded that Observer 2 provides a good estimate down to $\approx 1.3\ m/s^2$ on the front axle, where the force excitation is expectedly higher, and down to $\approx 4\ m/s^2$ on the rear axle. It is also worth remarking that thanks to the limited temperature variation at the rear axle due to low power input, BLCF is not expected to lay far from its nominal value. On the contrary, BLCF at the front axle exhibits much more remarkable variations due to evident temperature increase. This can be verified by considering the estimation error committed at the front and rear axles when the observers are switched off and a constant BLCF, defined in accordance with SAE J2522, is employed. The results suggest that Observer 2 shall be switched on upon exceeding $\approx 1.3\ m/s^2$ at the front axle and $\approx 4\ m/s^2$ at the rear axle. Under all other conditions, the previous BLCF estimate is considered. These results provide important information, which are used for HIL verification in Chapter 5. These thresholds are instead not considered for the observer validation on the proving ground

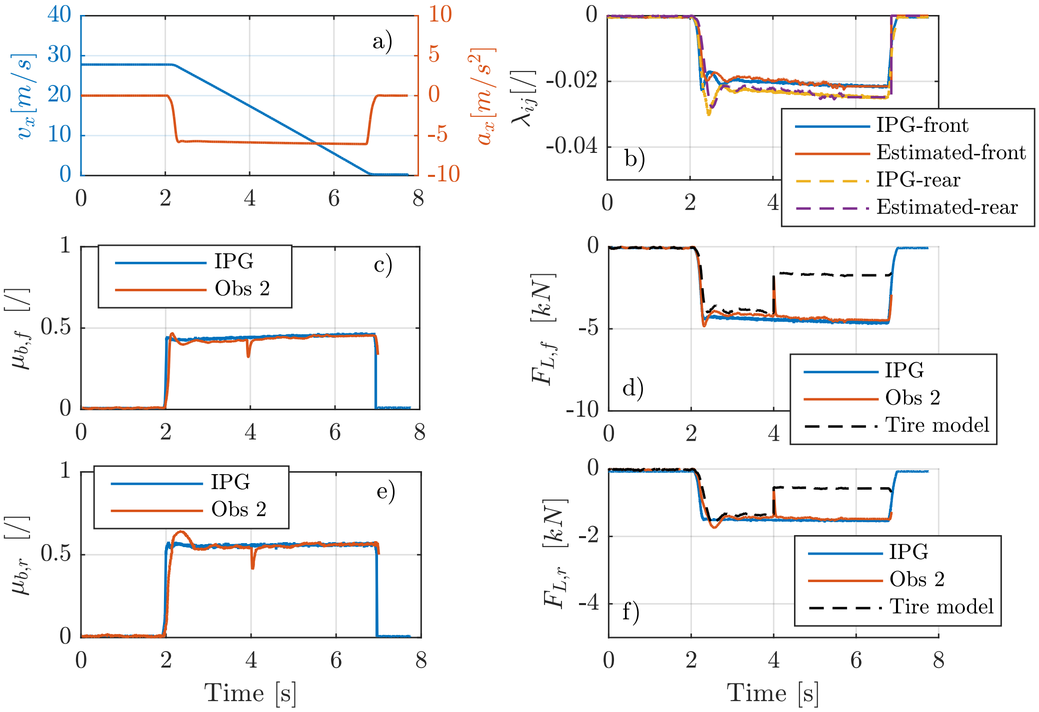

Figure 4.11: *Fault tolerance capability of Observer 2 against error injection in the estimated tyre longitudinal slip stiffness. a) vehicle kinematics; b) reference vs estimated longitudinal wheel slip; c) and e) reference vs estimated BLCF for front and rear axle, respectively; d) and f) reference, observed and tyre modelled longitudinal wheel force.*

(Chapter 6) where the intent is to explore the observer functionality under real braking conditions.

4.7 Chapter summary

In this chapter, two observer-based BLCF estimation variants are proposed. Observer 1 demonstrates that a very accurate BLCF estimate can be achieved by measuring the longitudinal wheel forces. Observer 2 represents the cost-effective estimation variant that replaces the expensive tyre longitudinal force measurements with a virtual sensor. MIL/SIL simulations carried out in the vehicle dynamics simulator IPG CarMaker® demonstrate the suitability of the low-cost state observer at providing a satisfactory estimate of the BLCF when the vehicle deceleration intensity exceeds certain thresholds. Particularly, the results show that, whilst a satisfactory estimation accuracy can be achieved on the front axle for almost all RDE-compliant deceleration values, the BLCF estimation on the rear axle represents a rather awkward task. The poor estimation performance at the rear axle may be compensated by using alternative estimation methods (please, refer to Chapter 2) or dynamically allocating the brake torque in order to perform

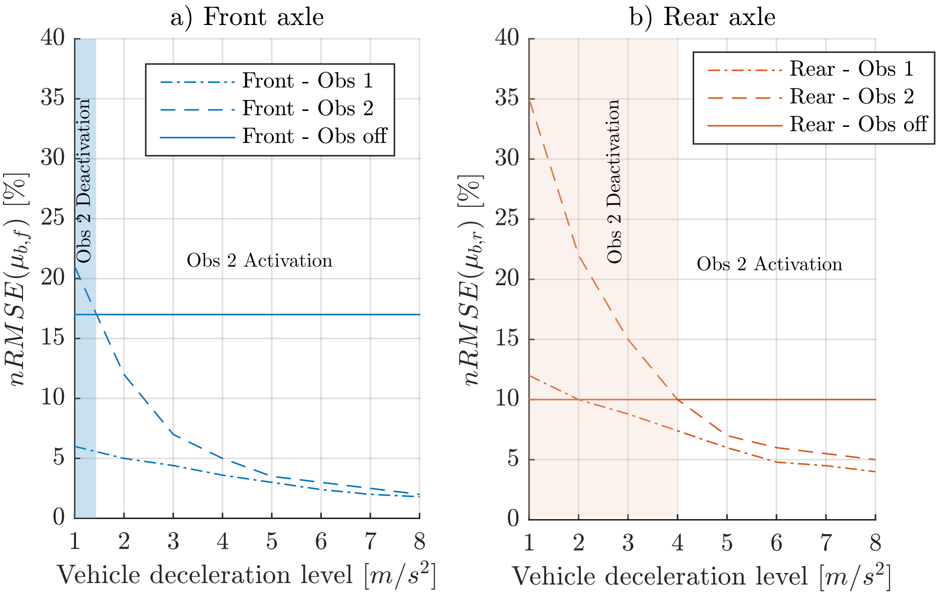

Figure 4.12: *Estimation performance of the proposed observer designs with respect to front brakes a) and rear brakes b). Obs 1 refers to the observer design based on direct measurement of longitudinal wheel forces; Obs 2 represents the observer design based on the virtual force sensor; Obs off represents the case when all observer are switched off and a constant BLCF estimate (SAE J2522) is provided. The coloured areas refer to the regions where Observer 2 shall be deactivated.*

an accurate BLCF estimation. Nonetheless, the proposed estimator based on Observer 2 represents a cost-effective solution suitable for current production vehicles. Hereafter, no further attention is paid to Observer 1 since it relies on expensive and generally unavailable tyre force transducers. In Chapter 5, Observer 2 is implemented on the HIL platform and the functionality of the BLCF compensation verified in real time. Chapter 5 also shows that brake blending with electric motors plays an important role in the BLCF estimation error.

Chapter 5

Hardware-in-the-loop verification

5.1 Introduction

As seen in the introductory section, automatic brake functions in decoupled brake architectures require the provision of a BLCF estimate. The BLCF actual value is necessary to maintain the brake force allocation in the safe region and evaluate the actual braking torque. In addition, modern electric vehicles require precise tracking of the regenerative and friction torques for safety and performance requirements [9, 80]. In accordance with ECE R13H [73], regenerative brakes still need to be supported by conventional friction brakes in case of failure occurrence, fully charged battery and unexpected variations of tyre-road friction conditions. Chapter 4 proposed a novel approach that does not require BLCF modelling and parametrisation thereof. The results demonstrate that the state estimation is robust under a wide range of deceleration values. The developed tool is independent of the chosen brake torque allocation strategy and satisfactory BLCF estimation performance can be achieved upon generating detectable wheel slip.

This chapter puts forth the HIL verification of Observer 2 presented in Chapter 4. The HIL platform at Technische Universität Ilmenau provides plug-in adaptation of vehicle subsystems as additional modules. To this effect, ILVO model presented in Chapter 3 is embedded in the HIL platform to simulate the real BLCF dynamics. The HIL setup includes the real electrohydraulic brake system (EHB) presented in Appendix A and allows for real time verification of the proposed algorithm. Under this framework, HIL verification is also used to develop the BLCF compensation function. A method to compensate disturbances induced by BLCF variations through modification of the brake torque demand sent to the EHCU is thus shown. Herein, the resulting improvements in brake control functions are analysed against longitudinal base braking manoeuvres in presence of blended operation with electric motors. For all manoeuvres, the brake pedal actuation speed is equal to 150 mm/s. The compensation function shall provide a smooth and constant braking deceleration based on the brake pedal position, thus improving the comfort and braking linearity.

5.2 Hardware-in-the-loop setup

The hardware subsystem included in the HIL test rig is the EHB presented in Appendix A. The EHB is a brake-by-wire based on the slip control boost (SCB) technology of ZF TRW [86]. Compared to a conventional brake system, the EHB offers a much faster dynamics and represents a necessary component on hybrid and full electric vehicles provided with energy recuperation where the brake blending shall occur without the driver noticing it. In accordance with Appendix A, the vehicle model, subsystems and controllers have software realisation in MATLAB/Simulink®. The dSPACE® hardware components for digital and analogue data input/output as well as for controller area network (CAN) bus protocol communication compose the framework reported in Figure 5.1.

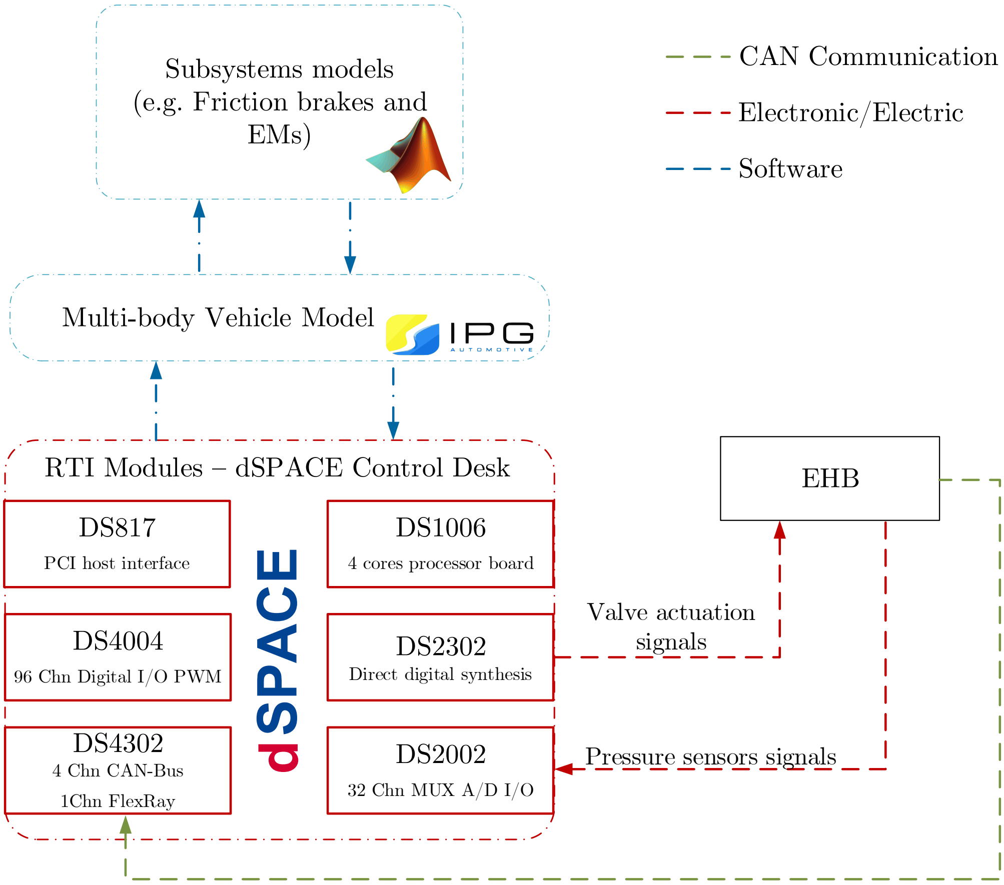

Figure 5.1: *Schematic of the HIL test rig at Technische Universität Ilmenau (after [87]).*

The DS1006® board represents the main element of the HIL platform and is capable of distributing computing tasks between four core processors that guarantee real-time simulation. This board communicates via UDP with a local host computer. Analog input signals information from the pressure sensors of the EHB are digitalised by multi-channel A/D board DS2002®. The DS2002® features a total of 32 A/D channels at 16-bit resolution with an ADC conversion time of less than 5 μs.

A set of pressure sensors allow measurement of brake pressure in the master cylinder as well as in each brake calliper. The EHB does not require the actuation of the brake pedal since the pressure request can be generated directly via software and sent via CAN bus to the EHB control module. For this task, one of the four CAN interfaces of the DS4302® is used. To configure the CAN network and to combine dSPACE® boards with CAN networks, the real-time interface (RTI CAN) multi-message blockset is used. The control on the ZF TRW SCB unit uses the direct digital synthesis board DS2302®. This board can generate waveform signals and is required for the operation of emulators of wheel angular speed sensors. The communication between dSPACE® platform and the host computer is organised through the link board DS817® (32-bit PCI host interface).

5.3 Control structure

The real EHB is interfaced with the IPG CarMaker® vehicle model in accordance with Figure 5.1. A schematic of the implemented vehicle controller is reported in Figure 5.2, where the EHB finds physical realisation in the HIL platform and estimation and control functions are implemented in the MATLAB/Simulink® and integrated via host PC.

The base brake controller is responsible for the correct operation of the service braking in a decoupled brake-by-wire system. It includes the generation of the torque demand according to the brake pedal position and distribution of the torque demand among the wheels. The relation between the brake pedal and overall torque demand follows a non-linear function of the brake pedal position.

The calculation leading the overall demanded brake torque, T_b^{dem}, as a function of the brake pedal is as follows:

$$T_b^{dem} = \hat{m}_v \; a_x^{dem}(s_{ped}) \; \hat{r}_\omega \tag{5.1}$$

where, $\hat{m_v}$ is the estimate vehicle mass, a_x^{dem} is the reference deceleration as function of the brake pedal displacement and $\hat{r}_\omega$ is the wheel radius, herein assumed constant. The brake force distribution block allocates the demanded brake torque on the front and rear wheels, $T_{b,ij}^{dem}$, in accordance with the guidelines provided in ECE R13H [73]. Without loss of generality, in the framework of HIL simulations, the ideal brake force distribution of Chapter 4 is adopted. In case of excessive wheel slip or yaw rate, the ABS/ESP controller reduces the wheel torque in order to keep the wheel slip close to the reference value [88, 89]. As analysed in Chapter 4, the BLCF observability might

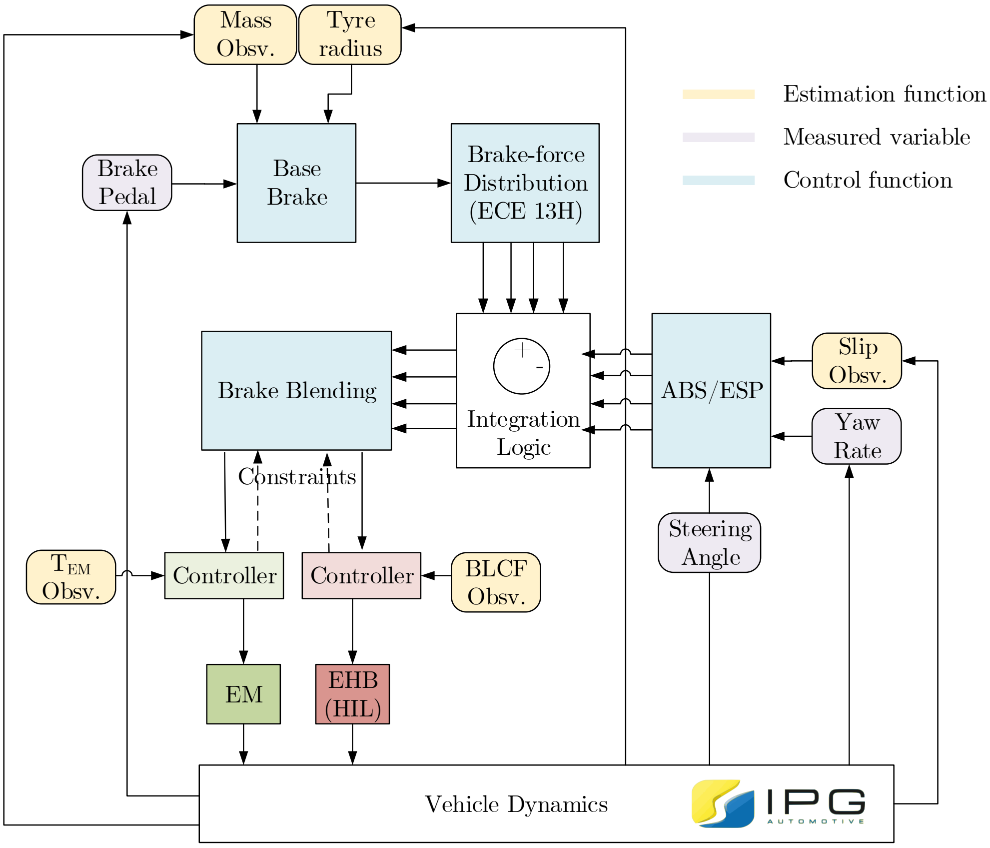

Figure 5.2: *Schematic of the brake controller employed for HIL verification.*

not hold in case wheel lock occurs. Therefore, the ABS/ESP reference slip tracking performance under emergency braking might have a detrimental impact on the BLCF observability and are for this reason kept out of the scope of the present work.

The brake blending block coordinates EHB and EMs by providing the demanded torque signals $T^{dem}_{EHB,ij}$ and $T^{dem}_{EM,ij}$, respectively. It is worth noting that ECE R13H [73] prescribes that in vehicles where electric motors can concur to service braking, any variation in the torque output from the regenerative braking must be automatically compensated by the foundation brakes. In fact, an electric regenerative braking system might not be able to produce sufficient braking force under certain operating conditions (e.g. low vehicle speed and under emergency braking). Hence, a combination of conventional friction braking and regenerative braking is always necessary to provide full braking capability. Foundation brakes might be actuated concurrently with the electric motors (i.e. parallel phasing) or in succession (series phasing). Figure 5.3 graphically reports the blending strategies. In the parallel model, electric motors and EHB are actuated at the same time. EMs provide regenerated energy in accordance with the set blending share. The maximum regenerated torque is a dynamic variable, which not only depends on the battery state of charge but also on the EM operating speed. As reported in Figure A.7 of Appendix A, at high driving speed, the EM is not able to provide high torque values, whilst at very low speed the EM is switched off because incapable of regenerating energy. In the serial phasing, EHB is activated upon saturating the EM regenerative torque reservoir.

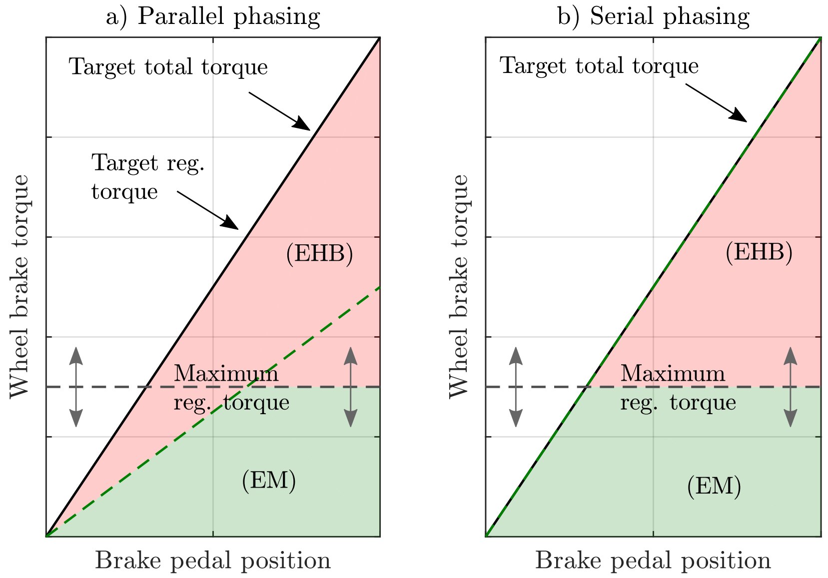

Figure 5.3: *Brake blending strategies. On the left, parallel phasing; on the right, serial phasing. The maximum regenerative torque depends upon the EM speed and the battery state of charge.*

A brake blending factor, namely f_{ij}, is defined to allocate the actuators level of intervention at each corner. When f_{ij} is equal to one, the series type phasing is enabled. All other blending configurations are of parallel type. In accordance with ECE R13H [73], the intervention of EHB is always requested upon saturating the EMs regeneration capability, even in the case of pure series configuration ($f_{ij} = 1$). The generic blending law follows:

$$\begin{cases} T^{dem}_{EM,ij} = sat_0^{(T^{max}_{EM,ij})}(f_{ij}\; T^{dem}_{b,ij}), & (5.2a) \\ T^{dem}_{EHB,ij} = (1 - f_{ij})\; T^{dem}_{b,ij} + \underbrace{max\left(0, \left[T^{dem}_{EM,ij} - T^{max}_{EM,ij}\right]\right)}_{\text{ECE R13H}}, & (5.2b) \end{cases}$$

where,

$$\begin{cases} Disabled\ blending \quad if \quad f_{ij} == 0; & (5.3a) \\ Series\ phasing \quad if \quad f_{ij} == 1; & (5.3b) \\ Parallel\ phasing \quad if \quad 0 < f_{ij} < 1. & (5.3c) \end{cases}$$

In the previous equations, $(T^{max}_{EM,ij})$ represents the EM torque limit, as per Figure 5.3. The demanded EM and EHB torques are then sent to the actuators controllers, which take care of converting the torque requests into a control signal understandable from the actuators. The actuation undergoes the physical limits of both EHB and EM. To ensure that the actuators provide an actual brake torque close to the demanded signal, an additional close loop control shall be implemented. To this effect, the motor torque can be easily estimated from the electric motors current; whilst, for the foundation brakes, the BLCF observer presented in Chapter 4 is used.

5.4 Observer verification and robustness analysis

A preliminary test involves a simple straight-line braking manoeuvre on a dry road ($\mu = 1$) with fixed brake pedal displacement. In this test, the blending factor is null; therefore, only EHB is activated. The simulation starts from an initial vehicle speed of 75 km/h. Thereafter, the driver steps on the brake pedal and keeps its position to a fixed value so to induce a deceleration of around 4 m/s^2. Below, the BLCF estimate is omitted, instead the estimated wheel brake torque computed in accordance with Equation (A.19) is considered. Figure 5.4 reports a comparison between reference and observed signals. The results of longitudinal force estimation and wheel brake torque prove the functionality of the proposed observer in real-time.

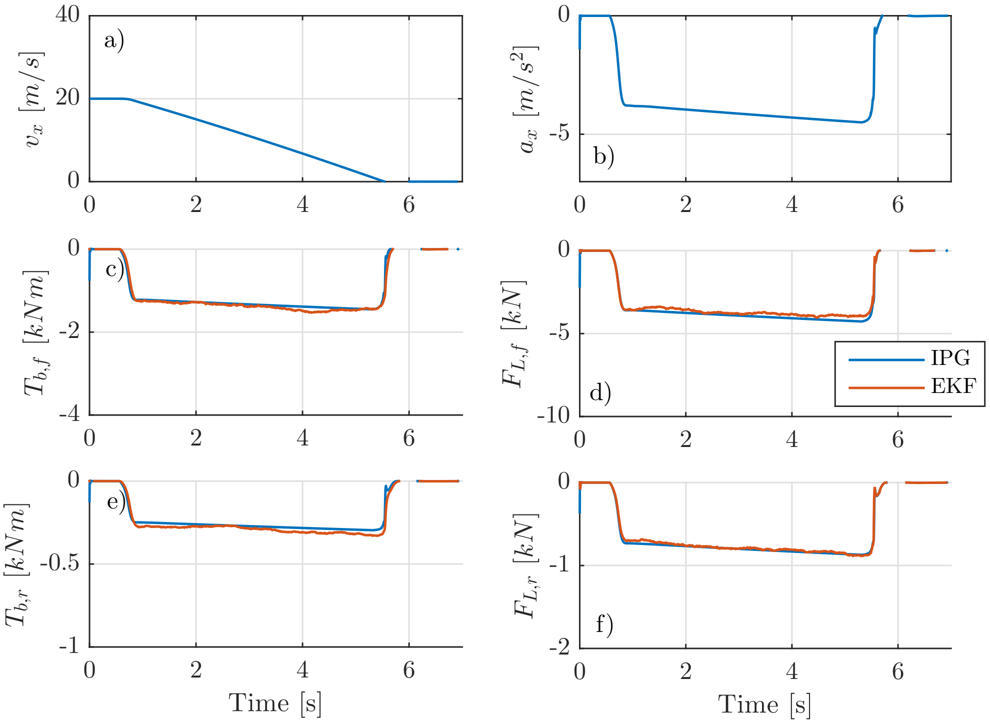

Figure 5.4: *Result of braking test performed in real-time on the HIL platform. Graph a) reports the vehicle speed; b) reports the vehicle deceleration; c) and e) report the estimated brake torque; d) and f) report the estimated wheel longitudinal force.*

The observer robustness is verified with respect to a braking manoeuvre typically used for the evaluation of ABS performance, i.e. braking on a low-grip patch. To preserve BLCF observability, ABS/ESP controller is deactivated. Hence, the vehicle transition on the slippery surface at $t = 2\ s$ induces wheel lock. To account for the consequent excessive wheel slip, Observer 2 needs to be modified by inclusion of a non-linear tyre model. For this analysis, the non-linear Burckhardt tyre model with fixed parametrisation is used due to its compact form and ease of implementation [81]. The observer scheme remains unchanged. The tyre model is initialised for a dry road surface. The results are reported in Figure 5.5. During the braking manoeuvre, the vehicle crosses a slippery surface ($\mu = 0.2$) that induces a rapid deterioration of the maximum tyre-road contact force. During the whole manoeuvre, the brake pedal is kept fixed. The results demonstrate that Observer 2 based on the linear tyre model (EKF) fails at providing the right brake torque and longitudinal force estimate. Instead, Observer 2 enhanced with a non-linear tyre model (EKF - NNTM) is capable of adapting to the changing road conditions thanks to the correction factor $\hat{K}_f$ presented in Chapter 4.

As from the results, the algorithm adaptation time to changing road conditions is of finite type ($\approx 300\ ms$) and hinges upon the forgetting factor of the $\hat{K}_f$ RLS estimation. The same process occurs when the vehicle returns to dry road conditions. The correction factor makes up for variations in road conditions by conveniently scaling the longitudinal tyre forces provided by the non-linear tyre model. The observer with embedded non-linear tyre model attains around 50% reduction in the nRMSE of longitudinal tyre force and wheel brake torque.

The results presented in this section underline the limitations of the proposed observer when the tyre is excited beyond the linear limit. In the event of excessive wheel slip, the adoption of a non-linear tyre model reveals necessary.

5.5 Sensitivity analysis under brake blending

In this section, Observer 2 estimation functionality is tested against varying blending conditions. For these tests, the initial vehicle speed is set lower than 80 km/h to avoid that the non-linear EM characteristics conflict with the demanded brake blending factors (refer to Figure A.7). To this effect, the test involves an initial cruising speed of 75 km/h; thereafter, a braking manoeuvre with 60% pedal displacement is performed. This causes a deceleration of around 4 m/s^2 for the vehicle under analysis. All tests are characterised by equal brake torque request; nevertheless, different blending conditions cause different BLCF dynamics. The results of consecutive tests are reported in Figure 5.6.

The results show that higher blending factors produce a deterioration of the estimation performance. As already seen in Chapter 4, Observer 2 estimation performance deteriorates when the frictional brake torque demand is confined to low values. A complete list of test results is provided in Table 5.1.

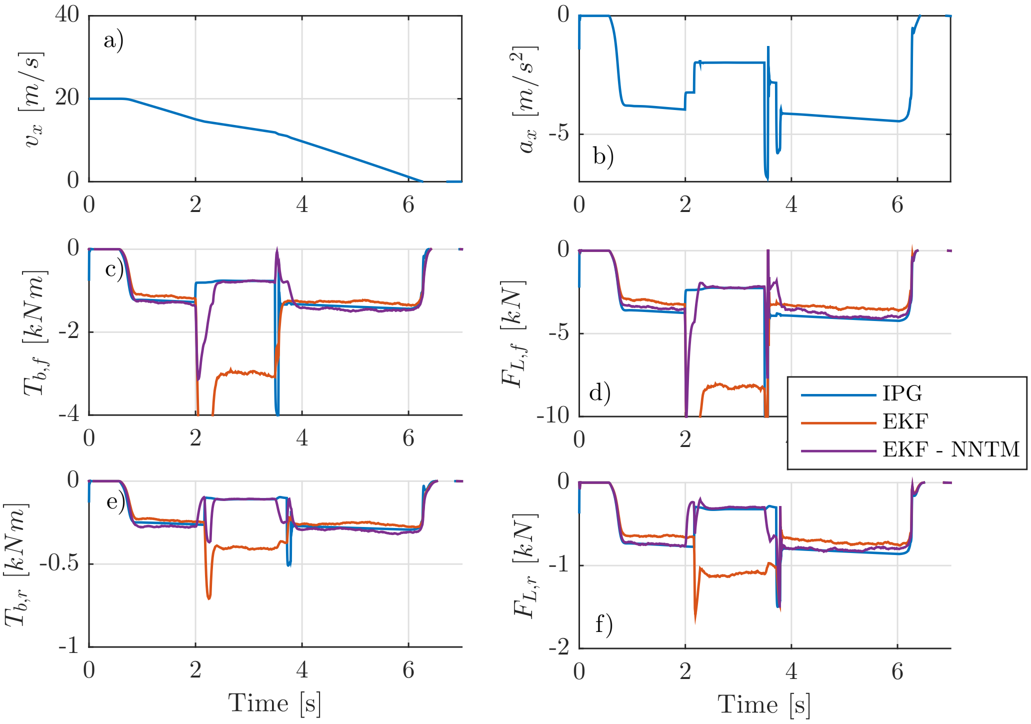

Figure 5.5: *Results of braking on a low-grip patch performed in real-time on the HIL platform. Graph a) reports the vehicle speed and b) the vehicle deceleration. Graphs c) and e) refer to the torque estimation provided by the observer and its enhanced version with inclusion of the non-linear tyre model. Graphs d) and f) report the estimated longitudinal wheel force in compliance with the observer and its upgraded version including the non-linear tyre model.*

Table 5.1: Normalised round mean square error of Observer 2 with respect to varying blending conditions.

Test	f	$nRMSE(\mu_{b,f})$	$nRMSE(\mu_{b,r})$
#1	0	3.12%	6.26%
#2	0.2	5.42%	8.16%
#3	0.4	8.27%	11.33%
#4	0.6	11.89%	15.87%
#5	0.8	13.43%	20.46%

5.6 Compensation function

The base brake controller requires the provision of the BLCF estimate for the calculation of the reference pressure to be sent to each calliper. This is done in accordance with the non-linear Equation (5.4) where the BLCF estimate appears at the denominator.

$$p_{b,ij}^{dem} = \frac{T_{EHB,ij}^{dem}}{2n_p\ \hat{\mu}_{b,ij}\ \pi\frac{d_p^2}{4}r_{eff,i}} + p_0, \tag{5.4}$$

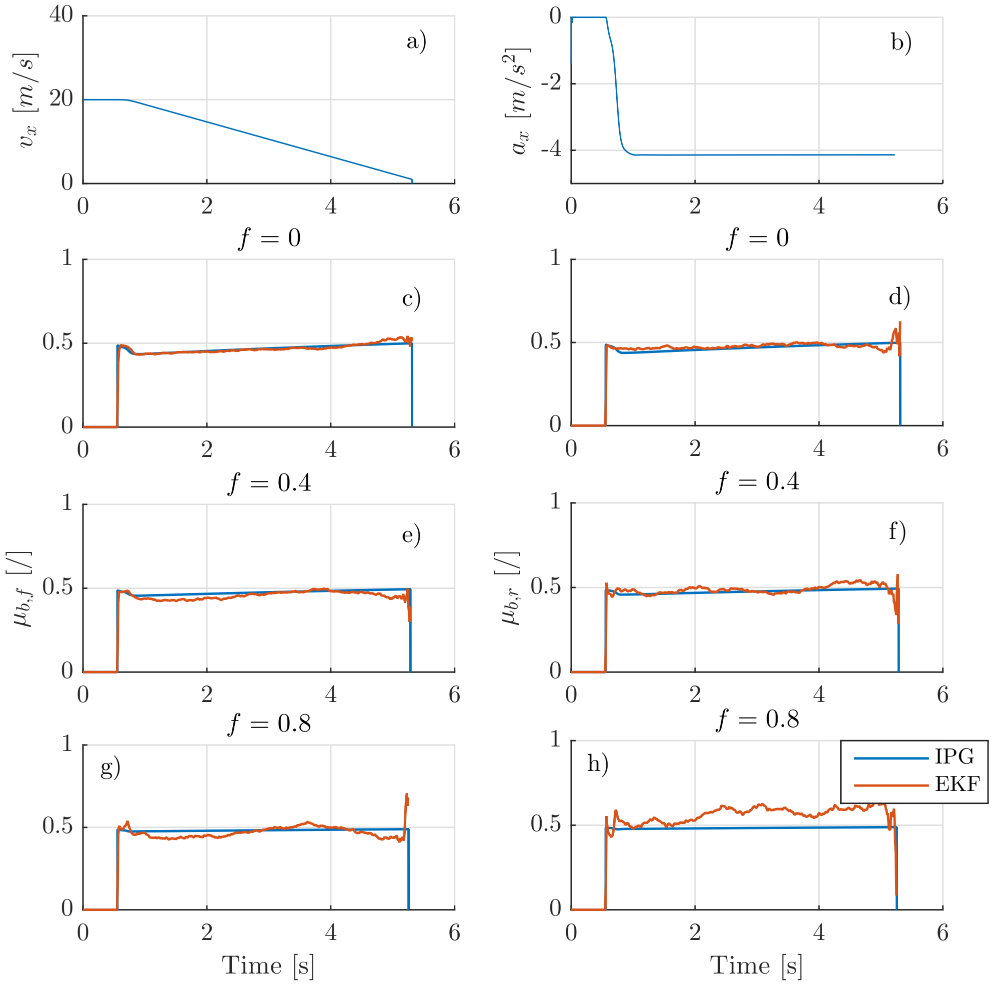

Figure 5.6: *Analysis of the observer estimation performance with respect to varying blending factor. Graph a) and b) report the vehicle kinematics variable; c), e) and g) relate to the BLCF estimation performance for the front axle; d), f) and h) refer to the BLCF estimation performance for the rear axle.*

where "^{dem}" superscript indicates demanded quantities. Hereunto, three situations may arise for a given driver's deceleration request:

- under-braking, that is, the BLCF estimate provided in the base brake controller is larger than the true value, leading to a reduced braking action;
- over-braking, that is, the BLCF estimate provided in the base brake controller is smaller than the true value, leading to an increased braking action;
- compensated braking, that is, the BLCF estimate provided in the base brake controller lays close to its true value.

It is clear that the definitions given above require the introduction of an ideal case of braking without any disturbances where the vehicle realises the deceleration demanded by the driver. This condition is only achievable when the estimated BLCF equals its true value.

Under all circumstances, to avoid numerical instabilities that might be caused by a noisy BLCF estimate, Equation (5.4) is linearised around the BLCF estimate of the last braking manoeuvre $\hat{\mu}_{b0}$. In case no previous estimate is available, the nominal BLCF (SAE J2522) is provided. The algorithm allows a maximum compensation of ±30% around the previous BLCF estimate. By Tylor expansion, Equation (5.4) can be approximate as follows:

$$p_{b,ij}^{dem^*} = p_{b0,ij}^{dem} - p_{b0,ij}^{dem}\frac{\Delta\hat{\mu}_b}{\hat{\mu}_{b0}} + p_{b0,ij}^{dem}\left(\frac{\Delta\hat{\mu}_b}{\hat{\mu}_{b0}}\right)^2 + O^3, \tag{5.5}$$

where, $p_{b0,ij}$ represents the control signal that would be sent to the EHCU if BLCF did not change from its last estimate; $p_{b,ij}^{dem^*}$ represent the compensated pressure demand in presence of BLCF variations; $\Delta\hat{\mu}_b$ represents the BLCF variation with respect to its previous estimate defined as:

$$\Delta\hat{\mu}_b = sat_{\pm 30\%}\left(\hat{\mu}_b - \hat{\mu}_{b0}\right), \tag{5.6}$$

Equation (5.5) can also be rewritten as:

$$p_{b,ij}^{dem^*} = p_{b0,ij}^{dem}\left[1 - \frac{\Delta\hat{\mu}_b}{\hat{\mu}_{b0}} + \left(\frac{\Delta\hat{\mu}_b}{\hat{\mu}_{b0}}\right)^2\right] + O^3. \tag{5.7}$$

Given the BLCF estimate $\hat{\mu}_b$ from the BLCF observer and by truncating to second order Taylor, the compensation algorithm in Equation (5.8) can be applied:

$$p_{b,ij}^{dem^*} = \left[\frac{T_{b,ij}^{dem}}{2n_p\ \hat{\mu}_{b0,ij}\ \pi\frac{d_p^2}{4}r_{eff,i}} + p_0\right]\left[1 - \frac{\Delta\hat{\mu}_b}{\hat{\mu}_{b0}} + \left(\frac{\Delta\hat{\mu}_b}{\hat{\mu}_{b0}}\right)^2\right]. \tag{5.8}$$

In the next section, the compensation function is implemented in the framework of HIL verification tests. To this effect, the results of the compensated case will be compared with the undesired cases without compensation, namely under-braking and over-braking. It is worth noting that the undesired braking behaviour is simulated by providing a constant BLCF estimate 15% greater than the true value in the case of under-braking and 15% smaller than the true value in the case of over-braking. The nominal BLCF value for the vehicle under analysis can be found in the technical specification of the full electric SUV in Appendix D.

5.7 Results

To test the BLCF compensation function in real-time on the HIL platform, two test cases are devised. The first test involves straight line braking until vehicle standstill from an initial speed of 75 km/h and an initial disc temperature of 150°C. This manoeuvre is repeated for different blending factors. The second test includes a series of repeated brake applications that lead to increasing brake disc temperature and noticeable BLCF variations. The vehicle starts from an initial speed of 130 km/h and the brakes are at an initial temperature of 150°C. To assess the system compensation capability under different working conditions, the second test is conducted for two blending configurations, namely full frictional brake intervention ($f = 0$) and blending at 70% ($f = 0.7$). In accordance with previous HIL studies [9], a blending factor of 70% represents for the vehicle under analysis a good compromise between energy recuperation and braking performance. The brake pedal displacement is limited to 60% of the maximum travel to prevent excessive wheel slip. It is also worth noting that the observer activation thresholds defined in Chapter 4 are considered in the framework of HIL simulations.

5.7.1 Single brake application

The results of the first test for pure intervention of foundation brakes ($f = 0$) are reported in Figure 5.7. The upper graphs refer to the vehicle kinematics for the three braking situations, under-braking, over-braking and compensated braking, respectively. The lower graphs put into comparison the simulated BLCF values and longitudinal wheel forces for the front and rear axles, respectively. Moreover, the estimated friction coefficient provided for compensation purposes in the base brake controller is also reported (red profile).

The results show that the compensation function allows tracking the ideal profile by keeping the vehicle velocity very close to the driver's desired trajectory. The previous test is repeated for different blending configurations. The compensation capability of the proposed approach is quantified through the normalised RMSE between the overall demanded and simulated torque. As shown in Figure 5.8, the compensation function abates the error between the driver requested deceleration and the actual deceleration level. Since all sources of disturbances are attributed to BLCF variations, it is clear that the higher the blending with EM is, the lower the disturbances on the brake control are.

5.7.2 Repeated brake application

The second test case involves several pedal actuations, which lead to a remarkable variation in the BLCF. The results of this trial are reported in Figures 5.9 and 5.10 for the case of pure conventional brake intervention and blending at 70%, respectively. The results show that the proposed observer allows for an effective compensation action even in case of large BLCF variations and blending conditions.

Based on the results of the previous simulations, Figure 5.11 reports the brake pedal travel against the vehicle deceleration. For the non-compensated cases, the driver's workload is increased and the pedal-deceleration curve lays far from the ideal

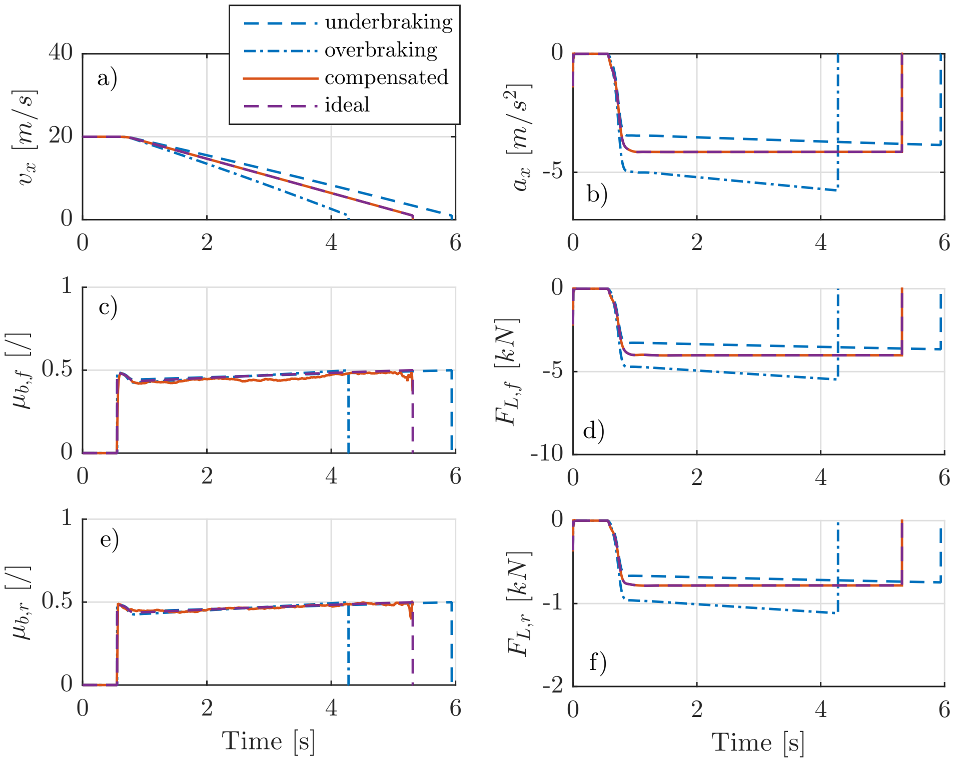

Figure 5.7: *Results of BLCF compensation function for a pure friction straight line braking manoeuvre with respect to three operating instances, underbraking, overbraking and compensated case. Electric motors are deactivated, full brake power is used to decelerate the vehicle. Graphs a) and b) report the vehicle kinematics; c) and e) refer to the simulated BLCF for front and rear axle, respectively; d) and f) report the simulated wheel longitudinal force for front and rear axle, respectively.*

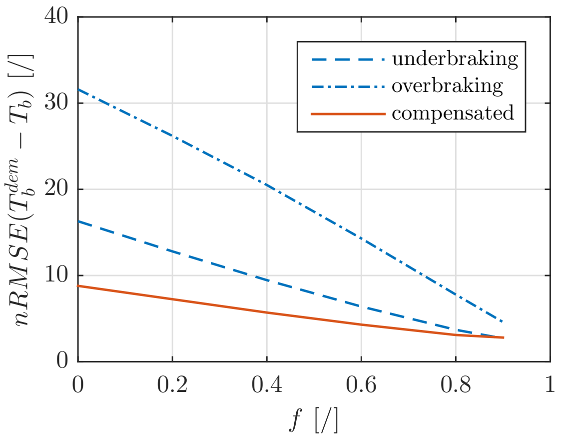

Figure 5.8: *The BLCF compensation function drastically abates the error between demanded and actual torque for all blending conditions.*

profile. Particularly, in the under-braking case, higher brake pedal travel must be applied to realise the same deceleration level. Conversely, in the over-braking case, the same pedal actuation leads to higher deceleration levels. In the non-compensated

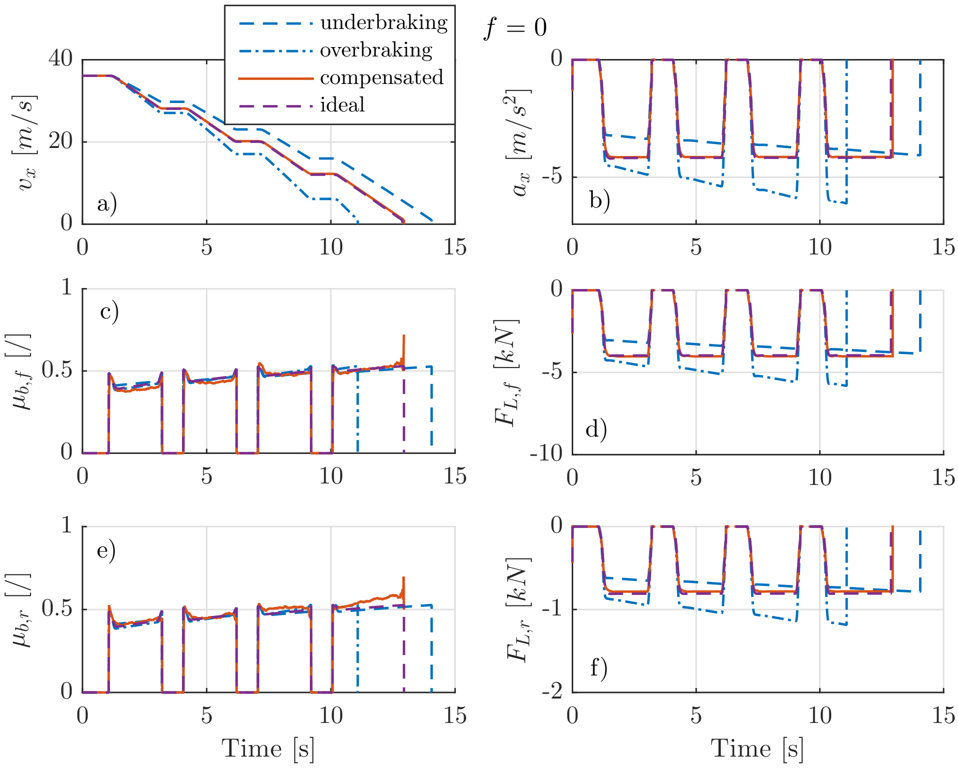

Figure 5.9: *Results of BLCF compensation function in case of repeated brake actuation with respect to three operating instances, underbraking, overbraking and compensated case. Electric motors are deactivated and only foundation brakes are used to decelerate the vehicle. Graphs a) and b) report the vehicle kinematics; c) and e) refer to the simulated BLCF for front and rear axle, respectively; d) and f) report the simulated wheel longitudinal force for front and rear axle, respectively.*

cases, the deviations in deceleration are directly dependent on the current BLCF value. The compensation algorithm, by detecting BLCF variations, aligns the pedal travel-deceleration curve to the ideal profile. Therefore, the curve for the compensated case lays closer to the ideal characteristic. It is also worth noting that in presence of blending, the disturbances induced by BLCF variations on the vehicle deceleration are drastically reduced (Figure 5.11b).

The same test is repeated by lowering the brake pedal actuation speed down to 50 mm/s in Figure 5.12. The results confirm that the compensation algorithm aligns the pedal-travel deceleration curve to the desired profile.

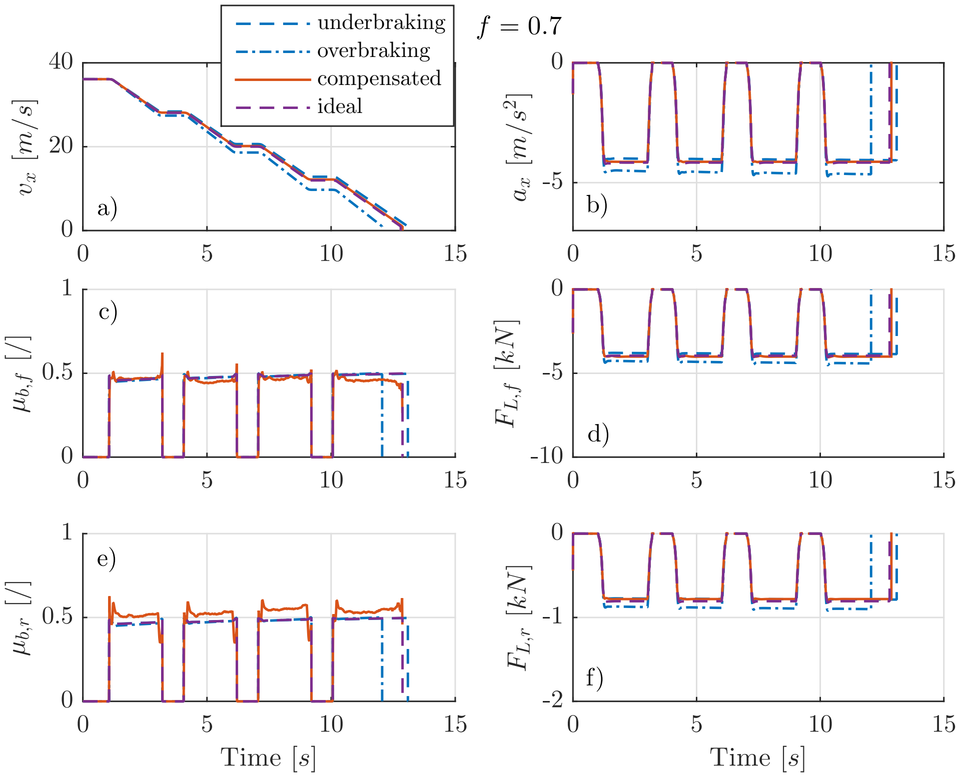

Figure 5.10: *Results of BLCF compensation function in case of repeated brake actuation with respect to three operating instances, underbraking, overbraking and compensated case. The electric motor are phased in parallel with* 70% *intervention. Graphs a) and b) report the vehicle kinematics; c) and e) refer to the simulated BLCF for front and rear axle, respectively; d) and f) report the simulated wheel longitudinal force for front and rear axle, respectively.*

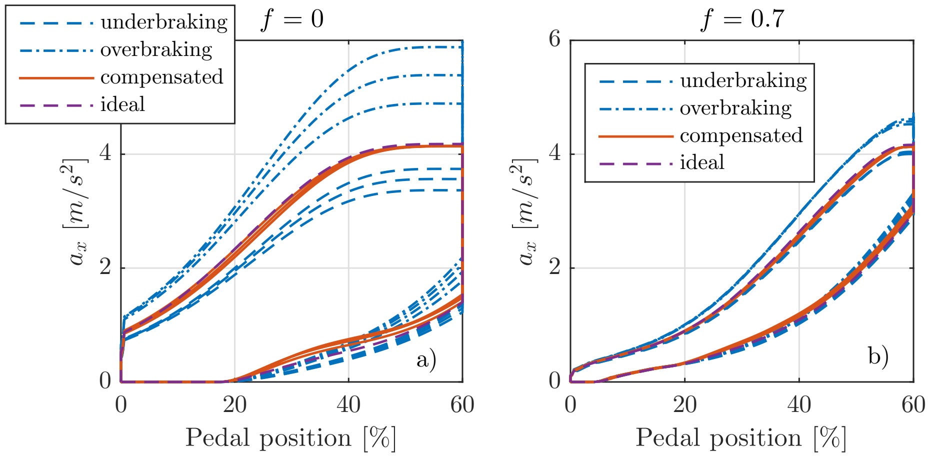

Figure 5.11: *Deceleration-pedal position characteristic curves for different operating modes. Graph a) refers to full friction brakes actuation; b) refers to blending with parallel phasing at* 70%*. The brake pedal actuation speed is equal to* 150 *mm/s.*

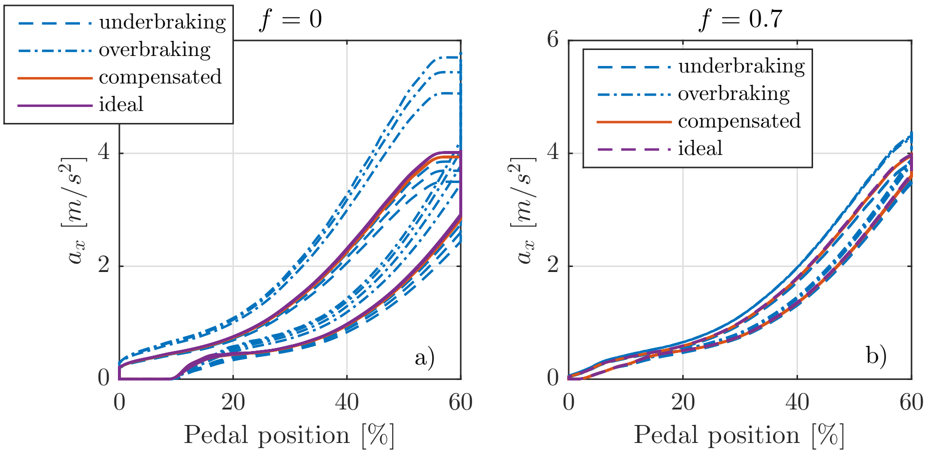

Figure 5.12: *Deceleration-pedal position characteristic curves for different operating modes. Graph a) refers to full friction brakes actuation; b) refers to blending with parallel phasing at 70%. The brake pedal actuation speed is equal to* 50 *mm/s.*

5.8 Chapter summary

A reliable BLCF estimate allows for an optimal blended control of foundation brakes with electric motors, in accordance with ECE R13H. The results show that the proposed controller effectively abates disturbances induced by BLCF variations. HIL simulation results confirm the real-time functionality of the developed BLCF observer and disturbance compensator. The compensation mechanism during brake torque generation in presence of brake blending enhances braking performance by reducing the reference deceleration tracking error. The results also demonstrate that the driver's workload can be either reduced by compensating the BLCF or by increasing the EM blending share during decelerations.

Chapter 6

Experimental validation on the proving ground

6.1 Introduction

This chapter deals with the experimental validation of the BLCF observer introduced in Chapter 4. The full electric SUV demonstrator was provided by Flander's Make (Lommel, Belgium). Technical specifications are reported in Appendix D. The tests were performed at the Ford proving ground in Lommel (Belgium) by a professional driver, who was properly briefed before the tests execution. The braking tests involved straight-line braking manoeuvres under clean environmental conditions on a dry flat road. During all manoeuvres, the ABS mode was deactivated, the regenerative mode disabled and the braking intensity limited to 6 m/s^2 to avoid wheel lock, condition under which the observability of the states cannot be proved (please, refer to Chapter 4). The observer functionality is demonstrated by means of two KPIs, namely the BLCF normal round mean square error and the average BLCF deviation, computed in accordance with SAE J2522. The experimental BLCF is extracted from brake torque measurements of the wheel force transducers. The data post-processing is performed in accordance with Annex 5 - Appendix 2 of ECE R13H [73]: torque signals are filtered using a five-point, on-centre moving average for each data channel and a recursive least square algorithm is then used to estimate the BLCF based on the measured torque output as a function of the measured line pressure. Only torque output values obtained from data collected when the vehicle deceleration is within the range of 0.15 G to 0.8 G are used in the regression analysis. For the sake of simplicity, despite the required post-processing action, the reference BLCF estimated from direct wheel torque and brake pressure measurements is herein referred to as measured.

6.2 Tests on the proving ground

The measurement campaign consists of three test sessions:

- the first test session involving a series of full-stop braking manoeuvres characterised by fixed pedal displacement is used to calibrate a suboptimal observer;
- the second test session includes full-stop braking manoeuvres characterised by constant deceleration and is employed to validate the observer robustness with respect to different braking conditions;
- the third test session is an AMS type test, herein referred to as fade test, where consecutive full-stop braking manoeuvres are performed to test the observer robustness against increasing brake temperature.

It is worth noting that during the first two test sessions, a pause of 5 min is set between consecutive test runs to let the brakes cool down. The suboptimal observer stemming from the first test is then validated against the successive ones. The third test is conducted without any pause between runs; however, the braking intensity is limited to $3-4$ m/s^2 to avoid excessive brake overheating, which could in turn damage the wheel force transducers. The high precision optical speed sensor, employed during the test sessions, allows for accurate estimation of the wheel slip. The vehicle setup also includes ABS mode deactivation and disabled regeneration. The observer being validated in this chapter corresponds to the design 2 introduced in Chapter 4. The reader is therefore referred to Chapter 4 for details on the BLCF observer scheme.

6.2.1 Fixed pedal braking

The first test session involves three full-stop brake runs from an initial vehicle speed of 100 km/h. Three runs are performed by keeping the brake pedal to fixed position with 20%, 40% and 60% of the pedal displacement limit, respectively. The keeping of a reference pedal displacement is ensured by a visual feedback provided via host PC to the expert driver. This session also includes three additional runs where the brake pedal is repeatedly actuated with 40% of its displacement limit with bursts of 2 s. This second test is employed to excite the vehicle pitch dynamics, which might play a detrimental role on the vehicle global longitudinal force estimation.

Numerous techniques were considered to optimise the choice of the process covariance matrix components and, thus, define a suboptimal observer [62]. In the present study, a first tuning of the observer covariance matrices is manually attempted. The process covariance matrix features three components reflecting the uncertainty associated with the model of the process. The measurement covariance matrix is constituted by two variance components associated with the wheel encoders white noise and the virtually sensed wheels longitudinal force. In accordance with common practice, the measurement covariance matrix components are set equal to the wheel encoders white noise. The virtual force sensor associated variance and the process covariance matrix are instead optimised by means of genetic algorithms to find the suboptimal observer that minimises the normal round means square error of the BLCF estimate [90].

For the sake of space, only partial results of the third and fifth runs are herein graphically included; the full results are instead reported under the form of Table 6.1. Figures 6.1 and 6.2 report the results of the third and fifth run, respectively, where the manually tuned observer is referred to as EKF and its suboptimal variant as GA EKF.

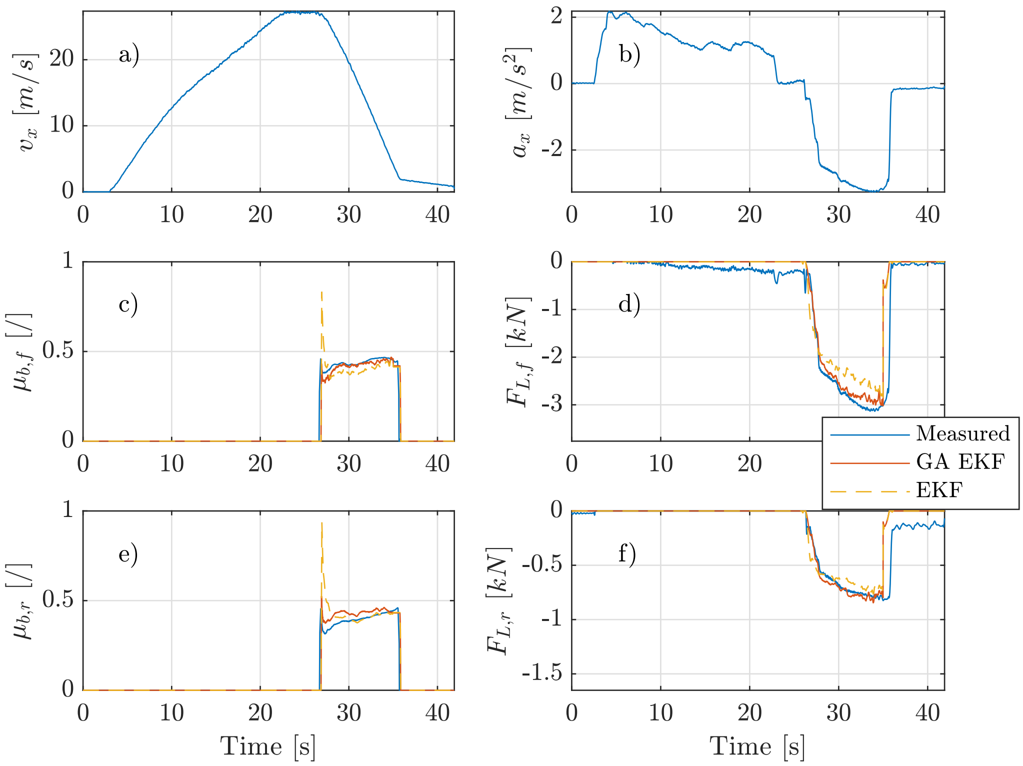

Figure 6.1: *Third run of the first test session featuring a full stop braking with a maximum pedal displacement of* 60%. *Graph a) and b) report the vehicle kinematics; c) and e) report the estimated BLCF for front and rear axle, respectively; d) and f) report the estimated wheel longitudinal force for front and rear axle, respectively. GA EKF is the suboptimal observer; EKF represents the manually tuned observer.*

The suboptimal GA EKF exhibits superior tracking performance when compared to its manually tuned variant. The suboptimal observer gets rid of undesired overshoots in the BLCF estimation that instead occurs in the case of manually tuned EKF. With respect to the fifth run in Figure 6.2, several braking applications are performed to first decelerate the vehicle and later, after a second acceleration, lead it to a full stop. Due to increasing disc temperature, it can be noted that the front BLCF exhibits a sinking behaviour, which leads to a decreasing deceleration intensity for a fixed brake pedal displacement. Compared to the manually tuned variant, the suboptimal observer allows for superior tracking performance.

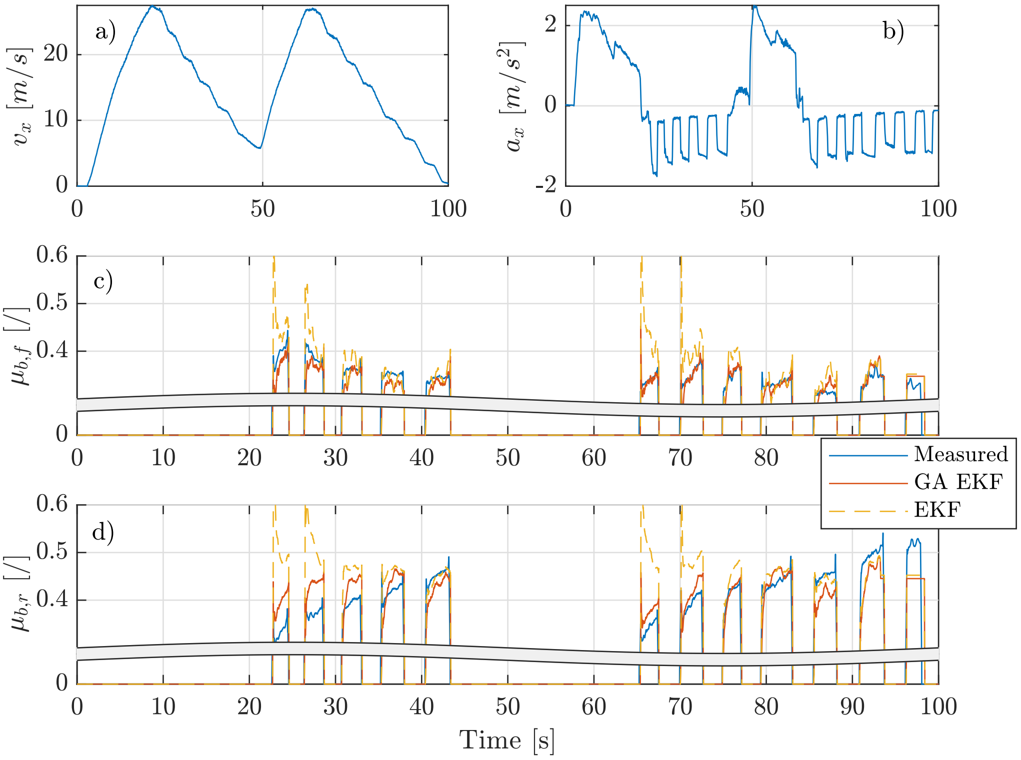

Figure 6.2: *Fifth run of the first test session featuring repeated brake actuations with a maximum pedal displacement of* 40%*. Graphs a) and b) report the vehicle kinematics; c) and d) report the estimated BLCF for front and rear axle, respectively. GA EKF is the suboptimal observer; EKF represents the manually tuned attempt.*

The results corresponding to the first test session are reported in Table 6.1. The observer functionality is quantified in terms of two KPIs, namely the BLCF nRMSE and the BLCF average value, computed in accordance with SAE J2522. The results show that the suboptimal observer allows for improved estimation accuracy under all investigated operating conditions. It is also worth noting that the high precision optical speed sensor, employed during these tests, allows for accurate estimation of the wheel slip, which reflects into a very accurate BLCF estimation even for limited deceleration values. It can be also noted that the estimation accuracy at the rear axle is worse under all operating conditions; nevertheless, the suboptimal observer succeeded at reducing the estimation error.

TABLE 6.1: Results of the proposed observer with respect to fixed pedal braking tests. The table vertically divides the results of the manually tuned observer and its suboptimal variant.

	Run #	Pedal	$\bar{a}_x$	$nRMSE(\mu_b)$		$\bar{\mu}_b$			
				Front	Rear	Front		Rear	
						Meas.	Obs.	Meas.	Obs.
Manually tuned observer	Run 1	20%	$\approx 1\ m/s^2$	18.78%	31.70%	0.446	0.512 (+14.80%)	0.443	0.595 (+34.31%)
	Run 2	40%	$\approx 1.5\ m/s^2$	13.52%	20.70%	0.415	0.453 (+9.16%)	0.427	0.526 (+23.18%)
	Run 3	60%	$\approx 3\ m/s^2$	7.01%	10.74%	0.436	0.409 (−6.19%)	0.393	0.427 (+8.65%)
	Run 4	40%	$\approx 1.6\ m/s^2$	12.42%	20.90%	0.446	0.489 (+9.64%)	0.412	0.506 (+22.82%)
	Run 5	40%	$\approx 1.5\ m/s^2$	12.12%	20.36%	0.345	0.388 (+12.46%)	0.405	0.467 (+15.31%)
	Run 6	40%	$\approx 1.6\ m/s^2$	12.50%	20.33%	0.367	0.408 (+11.17%)	0.391	0.445 (+13.81%)
Suboptimal observer	Run 1	20%	$\approx 1\ m/s^2$	8.84%	22.44%	0.446	0.417 (−6.50%)	0.443	0.529 (+19.41%)
	Run 2	40%	$\approx 1.5\ m/s^2$	7.35%	15.88%	0.415	0.399 (−3.86%)	0.427	0.485 (+13.58%)
	Run 3	60%	$\approx 3\ m/s^2$	3.75%	10.11%	0.436	0.419 (−3.99%)	0.393	0.429 (+9.16%)
	Run 4	40%	$\approx 1.6\ m/s^2$	7.96%	18.13%	0.446	0.433 (−2.91%)	0.412	0.489 (+18.69%)
	Run 5	40%	$\approx 1.5\ m/s^2$	8.33%	15.27%	0.345	0.335 (−2.99%)	0.405	0.457 (+12.96%)
	Run 6	40%	$\approx 1.6\ m/s^2$	9.33%	14.98%	0.367	0.364 (−0.82%)	0.391	0.439 (+12.28%)

6.2.2 Fixed deceleration braking

The suboptimal observer is here validated against the second test session, which includes six deceleration controlled full-stop braking manoeuvres characterised by different initial braking speeds and braking intensities. Similarly to the first test, the expert driver, by means of visual feedback on the host PC, makes sure that the deceleration level is kept close to the desired value. The purpose of this test is to validate the suboptimal observer with respect to different braking conditions. The experiments involve two initial speed values, i.e. 50 km/h and 100 km/h, and three deceleration levels, in the range $(1-2)\ m/s^2$, $(3-4)\ m/s^2$ and $(5-7)\ m/s^2$. For the sake of space, graphic results are omitted. The suboptimal observer validation results are reported in Table 6.2.

In accordance with the simulation results, higher deceleration levels allow for improved estimation accuracy. The experimental results also suggest that the initial braking speed value does not affect the BLCF estimation performance, provided that the wheel slip can be estimated with great accuracy. It is also worth pointing out that a reduction in the estimation performance can be noted on the front axle in case of higher deceleration

Table 6.2: Validation results of the suboptimal observer with respect to fixed deceleration braking.

Run #	$v_{x,in}$	$\bar{a}_x$	$nRMSE(\mu_b)$		$\bar{\mu}_b$			
			Front	Rear	Front		Rear	
					Meas.	Obs.	Meas.	Obs.
Run 1	50 km/h	$\approx 1.3\ m/s^2$	14.08%	35.02%	0.392	0.348 (-11.22%)	0.399	0.540 ($+35.34\%$)
Run 2	50 km/h	$\approx 3.5\ m/s^2$	4.31%	16.80%	0.457	0.448 (-1.97%)	0.459	0.543 ($+18.30\%$)
Run 3	50 km/h	$\approx 6\ m/s^2$	10.10%	12.70%	0.409	0.465 ($+13.69\%$)	0.354	0.379 ($+7.06\%$)
Run 4	100 km/h	$\approx 1.3\ m/s^2$	13.70%	45.40%	0.465	0.409 (-12.04%)	0.422	0.661 ($+56.63\%$)
Run 5	100 km/h	$\approx 3.5\ m/s^2$	3.87%	16.40%	0.468	0.450 (-3.85%)	0.483	0.575 ($+19.05\%$)
Run 6	100 km/h	$\approx 6\ m/s^2$	9.70%	10.19%	0.404	0.449 ($+11.14\%$)	0.490	0.475 (-3.06%)

requests, namely Run 3 and 6, due to the excessive load transfer, which in turn might compromise the assumption of load proportionality principle considered in the observer scheme.

6.2.3 Brake fade test

The fade test session consists of ten identical runs and is used to verify the observer robustness against increasing disc temperature. In accordance with the experimental results of Chapter 3, the increasing brake temperature leads to a BLCF decay, which results in reduced braking performance. In accordance with experimental data of Figure 6.3, while moving to successive braking manoeuvres, the driver needs to increase the pedal displacement to ensure equal braking intensity. All test runs are characterised by an initial braking speed of 100 km/h down to a final speed of 20 km/h. During the braking, the driver keeps the deceleration between 3 m/s^2 and 4 m/s^2.

The results are conveniently reported in Figure 6.4 where the acceleration phases are removed for the sake of space. It can be easily noted that consecutive braking applications feature a decreasing BLCF. This phenomenon can be accurately captured by the suboptimal observer. After the fourth brake application, the BLCF has decreased by 20% below its nominal value. At the rear axle, the suboptimal observer exhibits an overestimating behaviour. Nevertheless, the reader must be informed that due to the limited axle excitation level, the very estimation of the BLCF from the wheel torque measurement might be affected by error. Table 6.3 conveniently reports the results of the fade test.

The experimental results show that the decaying BLCF causes the pedal-deceleration to shift to the right, as per Figure 6.3. As a consequence, the driver needs to increase the brake pedal displacement to achieve the same deceleration level. HIL simulations in

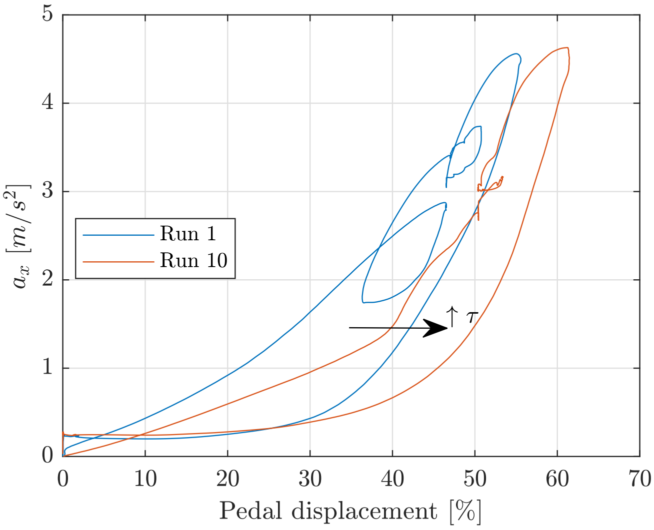

Figure 6.3: *Results of the fade test show that the pedal-deceleration curve is affected by the increased disc temperature τ, which corresponds to a BLCF decay. The driver needs to increase the pedal displacement to ensure the same deceleration level.*

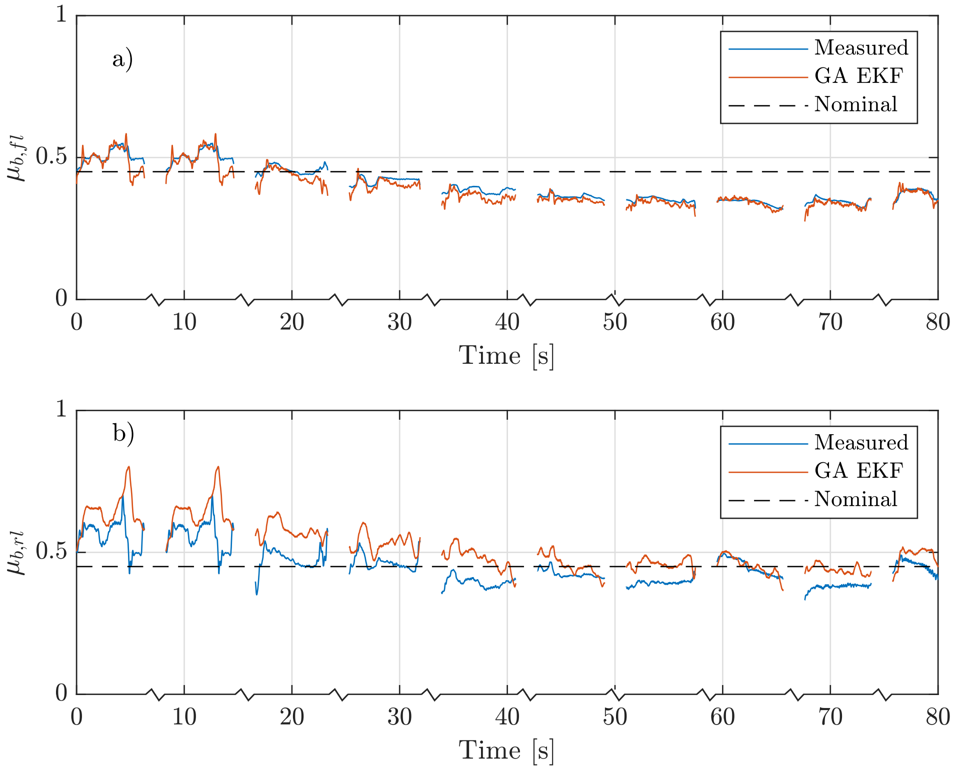

Figure 6.4: *Results of the fade test. Graphs a) and b) report the measured and observer BLCF with respect to the front and rear axle. GA EKF is the suboptimal observer; Nominal is the brake BLCF computed in accordance with SAE J2707.*

Table 6.3: Validation results of the suboptimal observer with respect to fade test.

			$nRMSE(\mu_b)$		$\bar{\mu}_b$			
Run #	$v_{x,in}$	$\bar{a}_x$	Front	Rear	Front		Rear	
					Meas.	Obs.	Meas.	Obs.
Run 1	100 km/h	3.7 m/s^2	9.55%	19.02%	0.517	0.482 (−6.77%)	0.560	0.624 (+11.43%)
Run 2	100 km/h	3.2 m/s^2	7.78%	18.80%	0.500	0.480 (−4.00%)	0.548	0.629 (+14.78%)
Run 3	100 km/h	3.2 m/s^2	8.45%	22.00%	0.453	0.423 (−6.62%)	0.466	0.566 (+21.46%)
Run 4	100 km/h	3.2 m/s^2	6.65%	17.60%	0.416	0.397 (−4.57%)	0.459	0.529 (+15.25%)
Run 5	100 km/h	3.2 m/s^2	6.85%	19.40%	0.383	0.356 (−7.05%)	0.390	0.472 (+21.03%)
Run 6	100 km/h	3.5 m/s^2	4.94%	7.94%	0.362	0.347 (−4.14%)	0.422	0.449 (+6.40%)
Run 7	100 km/h	3.2 m/s^2	6.80%	18.60%	0.346	0.332 (−4.05%)	0.386	0.456 (+18.13%)
Run 8	100 km/h	3.4 m/s^2	3.75%	4.72%	0.339	0.335 (−1.18%)	0.447	0.446 (−0.22%)
Run 9	100 km/h	3.3 m/s^2	5.63%	14.60%	0.341	0.328 (−3.81%)	0.374	0.432 (+15.51%)
Run 10	100 km/h	3.1 m/s^2	8.99%	14.30%	0.357	0.356 (−0.28%)	0.428	0.472 (+10.28%)

Chapter 5 have shown that such disturbances can be avoided by compensating BLCF. Hence, the BLCF compensation function can ensure that the brake system always provide the desired feedback to the driver, preventing the pedal-deceleration curve from shifting.

6.3 Chapter summary

The BLCF observer functionality is validated on the proving ground with respect to several braking manoeuvres performed by a professional driver. Genetic algorithms are used to find the sub-optimal extended Kalman filter for the vehicle under analysis. In accordance with the simulations of Chapter 4, the experimental results demonstrate that gentle and mild deceleration values play a detrimental role on the rear axle BLCF estimation. Nonetheless, the proposed BLCF estimator reveals robust against repeated braking manoeuvres, despite the dramatic increase in the disc temperature and consequent BLCF decay.

Chapters 7 and 8 demonstrate applicability of the proposed BLCF observer to enable advanced brake monitoring functions through estimation of the actual brake torque. The BLCF observer is switched on, upon achievement of the minimum deceleration requests identified in Chapter 4. Under all other conditions, a constant BLCF equal to its last estimate is used. Particularly, in Chapter 7, a novel wear prognosis function driven by data collected on the brake dynamometer and validated on an experimental vehicle is presented. In Chapter 8, a novel estimation tool for brake-related particle emissions stemming from on-road measurement is put forth and validated.

Chapter 7

A novel brake wear prognosis function

7.1 Introduction

Former investigations performed by Archard in 1953 demonstrate that normal load, sliding velocity and hardness of the rubbing materials play a role in the mechanisms of wear [91]. Despite his conclusions, studies published during the past 70 years do not provide satisfactory results on modelling brake-related wear and do not support the proposed theories with experimental evidence. Wear tests imply high costs and time-spending measurement protocols as the wear can only be assessed upon completion of a brake test. Moreover, brake tests must be designed so that the produced wear volume is order of magnitudes larger than the measurement equipment precision. For this reason, existing wear studies feature very elementary design of experiments, the majority of which relates to pin-on-disc [92, 93].

This chapter proposes a novel semi-empirical wear model driven by RDE-compliant wear data. In accordance with [94], designing wear tests that duplicate the brakes' real usage conditions enables the formulation of a wear-energy relationship. This latter constitutes the basis for a wear prognosis function, which relies on the BLCF observer proposed in Chapter 4. In accordance with the schematic of Figure 7.1, the brake disc temperature estimate $\hat{\tau}$ is provided by the lumped capacitance model discussed in Chapter 3 and identified against experimental data collected from the sedan in Appendix D. This latter requires the vehicle speed $\hat{v}_x$ to be estimated in order to account for the brake cooling coefficient $\hat{\delta}_{ht}$. The ambient temperature τ_0 is instead assumed measurable. The BLCF observer in Chapter 4 allows for estimation of the brake torque $\hat{T}_b$, provided that the brake calliper pressure p_b is measured, in accordance with Equation (A.19). Ultimately, also the measured wheel speed ω is fed to the pad wear model for the brake power calculation.

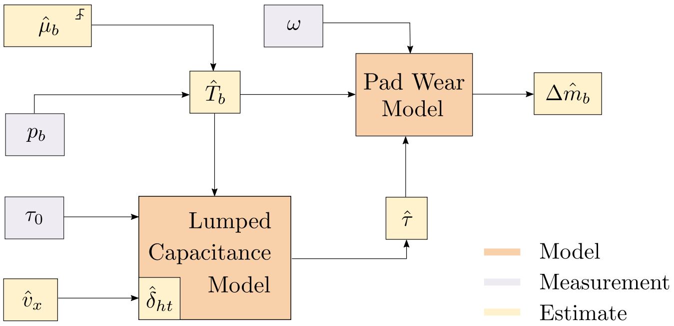

Figure 7.1: *Schematic of the proposed brake pad wear prognosis function based on the BLCF observer of Chapter 4 and the lumped brake temperature model of Chapter 3.*

Wear tests on the brake dynamometer allow investigating the functional dependencies of the pad wear rate with respect to sliding speed, brake torque and disc temperature. The model is therefore parametrised with respect to wear data collected from a floating calliper brake system equipped with gray cast iron disc and ECE linings. The functionality of the wear model is demonstrated with respect to data collected from the sedan in Appendix D equipped with the same brake system at the front axle. Under the investigated RDE-compliant conditions, the collected data demonstrate that brake linings wear down much faster than the brake discs. For this reason, the brake disc wear is not addressed in this work.

7.2 A novel brake lining wear model

Scientific studies of the past decade demonstrate that the brake lining wear rate can be expressed as a function of sliding speed, brake line pressure and brake disc temperature [95, 96, 38]. These considerations lead to the following equation:

$$m_b = \int_{t_0}^{t_0+\Delta t_b} k_b(\omega, p_b, \tau)\ \omega\ T_b\ dt, \tag{7.1}$$

where, m_b represents the wear mass, k_b is the brake lining specific wear rate and $[t_0; t_0 + \Delta t_b]$ represent the absolute braking interval. By expanding Equation (7.1) with the chain rule, wear rate can be expressed as:

$$\dot{m}_b = \frac{\partial m_b}{\partial t} + \frac{\partial m_b}{\partial \omega}\frac{d\omega}{dt} + \frac{\partial m_b}{\partial p_b}\cancelto{0}{\frac{dp_b}{dt}} + \frac{\partial m_b}{\partial \tau}\frac{d\tau}{dt}. \tag{7.2}$$

The third term containing the brake line pressure derivative is assumed to be negligible when compared to other terms due to short duration of pressure transients when braking. Hence, Equation (7.2) can be rewritten as:

$$\dot{m}_b = \underbrace{k_{b,0}(\omega, p_b, \tau)}_{f(\omega,p_b,\tau)>0}\ \omega\ T_b + \underbrace{\frac{\partial m_b}{\partial \omega}}_{g(\omega,p_b,\tau)>0}\ \dot{\omega} + \underbrace{\frac{\partial m_b}{\partial \tau}}_{h(\omega,p_b,\tau)>0}\ \dot{\tau}. \tag{7.3}$$

The first term $f(\omega, p_b, \tau)$ in Equation (7.3) expresses the quasi-static wear rate, valid for steady-state sliding speed, brake line pressure and brake disc temperature conditions (drag test with cooling). The second term $g(\omega, p_b, \tau)$ features the impact of varying sliding speed under steady-state temperature and pressure conditions and fixed braking time (time controlled test with cooling). The third term $h(\omega, p_b, \tau)$ represents the impact of the brake disc temperature dynamics when all other factors and braking time reach the steady-state (time controlled drag test). All terms are assumed to be strictly positive.

It is now worth transferring the wear problem to the specific use case, that is, the sedan in Appendix D. The wheel dynamics and lumped capacitance model during a braking shall be considered. This leads to Equations (7.4a) to (7.4c):

$$\begin{cases} \dot{\omega} = -\dfrac{1}{I_\omega}(T_b - F_L r_\omega - T_d), & (7.4a) \\ \dot{\tau} \simeq \xi \; \omega \, T_b, & (7.4b) \\ \dot{m}_b = f(\omega, p_b, \tau) \, \omega \, T_b + g(\omega, p_b, \tau) \, \dot{\omega} + h(\omega, p_b, \tau) \, \dot{\tau}. & (7.4c) \end{cases}$$

Equation (7.4a) represents the wheel dynamics, Equation (7.4b) describes the disc temperature dynamics by neglecting the cooling effect (please, refer to Chapter 3) and Equation (7.4c) is the proposed wear model. By replacing Equation (7.4b) in Equation (7.4c) and including the lumped capacitance model parameter ξ in the function $h(\omega, p_b, \tau)$, the following equation can be formulated:

$$\dot{m}_b = f(\omega, p_b, \tau) \, \omega \, T_b + g(\omega, p_b, \tau) \, \dot{\omega} + h^*(\omega, p_b, \tau) \, \omega \, T_b. \tag{7.5}$$

In accordance with the sifted literature instances, pin-on-disc tests performed under constant sliding speed and steady-state temperature conditions suggest that the quasi-static term $f(\omega, p_b, \tau)$ is only temperature dependent. In [93, 97, 98], the authors argue that the wear-energy linearity hypothesis holds upon considering the influence of the brake temperature. Moreover, in accordance with [99, 94, 100, 101], the wear-energy linearity shows larger slope at higher temperature values. The second and third terms, namely $g(\omega, p_b, \tau)$ and $h^*(\omega, p_b, \tau)$, represent the increased wear due to increasing wheel speed and due to increasing temperature, assumed proportional to the applied brake torque and to the resulting brake power, respectively. In accordance with the definition given in Equations (7.1) and (7.2), the previous assumptions lead to the following stances:

$$f(\tau) = \gamma_1(\tau), \quad g(\omega, p_b, \tau) = \gamma_2(\tau) \, T_b, \quad h^*(\omega, p_b, \tau) = \gamma_3(\tau) \, \omega \, T_b, \tag{7.6}$$

where the identification of γ parameters is left with the data driven method.

7.3 Experimental methodology

The experiments on the brake dynamometer are designed so as to duplicate the brakes usage under real driving conditions. For a better understanding, Figure 7.2 reports the methodological flow chart schematic of the reference on-road data generation, model identification and validation, respectively. On-road tests on the experimental sedan of Appendix D are used to generate reference driving cycles. These latter are organised under the form of driving blocks, each of which is composed of two or more driving cycles, in accordance with minimum detectable wear volume requirements. Real driving data is then properly selected to constitute a reference identification data set of N driving blocks. These latter are post-processed under the form of deceleration controlled brake test for the brake dynamometer. Each $i-th = [1, N]$ driving block of the identification data set involves $j = [1, N_{b,i}]$ brake applications. The reference driving blocks are run on the brake dynamometer to generate N wear data points, which constitute the model identification dataset. The dynamometer ensures improved repeatability of the wear measurements in comparison with on-road tests.

A set of candidate functions, taken from a functions database, constitute the linear parametric law rendering the wear rate. The model formulation is based on up-to-date knowledge of the wear process and is data driven. For each $i-th$ driving block, the wear rate differential model in Equation (7.5) must be rewritten in the linear integral form by integrating across the $j = [1, N_{b,i}]$ braking application to solve with respect to M parameters. The model identification corresponds to a least square problem, which can be solved upon verifying that the number of linear independent measurements N is greater than or equal to the model parameters cardinality M. Finally, the model is validated against newly generated on-road wear measurements under real driving conditions.

7.3.1 Real driving cycles

The instrumented sedan of Appendix D is used to generate real driving data, which are then provided as a reference for the brake dynamometer tests. In the framework of this study, different real driving sections, namely urban, rural and motorway span different regions of brake operating conditions, in terms of sliding speed, brake torque and brake disc temperature. Moreover, multiple drivers and different traffic conditions enhance even further the cycle-to-cycle variability. Driving cycle type and driving style allow generating model inputs representative of real driving conditions. Figure 7.3 reports the average braking conditions of partial driving data collected on the instrumented sedan.

In accordance with Figure 7.3, urban driving sections involve lower initial braking speed but higher temperature values due to the limited cooling effect (Figure 7.3b). Rural sections are characterised by higher initial braking speed values with mild deceleration levels (Figure 7.3a). Motorway sections feature very high speed values and enhanced brake cooling effect. However, a general trend cannot be defined without taking the driving style into consideration. In Figure 7.3, driver B identifies an aggressive driving behaviour that corresponds to higher cruising velocity on the motorway, higher deceleration intensity and higher disc temperature due to repeated brake actuation.

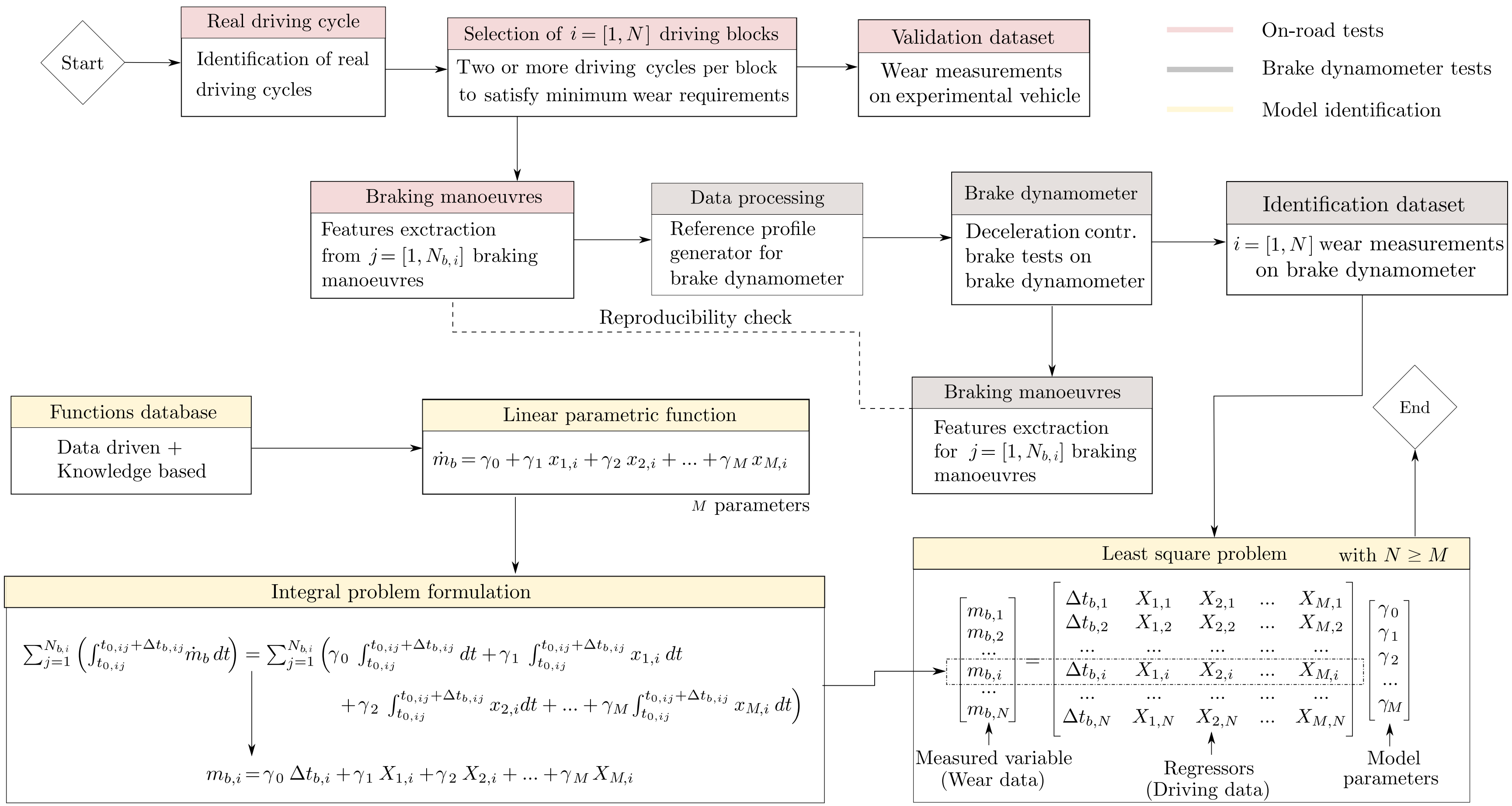

Figure 7.2: *Flow chart schematic of the methodology employed for the wear model identification. Real driving conditions are used to generate deceleration controlled brake dynamometer tests. Wear data collected on the brake dynamometer lead to the model parameters identification. The differential problem is brought to the integral form and, eventually, the LSQ problem is formulated. The linear square problem has a solution if the number of linear independent wear measurements N (rank of $\mathbf{X}$) is grater than or equal to the model parameters number M.*

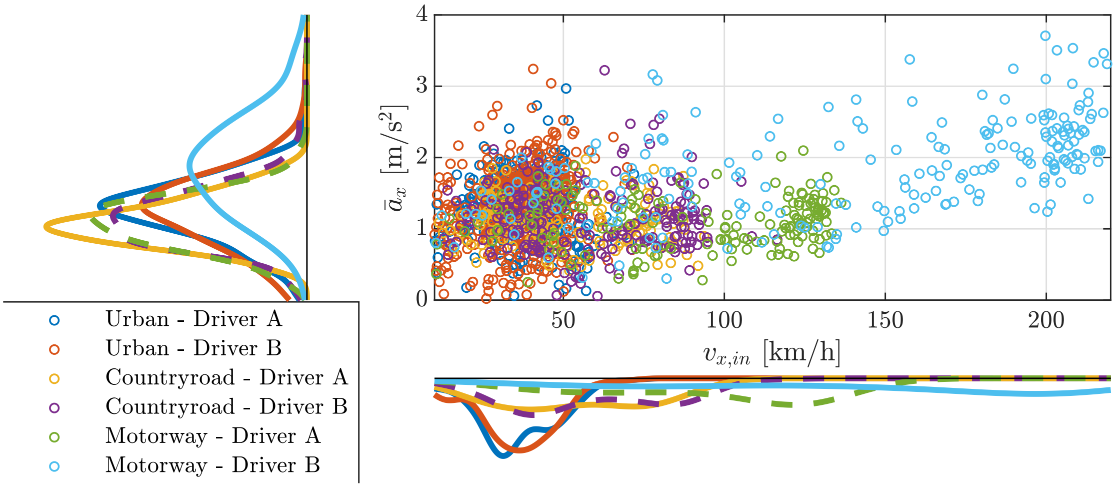

(a) *Average braking conditions with respect to initial braking speed and average deceleration level.*

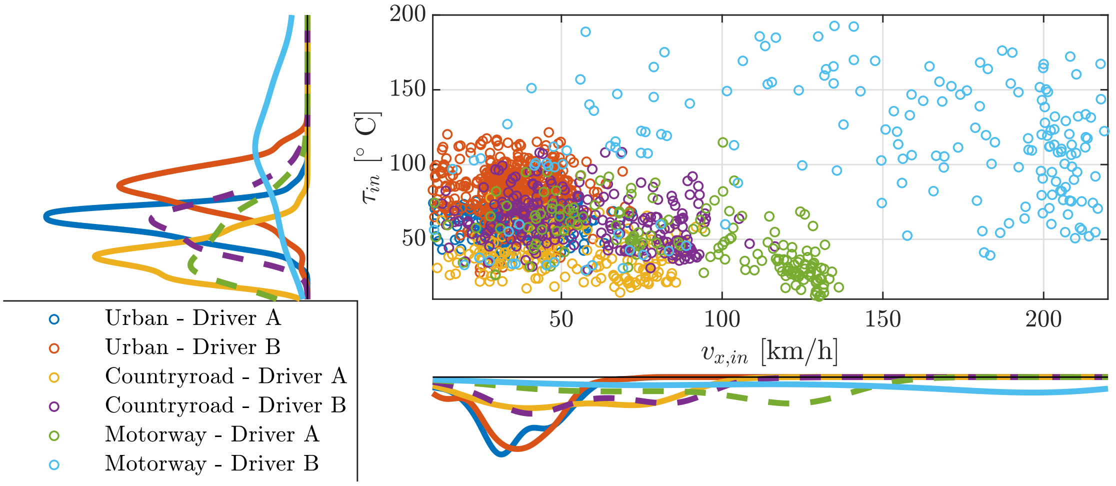

(b) *Average braking conditions with respect to initial braking speed and initial disc temperature.*

Figure 7.3: *Variability in braking conditions due to driving style and driving cycle (urban, rural road and motorway). At the graphs corners, the statistics of initial braking speed, average deceleration level and initial brake temperature are reported.*

The statistical analysis in Figure 7.4 shows that the number of braking applications is strongly dependent on the drive cycle type, being in the urban section much larger than other driving scenarios. Moreover, despite the high number of braking applications taking place in the urban section (Figure 7.4a), the cycle to cycle variability due to driving style and traffic conditions plays a major role in other driving sections (Figure 7.4b). A 2σ analysis shows that the driver's impact on wear rate results dramatically reduced in the urban section due to stricter speed limits. Conversely, the enhanced brake cooling due to higher speed values and the greater cycle to cycle variability due to reduced traffic control measures in rural and motorway driving sections cause an increased impact of the driver on the wear rate. It is also worth noting that the enhanced cooling in motorway section improves the specific wear rate of the front linings.

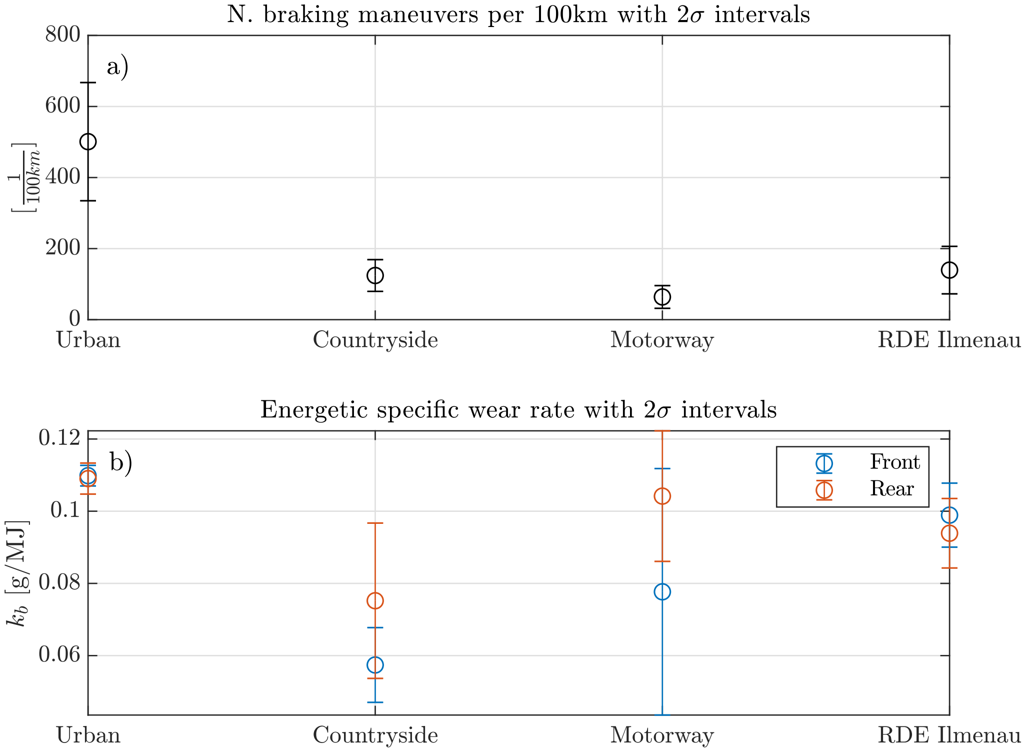

Figure 7.4: *On-road brake wear cycle dependence with 2σ intervals. Graph a) reports the average number of brake applications per equivalent 100 km per cycle type and b) the energy specific wear rate per cycle type.*

To ensure compliance with minimum detectable wear requirements, real driving data collected from the instrumented vehicle are packed into test blocks. Depending on the braking intensity and driving style, each test block may contain up to four driving cycles. The data are then post processed to extract the occurred braking manoeuvres. These latter are fed to the brake dynamometer control system, which performs a reference-deceleration control between speed levels. Wear measurements on the instrumented sedan suggest that approximately 250 braking manoeuvres reveal necessary to produce wear volume one order of magnitude larger than the measurement equipment accuracy.

7.3.2 Brake dynamometer tests

The single-end full-scale inertia brake dynamometer at Technische Universität Ilmenau is used to generate wear data based on real driving inputs collected on the sedan of Appendix D. The brake dynamometer reproduces the quarter car vehicle inertia on a front wheel. The brake dynamometer construction is similar to Figure 3.1. However, climatic conditions and air cooling cannot be controlled. The full-scale inertia dynamometer control is based on the real time dSPACE DS1007® platform. The DS2002® A/D multi-channel board allows for data acquisition of brake pressure, sliding speed, brake torque and disc temperature with a sampling rate of 100 Hz. The compressed air hydraulic actuator increases the pressure up to 210 bar within the master cylinder. A flow meter measures the consumption of brake fluid and a pressure sensor mounted in the vicinity of the brake calliper measures the brake line pressure. The disc temperature is measured by a rubbing thermocouple of the type used on the experimental sedan in Appendix D. The brake torque is measured through a sensor positioned inside the flywheel. The dynamometer allows a maximum operating regime of 2500 rpm and features a peak power of 186 kW and a maximum torque of 5000 Nm. The brake pads are disassembled after each test in order to assess the linear wear and wear mass. To ensure repeatability of the wear measurement on the brake dynamometer, the brake pads are bedded before the test campaign is started, in accordance with SAE J2522 Sec. 2.

The reference cycle for brake dynamometer tests in based on criteria of vehicle speed and energy reproducibility and real-time capability requirements. A sensitivity analysis conducted on the brake dynamometer demonstrates that superior on-road tests reproducibility and cycle to cycle repeatability on the brake dynamometer are achieved under brake deceleration control mode between speed levels. The implemented rule based controller is of the form reported in Figure 7.5. The new brake manoeuvre is started upon reaching the reference initial brake disc temperature τ_{in} from on-road tests measurements. The brake dynamometer accelerates to the reference initial braking speed $v_{x,in}$ extracted from on-road tests. Thereafter, a deceleration controlled braking takes place until the reference exit braking speed $v_{x,end}$ from on-road tests is achieved. The new braking is thereafter loaded. Due to the limited brake cooling effectiveness under laboratory conditions, the temperature check is switched-off upon reaching a brake disc temperature of 65 $°C$.

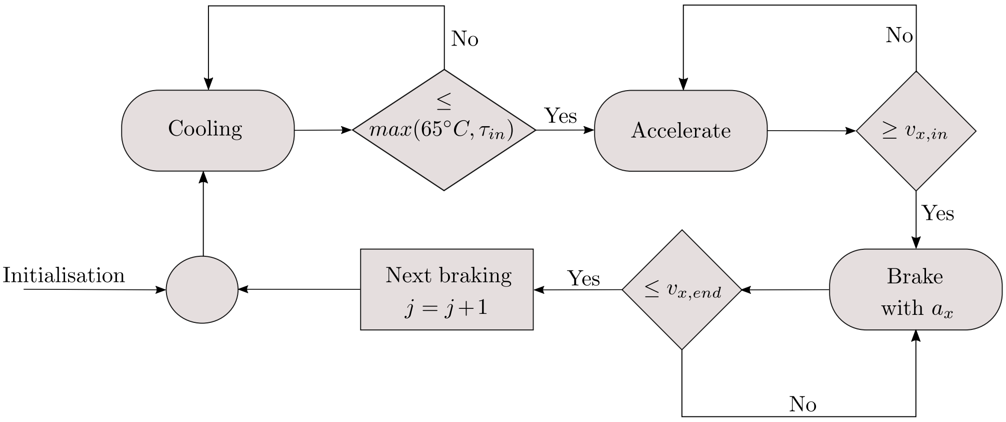

Figure 7.5: *Flowchart of the rule based brake dynamometer controller. The new brake manoeuvre is started upon reaching the reference initial brake disc temperature. The brake dynamometer accelerates to the reference initial braking speed extracted from on-road tests. The deceleration controlled braking continues until the reference end speed from on-road tests is achieved.*

Figure 7.6 reports partial results of a real driving wear test conducted on the brake dynamometer. With respect to on vehicle data, the brake dynamometer features satisfactory tracking performance being able to maintain the $nRMSE$ of the wheel speed under 6%. The brake dynamometer is not able to reproduce the driving resistance forces (e.g. rolling resistance and air drag) resulting in a slightly longer braking time. Consequently, the achievement of the reference end braking speed causes a prolonged brake actuation. This phenomenon and its effect on the wear measurement reproducibility on the brake dynamometer are further discussed in the text.

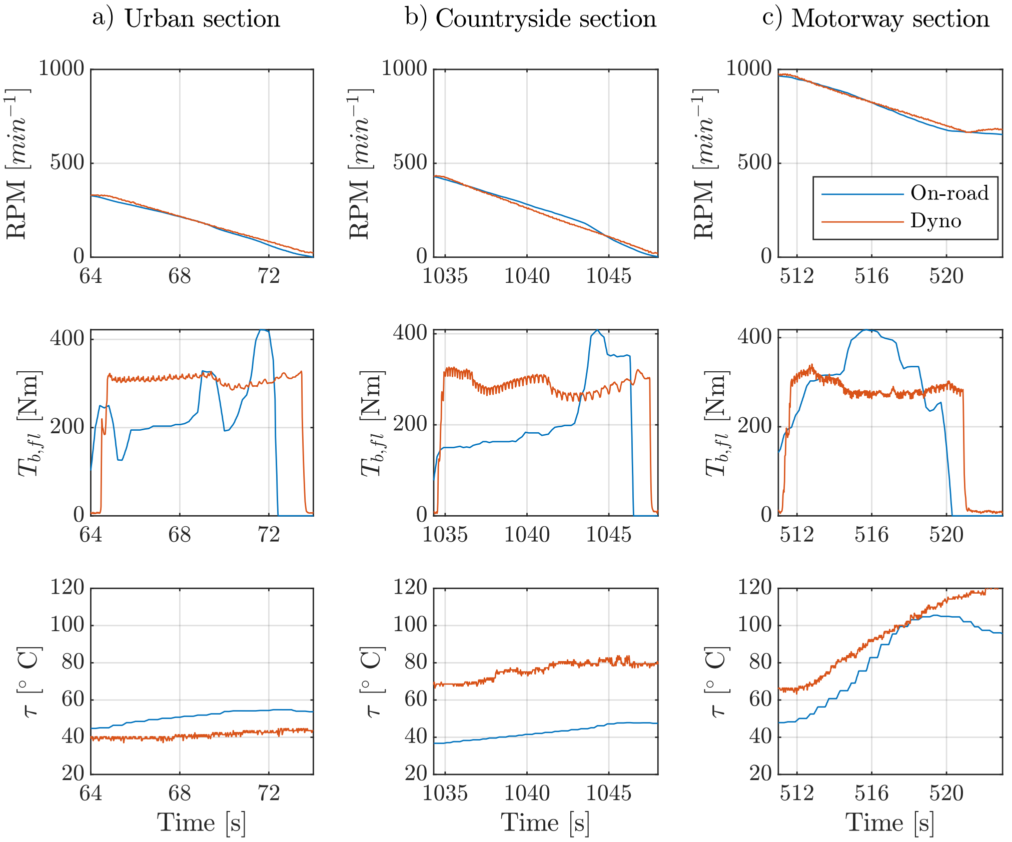

Figure 7.6: *Partial results of a RDE-compliant brake test on the brake dynamometer (Dyno, red) compared to the real on-road acquisitions (On-road, blue) for a urban a), rural b) and motorway c) brake application. All signals refer to the front-left wheel.*

7.3.3 Wear measurements

The wear measurement procedure complies SAE J2707 standards for brake dynamometer wear tests. Upon test completion, the brake pads of a front brake disc are blown clean with compressed air and both thickness and mass are assessed. In the case of on-road tests, the post-treatment in a climatic chamber reveals necessary to free the linings from excessive humidity absorbed during the test. A micrometer with an accuracy of ±10 μm is used for measuring the linear pad wear. To ensure accurate measurement of brake pad wear, six points equally spaced on the contact surfaces are measured. Measurement locations are numbered starting from the outer leading edge of the finger-side pad and move in the clockwise direction. The last measurement location is thus on the inner leading edge of the pad. The average linear wear is calculated taking into account the average value of the friction material linear wear measured on the defined six points. The wear mass is measured by means of a scale with an accuracy of ±10 mg.

With reference to on-road wear tests, debris accumulation might compromise the correctness of wear measurements. Hereunto, a least square approach is used to blend the linear wear and wear mass measurements to ensure data consistency and reliability. It is worth considering an auxiliary plane reporting on the x-axis the equivalent wear mass computed from the linear wear measurements $x_i \in \mathbf{X}_w$, and on the y-axis the actual wear mass measurements $y_i \in \mathbf{Y}_w$. The equivalent wear mass can be easily computed from the linear wear measurements, knowing the rubbing surface area. This latter must be expressed as a function of the wear depth due to the presence of chamfers. It is worth remarking that the proposed methods do not require the brake lining density to be known as it is implicitly accounted for in the least square solution.

With respect to the generic set of wear measurements in Figure 7.7, the least square curve of slope K_{LSQ} can be computed by applying the following equation:

$$K_{LSQ} = \left(\mathbf{X}_w^T \mathbf{X}_w\right)^{-1} \mathbf{X}_w^T \mathbf{Y}_w. \tag{7.7}$$

For the generic wear measurement of coordinates (x_i, y_i), the projections directions fo_i and fv_i and the perpendicular projection $f_{\perp i}$ can be formulated as follows:

$$fo_i(x):\ y = y_i;\quad fv_i(x):\ x = x_i;\quad f_{\perp i}(x):\ (y - y_i) = \frac{1}{K_{LSQ}}(x_i - x). \tag{7.8}$$

The generic projection fb_i can be expressed as a linear combination of Equation (7.8). Thereafter, a blending parameter α_w is introduced:

$$fb_i(x):\ (y - y_i) = \frac{\alpha_w}{K_{LSQ}}(x_i - x), \tag{7.9}$$

where,

$$fb_i = \begin{cases} fo_i & if \quad \alpha_w == 0 \\ fv_i & if \quad \alpha_w \to +\infty \\ f_{\perp i} & if \quad \alpha_w == 1 \\ (y - y_i) = \dfrac{\alpha_w}{K_{LSQ}}(x_i - x) & if \quad otherwise \end{cases} \tag{7.10}$$

The generic projection $(\tilde{x}_i, \tilde{y}_i)$ onto the LSQ curve is thus equal to:

$$LSQ \wedge fb_i: \; \tilde{x}_i = \frac{y_i + \frac{\alpha_w}{K_{LSQ}} x_i}{K_{LSQ} + \frac{\alpha_w}{K_{LSQ}}}; \; \tilde{y}_i = \frac{K_{LSQ}\, y_i + \alpha_w\, x_i}{K_{LSQ} + \frac{\alpha_w}{K_{LSQ}}} \tag{7.11}$$

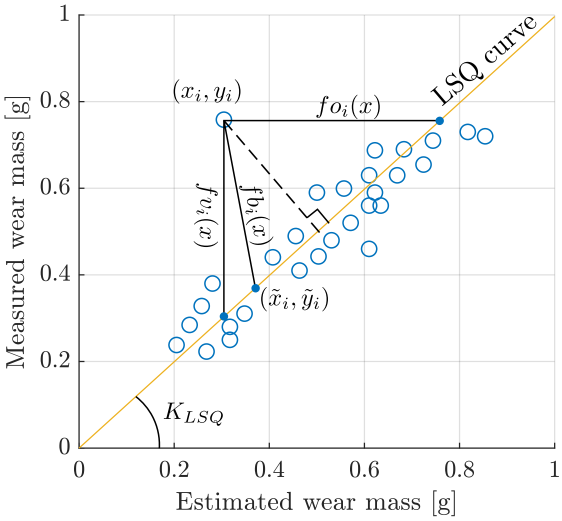

Figure 7.7: *The generic wear mass measurement (x_i, y_i) is corrected by projection onto the least square curve. The projected point is defined by coordinates $(\tilde{x}_i, \tilde{y}_i)$. Depending on the measurement reliability, the projection can take place along the horizontal direction fo_i if the linear wear measurement is completely inaccurate, or along the vertical direction fv_i if the wear mass measurement is deemed unreliable. The wear mass and linear wear measurements are blended if the projection occurs along the direction of fb_i.*

The wear correction algorithm leads to the results in Figure 7.8. With respect to on-road wear measurements where tests might occur even under rainy weather conditions, more weight is given to the linear wear measurements ($\alpha_w > 1$) as the mass measurement may be affected by accumulated dirt or excessive water absorption. In the case of brake dynamometer tests, more weight is given to the mass wear ($\alpha_w < 1$) as laboratory tests are performed under almost constant ambient conditions and in absence of road dust resuspension or water spill. It is worth noting that the results in Figure 7.8 also show a difference in the brake pad wear behaviour between the two sides of the brake disc, which may be attributed to the larger thermal shielding offered by the calliper on the piston side (refer to Figure 2.1a).

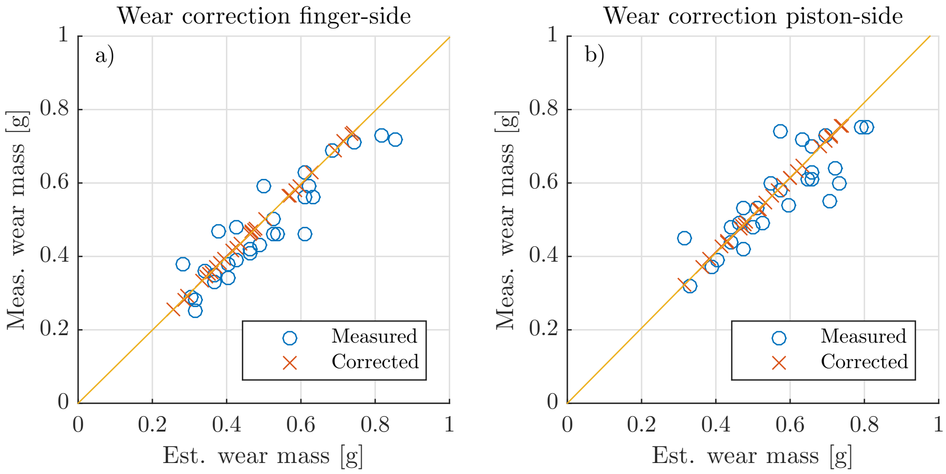

Figure 7.8: *Partial results of the RLS algorithm for fusion of linear wear and wear mass measurements from brake dynamometer test data. Each marker corresponds to a measurement performed at the end of a test block on the brake dynamometer. Graph a) reports the results for the outboard pad (finger side); b) refers to the inboard pad (piston side).*

The wear correction algorithm also implies that the correction performance improves with larger measurement dataset. Alternatively, including multiple driving cycles in the same driving block may have the same effect due to the higher wear values but to the detriment of experimental effort.

7.4 Model identification

In accordance with the scheme in Figure 7.2, the differential problem in Equation (7.5) must be brought to an integral linear form for the regressors and parameters identification. The initial γ functions candidates are initialised so as to contain linear and quadratic temperature dependent terms, as follows:

$$\begin{aligned} \gamma_1(\tau) &= \gamma_{10} + \gamma_{11}\,\tau + \gamma_{12}\,\tau^2, \\ \gamma_2(\tau) &= \gamma_{20} + \gamma_{21}\,\tau, \\ \gamma_3(\tau) &= \gamma_{30} + \gamma_{31}\,\tau. \end{aligned} \tag{7.12}$$

The identification of the newly defined γ parameters is led by a data driven approach. The identification data set is composed of eight driving blocks, each of which consisting of two or three identical real driving cycles executed multiple times on the brake dynamometer in accordance with the minimum detectable wear volume requirements. The driving cycle employed for identification tasks are the RDE Ilmenau, a pure urban cycle, a pure countryroad cycle and a pure motorway cycle performed by two different drivers under similar traffic conditions. By spanning different brake operating conditions as per Figure 7.3, this choice leads to eight linearly independent equations.

The brake pad specific wear rate can be defined as:

$$k_b = \underbrace{\left(\gamma_{10} + \gamma_{11}\,\tau + \gamma_{12}\,\tau^2\right)}_{\gamma_1} + \underbrace{\left(\gamma_{20} + \gamma_{21}\,\tau\right)}_{\gamma_2}\frac{\dot{\omega}}{\omega} + \underbrace{\left(\gamma_{30} + \gamma_{31}\,\tau\right)}_{\gamma_3} T_b\,\omega, \tag{7.13}$$

where, it is worth reminding, γ_1 represent the quasi-static temperature dependent wear coefficient; γ_2 accounts for the speed variation while braking; γ_3 account for temperature variations while braking. It is worth noting that under the hypothesis of pure quasi-static wear, γ_2 and γ_3 become null (see Equation (7.3)) and a temperature dependent Archard's law is derived:

$$k_{b,q.s.} = \left(\gamma_{10} + \gamma_{11}\,\tau + \gamma_{12}\,\tau^2\right). \tag{7.14}$$

Upon collection of wear data from brake dynamometer tests, the model parameters can be identified by solution of an optimisation problem led by criteria of error minimisation. Hereafter, Equation (7.13) is referred to as "Ilmenau extended", whilst its quasi-static variant in Equation (7.14) is referred to as "Ilmenau". Considering the generic $i-th$ driving block and corresponding wear measurement, Equation (7.13) can be rewritten in the integral form:

$$\begin{aligned} m_{b,i} = \sum_{j=1}^{N_{b,i}} \int_{t_{0,ij}}^{t_{0,ij}+\Delta t_{b,ij}} \Big\{ \Big[\left(\gamma_{10} + \gamma_{11}\,\tau + \gamma_{12}\,\tau^2\right) + \left(\gamma_{30} + \gamma_{31}\,\tau\right) T_b\,\omega\Big]\, T_b\,\omega \\ + \left(\gamma_{20} + \gamma_{21}\,\tau\right) T_b\,\dot{\omega}\Big\}\, dt, \end{aligned} \tag{7.15}$$

where, the index j ranges among the braking manoeuvres belonging to the $i-th$ driving block. In accordance with the experimental methodology overview in Figure 7.2, the problem can be rearranged in the linear form where the regressors represent the combinations of input variables. The previous is rewritten as:

$$\begin{aligned} m_{b,i} = \gamma_{10} \sum_{j=1}^{N_{b,i}} \left(\underbrace{\int_{t_{0,ij}}^{t_{0,ij}+\Delta t_{b,ij}} T_b\, \omega \, dt}_{X_{10,i}} \right) + \gamma_{11} \sum_{j=1}^{N_{b,i}} \left(\underbrace{\int_{t_{0,ij}}^{t_{0,ij}+\Delta t_{b,ij}} T_b\, \omega \, \tau \, dt}_{X_{11,i}} \right) \\ +\gamma_{12} \sum_{j=1}^{N_{b,i}} \left(\underbrace{\int_{t_{0,ij}}^{t_{0,ij}+\Delta t_{b,ij}} T_b\, \omega \, \tau^2 \, dt}_{X_{12,i}} \right) + \gamma_{20} \sum_{j=1}^{N_{b,i}} \left(\underbrace{\int_{t_{0,ij}}^{t_{0,ij}+\Delta t_{b,ij}} T_b\, \dot{\omega} \, dt}_{X_{20,i}} \right) \\ +\gamma_{21} \sum_{j=1}^{N_{b,i}} \left(\underbrace{\int_{t_{0,ij}}^{t_{0,ij}+\Delta t_{b,ij}} T_b\, \dot{\omega} \, \tau \, dt}_{X_{21,i}} \right) + \gamma_{30} \sum_{j=1}^{N_{b,i}} \left(\underbrace{\int_{t_{0,ij}}^{t_{0,ij}+\Delta t_{b,ij}} T_b^2\, \omega^2 \, dt}_{X_{30,i}} \right) \\ +\gamma_{31} \sum_{j=1}^{N_{b,i}} \left(\underbrace{\int_{t_{0,ij}}^{t_{0,ij}+\Delta t_{b,ij}} T_b^2\, \omega^2 \, \tau \, dt}_{X_{31,i}} \right). \end{aligned} \tag{7.16}$$

The terms in round brackets are the model regressors and are compute upon the $i-th$ driving block. The problem can be reformulated for all $i = [1, N]$ blocks as:

$$\begin{bmatrix} m_{b,1} \\ m_{b,2} \\ \cdots \\ m_{b,i} \\ \cdots \\ m_{b,N} \end{bmatrix} = \begin{bmatrix} X_{10,1} & X_{11,1} & X_{12,1} & X_{20,1} & X_{21,1} & X_{30,1} & X_{31,1} \\ X_{10,2} & X_{11,2} & X_{12,2} & X_{20,2} & X_{21,2} & X_{30,2} & X_{31,2} \\ \cdots & \cdots & \cdots & \cdots & \cdots & \cdots & \cdots \\ X_{10,i} & X_{11,i} & X_{12,i} & X_{20,i} & X_{21,i} & X_{30,i} & X_{31,i} \\ \cdots & \cdots & \cdots & \cdots & \cdots & \cdots & \cdots \\ X_{10,N} & X_{11,N} & X_{12,N} & X_{20,N} & X_{21,N} & X_{30,N} & X_{31,N} \end{bmatrix} \begin{bmatrix} \gamma_{10} \\ \gamma_{11} \\ \gamma_{12} \\ \gamma_{20} \\ \gamma_{21} \\ \gamma_{30} \\ \gamma_{31} \end{bmatrix}, \tag{7.17}$$

which can be conveniently rewritten as:

$$\mathbf{m}_b = \mathbf{X}\, \mathbf{\Gamma}. \tag{7.18}$$

Equation (7.18) can be solved with respect to the γ vector by means of the least square algorithm. Necessary condition for the algorithm to work is that the regressors matrix rank shall be greater or equal to the model parameters cardinality. Moreover, model regressors are scaled to normal values to facilitate the elimination of unimportant terms during the identification procedure. Under these conditions, the solution to the unconstrained problem is given by:

$$\mathbf{\Gamma} = \left(\mathbf{X}^T \mathbf{X} \right)^{-1} \mathbf{X}^T \mathbf{m}_b. \tag{7.19}$$

The data driven identification leads to the parametrisation in Table 7.1 where the quasi static specific wear is of quadratic type against the temperature. The best fitting of brake dynamometer data is achieved with a temperature dependent quasi static wear coefficient (Ilmenau model) and constant speed and temperature dependent parameters (Ilmenau extended).

Table 7.1: Parametrisation of the wear models.

	Ilmenau	Ilmenau ext.	Unit
γ_{10}	0.1016	0.1016	g/MJ
γ_{11}	0	0	$g/MJ/K$
γ_{12}	$0.3984\,10^{-6}$	$0.3984\,10^{-6}$	$g/MJ/K^2$
γ_{20}	0	0.4887	g/MW
γ_{21}	0	0	$g/MW/K$
γ_{30}	0	0	$g\,s/MJ^2$
γ_{31}	0	$0.66\,10^{-2}$	$g\,s/(MJ^2\,K)$

In accordance with the collected brake dynamometer data, the specific wear rate has the shape reported in Figure 7.9. The extended wear model in Equation (7.13) (Ilmenau extended) features a quadratic dependence against the disc temperature and a non-linear dependence against the speed. The extended wear model suggests that due to temperature increase during a braking occurrence, in accordance with the dynamics of Equation (7.4), the expected wear rate can be up to two times larger than the quasi-static variant under the same operating conditions. The extended wear model also shows that higher braking intensities lead to increased wear formation. All these mechanisms cannot be captured by the quasi-static model.

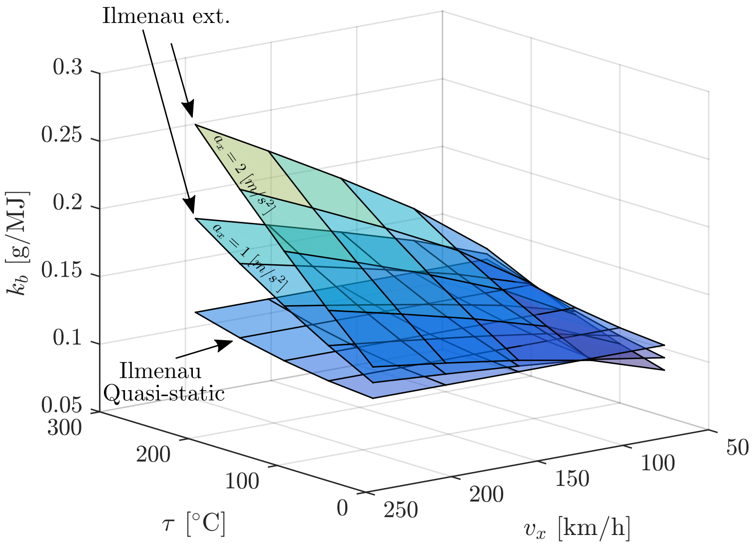

Figure 7.9: *Specific wear rate dependence versus braking speed and disc temperature in accordance with the extended wear model (Ilmenau extended) and its quasi-static variant (Ilmenau).*

Figure 7.10 reports the model sensitivity against artificially injected errors in the

BLCF and disc temperature estimates. The proposed models feature a quasi-linear dependence against BLCF estimation errors. In the case of Ilmenau extended, the sensitivity to BLCF estimation errors increases at higher operating brake temperature values (Figure 7.10a). Moreover, a wrong brake disc temperature estimate has a negligible effect on the quasi-static wear model and a temperature dependent impact on the extended wear model (Figure 7.10b). This suggests that the quasi-static model variant might be preferred to its extended version in case a reliable temperature estimate cannot be provided. The results also imply that the extended wear model shall be selected whenever the influence of large temperature variations on the wear rate are to be taken into account.

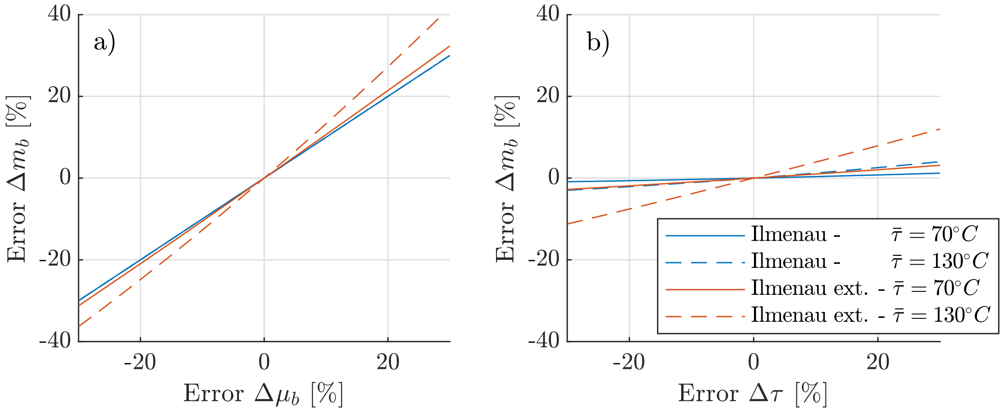

Figure 7.10: *Wear model sensitivity against artificial errors injected in the BLCF estimate, graph a), and in the estimated disc temperature, graph b). The results stem from a RDE-compliant Ilmenau cycle.*

7.5 Data reproducibility

The methodology schematically depicted in Figure 7.2 includes the analysis of the real driving cycle and associated wear volume reproducibility on the brake dynamometer. This analysis is mandatory to assess the feasibility of the proposed development method and allows for the definition of the prognosis function estimation potentials. Among other brake dynamometer control strategies, the deceleration based control between speed levels showed superior performance both in terms of wear measurements reproducibility and cycle to cycle repeatability. However, the brake dynamometer does not allow for simulation of the driving resistant forces such as air drag and tyre rolling resistance. It is therefore worth quantifying the impact that this might have on the wear measurements. The dissipated energy associated with a generic $j-th$ braking manoeuvre can be computed in accordance with Equations (7.20) and (7.21) for the instrumented vehicle and brake dynamometer, respectively:

$$\begin{aligned} E_{b,j}^{(Road)} &= \int_{t_{0,j}}^{t_{0,j}+\Delta t_{b,j}^{(Road)}} T_{b,f}^{(Road)}\, \omega_f\, dt \\ &= \frac{1}{2}\, J_f\, \left(\omega_{f,in}^2 - \omega_{f,end}^2\right) + \\ &- \int_{t_{0,j}}^{t_{0,j}+\Delta t_{b,j}^{(Road)}} \left(F_{L,drag,f}\, r_{\omega,f} + R_{L,f}\right) \omega_f\, dt, \end{aligned} \tag{7.20}$$

$$\begin{aligned} E_{b,j}^{(Dyno)} &= \int_{t_{0,j}}^{t_{0,j}+\Delta t_{b,j}^{(Dyno)}} T_{b,f}^{(Dyno)}\, \omega_f\, dt \\ &= \frac{1}{2}\, J_f\, \left(\omega_{f,in}^2 - \omega_{f,end}^2\right) - \int_{t_{0,j}}^{t_{0,j}+\Delta t_{b,j}^{(Dyno)}} T_R\, \omega_f\, dt, \end{aligned} \tag{7.21}$$

where, $E_{b,j}^{(Road)}$ and $E_{b,j}^{(Dyno)}$ represent the dissipated brake energy of the $j-th$ manoeuvre on the experimental vehicle and brake dynamometer, respectively; Δt^{Road} and Δt^{Dyno} is the braking manoeuvre duration from road and dynamometer test, respectively; $T_{b,f}^{(Road)}$ represents the estimated brake torque from on-road tests; $T_{b,f}^{(Dyno)}$ is the controlled dynamometer brake torque that ensures reproducible deceleration manoeuvres as in Figure 7.6; J_f is the equivalent vehicle inertia on a front wheel and T_R represents the sum of resistant torques on the brake dynamometer. By subtracting Equation (7.20) from Equation (7.21) and dividing by Equation (7.21), the reproducibility error ΔE_b can be represented as a function of the initial braking speed and deceleration intensity, as per Figure 7.11.

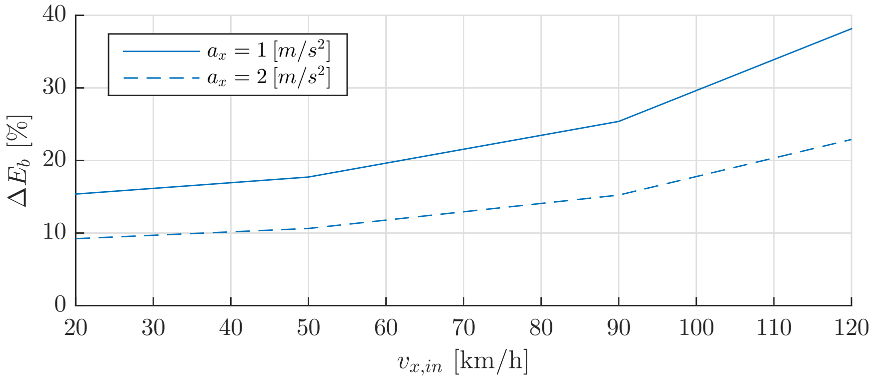

Figure 7.11: *Energy reproducibility error due to neglected driving resistant forces.*

Figure 7.11 shows that higher energy reproducibility error occurs under tests involving high driving speed values and gentle braking applications. This result allows qualitatively evaluating the expected reproducibility error with respect to RDE-compliant tests. In accordance with the statistical analysis of Chapter 1, more than 80% of all braking applications are characterised by a deceleration lower than 2 m/s^2. The energy reproducibility error on the brake dynamometer and the different temperature dynamics account for different wear behaviours between on-road tests and dynamometer tests, as reported in Figure 7.12.

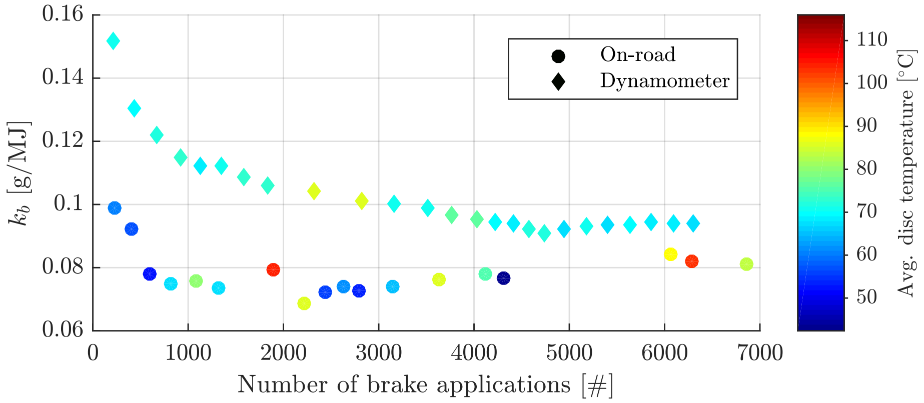

Figure 7.12: *Specific wear rate reproducibility on the brake dynamometer. The color represents the specific wear dependence against the average disc temperature recorded during the driving block.*

After an initial transient, the linings stabilise around a repeatable wear rate value. Particularly, the value recorded under dynamometer tests results 20% higher than the corresponding on-road value as anticipated earlier. In accordance with Figure 7.6, the increased dynamometer brake torque necessary to guarantee the same deceleration profile recorded on-road in presence of resistant forces is responsible for the increased wear rate.

7.6 Results

In accordance with the flow chart of Figure 7.2, on-road wear measurements constitute the validation data set. The brake wear models are identified and parametrised against the data collected on the brake dynamometer. The model calibration shall account for the offset in the specific wear rate between dynamometer and on-road tests. In this regard, only one wear measurement point corresponding to a RDE-compliant Ilmenau cycle is used to proportionally scale the models' coefficients. It is worth noting that on-road tests are conducted on public roads under varying traffic and environmental conditions. In accordance with the schematic of Figure 7.1, the BLCF observer is switched off upon reaching low deceleration values. The deactivation threshold complies with the results of Chapter 4, namely 1.3 m/s^2 for the front axle. Below this threshold, the previous BLCF estimate is used to compute the applied brake torque at the wheel. The estimation chain of Figure 7.1 also includes the brake disc lumped capacitance model, addressed in Chapter 3. This latter is herein parametrised against data collected on the experimental sedan to capture the brake disc temperature dynamics at varying driving speed. Technical specifications of the employed experimental vehicle are reported in Appendix D.

7.6.1 Brake temperature estimation

In the framework of this analysis, the tests performed under real driving conditions involve wide temperature variations under different environmental conditions. It is therefore important to guarantee that the lumped capacitance model parametrisation ensures satisfactory estimation performance under the whole temperature range and in presence of varying environmental conditions. Figure 7.13 graphically reports the lumped capacitance model effectiveness for a front and rear brake of the sedan in Appendix D with respect to a driving block involving a RDE-compliant Ilmenau cycle and a pure motorway section.

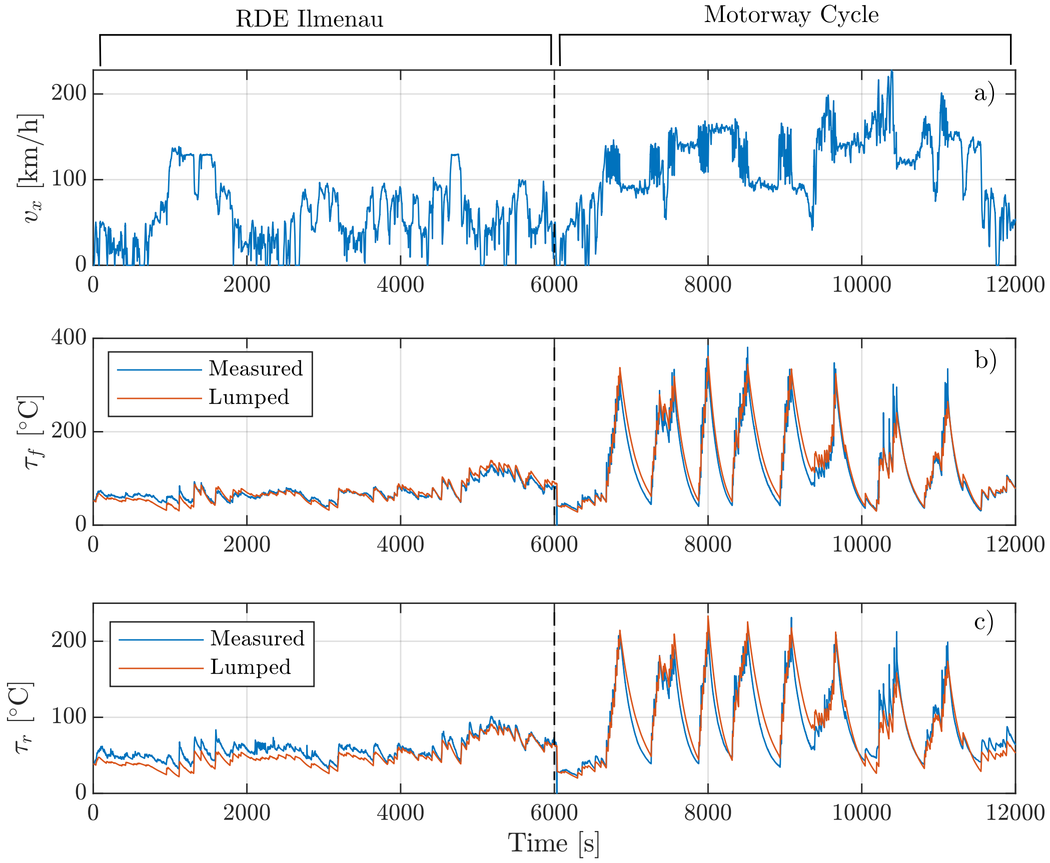

Figure 7.13: *Validation of the lumped brake temperature model with respect to a RDE compliant Ilmenau and a motorway cycle featuring repeated braking applications. Graph a) reports the vehicle speed, graphs b) and c) report the average front and rear disc temperature, respectively.*

The results show that the lumped capacitance model maintains good estimation performance along the whole driving cycle and for the whole range of temperatures. The model is not affected by bias integration error being able to correctly track the measured temperature until the very end of the driving block. Additional tests performed under rainy conditions at high driving speed suggest that a new lumped model parametrisation reveals necessary to account for the improved disc cooling due to rain (Figure 7.14).

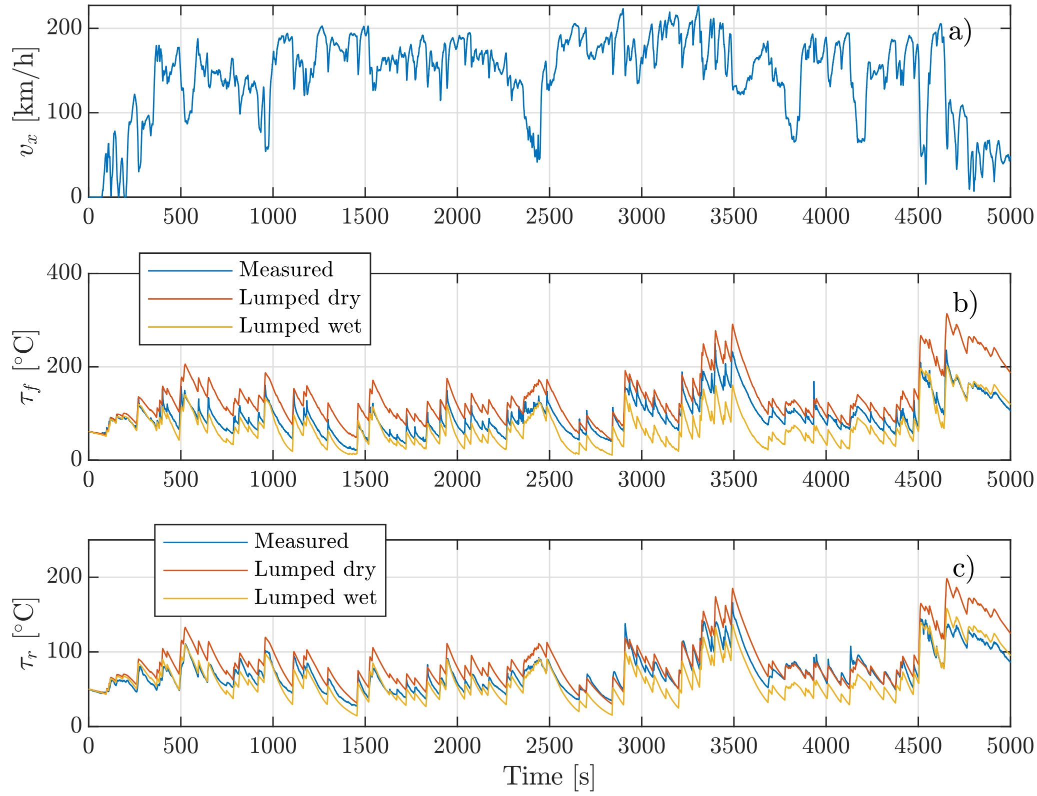

Figure 7.14: *Validation of the lumped brake temperature model with respect to a motorway cycle in presence of rain. Graph a) reports the vehicle speed, graphs b) and c) report the average front and rear disc temperature, respectively.*

Figure 7.15 reports two parametrisation for the brake disc cooling coefficient as a function of the driving speed under dry and wet ambient conditions, respectively. The resulting parametrisations confirm that at higher speed values the brake disc cooling due to rain is enhanced. The performance of the newly parametrised lumped capacitance model is reported in Figure 7.14. The temperature estimation scheme operates as to switch from a parametrisation to the other when rain is detected. This can be easily achieved on the vehicle by means of information provided by commonly used rain sensors. The results demonstrate that the wet parametrisation features enhanced tracking performance, which results in a drastic estimation error abatement.

Despite the large brake disc conductivity, thermographic analysis at Technische Universität Ilmenau demonstrates that the local disc temperature during a braking manoeuvre varies markedly across the radial disc direction [102]. Therefore, the temperature sensed by the sliding thermocouple represents a local measurement that might lay far from the actual temperature at the pad-disc interface. For this reason, provided that the disc brake satisfies the requirements on the Biot number (refer to Chapter 3), the

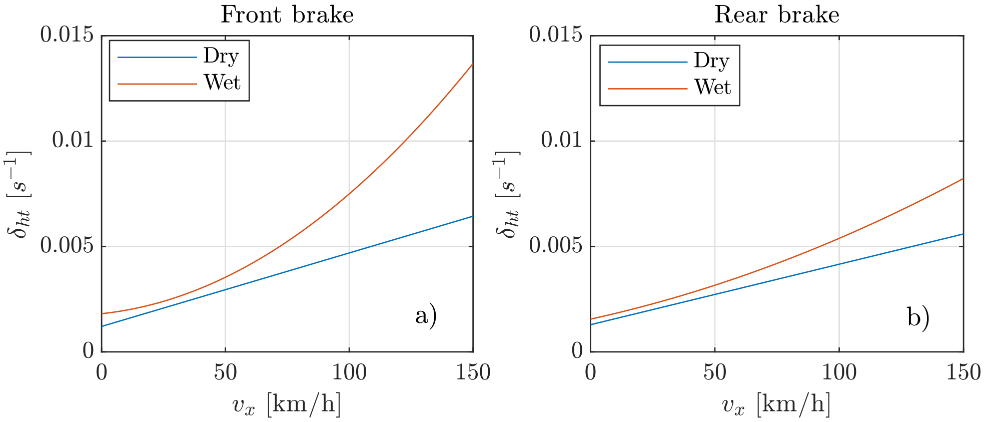

Figure 7.15: *Parametrisation of the cooling coefficient in case of dry and wet conditions, for front a) and rear brakes b), respectively.*

lumped temperature model is to be deemed as an indicator of the pad-disc contact temperature, whose parametrisation is directly dependent on the employed temperature sensing technique.

7.6.2 Brake wear prediction

The brake dynamometer wear measurements lead to the model parametrisation provided in Table 7.1. In this section, the models prediction capability with respect to wear data resulting from approximately 30.000 km under real driving conditions is validated. The employed brake pads feature a friction material thickness of 12 mm in new conditions and a residual thickness of 3 mm upon replacement. It is worth remarking that the residual pad thickness refers to the linings thickness without considering the backplate. The results in Figure 7.16 show that the extended wear model of Equation (7.13) exhibits improved fitting performance when compared to its quasi-static variant in Equation (7.14). This translates into correlation coefficients of $R^2 = 0.988$ for Ilmenau and $R^2 = 0.993$ for Ilmenau extended.

The slope between consecutive measurement points reflects the average wear rate of a driving block. Different slopes are due to different driving conditions in terms of average braking speed, applied brake pressure and brake temperature. Although both models converge to a similar solution, the extended model shows better fitting performance during the early stages of wear formation. As per Figure 7.10, the higher temperature sensitivity of the extended Ilmenau model with respect to its quasi-static variant motivates its superior wear tracking capabilities in presence of larger temperature variations, which results in a higher correlation coefficient. The results demonstrate that the model parametrised against brake dynamometer data predicts on-road brake wear formation within 10% accuracy after 30.000 km under real driving conditions.

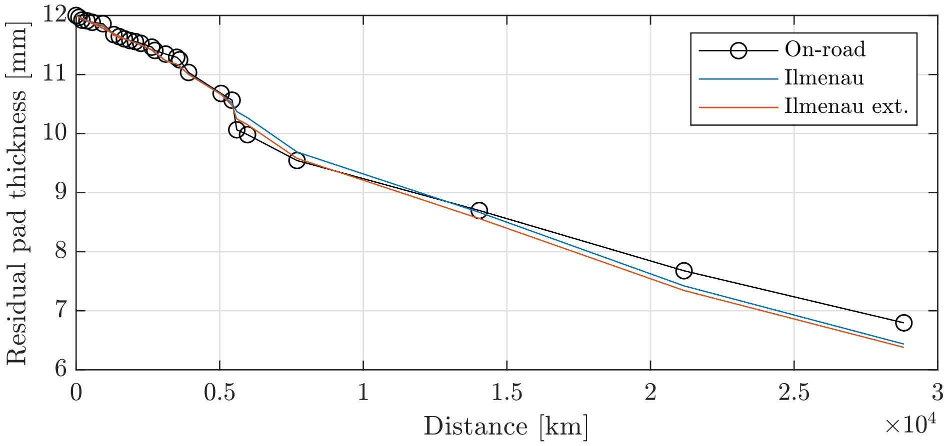

Figure 7.16: *Models prediction capability with respect to on-road linear wear data of a front brake pad.*

7.7 Chapter summary

A new in its kind design of experiment allows extracting meaningful information from on-road brake wear measurements to fit a novel wear model. To ensure good measurement repeatability, real driving cycles are reproduced on the brake dynamometer. The developed deceleration based controller between speed levels ensures satisfactory energy reproducibility. However, the driving resistance forces such as air drag and tyre rolling forces are not emulated under laboratory tests and explain the offset between on-road and brake dynamometer wear measurements. Thereafter, data collected on the brake dynamometer drive the formulation of a brake wear model. The identification data set is composed of eight driving blocks, each of which consisting of two or three identical real driving cycles executed multiple times on the brake dynamometer, in accordance with the minimum detectable wear volume requirements. The results demonstrate that the models parametrised against brake dynamometer experimental data predict on-road brake wear formation within 10% accuracy after 30.000 km under real driving conditions. Based on the performed experiments, the prediction errors of Ilmenau extended and its quasi-static variant are expected to lay below 15% by the end of the brake pad service life.

Chapter 8

A novel estimator of brake particle emissions

8.1 Introduction

The growth of electric propulsion systems motivates the automotive industry to transfer the focus from exhaust to non-exhaust emissions, with special attention to brake-related emissions. The factors influencing the particulate formation are still not fully understood but from recent experimental analysis carried on advanced laboratory equipment at Technische Universität Ilmenau it is possible to state that: (i) particulate number, particulate size distribution and the chemical compositions of the emitted brake dust particulate are mainly dependent on the system temperature and the frictional power [12]; (ii) the particle number per brake event increases with increasing sliding speed [103]; (iii) the brake pressure value does not directly impact the particle emission behaviour [104]; (iv) above a material-dependent critical temperature threshold between $170 - 200\,°C$, the formation of ultra fine particles is favoured [103]; (v) the emission behaviour in ECE linings with cast iron discs highly depends on thermal and mechanical treatments and duration of the preconditioning [105].

In this chapter, the estimation of brake-related particulate emissions in real driving conditions is addressed. This is done in the wake of the EU member States amendment adopted on May 3rd, 2018, to Directive 2007/46/EC, Commission Regulation (EC) No 692/2008 and Commission Regulation (EU) 2017/1151, which introduced the real driving emissions (RDE) tests as a mandatory part of the type-approval procedure for new passenger cars and light-commercial vehicles in EU. Due to the high non-linearity and stochasticity of the problem at hands, a novel meta-modelling approach based on artificial neural networks (ANN) is adopted for the estimation of particle emissions. Particularly, two network configurations are tested:

- static ANN, considers as input the average conditions during each braking;

- dynamic ANN, also accounts for the input variables transient behaviour.

The functionality of the proposed ANN is demonstrated with respect to emissions data collected from a light commercial vehicle (LCV) equipped with cast-iron brake discs and copper-free ECE brake linings. Brake related particulate emission are acquired along the RDE-compliant Ilmenau cycle by means of a portable emissions measurement system (PEMS). As discussed in Chapter 1, the reference cycle takes place in the vicinity of Ilmenau and includes 87 km of mixed urban, rural and motorway sections. The sampling system is based on the mobile brake enclosure developed at Technische Universität Ilmenau, whose effectiveness is demonstrated in [12]. More than 800 braking manoeuvres collected under real driving conditions are used to train the ANN. The variability among drivers and driving conditions is also accounted in this study.

8.2 Experimental methodology

The measurement of emitted brake dust particulate under real driving conditions is complex due to external, continuously changing factors (e.g. flow conditions, driving dynamics, fine dust particulate from other sources). At present, there is still no standardised testing protocol and/or measurement method. Common procedures for the characterisation of brake emissions factors generally draw upon receptor modelling that associates brake particulate to a range of sources that are easy to measure [106, 107]. Nevertheless, studies conducted in the past few years involve direct measurement of brake particles under controlled laboratory conditions, which require the use of more sophisticated sensors [108, 17]. In [109], the authors argue that the test reproducibility represents a critical factor ascribable to the employed test procedure, pad soak, environmental conditions, calliper residual torque and temperature control. In [17], it is instead demonstrated that the cycle-to-cycle repeatability is affected by the progressive wear of the brake pad-disc couple, whereby the variability tends to become lower for successive manoeuvres. The authors also concluded that the repeatability of the brake particulate measurements at disc temperature above $200°C$ is questionable owing to the formation of unstable friction layer. In [110], the authors conduct measurements of brake-related particulate emissions produced by a LCV on a chassis dynamometer. Although the experimental arrangement is very similar to a RDE-type test, the performed braking manoeuvres are not representative of real driving conditions and the particulate sampling system is of open type, which does not ensure good measurement repeatability [12].

In this work, on-road tests carried out on a LCV equipped with PEMS allow investigating driver's influence on brake-related emissions under different driving conditions. The LCV specifications and measurement setup are reported in Appendix D. The drive cycles reproducibility under RDE conditions is discussed in [12] where a good correlation between RDE and laboratory results is quantitatively demonstrated. A training data set is back-propagated for the identification of static and dynamic networks architectures. ANN represent a flexible modelling framework, which enables the continuous training of the model parameters when new data are available. ANN can predict with satisfactory accuracy the effect of braking conditions on tribological performance, provided that a demanding experimental campaign is a justified mean. It is worth remarking that although brake-related emissions may also occur during vehicle accelerations [110], they are not accounted in the present study.

8.3 Measurement equipment

The LCV equipped with PEMS allows for measurements of brake-related particulate number concentration (PNC). A schematic of the test setup is reported in Figure 8.1. The particulate emitted by the front-right brake system is evacuated by means of the closed CVS-sampling system engineered and developed at Technische Universität Ilmenau [12]. The vacuum created by a blower leads the emitted brake particulate through the measurement tunnel to the external environment. Samples are extracted from the measurement tunnel using an isokinetic probe compliant to EN 13284-1. At the outlet of the sample probe, the PEMS-PN MAHA-AIP measures particulate number concentrations (PNC) in the range 23 nm to 2.5 μm. Although designed for tailpipe emissions, the measurement device is retrofitted to assess brake-related particle emissions. The measurement principle is based on particulate condensation counting (CPC) [12]. The brakes are equipped with sliding thermocouples and pressure sensors. The vehicle is also provided with the RaceLogic VBoX to log relevant kinematics quantities such as vehicle speed and acceleration. The developed setup allows analysing the influence of driver, traffic, driving conditions and environment on the emissions level. Relevant vehicle and brake state variables such as vehicle speed, vehicle acceleration, brake temperature and brake pressure are sampled at 10 Hz, whilst PEMS samples PNC at 1 Hz. The measurement system provides the particulate number concentration, expressed as number of particulate per cubic centimetre, in correspondence of the probed point. Knowing the volumetric flow rate of the sampling system, and supposing the PNC uniform across the tunnel section in the sampling point, the absolute number of emitted particulate PN during a braking manoeuvre can be computed. For a matter of convenience, a logarithmic transformation is adopted for each $j-th$ brake application to conduct a sensitivity analysis across the data. This leads to an adimensional quantity, herein referred to as emission factor (EF).

$$EF_j \ [/] = \log \left[\int_{t_{0,j}}^{t_{0,j}+\Delta t_{b,j}} PN(t) \ dt \right]. \tag{8.1}$$

Table 8.1 reports the most relevant features for the RDE-compliant Ilmenau cycles considered in the present study. The second and third column of the table report the

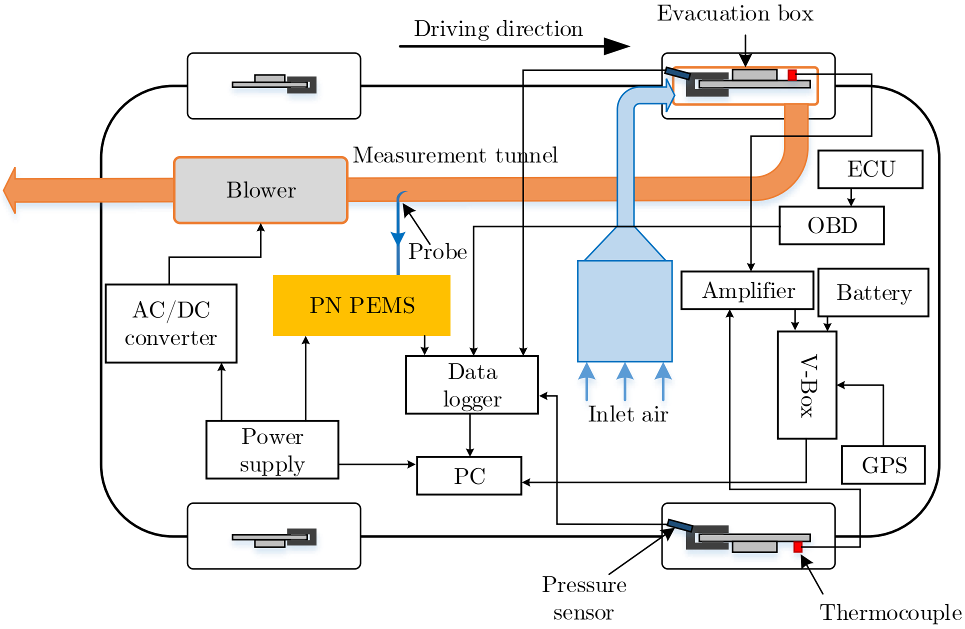

Figure 8.1: *Depiction of the LCV used for RDE-compliant brake particulate emission tests. The front-right wheel is equipped with evacuation box (in orange). The particulate is evacuated and sampled by the probe. PN PEMS counts the particulate and determines their concentration for a specific evacuated air volume. The air filter ensures that fresh air accesses the evacuation system.*

deceleration mean and standard deviation, respectively; the fourth column reports the total number of braking events for the specific trip; the fifth and sixth column report the total fiction energy and the emitted particulate per driven km with respect to the front-right brake. It is worth noting that the trip-to-trip variability depends on many factors ranging from the driving style to the traffic conditions. Overall, the performed cycles account for more than 800 braking events. A sensitivity analysis allows for the identification of the relative importance of the control variables with respect to the number of emitted particles. The collected data are organised so that Trip 1 to Trip 7 are used to train and validate the proposed meta-models, whilst Trip 8 is used to test their prediction performance under RDE-compliant driving conditions. For the sake of clarity, the particle number concentration measured by PEMS in the partial volume flow is referred to as PNC, whilst the overall emitted brake particle number per unit time or per brake application is referred to as PN. The overall emitted brake particle number per driven km is instead referred to as ΣPN.

Table 8.1: Dataset used for the model identification (green) and testing (blue). Brake energy and ΣPN refer to the front-right corner.

Trip #	$\bar{a}_x$ $[m/s^2]$	$var(a_x)$ $[m/s^2]$	N. brake applications	E_b $[MJ]$	ΣPN $[\#/km]$
Trip 1	1.18	0.35	78	2.13	$2.67 \cdot 10^9$
Trip 2	0.91	0.42	112	5.63	$2.04 \cdot 10^9$
Trip 3	0.92	0.41	110	5.59	$1.57 \cdot 10^9$
Trip 4	0.97	0.43	82	2.80	$0.45 \cdot 10^9$
Trip 5	1.07	0.49	121	4.75	$3.17 \cdot 10^9$
Trip 6	0.97	0.44	84	2.75	$3.32 \cdot 10^9$
Trip 7	0.99	0.39	86	3.49	$3.00 \cdot 10^9$
Trip 8	1.21	0.44	102	4.41	$2.77 \cdot 10^9$

8.4 Data pre-processing

As demonstrated in [12], the used RDE measurement equipment features a good cycle-to-cycle repeatability and satisfactory reproducibility when compared to laboratory test data. However, given the installation position of the evacuation box, PEMS is more sensitive to background particulate concentration (BGC). Therefore, before proceeding with the feature extraction of the driving cycles, BGC is estimated from PEMS measurements by considering the lowest emission level when cruising. BGC is thus mapped against the vehicle speed, leading to the results of Figure 8.2. The reported particle concentration numbers refer to the PEMS measured value in the partial flow.

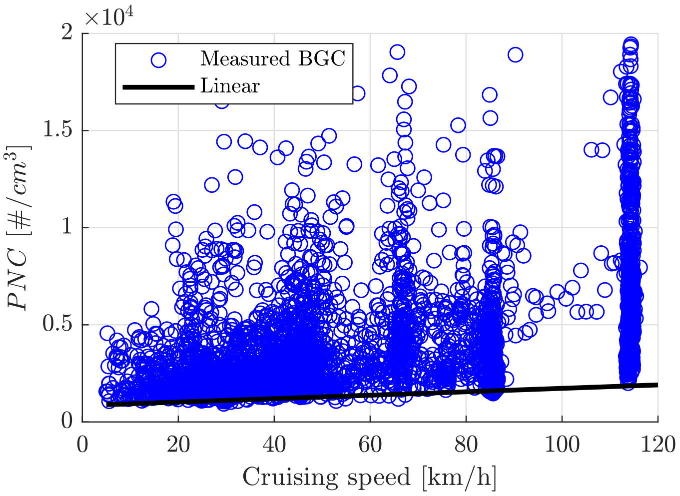

Figure 8.2: *Background concentration when cruising and its linear mapping against the vehicle speed. PNC refers to the particle concentration number in the partial volume flow.*

Afterwards, the raw data are reduced in dimensionality by extracting meaningful information during braking manoeuvres. Figure 8.3 reports an example of braking features extraction from one of the recorded RDE cycle. For a matter of clarity, the variables of interest are underlined in orange during braking occurrence. The numbering refers to $j-th$ braking manoeuvre and the black markers refer to the corresponding average quantity. The feature extraction is limited to the deceleration manoeuvres, whilst brake-related emissions might also occur during acceleration manoeuvres due to the release of deposited particulate [110].

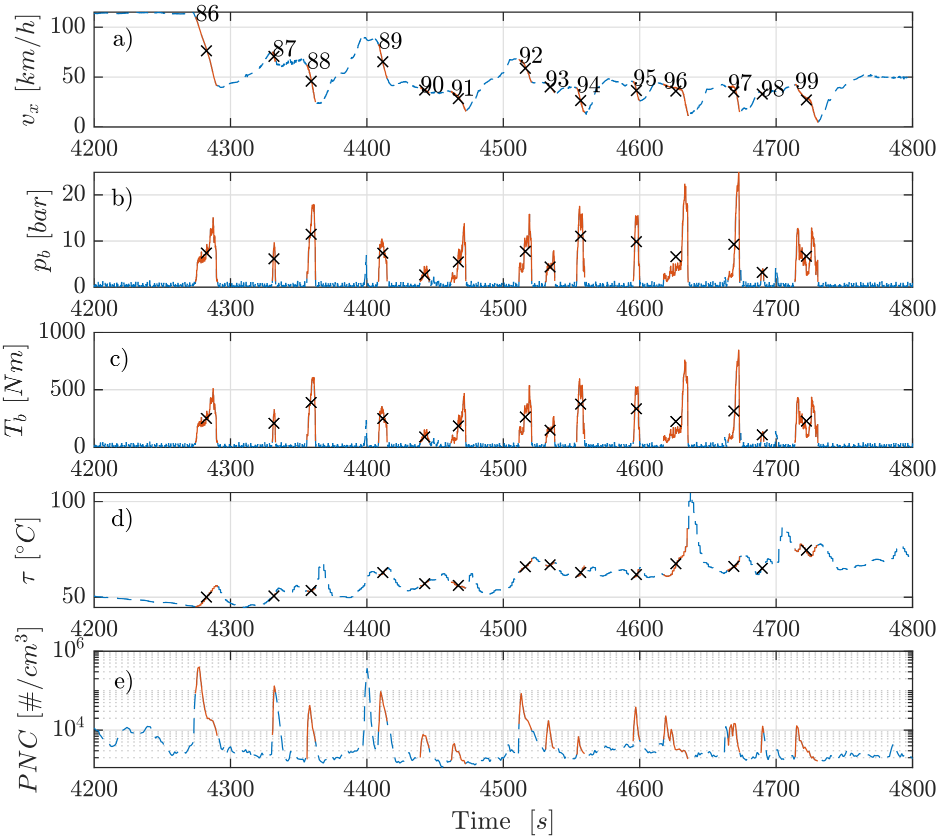

Figure 8.3: *Example of data feature extraction from one trip. Braking manoeuvres are marked in orange; the black cross symbols represent average quantities. Graph a) reports the vehicle speed; b) brake pressure; c) estimated brake torque; d) disc temperature; e) PNC from PEMS partial flow. Data refer to the front-right corner.*

A scheme of the data pre-processing procedure is reported in Figure 8.4. In the case of static ANN, the input variables are condensed into stationary quantities, characteristics for the specific brake application. Hence, the average brake torque, the initial braking speed, the final braking speed, the average disc temperature and the brake duration are computed for each brake application. In the case of dynamic ANN, the braking manoeuvres are allocated to an array of fixed length. This step is referred to as sequencing. The length of this array has been chosen based on the longest braking manoeuvre registered along the RDE cycles. All other manoeuvres, being characterised by a shorter duration, are scaled accordingly. The duration of a $j-th$ braking is also provided as input to the network.

The training is performed upon scaling input and output down to the same range. This step is necessary to ensure even importance among braking manoeuvres. Thereafter, the resampling takes place based on the assumption that all braking manoeuvres are uniformly distributed. This step is fundamental to prevent the model from over-fitting braking manoeuvres with higher occurrence rates.

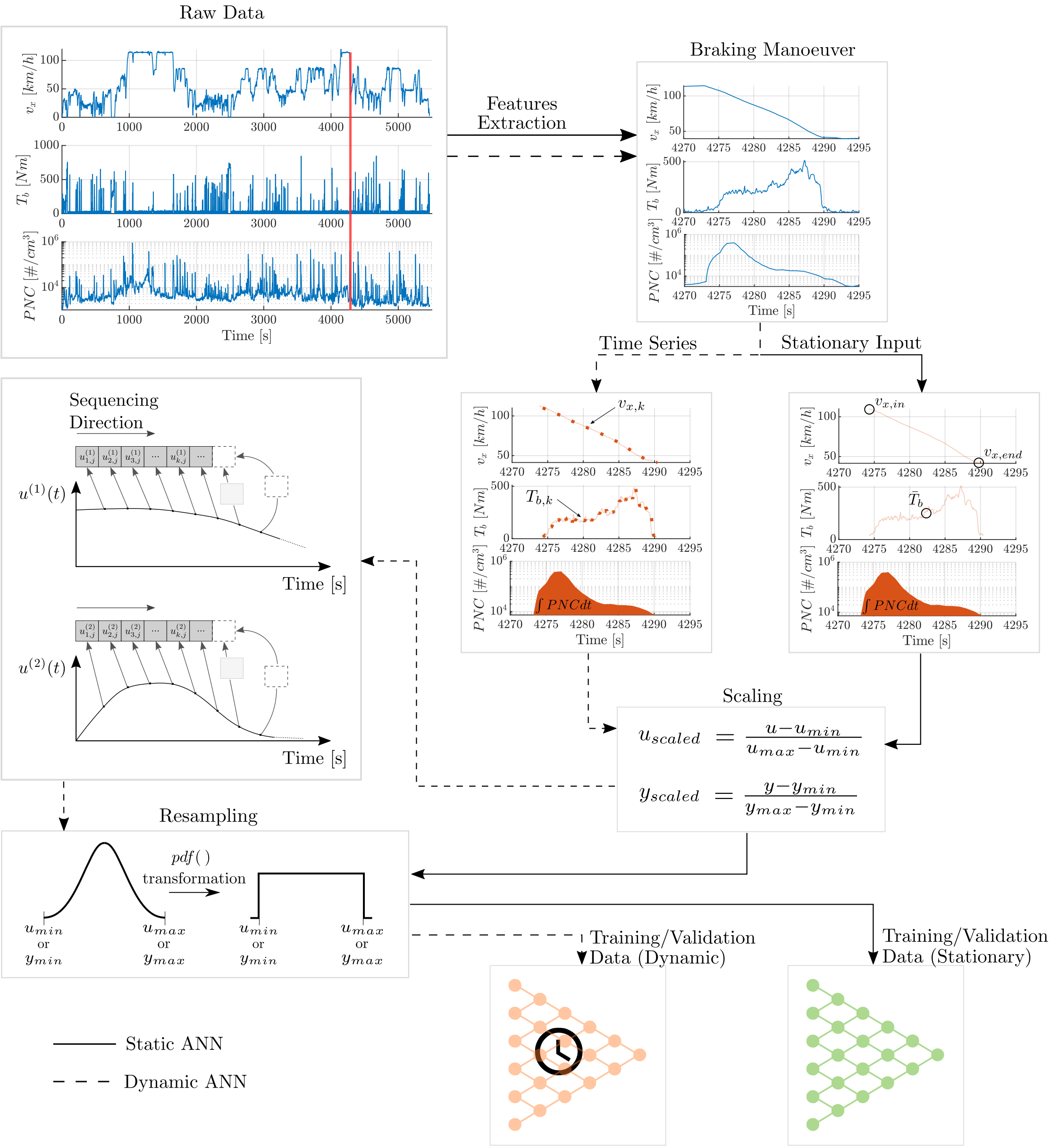

Figure 8.4: *Flow diagram of data preprocessing to train and validate the proposed ANN.*

8.5 Data analysis

Previous literature instances propose look-up-tables to capture the characteristic emission behaviour of a brake system [111]. Particularly, in [38] the author shows that PNC correlates well with disc sliding velocity and applied normal pressure. By adopting the same representation criterion, a two-sigma benchmark can be performed across the collected experimental data leading to the results in Figure 8.5. It is worth noting that a two-sigma analysis requires the PNC to be normally distributed.

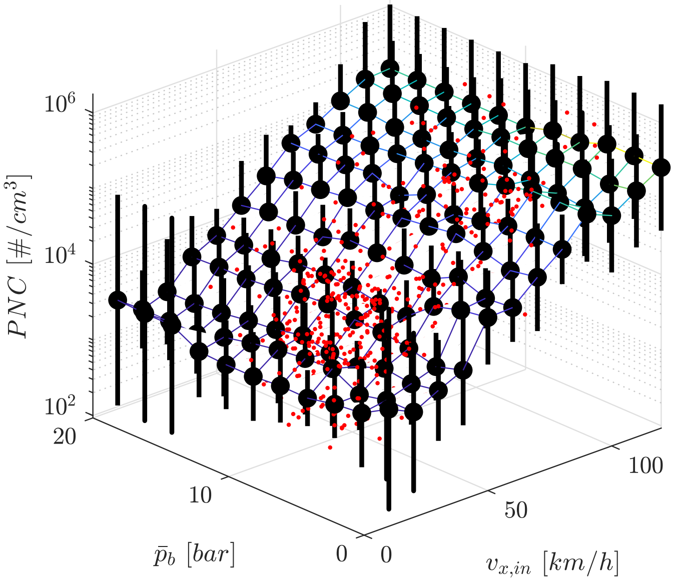

Figure 8.5: *Two-sigma benchmark of PEMS measured PNC in the partial flow (red dots) . The interpolating surface identifies the expected emission level for a specific braking condition, whilst the black bars identify two-sigma values (95%).*

The results confirm that initial braking speed and average brake pressure well correlate with PNC only in the area of more severe braking manoeuvres. This suggests that a simple map-based approach, as proposed in [38], might not perform accurately in the case of more gentle braking manoeuvres, which account for more than 80% of the RDE-compliant driving cycle (see Chapter 1). This result also suggests that other input variables must be considered to reduce the prediction error and increase the variance accounted for.

A sensitivity analysis conducted across the experimental data shows that initial speed ($v_{x,in}$) and brake duration (Δt_b) strongly correlated with EF (Figure 8.6). Expectedly, the friction energy (E_b) also exhibits a remarked correlation being it proportional to the product of the applied brake torque (T_b), the disc rotational speed and braking duration. The Spearman coefficients are reported in Figure 8.6 where data are equally scaled for ease of representation. Although brake torque and disc temperature show a weak Spearman correlation with EF, their combined effect might still play a role in determining its value and are therefore considered in the ANN regression. To this effect, compared with conventional map-based approaches, ANN represent a promising solution as they are designed to handle multi-input single-output problems. Depending on the type of ANN, namely static or dynamic, the input can be provided in a stationary or dynamic fashion, as later reported.

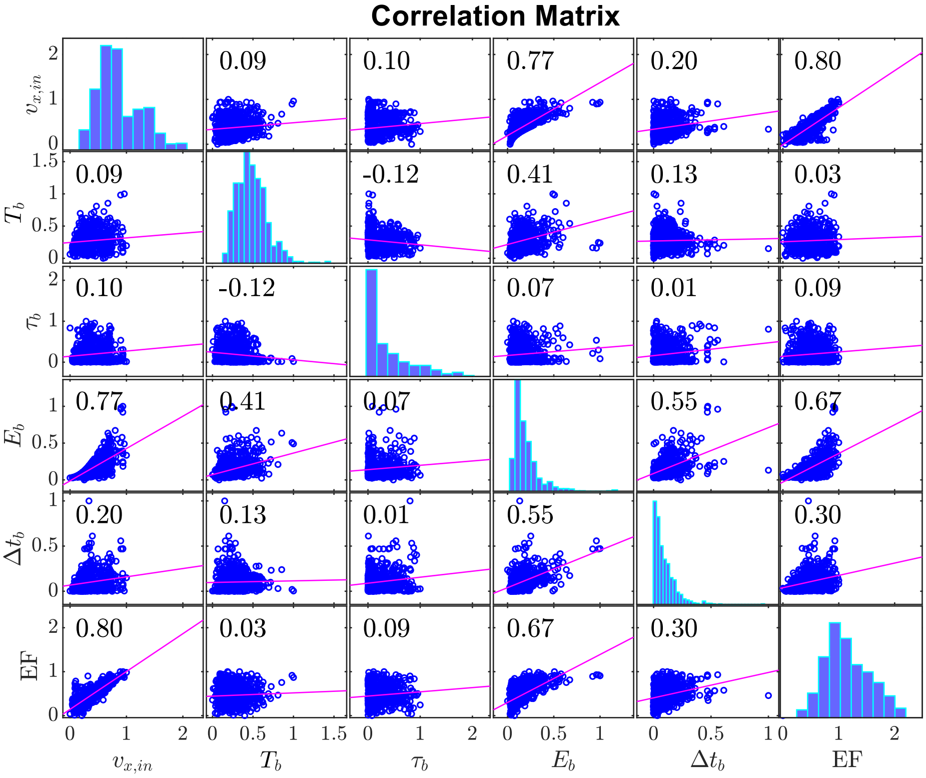

Figure 8.6: *Spearman correlation matrix among the variable under analysis. On the diagonal, the histograms of the main variables under analysis.*

8.6 Artificial neural networks

Upon performing the data pre-processing in accordance with the above mentioned procedure, the proposed ANN can be trained. For the sake of clarity, a qualitative representation of the proposed ANN is reported in Figure 8.7 where neurons are represented by yellow nodes, whilst input and output are reported in the violet boxes. Both ANN are fully connected, that is, each layer communicate with the previous and following ones.

Although static and dynamic ANN feature similar structures, they differ in the way input data are provided. The static ANN is fed with the quasi-static inputs reported under the bar symbol in Figure 8.7. The index j corresponds to the $j-th$ brake

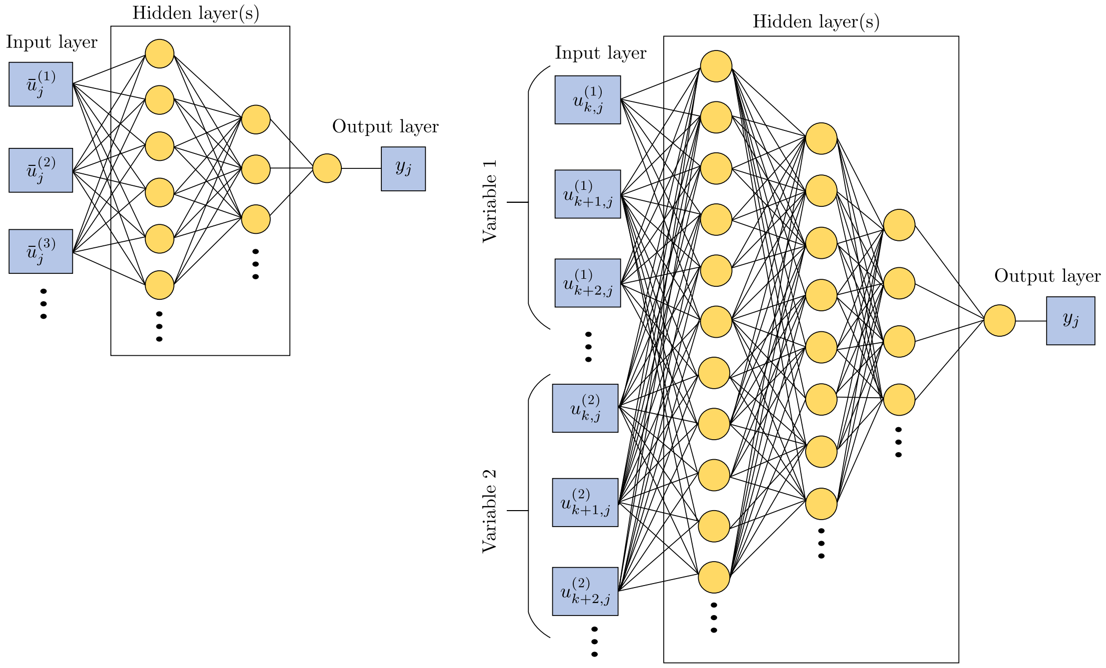

Figure 8.7: *Qualitative representation of the ANN proposed in this study. On the left, the static ANN; on the right, the dynamic ANN.*

application. In this scenario, the set of stationary inputs is as follows:

$$\left[\bar{u}_j^{(1)},\bar{u}_j^{(2)},\bar{u}_j^{(3)},\bar{u}_j^{(4)},\bar{u}_j^{(5)}\right]=\left[v_{x,in_j},v_{x,end_j},\bar{T}_{b_j},\bar{\tau}_j,\Delta t_{b_j}\right], \tag{8.2}$$

In the case of dynamic ANN, dynamic inputs must be provided in a discrete form. The time varying input are included as set of arrays of fixed length. With reference to a generic $j-th$ brake application, each time element $k-th$ of the input variables array counts as a separate input. The input variable array length is set by the longest braking manoeuvre. All other manoeuvres are scaled accordingly in order to fill the vector elements. To account for the dynamics of the generic braking manoeuvre, the brake duration is included as last input. Expectedly, given the higher amount of input variables, a dynamic ANN lead to a higher parameter cardinality and, thus, increased computational burden. The input vector for the dynamic ANN is defined as follows:

$$\begin{aligned}&\left[u_{k,j}^{(1)},u_{k+1,j}^{(1)},...,u_{k,j}^{(2)},u_{k+1,j}^{(2)},...,u_{k,j}^{(3)},u_{k+1,j}^{(3)},...,u_{j}^{(4)}\right]=\\&=\left[v_{x_{k},j},v_{x_{k+1},j},...,T_{b_{k,j}},T_{b_{k+1,j}},...,\tau_{k,j},\tau_{k+1,j},...,\Delta t_{b,j}\right],\end{aligned} \tag{8.3}$$

In both cases, the output represents the stationary brake-related particulate number emitted upon completing the $j-th$ brake application, i.e.:

$$y_j=EF_j=\log_{10}\left[\int_{t_{0,j}}^{t_{0,j}+\Delta t_{b,j}} PN(t)\ dt\right], \tag{8.4}$$

The problem at hands is an example of supervised learning. The networks weights and biases are identified by means of the back-propagation algorithm (please, refer to Chapter 2).

8.7 Results and discussion

The functionality of the proposed meta-models is herein assessed by comparing the model responses and the experimental data with respect to trip 8. Moreover, ANN are benchmarked against the look-up-table proposed in [38]. Herein, this latter is referred to as LUT (look-up-table) and has the form reported in Figure 8.5 where the emitted particles number pro braking application is related to the initial braking speed and average brake pressure. The results reported in Figure 8.8 show that all models exhibit very good correlation with the target values. Nevertheless, ANN feature a much higher correlation coefficient when compared to the map-based approach. As discussed in the previous sections, the inputs used in [38] are not sufficient to render the brake-related emissions under all operating conditions. The PN prediction error per driven km, with respect to Trip 8, is reported in Table 8.2.

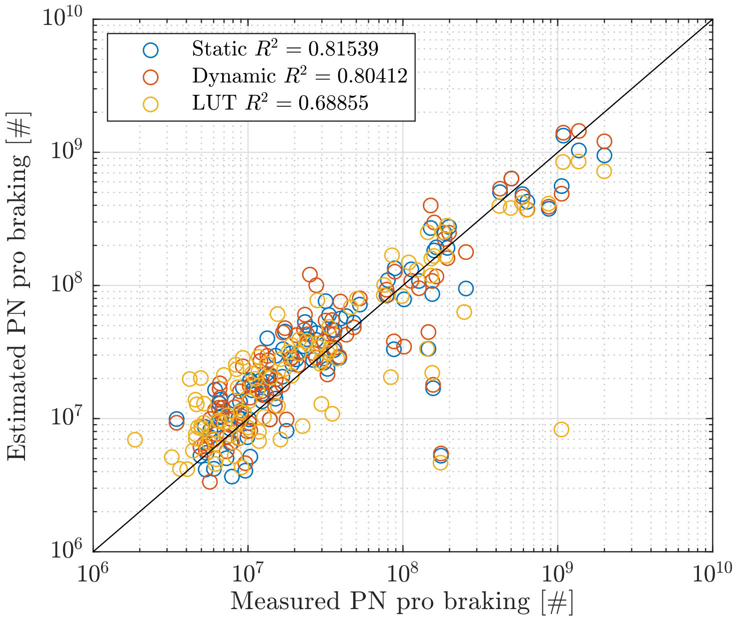

Figure 8.8: *ANN and LUT test results compare the measured and predicted PN per braking manoeuvre. PN refers to the global evacuated flow through the measurement tunnel per brake application.*

The proposed methods are evaluated by means of the performance indexes of Table 8.3. The training time is defined as the time required to perform ANN training on the used host PC. Space in memory relates to the number of parameters stored on the hardware and necessary to implement the estimation method. This index also affects the real time

Table 8.2: Overall ΣPN prediction error, Trip 8.

Target	Static ANN	Dynamic ANN	LUT
$2.77 \cdot 1e^{9}$ $[\#/km]$	$2.52 \cdot 1e^{9}$ $[\#/km]$ (-9.07%)	$2.66 \cdot 1e^{9}$ $[\#/km]$ (-3.95%)	$1.86 \cdot 1e^{9}$ $[\#/km]$ (-32.68%)

capability of the method. The average EF prediction error is computed by means of the $nRMSE$. EF refers to the target and $\hat{EF}$ to the model response. The j index ranges among N_b braking applications characterising Trip 8. The cumulate PN prediction error relates to the model capability of correctly predicting the emitted PN with respect to the whole driving cycle. PN refers to the target and $\hat{PN}$ to the models response. At last, the variance accounted for (VAF) reflects the model capability of explaining the variance in the target signal. If the residual VAF is close to one, the model exhibits a high correlation with experimental data.

Table 8.3: Key performance indexes used to evaluate models performance.

KPI	Definition
Training time	Time required to complete ANN training (Not defined for LUT-based method)
Space in memory	Number of stored parameters
Average EF prediction error	$nRMSE = \frac{\sqrt{\frac{1}{N_b}\sum_{j=1}^{N_b}\left(EF_j - \hat{EF}_j\right)^2}}{\frac{1}{N_b}\sum_{j=1}^{N_b} EF_j}$
Cumulate PN prediction error	$\Delta\Sigma PN = 1 - \sum_{j=1}^{N_b} \hat{PN}_j / \sum_{j=1}^{N_b} PN_j$
Variance accounted for	$VAF = 1 - var\left(PN - \hat{PN}\right)/var(PN)$

For the sake of clarity, the benchmark results are graphically reported in Figure 8.9. The time dependence of dynamic ANN explains the low cumulated error, as reported in Table 8.2. Moreover, because of dynamic ANN capability of following transient manoeuvres, it also exhibits a higher VAF index. However, compared to static ANN, dynamic ANN requires a much larger number of parameters to be stored in memory, which negatively affects its real-time capability. As anticipated in the previous sections, the map-based approach accounts only partially for the variance in the brake-related emissions (low VAF index). The map-based approach requires limited space in memory to the detriment of prediction error. The results suggest that a static ANN complies criteria of error minimisation and computational burden. In consideration of its satisfactory PN prediction performance, static ANN are indicated as the optimal solution for the estimation of brake-related particle emissions.

The method based on ANN correlates well with the experimental data; however, it might not well reproduce the emissions behaviour when the actual brake operating conditions are far from the investigated ones. Moreover, ANN are purely black box, therefore they are not able to describe the actual phenomenology of the tribological

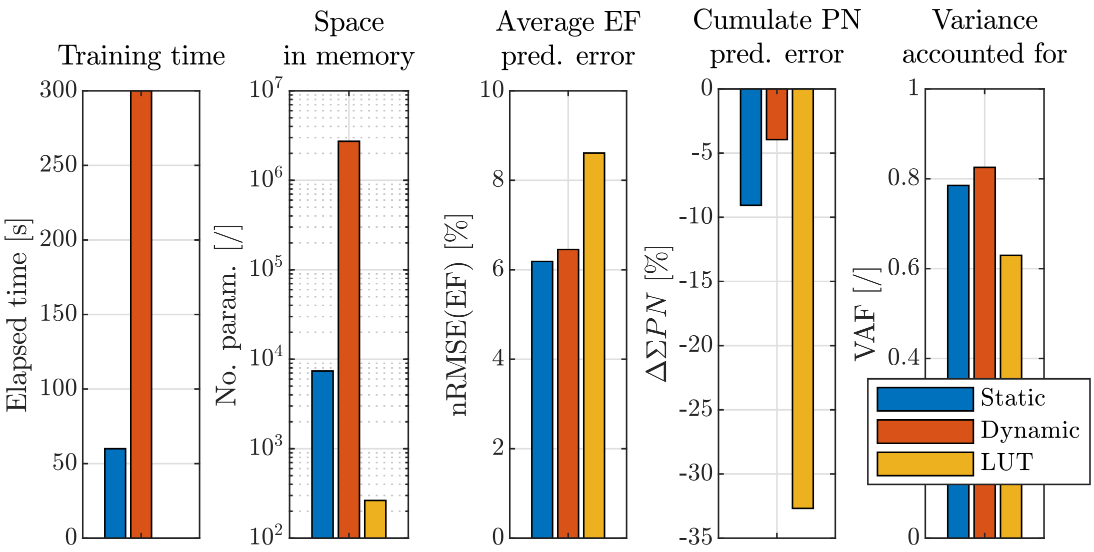

Figure 8.9: *ANN benchmark analysis with respect to the defined KPIs.*

contact. Hence, although the propose approach can reproduce the effect of brake-related particulate emissions, it is not capable of describing its causes.

The concept of brake particle emissions estimation lays the groundwork for a control method aimed at reducing brake wear emissions. Depending on the traffic situation, the driver's deceleration request and the vehicle actuators status, the control method may enable wear-optimised deceleration manoeuvres. Such a procedure is especially suitable for vehicles that allow semi-autonomous or autonomous driving and where situation-dependent driving decisions have to be implemented with safety prioritisation but with minimization of fine dust emissions. In the first instance, a clear reduction of brake particle emissions can be achieved by limiting the friction brake power through more frequent intervention of the electric motors. In the second instance, the brake force distribution between the front and rear axles could be adjusted so as to avoid critical temperature levels that cause a significant increase in the amount of fine dust emissions. In the third instance, semi-autonomous and autonomous vehicles equipped with environmental sensors may guarantee a more conservative driving style by limiting the vehicle deceleration intensity when cruising with simultaneous fulfilment of the vehicle safety requirements.

8.8 Chapter summary

In this chapter artificial neural networks are deployed to predict the brake-related particulate emissions under RDE-compliant driving conditions. To this effect, the model identification is performed on data collected from a light commercial vehicle equipped with a portable emissions measurement system at Technische Universität Ilmenau. Two neural networks are benchmarked against the state-of-the-art approach based on look-up-table. The most promising solution is found under criteria of error minimisation and computational burden. The results are graphically presented and supported by performance indexes and indicate that static neural networks comply both criteria of error minimisation and variance accounted for by simultaneously guaranteeing an acceptable computational burden.

The results also suggest that there is a clear reduction potential in brake-related emissions. Limiting the friction brake power by blending with electric motors and minimising the brake intervention time may result in a clear reduction of brake-related particle emissions. The optimal control is to be regarded as a compromise between fulfilling the driver's request and reducing brake-related emissions. Such a method reveals especially suitable for vehicles equipped with environmental sensors, which enable semi-autonomous or autonomous driving and where driving situation-dependent decisions could be implemented without compromising vehicle safety.

Chapter 9

Discussion and Conclusion

Novel control and estimation solutions for low-emission multi-actuated ground vehicles serve to improve braking performance and monitor brake-related wear and particle emissions. Unexpected disturbances induced by variations in the brake lining coefficient of friction can lead to unpredictable vehicle behaviour and deterioration of the braking performance and vehicle safety. The knowledge of the brake lining coefficient of friction plays a crucial role in the performance of base brake control algorithms since large deviations in its actual value from the reference value employed in the controller may lead to undesirable deterioration of the brake control functions. Experiments performed on the proving ground shows that a decaying brake lining coefficient of friction causes a reduced brake effectiveness. As a consequence, the driver needs to increase the brake pedal displacement to achieve the same deceleration level. Existing brake lining coefficient of friction estimation approaches are not validated under real driving conditions and imply high costs for their identification. Moreover, existing approaches completely fail if the operating conditions lay far from the identification data set or when the plant characteristics change due to replacement of system components with aftermarket products. For these reasons, this work proposes a novel brake lining coefficient of friction observer, real time capable and robust against external disturbances. Achieving this goal brings up interdisciplinary methods ranging among advancements in numerical modelling and simulation tools, and application of innovative experimental and sensors fusion techniques.

Under the framework of this research, the development of control and estimation functions is supported by model-, software- and hardware-in-the-loop techniques enhanced by means of a novel brake friction coefficient model resulting from a collaboration between Technische Universität Ilmenau (Ilmena, Germany) and Volvo Cars (Göteborg, Sweden). A full factorial design of experiments on the brake dynamometer at Volvo Cars leads to a dynamic brake model that outperforms state-of-the-art solutions. To prove its robustness, the model is identified and validated on three different brake systems composed of cast iron discs and ECE brake linings. The model also includes an enhanced version of the well-known disc brake lumped temperature model. The proposed model is capable of extrapolating the dynamics of the brake lining coefficient of friction in correspondence of large braking temperatures where state-of-the-art approaches fail. The integration of this latter in the IPG CarMaker® software ensures reliable and more realistic vehicle dynamics simulations.

The sought brake lining friction coefficient observer is developed under model- and software-in-the-loop environments. The proposed non-linear Kalman observer demonstrates that a reliable brake friction coefficient estimate can be either obtained by measuring the longitudinal tyre forces or by using a cost-effective virtual sensor of longitudinal tyre forces. The state-space formulation associated with the observer stems from the quarter-car model and the linear tyre model with relaxation length. The observability and robustness of the brake lining friction coefficient observer is demonstrated under different operating conditions and in presence of artificially injected faults. The results show that lower estimation errors result from larger deceleration requests and, due to typical brake force allocation strategies, a greater estimation accuracy is achieved on the front axle. The estimation based on longitudinal tyre force virtual sensing achieves 5% accuracy on the front axle and 10% accuracy on the rear axle for a deceleration request of approximately $4\,m/s^2$. Below this deceleration threshold, the observer based on longitudinal tyre forces virtual sensing slowly decays on the front axle up to 17% error, whilst it is switched off on the rear axle and the previous brake lining coefficient of friction estimate is provided. In accordance with the identified activation thresholds for the front and rear axles, the observer exhibits superior performance when compared to the case where a constant estimate of the brake lining coefficient of friction, equal to its nominal value, is used.

Thereafter, the brake lining coefficient of friction compensation function is implemented and verified on the brake-by-wire hardware-in-the-loop platform at Technische Universität Ilmenau. The compensation algorithm updates the brake lining coefficient of friction estimated value in the brake-by-wire controller, ensuring that the brake system always provides the desired feedback to the driver. The experiments demonstrate that the proposed observer based on longitudinal tyre force virtual sensing shall be enhanced with a non-linear tyre model in case of excessive wheel slip. The functionality of the compensation method is demonstrated under different operating conditions, also including blended braking with electric motors. The proposed observer features satisfactory estimation performance in case of repeated brake actuations. Hardware-in-the-loop verification results demonstrate that higher blending factors go to the detriment of the brake lining friction coefficient estimation accuracy. Nonetheless, the brake lining coefficient of friction compensation function improves the reference deceleration tracking performance under all brake blending conditions by simultaneously reducing the driver's workload on the brake pedal.

The developed observer is then validated on the full electric sport utility vehicle provided by Flander's Make. Three test sessions carried out on the Ford's Lommel (Lommel, Belgium) proving ground allows for the observer tuning and validation under fixed pedal braking and constant deceleration braking. Genetic algorithms lead to a suboptimal observer with an estimation performance increased by 50% if compared to the manually tuned variant. The observer robustness against large brake temperature variations is proved by means of a fade test where consecutive full-stop braking manoeuvres are performed. Under all operating conditions, the observer features an estimation accuracy consistent with the model-, simulation- and hardware-in-the-loop results.

The availability of a brake lining coefficient of friction estimate enables advanced estimation functions for brake-related wear and particle emissions. Extensive measurement campaigns carried out on the brake dynamometer at Technische Universität Ilmenau lead to a data driven brake wear model. Particularly, two formulations are proposed: the quasi-static wear model and its extended version, which takes into account temperature and speed variations during braking occurrence. Despite evident difficulties in mining brake wear data, a complex design of experiments allows capturing the influence that brake control and state variables have on the wear formation process. A proper control of the brake dynamometer based on real driving data collected from a sports sedan allows good reproducibility and superior cycle-to-cycle repeatability. The functionality of the novel brake wear models is validated with respect to on-road wear measurements resulting from approximately 30.000 km under real driving conditions. The results suggest that the wear prognosis function can predict the brake pad wear with 15% accuracy by the end of its service life.

Finally, a particle emissions measurement system typically used for tail pipe emissions is retrofitted on a light commercial vehicle to assess brake-related particle emissions under real driving conditions. Real driving emissions data resulting from more than 800 braking manoeuvres are employed to define a correlation between relevant brake control variables and the number of emitted brake particles. Due to the high non-linearity and stochasticity of the brake particle formation mechanisms, complex regression models based on artificial neural networks are devised. Particularly, two fully-connected neural architectures are proposed, namely static and dynamic, which differ in the way input data are provided. The proposed regression models exhibit superior performance when compared to state-of-the-art approaches, being able to predict the overall number of emitted particles per driven km with 10% accuracy for the static architecture and 4% for the dynamic architecture. Nonetheless, the results suggest that a static neural network might be preferred as it complies both criteria of error minimisation and reduced computational burden. The developed brake wear and particle emissions monitoring functions could be applied as a basis for motion control algorithms in semi-autonomous and autonomous vehicles aimed at abating non-exhaust emissions.

The research objectives are thereby accomplished and the following conclusions can be drawn:

- the novel brake model allows for enhanced simulation fidelity of model-, software- and hardware-in-the-loop frameworks by inclusion of the pad-disc contact dynamics;
- the proposed controller of brake-by-wire architectures compensates for variations in the brake lining coefficient of friction, also in presence of blended actuation with electric motors;
- a reliable and robust brake lining coefficient of friction estimate enables advanced monitoring functions of brake-related wear and particle emissions;
- the enhanced version of the lumped capacitance model, which accounts for vehicle speed and environmental conditions, is required for brake-related wear monitoring functions;
- meta-modelling techniques such as neural networks are necessary to account for the high non-linearity and stochasticity of the brake particle formation process.

Outlook

By pursuing control and estimation solutions for brake systems, important issues such as states observability, virtual sensing techniques and data-driven models are addressed in this thesis. The feasibility and functionality of a real-time, on-board estimation of the brake lining coefficient of friction is demonstrated. Despite the innovative contributions to the tribology and control communities, the author acknowledges that the proposed solutions may require further investigations. The following list provides the main recommendations that complement this research.

- *Enhanced control functionality in decoupled brake architectures of electric vehicles.* The proposed compensation function can be integrated with already existing brake-by-wire systems to enhance braking performance in presence of blended operation with electric motors. A proper experimental validation of the compensation function shall be carried out under real driving situations on a large fleet of vehicles with decoupled brake architectures. Among others, the effect of the compensation function on the driving experience shall be quantified.
- *Improvement of the brake temperature measurements.* The lumped capacitance model is identified with respect to temperature data provided by a sliding thermocouple. Despite the large brake disc conductivity, the temperature profile in the brake discs can exhibit high spatial non-uniformity. This can bring limitations to commonly used sliding thermocouples. Therefore, alternative temperature sensing techniques (e.g. pyrometer remote temperature sensing) shall be investigated and their influence on the lumped model estimation performance quantified.

- *Improvement of the brake particle emissions estimator.* Numerous studies addressing the health impact of brake-related particle emissions argue that deeper attention shall be paid to particle mass rather than particle number, also under a regulatory point of view. Without loss of generality, the proposed artificial neural networks can be upgraded to account for brake particle mass emissions in addition to the number of emitted particles.

- *Development of a control method for reduced brake wear.* From an application perspective, numerous solutions to reduce brake-related emissions are possible. In addition to brake blending, a more conservative driving style, reduced brake intervention when cruising, variable brake force distribution between axles and mitigation of brake temperature peaks are factors contributing to emissions reduction. A motion control algorithm for semi-autonomous and autonomous vehicle shall include the previously mentioned mechanisms to enable wear-optimised deceleration control with simultaneous fulfilment of safety requirements.

Funding Acknowledgement

The project leading to this study has received funding from the European Union's Horizon 2020 research and innovation programme under the Marie Skłodowska-Curie grant agreement No. 675999, ITEAM project. ITEAM aimed at establishing and sustainably maintaining the European training network with high grade of interdisciplinarity by training early stage engineers in researching and developing cutting-edge technologies in the field of multi-actuated ground vehicles. This research required support of other industrial research projects for the achievement of advanced functions in the vehicle chassis and powertrain control.

Peer-reviewed Contribution

Ricciardi, V., Augsburg, K., Gramstat, S., Schreiber, V. and Ivanov, V. (2017). Survey on modelling and techniques for friction estimation in automotive brakes. Applied Sciences, 7(9), 873.

Ricciardi, V., Augsburg, K., Ivanov, V. (2017). A novel approach for the estimation of the brake friction coefficient for environmental and safety control applications. EuroBrake; FISITA: Dresden, Germany.

Ricciardi, V., Savitski, D., Augsburg, K. and Ivanov, V. (2017). Estimation of brake friction coefficient for blending function of base braking control. SAE International Journal of Passenger Cars-Mechanical Systems, 10(2017-01-2520), 774-785.

Ricciardi, V., Acosta, M., Augsburg, K., Kanarachos, S. and Ivanov, V. (2017, October). Robust brake linings friction coefficient estimation for enhancement of EHB control. In 2017 XXVI International Conference on Information, Communication and Automation Technologies (ICAT) (pp. 1-7). IEEE.

Ricciardi, V., Ivanov, V. and Augsburg, K. (2018, October). Estimation of Power Dissipation in Disc Brakes and Tires for Motion Control Applications in Electric

Vehicles. In IECON 2018-44th Annual Conference of the IEEE Industrial Electronics Society (pp. 4531-4536). IEEE.

Ricciardi, V., Ivanov, V., Dhaens, M., Vandersmissen, B., Geraerts, M., Savitski, D. and Augsburg, K. (2019). Ride blending control for electric vehicles. World Electric Vehicle Journal, 10(2), 36.

Aksjonov, A., Ricciardi, V., Augsburg, K., Vodovozov, V. and Petlenkov, E. (2020). Hardware-in-the-Loop Test of an Open Loop Fuzzy Control Method for Decoupled Electro-Hydraulic Antilock Braking System. IEEE Transactions on Fuzzy Systems.

Ricciardi, V., Travagliati, A., Schreiber, V., Klomp, M., Ivanov, V., Augsburg, K. and Faria, C. (2020). A novel semi-empirical dynamic brake model for automotive applications. Tribology International, 146, 106223.

Ricciardi, V., Schiele, M., Hesse, D., Hauschild, P. and Augsburg, K. (2020). Artificial Neural Networks Regression Models for the Prediction of Brake-related Emissions. EuroBrake; FISITA.

Appendices

Appendix A

MIL/SIL/HIL simulation frameworks

A.1 Full electric vehicle model

The experimentally validated model of full electric SUV is simulated under the proprietary software IPG CarMaker®. Its experimental validation has been carried out under the framework of E-VECTOORC Project (Seventh Framework Programme 284708). For the interested readers, the validation results can be found at [112]. Additional subsystems such as the brakes, electric motors and the brake hydraulic circuit, are modelled as external Simulink® blocks, directly interfaced with the IPG CarMaker®. Although the proprietary IPG CarMaker® vehicle model features more than 14-DoF, here it is worth reporting, without loss of generality, the vehicle dynamics laws relevant to the MIL/SIL/HIL simulations of the present study. The two-track model represents a simplified problem, which has been used in several applications ranging from state estimation to vehicle control [85, 81]. A schematic of the 14-DoF two-track model is reported in Figure A.1. This model considers the longitudinal, lateral, vertical, pitch, roll and yaw dynamics of the vehicle body, together whith vertical and rotational dynamics of the wheels.

This simplified model describes the relative motion of sprung and unsprung mass. The unsprung part includes the suspensions, wheels, brakes and suspension knuckles. The sprung part is fundamentally composed of all the components supported by the suspensions, such as the vehicle body, internal components, passengers and load. Due to the absence of an accurate brake model in the IPG CarMaker® vehicle dynamics simulator, particular attention has been put to its development and integration for simulation purposes. More details can be found in Chapter 3.

A.1.1 Vehicle planar dynamics

For a clear understanding of the basic vehicle dynamics laws, it is worth starting from the planar dynamics. This represent a reduced order problem of 7-DoF, which is obtained by projecting the 14-DoF dynamics (Figure A.1) into the vehicle plane of motion. It reveals

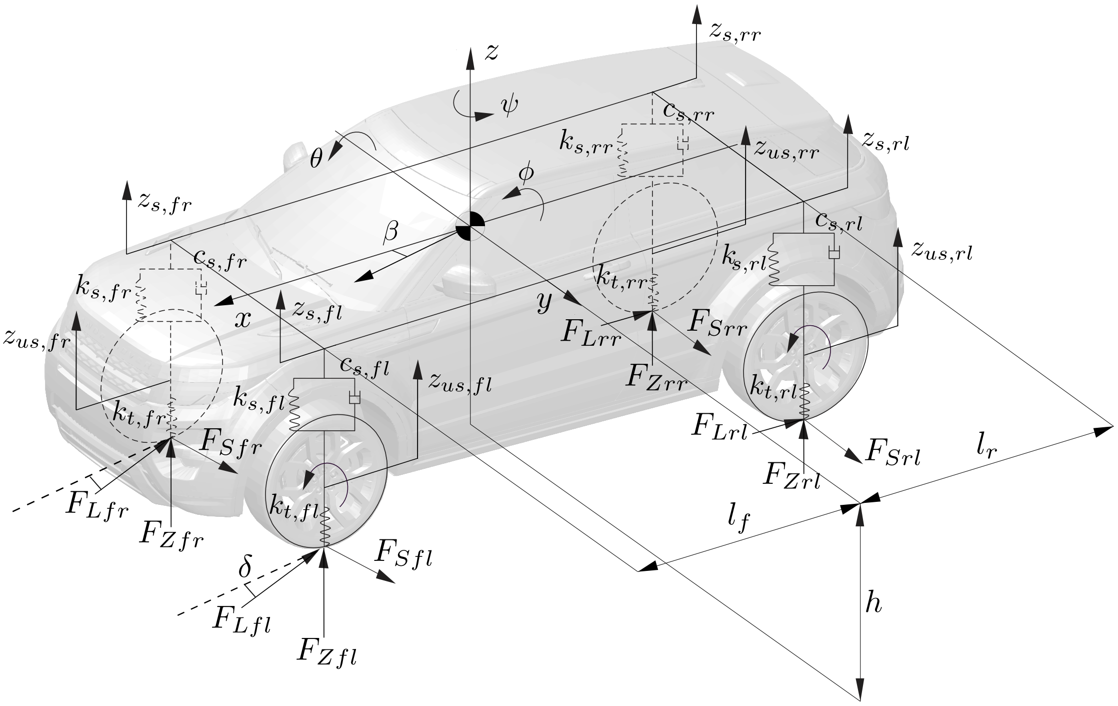

Figure A.1: *14-DoF vehicle model identifies the vehicle dynamics states relevant to this study.*

particularly suitable for the analysis of braking, acceleration and handling manoeuvres in case of non-critical driving situations where pitch and roll dynamics are confined to small displacements. The resulting problem is conveniently depicted in Figure A.2.

The side-slip at the vehicle center of gravity β is the angle between the velocity vector v_{CoG} (direction of travel) and the vehicle longitudinal axis. The yaw rate $\dot{\psi}$ is the angular velocity of the vehicle about its vertical axis, with I_{zz} being the yaw moment of inertia. The longitudinal and lateral velocity vectors are referred to as v_x and v_y, respectively. The simplified two-track model for planar motion is formulated by the following set of Equations (A.1a) to (A.1c):

$$\begin{cases} \dot{v}_x = \dfrac{1}{m_v}\Big[(F_{Lfl} + F_{Lfr})cos\delta - (F_{Sfl} + F_{Sfr})sin\delta \\ \quad +(F_{Lrl} + F_{Lrr}) + \dot{\psi}v_y - F_{X,drag}\Big] , & \text{(A.1a)} \\ \dot{v}_y = \dfrac{1}{m_v}\Big[(F_{Sfl} + F_{Sfr})cos\delta + (F_{Lfl} + F_{Lfr})sin\delta \\ \quad +(F_{Srl} + F_{Srr}) - \dot{\psi}v_x + F_{Y,drag}\Big] , & \text{(A.1b)} \\ \ddot{\psi} = \dfrac{1}{I_{zz}}\Big[l_f(F_{Lfl} + F_{Lfr})sin\delta - l_r(F_{Srl} + F_{Srr}) + l_f(F_{Sfl} + F_{Sfr})cos\delta \\ \quad +\dfrac{b}{2}(F_{Lfr} - F_{Lfl})cos\delta + \dfrac{b}{2}(F_{Lrr} - F_{Lrl}) + \dfrac{b}{2}(F_{Sfl} - F_{Sfr})sin\delta\Big] , & \text{(A.1c)} \end{cases}$$

where, the total vehicle mass m_v represents the sum of the vehicle body (sprung) m_s and wheel corner (unsprung) m_{us} masses; $F_{X,drag}$ and $F_{Y,drag}$ are the aerodynamic drag

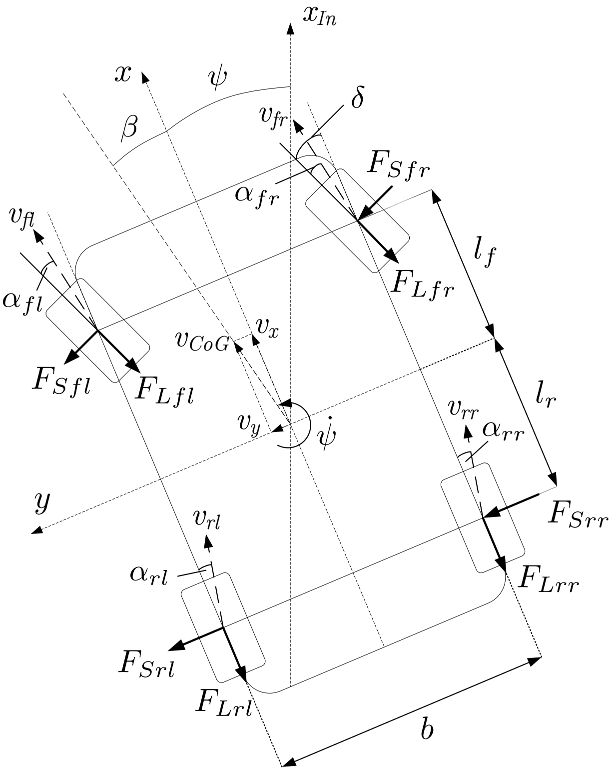

Figure A.2: *Two-track 7-DoF vehicle model.*

forces in the longitudinal and lateral directions, respectively.

The tyre side slip angles α_{ij} can be computed from Equations (A.2a) to (A.2d):

$$\begin{cases} \alpha_{fl} = \delta - \arctan\left[\dfrac{v_y + l_f\dot{\psi}}{v_x - \dot{\psi}b/2}\right], & \text{(A.2a)} \\ \alpha_{fr} = \delta - \arctan\left[\dfrac{v_y + l_f\dot{\psi}}{v_x + \dot{\psi}b/2}\right], & \text{(A.2b)} \\ \alpha_{rl} = -\arctan\left[\dfrac{v_y - l_f\dot{\psi}}{v_x - \dot{\psi}b/2}\right], & \text{(A.2c)} \\ \alpha_{rr} = -\arctan\left[\dfrac{v_y - l_f\dot{\psi}}{v_x + \dot{\psi}b/2}\right]. & \text{(A.2d)} \end{cases}$$

This model also includes the rotational wheel dynamics, yielding the 7-DoF vehicle model. The wheel dynamics must be taken into account to enable the tyre-road interaction. In general, the tyre feature a rotational inertia of around $1-2\ kgm^2$, which makes its dynamics not negligible, especially for manoeuvres involving fast dynamics.

The four wheel rotational speeds are therefore included as additional dynamics according to Equation (A.3):

$$\dot{\omega}_{ij} = \frac{1}{I_\omega}\left(T_{\omega,ij} - F_{L,ij}\ r_{\omega,ij} - R_{L,ij}\right), \tag{A.3}$$

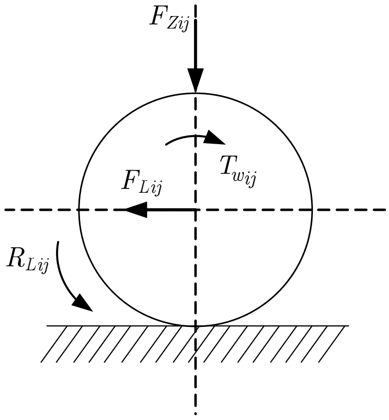

Figure A.3: *Wheel dynamics where the i-th index refers to one wheel.*

where,

$$r_{\omega,ij} = \frac{sin\left[arccos\left(1 - \frac{F_{Z,ij}}{r_{0,ij}\ K_{Z,ij}}\right)\right]}{arccos\left(1 - \frac{F_{Z,ij}}{r_{0,ij}\ K_{Z,ij}}\right)}. \tag{A.4}$$

It is worth noting that the frictional forces are defined in the wheel reference frame. The effective tyre radius $r_{\omega,ij}$ relates the angular velocity of the wheel to its linear longitudinal velocity and differs from the undeformed tyre radius $r_{0,ij}$. Equation (A.4) stems from geometrical consideration on the wheel kinematics and is relevant to the estimation of the tyre longitudinal slip. The effective rolling radius takes into account the vertical tyre deformation equal to the wheel ground contact force $F_{Z,ij}$ divided by the tyre vertical stiffness $K_{Z,ij}$. Using the the vehicle kinematics, the translational velocity of each wheel hub in the rolling direction can be derived through Equations (A.5a) to (A.5d):

$$\begin{cases} v_{L,fl} = v_{fl}\cos\alpha_{fl} = \left(v_x - \dfrac{\dot{\psi}b}{2}\right)\cos\delta + \left(v_y + \dot{\psi}l_f\right)\sin\delta, & \text{(A.5a)} \\ v_{L,fr} = v_{fr}\cos\alpha_{fr} = \left(v_x + \dfrac{\dot{\psi}b}{2}\right)\cos\delta + \left(v_y + \dot{\psi}l_f\right)\sin\delta, & \text{(A.5b)} \\ v_{L,rl} = v_{rl}\cos\alpha_{rl} = v_x - \dfrac{\dot{\psi}b}{2}, & \text{(A.5c)} \\ v_{L,rr} = v_{rr}\cos\alpha_{rr} = v_x + \dfrac{\dot{\psi}b}{2}. & \text{(A.5d)} \end{cases}$$

The previous equations allow defining the longitudinal wheel slip ratio λ_{ij}, computed as the difference between the wheel rotational velocity and the wheel translational velocity in the rolling direction:

$$\lambda_{ij} = \frac{r_{\omega,ij}\ \omega_{ij} - v_{L,ij}}{max(r_{\omega,ij}\ \omega_{ij}, v_{L,ij})} \tag{A.6}$$

A.1.2 Vehicle vertical dynamics

During normal driving situations, the vertical forces acting on the wheels are a composition of the sprung weight and inertial forces acting on the suspension strut. During acceleration, braking and cornering, the vehicle body undergoes sensible translational and rotational displacements, known as heave z_s, pitch θ and roll ϕ. Road unevenness might affect the unsprung mass vertical position through the stiffness and damping characteristics of the tyre. In the schematics of Figure A.1, it is worth noticing that the suspensions are modelled as spring-damper connections between the sprung and unsprung masses, whilst the tyre rubber is modelled as a pure elastic component (with negligible damping). The suspensions reaction forces, herein referred to as F_{Vij}, and the tyre vertical ground forces F_{Zij} determine the unsprung mass vertical dynamics. The road hight is herein referred to as $z_{r,ij}$; however, its modelling is not directly accounted in this work. The equations describing the additional dynamics are Equations (A.7a) to (A.7d):

$$
\begin{cases}
\dot{v}_z = \dfrac{1}{m_s}\left[m_s g - F_{V,fl} - F_{V,fr} - F_{V,rl} - F_{V,rr}\right], & \text{(A.7a)}\\
\ddot{\theta} = \dfrac{1}{I_{yy}}\left[h_f(F_{L,fl} + F_{L,fr})\cos\delta + h_f(F_{S,fl} + F_{S,fr})\sin\delta\right. & \\
\quad \left. -h_r(F_{L,rl} + F_{L,rr}) - l_f(F_{S,fl} + F_{S,fr}) + l_r(F_{S,rl} + F_{S,rr})\right], & \text{(A.7b)}\\
\ddot{\phi} = \dfrac{1}{I_{xx}}\left[h_f(F_{S,fl} - F_{S,fr})\sin\delta + h_f(F_{L,fr} - F_{L,fl})\cos\delta\right. & \\
\quad \left. -h_r(F_{L,rr} - F_{L,rl}) - \dfrac{b}{2}(F_{S,fr} + F_{S,rr}) + \dfrac{b}{2}(F_{S,fl} + F_{S,rl})\right], & \text{(A.7c)}\\
\ddot{z}_{us,ij} = \dfrac{1}{m_{us,ij}}\left[-F_{V,ij} + F_{Z,ij}\right], & \text{(A.7d)}
\end{cases}
$$

where, the tyre vertical ground force follows:

$$F_{Zij} = -k_{t,ij}\left(z_{us,ij} - z_{r,ij}\right). \tag{A.8}$$

The suspension reaction forces consider the spring, damper and the stabiliser (anti rollbar) as follows:

$$F_{Vij} = k_{s,ij}\left(z_{s,ij} - z_{us,ij}\right) + c_{s,ij}\left(\dot{z}_{s,ij} - \dot{z}_{us,ij}\right) + k_{st,ij}\left(z_{s,il} - z_{us,il} + z_{s,ir} - z_{us,ir}\right), \tag{A.9}$$

where, $k_{s,ij}$ is the stiffness of the suspension spring, $c_{s,ij}$ is the damping of the shock absorber and $k_{st,ij}$ is the stiffness of the anti-roll bar. The characteristics of the modelled passive suspension derive from the experimental vehicle and for confidentiality reasons adimensional force values are reported in Figure A.4.

The previous set of equations complete the 14-DoF dynamics. The sprung mass position $z_{s,ij}$ identifies the suspensions top mount positions. Assuming a rigid vehicle

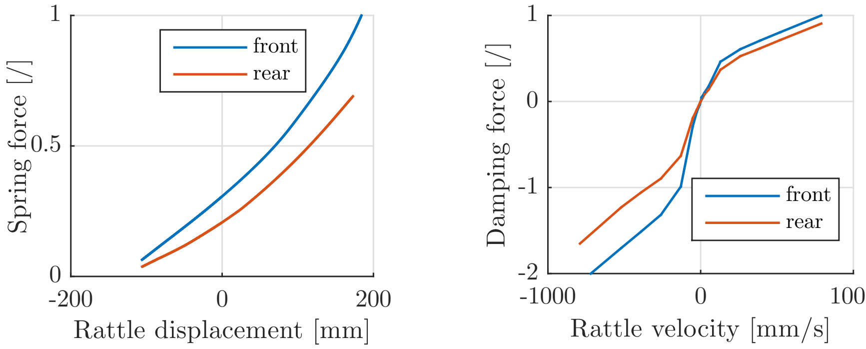

(a) *Suspension spring characteristics.*

(b) *Suspension damping characteristics.*

Figure A.4: *Non-linear characteristics of the suspension system for the front and rear axles as modelled in the proprietary software IPG CarMaker®.*

body, the following set of equations can be drawn:

$$\begin{cases} z_{s,fl} = z_s - l_f \sin\phi + \dfrac{b}{2}\sin\theta, & \text{(A.10a)} \\ z_{s,fr} = z_s - l_f \sin\phi - \dfrac{b}{2}\sin\theta, & \text{(A.10b)} \\ z_{s,rl} = z_s + l_r \sin\phi + \dfrac{b}{2}\sin\theta, & \text{(A.10c)} \\ z_{s,rr} = z_s + l_r \sin\phi - \dfrac{b}{2}\sin\theta. & \text{(A.10d)} \end{cases}$$

A.2 Vehicle subsystems models

This section features the models of tyres, electrohydraulic brake system and electric motors used in the framework of MIL/SIL/HIL simulations. It is worth noting that the electrohydraulic brake system model has been experimentally validated against the real system and is replaced by this latter in case of HIL simulations. The brake friction processes are rendered by means of the model introduced in Chapter 3. In the framework of this work, the transition between EMs and EHB is handled by the brake blending controller in Chapter 5.

A.2.1 Modelling the tyre-road interaction

The most recognised and widely used semi-empirical tyre model is the so-called Magic tyre model proposed by Pacejka in [113]. This model has contributed to a better understanding of the tyre behaviour during the past 40 years. The model describes the characteristics of longitudinal force, lateral force and self-aligning torque in pure and combined slip situations. The model is based on the physicality of the tyre-road interaction and requires experimental data for its identification. The basic Magic formula is represented by Equations (A.11) and (A.12):

$$y = D \sin \left[\arctan Bx - E(Bx - \arctan Bx) \right], \tag{A.11}$$

with

$$Y(x) = y(x) + S_v, \; and \; x = X + S_h. \tag{A.12}$$

In the previous equations, Y is the generic output variable, which stands for longitudinal force F_L, lateral force F_S or aligning moment M_z. X is the input variable, which stands for the longitudinal slip ratio λ_{ij} or lateral slip angle α_{ij}. In the framework of this work, it is worth mentioning that the model parameters, namely D, B, E, S_v, S_h, have been identified against experimental data collected on the proving ground. Figures A.5 and A.6 depicts the tyre forces on a dry surface in accordance with the Magic Formula employed in the framework of this work. The forces are expressed in terms of friction coeff. utilisation. Thus, the peak shown by the curves refers to the maximum friction coefficient on dry road, here assumed equal to 1.2.

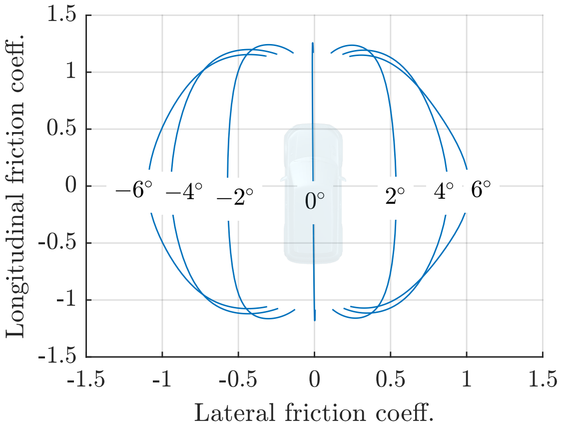

Figure A.5: *Kamm circle defines the limits of vehicle grip on dry road. The figure reports grip limits for different tyre lateral slip values.*

Among others, the model proposed by Pacejka in [113], accounts for variation in the tyre vertical load, cornering stiffness and camber angle. Figure A.5 show the vehicle grip limits (viz. Kamm circle) for a dry surface for different tyre side slip conditions. Expectedly, larger side slip values allow for the achievement of higher lateral forces to the detriment of longitudinal forces. Figure A.6 reports the longitudinal and lateral friction utilisation coefficients as functions of the longitudinal wheel slip at varying side slip angle, camber angle, and load conditions. It is worth noting that higher tyre load conditions lead to a reduced friction peak, whilst negative camber angle increases the lateral force of the outer tyre when cornering. The effects of camber is neglected in the present framework for the sake of simplicity. Nevertheless, the effect of combined tyre slip and varying vertical load is accounted.

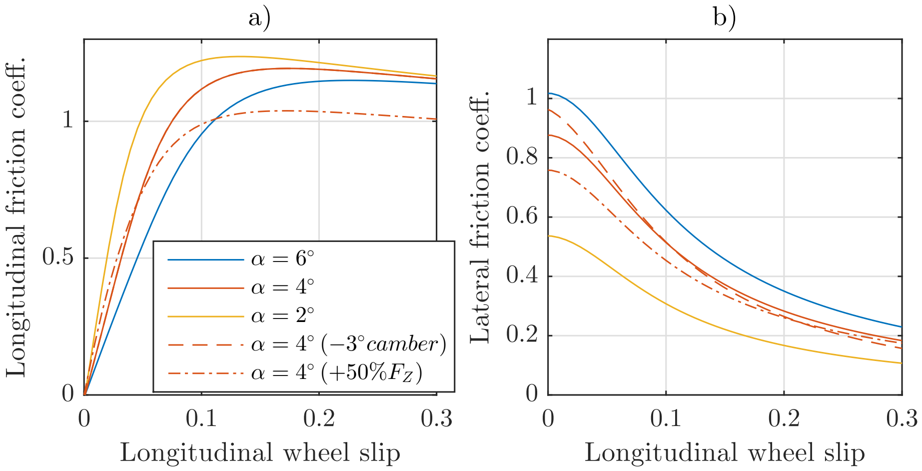

Figure A.6: *Features of the Pacejka tyre model. Figures a) and b) report the longitudinal and lateral friction utilisations, respectively, as a function of the tyre longitudinal slip at varying side slip angles and tyre load conditions.*

Tyre forces are not developed instantaneously when a certain input is applied but require a certain time to build up. The dynamic behaviour of the tyre-road force development to certain inputs can be well described by means of a transfer function. Such inputs include the applied wheel torque as well as the tyre vertical load, the steer angle and the camber angle. The vehicle dynamics simulation software IPG CarMaker® includes a transient tyre model based on a first order transfer function parametrised against the tyre relaxation length. This latter is defined as the distance needed to build-up the tyre forces:

$$\tau_{rl,(\bullet)}\dot{F}_{(\bullet)} + F_{(\bullet)} = F_{(\bullet)}^{(TM)}, \tag{A.13}$$

where, the $(\bullet)$ symbol stands either for a longitudinal or lateral component, $\tau_{rl,(\bullet)}$ represents the relaxation time constant, $F_{(\bullet)}$ is the dynamic tyre-road force and $F_{(\bullet)}^{(TM)}$ is the quasi-static tyre model force. In accordance with [85], the relaxation time constant can be approximated as:

$$\tau_{rl,L,ij} = \frac{C_{L,ij}}{K_L|v_x|} \; \textit{and} \; \tau_{rl,S,ij} = \frac{C_{S,ij}}{K_S|v_x|}, \tag{A.14}$$

where, K_L and K_S represent the longitudinal and lateral tyre stiffness, thus, the elastic compliance of the tyre to external longitudinal and lateral loads, respectively; whilst, $C_{L,\lambda_{i,j}}$ and $C_{S,\alpha_{i,j}}$ represent the tyre longitudinal and lateral slip stiffness, respectively:

$$C_{L,ij} = \frac{\partial F_{L,ij}}{\partial \lambda_{ij}} \; \textit{and} \; C_{S,ij} = \frac{\partial F_{S,ij}}{\partial \alpha_{ij}}. \tag{A.15}$$

It is worth remarking that whilst the tyre stiffness can be easily characterised and assumed constant for a sufficiently large range of load conditions, the tyre slip stiffness depends on several variables, among others the side slip angle, the road friction conditions, the vertical tyre load, the camber angle. In the framework of the present work, the tyre relaxation length is assumed pure function of the vehicle speed.

A.2.2 Powertrain model

The full electric SUV is equipped with four on-board switched reluctance motors. The EMs feature a nominal power of 42 kW (135 Nm) although they can operate up to 100 kW (200 Nm) for a limited period of time (peak 30 s). The maximum rotational speed is rated at 14000 rpm. The supply voltage is assumed equal to 800 V. Figure A.7 shows the quasi-static characteristics map of the EMs. The map describes the behaviour of the motor under quasi-static operating conditions. This latter has been obtained by dynamometer testing with under varying rotational speed and different load conditions. With reference to Figure A.7, the coloured regions refer to EMs functioning under peak conditions, which can be achieved by increasing the supplied current. The upper quadrant represents the EMs operation in motor mode. The positive iso-power lines reflect that energy expenditure is necessary to power the motor. The maximum motor efficiency is reached at higher torque levels and at an equivalent vehicle speed of about 100 km/h. The lower quadrant shows the EMs operation in generator mode. The negative iso-power lines reflect that energy can be stored into the batteries when the EMs work in this region. It is worth noting that when the motor is working in the lower quadrant, at low speeds, it cannot regenerate. However, a braking action can be still exerted upon providing energy from the battery (red triangle in Figure A.7).

Table A.1: Specifications of the employed motor model

Torque/Power @ 800 V	
Motor type	Switched reluctance
Peak (30 s)	200 Nm, 100 kW
Nominal (continuous)	135 Nm, 42 kW
Maximum speed	14000 rpm
Motor weight	50 kg

The on-board EMs architecture implies a connection to the wheels through a gearbox and half-shafts (Figure 4.1). Half-shafts have been demonstrated to produce a negative influence of the vehicle drivability and braking comfort [114]. The effect of the half-shaft dynamics are not explicitly investigated in the framework of this study as major attention is paid to the EHB. For this reason, the half-shafts dynamics is combined with the EMs dynamics and modelled by means of a first order transfer function. For a better understanding of the half-shaft dynamics and its validation, the interested reader is referred to [112]. The transient operation of EMs is described by means of a first-order transfer function:

$$\frac{T_{EM,ij}}{T_{EM,ij}^{dem}} = \frac{1}{0.0022s+1}e^{-0.0022s}, \tag{A.16}$$

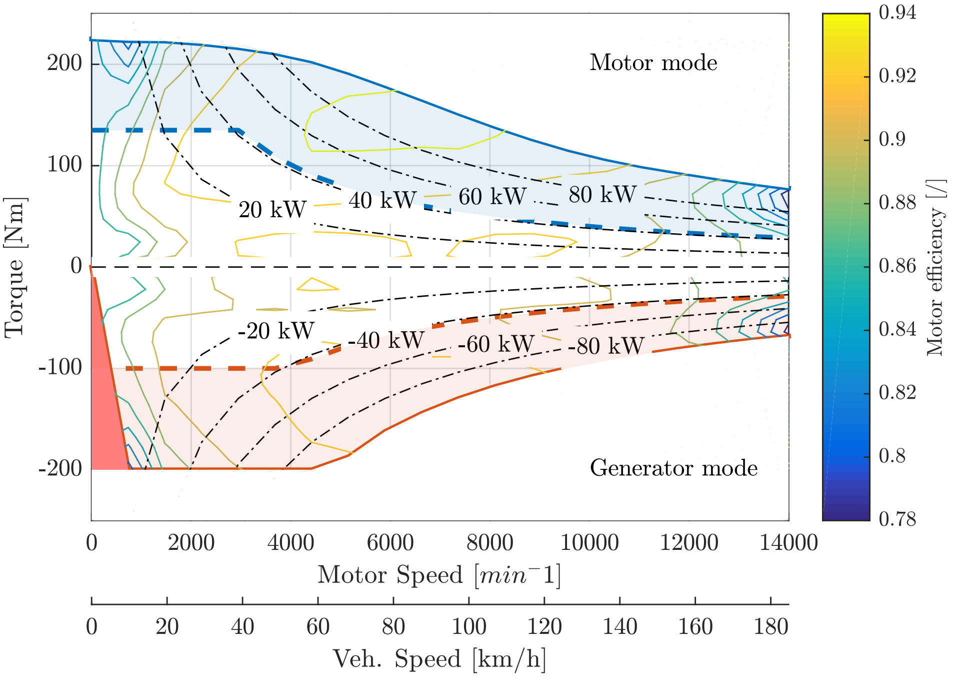

Figure A.7: *Characteristics of the switched reluctance on-board motors used in the simulation framework.*

where, $T_{EM,ij}^{dem}$ represents the torque demand and $T_{EM,ij}$ is the actual torque provided by the EMs.

A.2.3 Electrohydraulic brake system

The electrohydraulic brake (EHB) at Technische Universität Ilmenau is based on the slip control boost (SCB) technology by ZF TRW. A schematic of the EHB system is reported in Figure A.8. The notations FL, FR, RL and RR indicate the front left, front right, rear left and rear right corners respectively. The experimental campaign herein presented is aimed at exploring the dynamics of the EHB and realising a model that can be used for MIL/SIL simulations. In the case of HIL simulations the EHB finds physical realisation.

The EHB system finds wide use in electric vehicles because it ensures smooth coordination between conventional and regenerative brakes without the driver noticing it. The EHB has very good dynamics characteristics and accurate pressure tracking capabilities relative to a conventional automotive braking system with vacuum booster. Such a system also ensures faster response time, more flexible packaging and better integration with other chassis and powertrain control systems. This system features several operational modes; among others, the base brake control (BBC) and the anti-lock braking system (ABS).

In the BBC mode, when the driver steps on the brake pedal, the pedal stroke is measured, sent to the vehicle control unit (VCU) and converted into the reference vehicle deceleration level. A brake pedal force emulator provides force feedback to the driver.

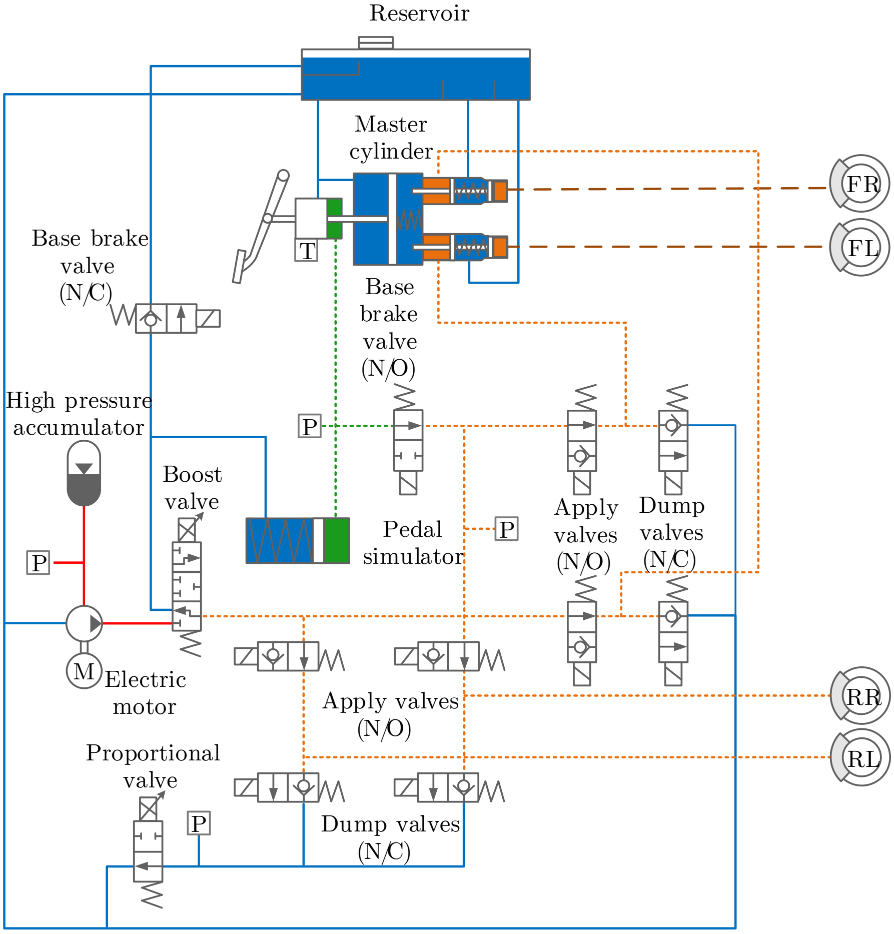

Figure A.8: *Simplified hydraulic schematic of the SCB unit. N/O: Normally open; N/C: Normally closed. P symbol represents a pressure sensor, T indicates hydraulic connection with the fluid reservoir.*

The VCU determines the total demanded braking torque and, according to the brake torque distribution rule, calculates the demanded brake pressure for each calliper. During this mode, the base brake valves are activated and the boost valve proportionally controls the pressure from the high pressure accumulator. The high pressure accumulator is charged up to 180 *bar* by the electric pump to ensure a fast system response during the pressure increase phases. Hence, the brake pressure on the wheels is continuously modulated in accordance with the algorithm of the electrohydraulic control unit (EHCU).

During the ABS mode, the four apply valves are activated due to excessive wheel slip to isolate the brake callipers from the boost valve. Thereafter, all apply and dump valves are individually controlled to modulate the pressure for each brake and reach the required wheel slip reference. The ABS is activated as soon as the wheel slip reaches a certain threshold. In order to reduce the wheel slip, by producing an acceleration of the wheel, the pressure in the corresponding brake calliper is released until a certain system state is reached, corresponding to either a wheel slip or acceleration threshold. After the new state is reached, pressure can be increased again. The frequency of these control loops is about 3 Hz [115] as long as significant deviations between the actual speed and the reference wheel speed occur.

EHB system characterisation

An experimental campaign was conducted at Technische Universität Ilmenau to investigate the dynamics of the EHB. The experimental campaign was aimed at identifying a model of the hydraulic brake pressure dynamics to be used for MIL/SIL simulations. The tests were aimed at determining the brake pressure response characteristics by considering:

- the dead time t_d, i.e. the time required to achieve 1 bar variation of the actual calliper pressure from the instant when a pressure step is requested;
- the rise time t_r, i.e. the time required for the actual pressure to reach 90% of the steady state reference value.

The above-defined time constants were assessed from a test repeated 10 times, consisting of 13 steps with 10 bar pressure increase across consecutive manoeuvres. For a matter of clarity, only the results referring to the front-left calliper are reported in Figure A.9a and Figure A.9b for the dead time t_d and the rise time t_r, respectively. The error bars represent the mean and standard deviation of the measured values for the 10 test repetitions. Figure A.10a shows the demanded and actual pressure profiles averaged across 10 tests. During the test, it was noticed that the system features different dead time characteristics during the build-up and release phases, respectively. Conversely, a clear separation in the rise time was not noticed between the build-up and release phases. No remarkable differences were noticed between front and rear brakes in terms of pressure dynamics.

The results prove the non-linearity of the system and demonstrate a clear dependence of the time constants versus the demanded pressure. For the sake of simplicity, the circuit dynamics and the overshoot during pressure build-up were captured by means of second order linear transfer functions with time delay [47]. To ensure good modelling performance, two models were identified for the build-up and release phases, respectively. The model was defined so that the demanded pressure represents the system input and the actual pressure is the output. This leads to the second-order linear model in Equations (A.17) and (A.18):

$$\frac{p_{b,ij}}{p_{b,ij}^{dem}\uparrow} = \frac{1}{0.00075s^2 + 0.037s + 1}e^{-0.026s}, \tag{A.17}$$

$$\frac{p_{b,ij}}{p_{b,ij}^{dem}\downarrow} = \frac{1}{0.00021s^2 + 0.045s + 1}e^{-0.015s}. \tag{A.18}$$

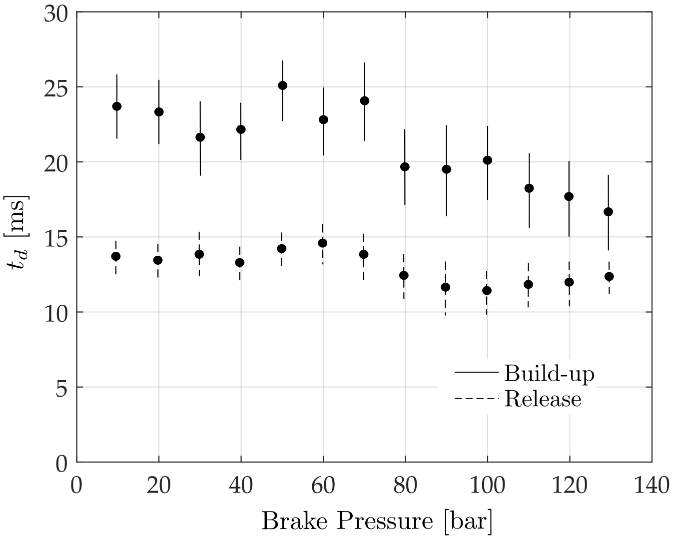

(a) *Error bars of the front-left calliper pressure dead time for the build-up and release phase, respectively.*

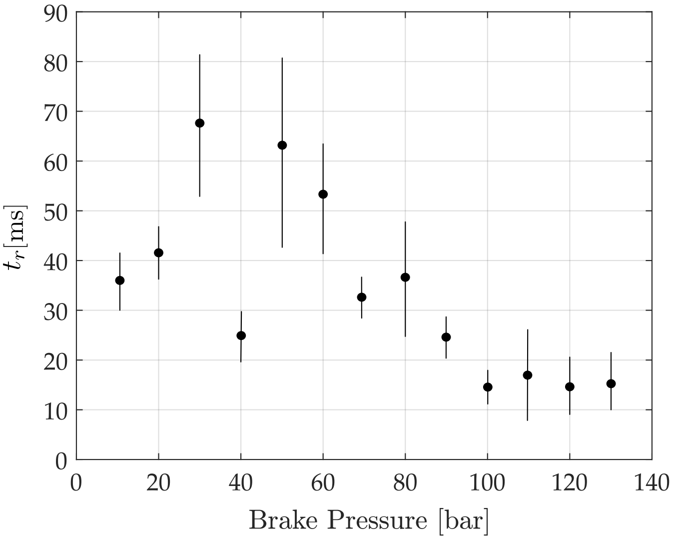

(b) *Error bars of the front-left calliper pressure rise time.*

Figure A.9: *Time constants of the EHB unit. The results refer to 10 repeated staircase tests consisting of 13 steps with 10 bar pressure increase.*

It is worth pointing out that during the measurement campaign a clear offset between demanded and measured pressure was observed for higher pressure values as reported in Figure A.10a. This is due to the limitations of the proprietary low-level control algorithm embedded into the EHB unit. Nevertheless, the model includes an inverse map to compensate the pressure offset. A qualitative assessment of the estimation accuracy of the proposed model is reported in Figure A.10a and conveniently zoomed in Figure A.10b.

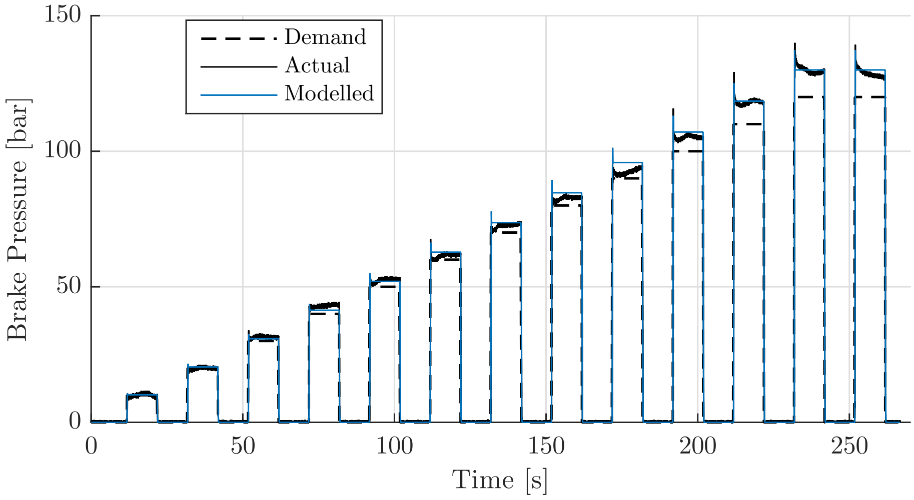

(a) *Average pressure profiles resulting from 10 staircase test repetitions.*

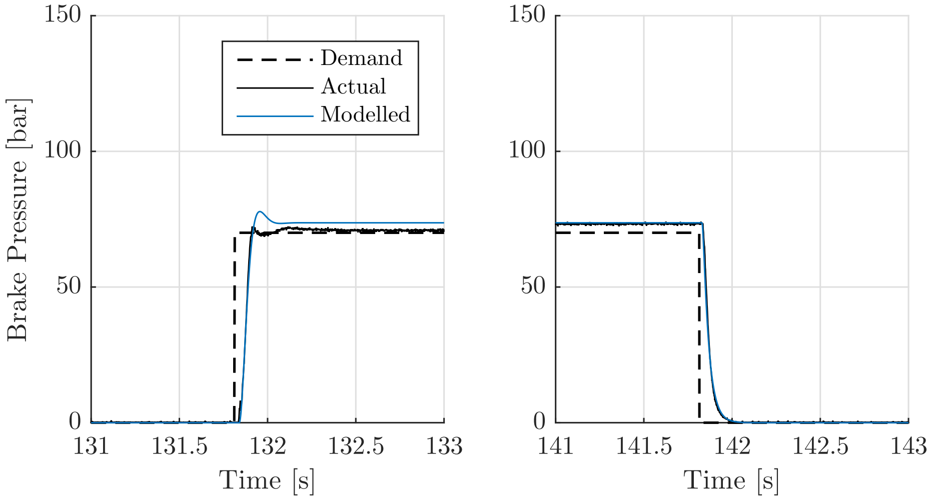

(b) *Zoom on the 7th staircase manoeuvre.*

Figure A.10: *Results of the characterisation procedure of the EHB dynamics by means of second order transfer functions. The profiles refer to the front-left brake calliper.*

A.2.4 Brake lining friction coefficient model

ILVO model presented in Chapter 3 is employed to render the disc brake temperature and BLCF dynamics. The model allows for improved fidelity of the SIL/MIL/HIL simulations because it accounts for the BLCF dependence against speed, pressure and temperature. The pressure set by the EHCU in the callipers actuates the brake cylinders, which in turn produce a friction force between brake pad and disc. Upon calculating the BLCF, the brake torque follows Equation (A.19):

$$T_{b,ij} = 2n_p\mu_{b,ij}\frac{\pi d_p^2}{4}(p_{b,ij} - p_0)r_{eff,i}, \tag{A.19}$$

where, n_p is the number piston calliper per side, μ_b is the BLCF, d_p is the calliper piston diameter, p_0 is the push-out pressure, r_{eff} is the effective brake disc radius. In the framework of these simulations, the parametrisations of Brake A and B of Chapter 3 have been used to simulate the front and rear brakes of the full electric SUV model. The initial brake temperature must be specified before the simulation starts to account for the initial brake thermal state.

Appendix B

Principal component analysis

B.1 General remarks

The principal component analysis (PCA) is a statistical tool that takes high-dimensional data and represents it in a lower-dimensional space. The main goal of PCA is to summarise the correlations among a set of observed variables with a smaller set of linear combinations, namely principal components (PCs). The first principal components is defined as the direction along which the data exhibit their maximum variation. The seond principal component is the direction that maximises the variance among all directions orthogonal to the first. Analogously, the j^{th} components is the direction orthogonal to all previous $j^{th} - 1$ components that maximises the variance. Therefore, the identification of the PCs reduces to the solution of an optimisation problem where the function variance should be maximised. This chapter presents the approach that led to the identification of the PCs for the case study in Chapter 3.

B.2 Identification of the principal components

Considering a $p-$dimensional space, the first step consists in selecting a generic direction in this space, identified by the unit vector $\mathbf{v}$. A $p-$dimensional space means that each $i - th$ point $\mathbf{x}_i$ has p dimensions. The same holds for the sought variance-maximising direction $\mathbf{v}$. The dinstance orthogonal to the unit vector $\mathbf{v}$ of a generic point $\mathbf{x}_i$ is defined in accordance with Equations (B.1a) to (B.1f):

$$\begin{aligned}
d_i &= \left\|\mathbf{x}_i - \mathbf{v}(\mathbf{x}_i \cdot \mathbf{v})\right\|^2, && \text{(B.1a)}\\
&= (\mathbf{x}_i - \mathbf{v}(\mathbf{x}_i \cdot \mathbf{v})) \cdot (\mathbf{x}_i - \mathbf{v}(\mathbf{x}_i \cdot \mathbf{v}), && \text{(B.1b)}\\
&= \mathbf{x}_i \cdot \mathbf{x}_i - \mathbf{x}_i \cdot \mathbf{v}(\mathbf{x}_i \cdot \mathbf{v}) - \mathbf{v} \cdot \mathbf{x}_i(\mathbf{x}_i \cdot \mathbf{v}) + \mathbf{v} \cdot \mathbf{v}(\mathbf{x}_i \cdot \mathbf{v})^2, && \text{(B.1c)}\\
&= \|\mathbf{x}_i\|^2 - 2(\mathbf{x}_i \cdot \mathbf{v})^2 + \mathbf{v} \cdot \mathbf{v}(\mathbf{x}_i \cdot \mathbf{v})^2, && \text{(B.1d)}\\
&= \|\mathbf{x}_i\|^2 - 2(\mathbf{x}_i \cdot \mathbf{v})^2 + (\mathbf{x}_i \cdot \mathbf{v})^2, && \text{(B.1e)}\\
&= \|\mathbf{x}_i\|^2 - (\mathbf{x}_i \cdot \mathbf{v})^2. && \text{(B.1f)}
\end{aligned}$$

This holds for any point belonging to the data (Figure B.1). Thereafter, it is possible to define the average distance MSE of the points in the $p-$dimensional space with respect to the the direction identified by $\mathbf{v}$:

$$\begin{aligned}
MSE(\mathbf{v}) &= \frac{1}{n}\sum_{i=1}^{n}\left(\|\mathbf{x}_i\|^2 - (\mathbf{x}_i \cdot \mathbf{v})^2\right), && \text{(B.2a)}\\
&= \frac{1}{n}\left(\sum_{i=1}^{n}\|\mathbf{x}_i\|^2 - \sum_{i=1}^{n}(\mathbf{x}_i \cdot \mathbf{v})^2\right). && \text{(B.2b)}
\end{aligned}$$

The original problem of fiding the variance-maximising direction is totally equivalent to looking for the projection with the smallest average mean squared distance, Equation (B.2a), between the data point and their orthogonal projections on to the vector $\mathbf{v}$. As the first term in Equation (B.2b) does not depend on $\mathbf{v}$, the mean squared distance can only be reduced by maximising the second term, viz. $\left(\frac{1}{n}\sum_{i=1}^{n}(\mathbf{x}_i \cdot \mathbf{v})^2\right)$. Using the definition of variance of a variable, the problem therefore reduces to Equation (B.3):

$$\frac{1}{n}\sum_{i=1}^{n}(\mathbf{x}_i \cdot \mathbf{v})^2 = \left(\frac{1}{n}\sum_{i=1}^{n}\mathbf{x}_i \cdot \mathbf{v}\right)^2 + Var[\mathbf{x}_i \cdot \mathbf{v}]. \quad \text{(B.3)}$$

As the sought direction $\mathbf{v}$, will be centered with respect to the data point, the first term of Equation (B.3) is zero. Hence, minimising the residuals, Equation (B.2), turns out to be equivalent to maximising the variance of the projections, Equation (B.3). Hereafter, it is worth adopting a matrix representation where the data point are stacked into a $n \times p$ matrix $\mathbf{X}$. The variance is therefore expressed as:

$$\begin{aligned}
\sigma_{\mathbf{v}}^2 &= \frac{1}{n}\sum_{i=1}^{n}(\mathbf{x}_i \cdot \mathbf{v})^2, && \text{(B.4a)}\\
&= \frac{1}{n}(\mathbf{X}\mathbf{v})^T(\mathbf{X}\mathbf{v}), && \text{(B.4b)}\\
&= \frac{1}{n}\mathbf{v}^T\mathbf{X}^T\mathbf{X}\mathbf{v}, && \text{(B.4c)}\\
&= \mathbf{v}^T\frac{\mathbf{X}^T\mathbf{X}}{n}\mathbf{v}, && \text{(B.4d)}\\
&= \mathbf{v}^T cov(\mathbf{X},\mathbf{X})\mathbf{v}, && \text{(B.4e)}
\end{aligned}$$

where the term $\mathbf{Xv}$ represents the projections and $\frac{\mathbf{X}^T\mathbf{X}}{n}$ is the covariance matrix of the given data. The optimisation problem is of constrained type as the solution only accepts unit vectors for $\mathbf{v}$. The constrained problem is turned into an unconstrained problem by using the Lagrange multipliers [116]. For the problem under consideration:

$$\mathcal{L}(\mathbf{v}, \lambda) = \sigma_{\mathbf{v}}^2 - \lambda(\mathbf{v}^T\mathbf{v} - 1), \tag{B.5a}$$

$$\frac{\partial \mathcal{L}}{\partial \lambda} = \mathbf{v}^T\mathbf{v} - 1, \tag{B.5b}$$

$$\frac{\partial \mathcal{L}}{\partial \mathbf{v}} = 2\, cov(\mathbf{X}, \mathbf{X})\, \mathbf{v} - 2\lambda\, \mathbf{v}. \tag{B.5c}$$

By imposing the derivatives in Equations (B.5b) and (B.5c) to zero, the following Equations (B.6a) and (B.6b) hold valid:

$$\mathbf{v}^T\mathbf{v} = 1, \tag{B.6a}$$

$$cov(\mathbf{X}, \mathbf{X})\, \mathbf{v} = \lambda\, \mathbf{v}. \tag{B.6b}$$

Hence, the sought vector $\mathbf{v}$ is seen as the eigenvector of the covariance matrix, which also represent the PCs of the data point. The eigenvectors alone describe the PCs of the data points in the $p-$dimensional space; the eigenvalues define the relative contribution of each PC to the data variance. The first PC is therefore associated with the largest eigenvalue λ_1. The second principal component, is the direction orthogonal to the first component with the most variance. As the PCs are orthogonal to each other, their projections are not correlated. The dimensionality reduction can be performed by truncating the system to a few PCs, leading to a subspace of $q-$dimensionality. The variance of the projections on to the first q principal components is thus $\sum_{j=1}^{q} \lambda_j$. As an example, PCs are found for the reduced CPC experimental set of Chapter 3, composed of the control variable initial temperature and the computed average BLCF in the two-dimensional space (Figure B.1).

In Figure B.1, the normalised data, indicated as red dots in the two-dimensional space, feature two PCs. PC1 identifies more than 80% of the variance in the data, whilst PC2 is liable for less than 20%. Although the PCs have been computed by solving Equation (B.6), it can be visually assessed that the PCs identify the direction along which Equation (B.2) is minimised, thus in accordance with the premises of this section.

It is worth pointing out that the PCA provides different results depending on whether the variable under analysis are standardised. In presence of variables featuring different scales, the PCA must be performed on the correlation matrix, rather than the covariance matrix. The correlation matrix provides a proper standardisation of the data, making these latter comparable to each other.

B.3 Correlation analysis

In Chapter 3, the PCA is used to assess the relative importance of the control variables initial disc sliding speed, initial disc temperature and brake pressure against the average

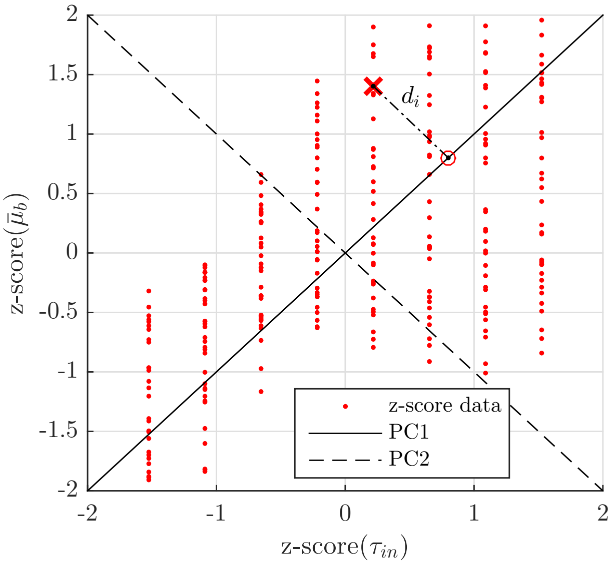

Figure B.1: *PCs for the two-dimensional space defined by the control variable initial disc temperature and the computed average BLCF.*

BLCF. The latter variables are extracted from the CPC data set and stacked in the form of a $n \times 4$ matrix $\mathbf{X}$, being n the number of observations. PCA is then applied to compute the PCs, showing that more than 90% of the variance is described by the first three PCs (Figure B.2). Therefore, without loss of too much information, the system can be reduced to a three-dimensional space.

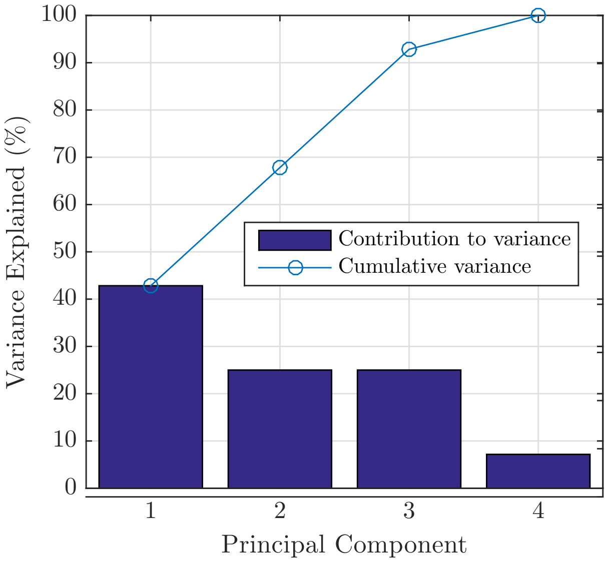

Figure B.2: *Pareto diagram for the four PCs in the space of data identified by CPC on Brake A.*

The PCs represent a linear combination of the four variables (Table B.1) and the corresponding eigenvalues provide information of the contribution of each PC to the data variance (Figure B.2). Additional information is drawn by visualising the new variable in the reduced order space. The reference of representation is changed, so that the PCs form the new orthogonal reference. The system variables are represented on a graph by a vector, and the direction and length of the vector indicate how each variable contributes to the three PCs (Figure B.3).

Table B.1: Orthonormal PC coefficients for each variable. From CPC, Brake A.

	PC1	PC2	PC3
v_{in}	-0.0961	0.9907	0
p_b	0.3656	0.0709	0.8530
τ_{in}	0.5976	0.1159	-0.5218
$\bar{\mu}_b$	0.7071	0	0

For example, the first principal component, which is on the horizontal axis in Figures B.3a and B.3b, has positive coefficients for all variables, except the initial sliding speed. The largest coefficient in the first principal component is the fourth (Table B.1), corresponding to the BLCF. The second principal component, which is on the vertical axis in Figure B.3a, has a very clear positive coefficient for the variable initial sliding speed and very small coefficients for other variables. The third principal component, which is on the vertical axis in Figure B.3b, has a very clear positive coefficient for the variable brake pressure and a negative coefficient for the variable initial disc temperature. This type of visual tool also allows to visualise the experimental data point, with coordinates indicating the score of each observation for the three principal components. For example, points near the left edge of the plot have the lowest scores for the first principal component.

It is important noticing that the control variables vectors, i.e. initial sliding speed, brake pressure and initial brake temperature, represent an orthogonal reference. This is by definition due to the full factorial DOE, where the control variables are varied one at a time. The relative importance of each input variable can be computed by projecting, through a scalar product, the vector of a control variable onto the vector of the average BLCF:

$$ri = \frac{\boldsymbol{\bar{\mu}_b} \cdot \{\boldsymbol{v_{in}}, \boldsymbol{p_b}, \boldsymbol{\tau_{in}}\}}{\|\boldsymbol{\bar{\mu}_b}\|}. \tag{B.7}$$

The results of this procedure carried out across the CPC data demonstrates that the contact temperature identifies more than 60% of the variance in the average BLCF. Although the results are well comparable with the rank partial correlation analysis [117], this tool allows for a graphical assessment of the interdependence between variables.

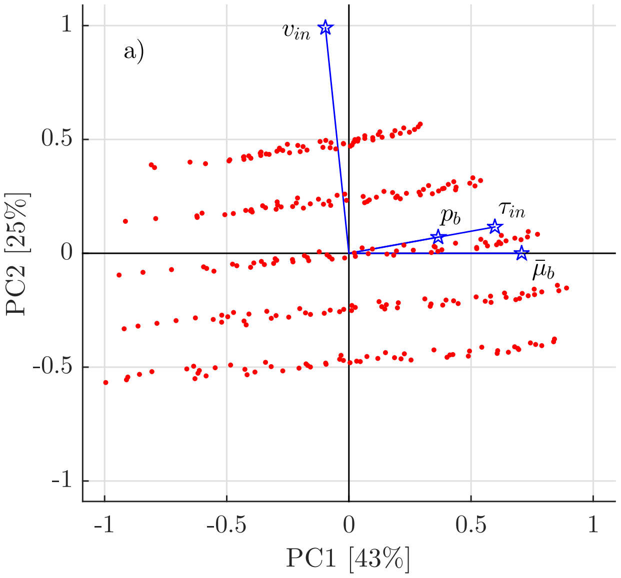

(a) *Projection onto the PC1-PC2 plane.*

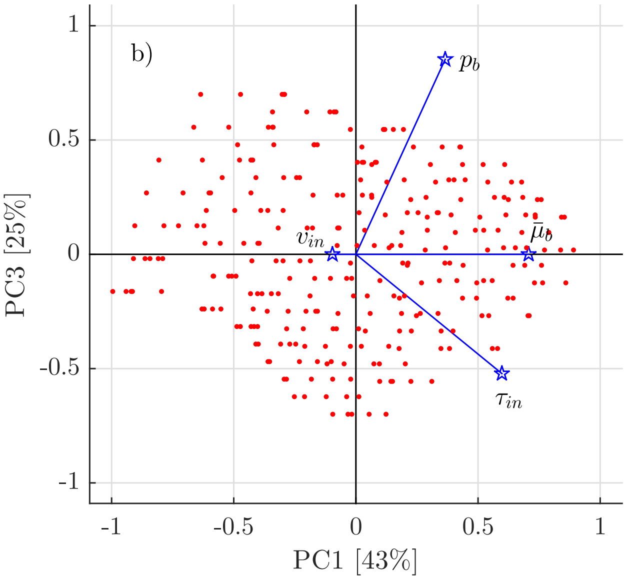

(b) *Projection onto the PC1-PC3 plane.*

Figure B.3: *Graphic visualisation of the variables' vectors (blue markers) and the data point (red dots) in the orthogonal reference identified by the PCs. From CPC, Brake A.*

Appendix C

Data driven method for model identification

C.1 Problem discretisation

Data driven methods (DDM) are capable of extracting functional relationships from measurement data [118]. In the present work, the optimisation problem aims at identifying the differential equations that better fit the experimental data. The generic differential equation for the state variable $\bar{\mathbf{x}}$ can be formulated according to C.1:

$$\dot{\mathbf{x}} = \mathbf{f}\left(\mathbf{x}, \mathbf{u}, \mathbf{w}\right), \tag{C.1}$$

where, the right hand contains the time invariant functions that resembles various linear and nonlinear components in accordance with the true state variables, input variables and the model parameters, $\mathbf{x}$, $\mathbf{u}$ and $\mathbf{w}$ respectively. With reference to the developed friction model, the state and input vectors can be expressed as C.2 and C.3, respectively:

$$\mathbf{x} = \left[\omega, \tau, \alpha_b\right]^T, \tag{C.2}$$

$$\mathbf{u} = p_b, \tag{C.3}$$

and $\mathbf{w}$ represent the set of sought parameters. To derive the function, a library of candidate terms $\mathbf{F}\left(\mathbf{x}, \mathbf{u}, \mathbf{w}\right)$ is considered. Furthermore, each candidate term is normalised so that the magnitude of each element in $\mathbf{w}$ reflects the relative importance of the corresponding component.

Equation (C.1) is rewritten with reference to the estimated state variable $\hat{\mathbf{x}}$ and discretised by means of the explicit Runge-Kutta fourth-order method. The discrete differential equation becomes:

$$\mathbf{\hat{x}_{k+1}} = \mathbf{\hat{x}_k} + \frac{1}{6}(\mathbf{z_1} + 2\mathbf{z_2} + 2\mathbf{z_3} + \mathbf{z_4}), \tag{C.4a}$$

$$\mathbf{z_1} = \Delta t\, \mathbf{F}(\mathbf{\hat{x}_k}, \mathbf{u_k}, \mathbf{w}), \tag{C.4b}$$

$$\mathbf{z_2} = \Delta t\, \mathbf{F}(\mathbf{\hat{x}_k} + \frac{\mathbf{z_1}}{2}, \frac{\mathbf{u_k} + \mathbf{u_{k+1}}}{2}, \mathbf{w}), \tag{C.4c}$$

$$\mathbf{z_3} = \Delta t\, \mathbf{F}(\mathbf{\hat{x}_k} + \frac{\mathbf{z_2}}{2}, \frac{\mathbf{u_k} + \mathbf{u_{k+1}}}{2}, \mathbf{w}), \tag{C.4d}$$

$$\mathbf{z_4} = \Delta t\, \mathbf{F}(\mathbf{\hat{x}_k} + \mathbf{z_3}, \mathbf{u_{k+1}}, \mathbf{w}), \tag{C.4e}$$

where, the index k refers to a time step of length Δt and $\mathbf{z_1}$ to $\mathbf{z_4}$ represent the intermediate discrete increments. In the case $\mathbf{z_2}$ to $\mathbf{z_4}$ are zero and the multiplicating coefficient in Equation (C.4a) is changed to $\frac{1}{2}$, the simple first-order Euler explicit is obtained. In the fourth-order Runge-Kutta higher accuracy can be reached by averaging the four increments. Thereafter, the problem reduces to determining the optimal set of parameters $\mathbf{w}$ that minimise the quadratic error function J, defined as:

$$J = \min_{\mathbf{w}} \left\| \mathbf{y} - \mathbf{\hat{y}} \right\|^2, \tag{C.5a}$$

$$= \min_{\mathbf{w}} \left\| \mathbf{y} - \mathbf{H}\, \mathbf{\hat{x}} \right\|^2, \tag{C.5b}$$

$$= \min_{\mathbf{w}} \sum_{k=1}^{N-1} (\mathbf{y_{k+1}} - \mathbf{H}\, \mathbf{\hat{x}_{k+1}})^2, \tag{C.5c}$$

with the initial condition given by:

$$(\mathbf{x_0} = \mathbf{H^{-1}}\, \mathbf{\hat{y}_0}). \tag{C.6}$$

In the previous equations, N represent the total number of discrete points, $\mathbf{y}$ and $\mathbf{\hat{y}}$ represent the measured and estimated output vector respectively, $\mathbf{H}$ is the time-invariant output matrix, relating the system states and outputs. The initial condition at $k = 0$ has been purposely removed from the sum since its value is computed based on the initial measurment vector (Equation (C.6)). The initial condition must be provided to launch the optimisation procedure.

With reference to the CPC data of Brake A in Chapter 3, Figures C.1a and C.1b help visualise the cost function in Equation (C.5c). Because of the quadratic cost function, the optimisation problem of the models under analysis is of convex type. Figures C.1a and C.1b also represent the trajectory of the search algorithm in the parameters space of ILVO and Ostermeyer, respectively. Both the non-linear least square method (LSQ) [119] and the derivative-free simplex search method (DSS) [70] converge to the same global minimum. However, being the LSQ a derivative based method, it converges to the solution much faster. For this reason, this algorithm was selected for the optimisation tasks.

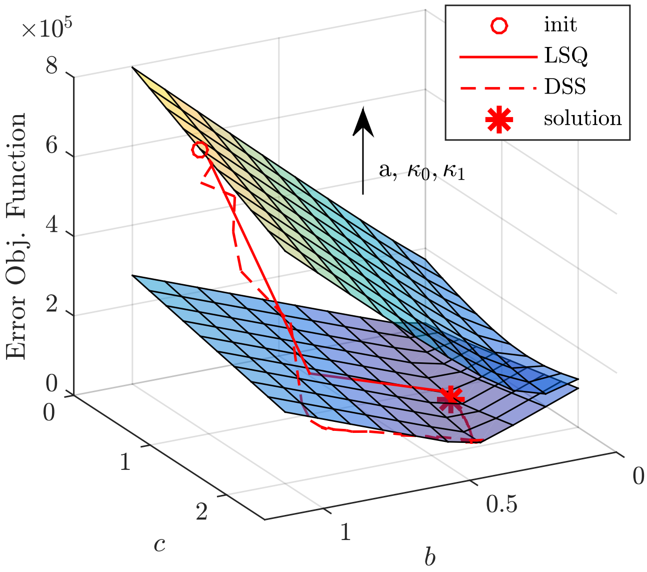

(a) *Convergence to the optimal solution of ILVO model identified on CPC data, Brake A.*

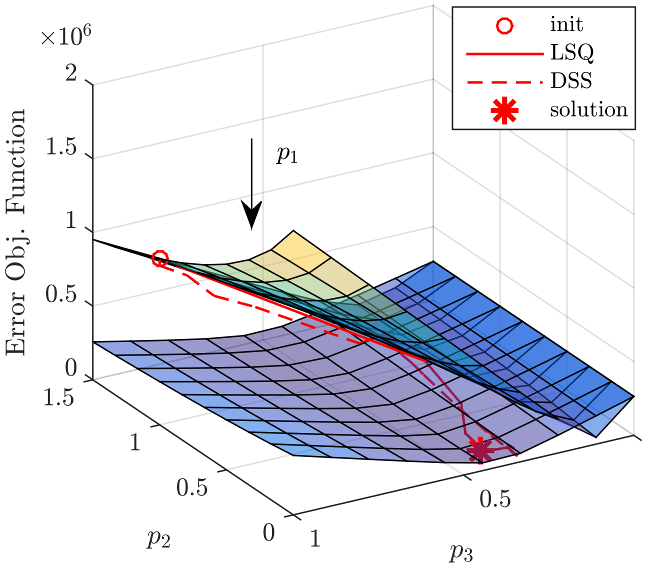

(b) *Convergence to the optimal solution of the Ostermeyer's model identified on CPC data, Brake A.*

Figure C.1: *Representation of the error objective function of Equation* (C.5c) *for the models benchmarked in Chapter 3. The problem is convex and a global minimum exists. The parameter have been standardised.*

Table C.1 reports the brake lumped temperature model parametrisation and Tables C.2 and C.3 report the BLCF models parametrisations.

TABLE C.1: Lumped capacitance model parametrisation.

Parameter	Value			Unit
	Brake A	Brake B	Brake C	
ξ	$0.2111 \cdot 10^{-3}$	$0.2668 \cdot 10^{-3}$	$0.1700 \cdot 10^{-3}$	$[m^{-1}N^{-1}K]$
$\delta_{ht,0}$	$0.1792 \cdot 10^{-2}$	$0.1547 \cdot 10^{-2}$	$0.2141 \cdot 10^{-2}$	$[s^{-1}]$
$\delta_{ht,1}$	$0.9108 \cdot 10^{-3}$	$0.7859 \cdot 10^{-3}$	$1.088 \cdot 10^{-3}$	$[m^{-1}]$

TABLE C.2: ILVO model parametrisation

Parameter	Value			Unit
	Brake A	Brake B	Brake C	
a	10^{-9}			$[m^3N^{-1}]$
κ_0	0.2687	0.1127	0.1854	$[/]$
κ_1	$0.3075 \cdot 10^{-3}$	$0.6395 \cdot 10^{-3}$	$0.4405 \cdot 10^{-3}$	$[K^{-1}]$
b	$0.2302 \cdot 10^{-1}$	$0.1640 \cdot 10^{-1}$	$0.2034 \cdot 10^{-1}$	$[m]$
c	$1.226 \cdot 10^{-10}$	$1.380 \cdot 10^{-10}$	$0.9605 \cdot 10^{-10}$	$[m^4N^{-1}K^{-1}s^{-1}]$

TABLE C.3: Ostermeyer's model parametrisation.

Parameter	Value			Unit
	Brake A	Brake B	Brake C	
p_1	$0.1123 \cdot 10^{-4}$	$2.918 \cdot 10^{-4}$	$0.2161 \cdot 10^{-4}$	$[m^{-1}N^{-1}]$
p_2	$0.3604 \cdot 10^{7}$	$0.6679 \cdot 10^{6}$	$0.1528 \cdot 10^{7}$	$[mNs^{-1}]$
p_3	$0.3599 \cdot 10^{4}$	$0.7008 \cdot 10^{3}$	$0.1478 \cdot 10^{4}$	$[mNK^{-1}s^{-1}]$

Appendix D

Experimental vehicles

D.1 Full electric sport utility vehicle

The full electric sport utility vehicle modelled in the IPG CarMaker® and used as vehicle demonstrator for the BLCF observer validation in Chapter 6 is the Range Rover Evoque of Figure D.1 provided by Flander's Make (Lommel, Belgium). The vehicle powertrain consists of 4 switched reluctance motors, each with a separate switched reluctance inverter unit. During the tests, the two on-board motors powering the front semi-axles are deactivated. The drivetrain is connected to a 600 V battery pack. The EHB is the ZF TRW SCB discussed in Appendix A and features a variable torque distribution that depends on the braking conditions. The vehicle technical specifications are reported in table D.1.

Figure D.1: *Range Rover Evoque at Flander's Make.*

The main motor generator unit is controlled by dSPACE MicroAutoBox®. The digital acquisition system is based on the processor board dSPACE DS1007®. For the CAN communication, the interface board DS4302® is used. Analog input signals information are digitalised by multi-channel A/D board DS2004®. The control of the brake actuators is realised through the digital input/output board DS4004®. Signals are sampled with

TABLE D.1: Specifications of the full electric sport utility vehicle demonstrator.

Vehicle type	Range Rover Evoque 5-doors
Curb mass	2105 kg
Driveline	Individual 4 wheel drive
Tyre size	235/55 R19
Wheelbase	2665 mm
Track width	1625 mm
Drag coefficient	0.35
Frontal surface	2.32 m^2
Motor type	4 Switched Reluctance motors
Nominal/Peak power	42 $kW(135\ Nm)/100\ kW(200\ Nm)$
Maximum motor speed	15000 rpm
Gearbox	Single-speed 1 : 10
Battery cell type	Lithium-titanate Oxide
Battery pack	600 VDC
Foundation brake	Floating callipers, cast-iron discs, copper-free ECE brake linings
Brake type	Slip Control Boost (ZF TRW)
Torque allocation front/total	Variable
Nominal brake μ_b front/rear	0.45/0.45
Effective brake radius front/rear	120.5/128.8 mm
N. of pistons front/rear	1/1
Calliper piston(s) diameter front/rear	60/34 mm

typical fast CAN Baud rate of 500 kbit/s. The EHB unit, in analogy with the HIL platform introduced in Chapter 5, uses the driver's braking request via the pedal travel sensor, calculates the total braking torque required to achieve the desired deceleration, and apportions the torque to the four wheels. The demand can be either a conventional pressure request or a reference torque for the electric motors.

The vehicle is equipped with the following measurement devices: wheel speed sensors on each wheel; inertial measurement unit (IMU) for acceleration and yaw rate; brake pressure sensors. A CORREVIT S350® non-contact 2-axis optical sensor is fitted to the vehicle to measure the vehicle ground speed. The measurement provided by the optical sensor is then used to estimate the wheels longitudinal slip. For direct measurement of wheel forces in longitudinal, lateral and vertical directions and wheel moments, the vehicle demonstrator is instrumented with two wheel force sensors RoaDyn S635® produced by Kistler. During the tests execution, the wheel force sensors have been mounted on the front axles. The technical data of the sensor are given in table D.2.

Figure D.2: *Kistler RoaDyn S635® wheel force sensor.*

TABLE D.2: Kistler RoaDyn S635® wheel force sensor specifications.

Measuring range		Accuracy	
F_X	$-35...35\ kN$	Crosstalk	
F_Y	$-20...20\ kN$	$F_Y \rightarrow F_X, F_Z$	$\leq 1\ \%$
F_Z	$-35...35\ kN$	$F_X \leftrightarrow F_Z$	$\leq 1\ \%$
M_X	$-5...5\ kNm$	$F_X, F_Z \rightarrow F_Y$	$\leq 0.2\ \%$
M_Y	$-5...5\ kNm$	Linearity	$\leq 0.5\ \%$ v.E
M_Z	$-5...5\ kNm$	Hysteresis	$\leq 0.5\ \%$ v.E
Rotary angle accuracy	$\approx 0.1°$	Maximum speed	2300 rpm ($\approx$ 280 km/h)

D.2 Conventional ICE sedan

The conventional internal combustion engine sedan is used to assess brake-related wear under real driving conditions. The vehicle technical specifications are reported in Table D.3. The data logging of relevant vehicle kinematics quantities is performed by means of the proprietary RaceLogic VBoX®. The VBoX-Datalogger® allows for CAN-bus data communication with a sampling rate up to 100 Hz. This device also includes a high accuracy GPS for the tracking of the vehicle speed with a resolution up to 0.1 km/h. The acquisition of relevant data via CAN is done by National Instruments cDAQ (9178)®. This latter is also used to log analogue signals coming from pressure and temperature sensors. The brake pressure is measured with a pressure transducer connected to the brake calliper, while two rubbing thermocouple of type K (NiCr-Ni) are surface-mounted on the inner and outer disc side of each corner for temperature measurements. The data acquired via CAN bus include IMU accelerations and yaw rate, brake pedal position, steering wheel angle, wheel speed signals.

TABLE D.3: Specification of the sports sedan.

Vehicle type	Sedan
Curb mass	2100 kg
Driveline	RWD with automatic transmission
Tyre size	275/40 $R19$
Wheelbase	3070 mm
Track width	1649 mm
Drag coefficient	0.26
Frontal surface	2.54 m^2
Engine type	Turbo diesel 3 l
Foundation brake	Floating callipers, cast-iron discs, copper-free ECE brake linings
Torque allocation front/total	0.685
Nominal brake μ_b front/rear	0.43/0.39
Effective brake radius front/rear	133/138 mm
N. of pistons front/rear	1/1
Calliper piston(s) diameter front/rear	60/42 mm

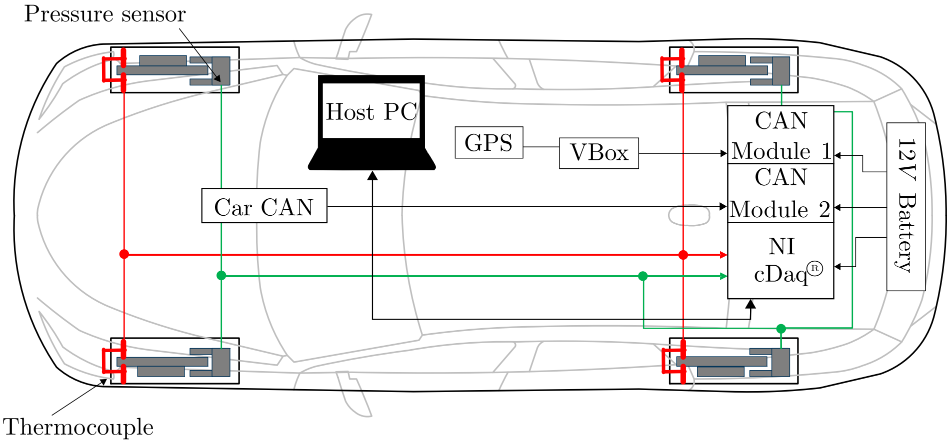

Figure D.3: *Schematic of the instrumented sedan used for RDE-compliant brake-related wear tests.*

D.3 Conventional ICE light commercial vehicle

The light commercial vehicle equipped with a portable emissions measurement system (PEMS) in Figure D.4 is used to assess brake-related particulate number concentration under RDE-compliant driving conditions. The vehicle technical specifications are reported in table D.4.

The particulate emitted by the front-right brake system is evacuated by means of the closed CVS-sampling system engineered and developed at Technische Universität Ilmenau [12]. The PEMS-PN MAHA-AIP is used to measure particulate number concentrations (PNC) in the range 23 nm to 2.5 μm. The brakes are equipped with rubbing thermocouples

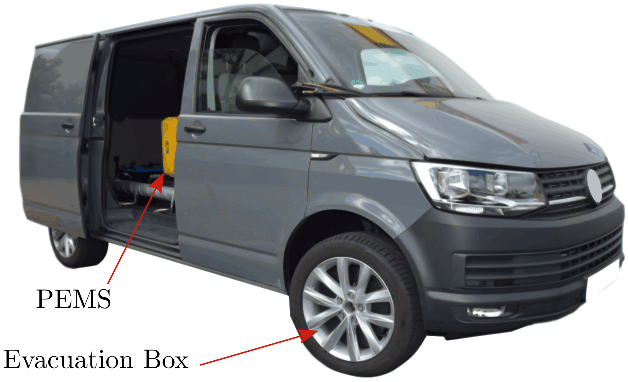

Figure D.4: *Depiction of the LCV used for RDE-compliant brake-related emissions tests. The front-right brake system is enclosed in the evacuation box. PN PEMS counts the particulate and determines their number for a specific evacuated air volume.*

of type K (NiCr-Ni). The pressure sensors are mounted at each corner and allow pressure measurements up to 250 *bar*. The vehicle is also equipped with the RaceLogic VBoX® to log relevant kinematics quantities such as vehicle speed and acceleration. The developed setup allows analysing the influence of driver, traffic, driving conditions and environment on the emissions level. Relevant vehicle and brake state variables such as vehicle speed, vehicle acceleration, brake temperature and brake pressure are sampled at 10 Hz, whilst PEMS provide the PNC at 1 Hz sampling rate.

TABLE D.4: Specification of the light commercial vehicle.

Vehicle type	Light commercial vehicle
Curb mass	1900 kg
Driveline	FWD with manual transmission
Tyre size	255/45 $R18$
Wheelbase	3000 mm
Track width	1904 mm
Drag coefficient	0.44
Frontal surface	3.1 m^2
Engine type	Turbo diesel 1.9 l
Foundation brake	Floating callipers, cast-iron discs, copper-free ECE brake linings
Torque allocation front/total	0.687
Nominal brake μ_b front/rear	0.42/0.41
Effective brake radius front/rear	126/126 mm
N. of pistons front/rear	1/1
Calliper piston(s) diameter front/rear	60/41 mm

Bibliography

[1] "Roadmap to a single European transport area, towards a competitive and resource efficient transport system," European Commission, Tech. Rep. Document COM(2011) 144 final, 2011.

[2] "Review of evidence on health aspects of air pollution - REVIHAAP Project," World Health Organization Regional Office for Europe, Tech. Rep., 2013.

[3] K. H. Kim and E. K. S. Kabir, "A review on the human health impact of airborne particulate matter," *Environment international*, vol. 74, pp. 136–143, 2015.

[4] S. Lawrence, R. Sokhi, and K. Ravindra, "Quantification of vehicle fleet pm10 particulate matter emission factors from exhaust and non-exhaust sources using tunnel measurement techniques," *Environmental pollution*, vol. 210, pp. 419–428, 2016.

[5] "Guidelines for estimating and reporting emission data under the convention on long-range transboundary air pollution (ECE/EB.AIR/97)," UNECE, Tech. Rep., 2009.

[6] "EMEP/EEA air pollutant emission inventory guidebook, EEA report no 21/2016," EEA (European Environment Agency), Tech. Rep., 2016.

[7] F. Amato, F. Cassee, H. van der Gon, R. Gehrig, M. Gustafsson, W. Hafner, and A. Prevot, "Urban air quality: the challenge of traffic non-exhaust emissions," *Journal of hazardous materials*, vol. 275, pp. 31–36, 2014.

[8] G. Kiesewetter, J. Borken-Kleefeld, W. Schöpp, C. Heyes, P. Thunis, B. Bessagnet, and M. Amann, "Modelling street level pm 10 concentrations across europe: source apportionment and possible futures," *Atmospheric Chemistry and Physics*, vol. 15, no. 3, pp. 1539–1553, 2015.

[9] B. Shyrokau, D. Wang, K. Augsburg, and V. Ivanov, "Vehicle dynamics with brake hysteresis," *Proceeding of the Institute of Mechanical Engineers, Part D: Journal of Automobiles Engineering*, vol. 272, no. 2, pp. 139–150, 2013.

[10] D. Crolla and A. Lang, "Brake noise and vibrations - the state of the art," *Tribology Series*, vol. 18, pp. 165–174, 1991.

[11] "Commission Regulation (EU) 2017/1151 of 1st June 2017 supplementing Regulation (EC) No 715/2007 of the European Parliament and of the Council," Economic Commission for Europe, Tech. Rep.

[12] D. Hesse and K. Augsburg, "Real driving emissions measurement of brake dust particles," *SAE Technical Paper*, no. 2019-09-2138, 2019.

[13] "Commission Regulation (EU) 2016/427 of 10 march 2016, amending Regulation (EC) No 692/2008 as regards emissions from light passenger and commercial vehicles (Euro 6)," Economic Commission for Europe, Tech. Rep.

[14] T. Bernhart, "Methodik zur Konzeption und Auslegung von Radbremsen für PKW mit elektrischem Antriebsstrang," Ph.D. dissertation, Technische Universität Ilmenau, 2019.

[15] V. Ricciardi, K. Augsburg, S. Gramstat, V. Schreiber, and V. Ivanov, "Survey on modelling and techniques for friction estimation in automotive brakes," *Appl. Sci.*, vol. 873, pp. 7–22, 2017.

[16] V. Ricciardi, D. Savitski, K. Augsburg, and V. Ivanov, "Estimation of brake friction coefficient for blending function of base braking control," *SAE Int. J. Passeng. Cars - Mech. Syst.*, vol. 10, no. 3, 2017, sAE Int. J. Passeng. Cars - Mech. Syst.

[17] K. Augsburg, D. Hesse, F. Wenzel, and G. Eichner, "Measuring and characterization of brake dust particles," in *EuroBrake*, 2017.

[18] S. Lin, C. Guan, A. Bakar, M. Jamaluddin, M. W. Harujan, and B. Ghani, "Disc brake squeal suppression through chamfered and slotted pad," *International Journal of Vehicle Structures and Systems*, vol. 3, no. 1, pp. 28–35, 2011.

[19] L. Matozo, A. Menetrier, and A. Tamagna, "Analysis of high damping underlayer materials for brake pads and its effects on nvh performance," *SAE Technical Paper*, 2006.

[20] A. Belvedi and S. Gerges, "Squeal noise in disc brakes and the influence of damping on the system dynamic stability," *Acta Acustica united with Acustica*, vol. 94, no. 2, pp. 254–264, 2008.

[21] J. LaDou, P. Landrigan, J. Baila, V. Foa, and A. Frank, "A call for an international ban on asbestos," *Cmaj*, vol. 164, no. 4, pp. 489–490, 2001.

[22] M. Eriksson, F. Bergman, and S. Jacobson, "On the nature of tribological contact in automotive brakes," *Wear*, vol. 252, pp. 26–36, 2011.

[23] C. Hamatschek, “Tiefgreifende tribologische Untersuchungen der Reibzone einer KFZ Reibungsbremse zur Beschreibung des Knarzphänomens in Zusammenhang mit Modellbildung für die Reibwertabschätzung bei niedrigen Geschwindigkeiten,” Master’s thesis, Technische Universität Ilmenau, 2019.

[24] S. Gramstat, “Methoden der in-situ Visualisierung der Reibzonendynamik trockenlaufender Reibpaarungen unter Ergänzung physikalischer und chemischer Charakterisierungen der Reibpartner,” Ph.D. dissertation, Technische Universität Ilmenau, 2015.

[25] M. Eriksson, F. Bergman, and S. Jacobson, “Surface characterisation of brake pads after running under silent and squealing conditions,” *Wear*, vol. 232, no. 2, pp. 163–167, 1999.

[26] W. Österle, I. Dörfel, C. Prietzel, H. Rooch, A. Cristol-Bulthé, G. Degallaix, and Y. Desplanques, “A comprehensive microscopic study of third body formation at the interface between brake pad and brake disc during the final stage of a pin-on-disc test,” *Wear*, vol. 267, no. 5-8, pp. 781–788, 2009.

[27] K. Kolbeck and K. Augsburg, “Brake particle movement inside the frictional system,” in *EuroBrake*, 2020.

[28] J. Balotin, P. Neis, and N. Ferreira, “Analysis of the influence of temperature on the friction coefficient of friction materials,” in *ABCM Symposium Series in Mechatronics*, vol. 4, 2010, pp. 898–906.

[29] F. Talati and S. Jalalifar, “Analysis of heat conduction in a disk brake system,” *Heat and mass transfer*, vol. 45, no. 8, p. 1047, 2009.

[30] D. Thuresson, “Thermomechanical analysis of friction brakes,” *SAE Technical Paper*, vol. 2000-01-2775, 2000.

[31] P. Blau, “Embedding wear models into friction models,” *Tribology Letters*, vol. 34, no. 1, pp. 75–79, 2009.

[32] M. Eriksson, A. Lundqvist, and S. Jacobson, “A study of the influence of humidity on the friction and squeal generation of automotive brake pads,” *Proceedings of the Institute of Mechanical Engineers, Part D: Journal of Automobile Engineering*, vol. 215, no. 3, pp. 329–342, 2011.

[33] S. Nagesh, C. Siddaraju, S. Prakash, and M. Ramesh, “Characterization of brake pads by variation in composition of friction materials,” *Procedia Materials Science*, vol. 5, pp. 295–302, 2014.

[34] P. Verma, R. Ciudin, A. Bonfanti, P. Aswath, G. Straffelini, and S. Gialanella, "Role of the friction layer in the high-temperature pin-on-disc study of a brake material," *Wear*, vol. 346, pp. 56–65, 2016.

[35] G. Straffelini, S. Verlinski, P. Verma, G. Valota, and S. Gialanella, "Wear and contact temperature evolution in pin-on-disc tribotesting of low-metallic friction material sliding against pearlitic cast iron," *Tribol. Lett.*, vol. 62, pp. 1–11, 2016.

[36] D. Hess and A. Soom, "Friction at a lubricated line contact operating at oscillating sliding velocities," *Journal of Tribology*, vol. 112, pp. 147–152, 1990.

[37] D. Chan and W. Stachowiak, "Review of automotive brake friction materials," *Proc. Inst. Mech. Eng. Part D J. Automob. Eng*, vol. 218, pp. 953–963, 2004.

[38] J. Wahlström, V. Matějka, Y. Lyu, and A. Söderberg, "Contact pressure and sliding velocity maps of the friction, wear and emission from a low-metallic/cast-iron disc brake contact pair," *Tribology in Industry*, vol. 39, no. 4, 2017.

[39] G. Riva, F. Varriale, and J. Wahlström, "A finite element analysis (fea) approach to simulate the coefficient of friction of a brake system starting from material friction characterization," *Friction*, vol. 9, pp. 191–200, 2020.

[40] V. Ricciardi, A. Travagliati, V. Schreiber, M. Klomp, V. Ivanov, K. Augsburg, and C. Faria, "A novel semi-empirical dynamic brake model for automotive applications. tribology international," *Tribology International*, vol. 146, 2020.

[41] K. Shin, M. Brennan, J. Oh, and C. Harris, "Analysis of disc brake noise using a two-degree-of-freedon model," *Journal of Sound and Vibration*, vol. 254, pp. 837–848, 2002.

[42] I. Kragelsky, M. Dobychin, and V. Kombalov, *Friction and Wear: Calculation Methods.* Elsevier, 2013.

[43] J. Kang and S. Chois, "Brake dynamometer model predicting brake torque variation due to disc thickness variation," *Proc. Insit. Mech. Eng. Part D J. Automob. Eng.*, vol. 221, no. 1, pp. 49–55, 2007.

[44] J. Behrendt, C. Weiss, and N. Hoffmann, "A numerical study on stick-slip motion of a brake pad in steady sliding," *J. Sound Vib.*, vol. 330, pp. 636–651, 2011.

[45] A. Grkic, S. Muzdeka, Z. Arsenic, and C. Duboka, "Model for estimation of the friction coefficient in automotive brakes under extremely high temperatures," *International Journal of Engineering and Technical Research*, vol. 2, pp. 290–294, 2014.

[46] N. Lee and C. Kang, "The effect of a variable disc pad friction coefficient for the mechanical brake system of a railway vehicle," *PloS one*, vol. 10, no. 8, 2015.

[47] C. Martinez, E. Velenis, D. Tavernini, and B. Gao, "Modelling and estimation of friction brake torque for a brake by wire system," in *IEEE, International Electric Vehicle Conference*, 2014, pp. 1–7.

[48] J. Shangshuai and O. Li, "Friction induced vibration and noise on a brake system," in *IEEE International Conference Information and Automation (ICIA)*, 2013.

[49] Z. Wan, X. Liu, H. Wang, Y. Shan, and T. He, "Friction coefficient model of friction pair composed of automotive brake materials," in *ASME 2014 International Mechanical Engineering Congress and Exposition*, 2014.

[50] G. Ostermeyer, "On the dynamics of the friction coefficient," *Wear*, vol. 254, no. 9, pp. 852–858, 2003.

[51] I. Argatov, "Artificial neural networks (ANNs) as a novel modeling technique in tribology," *Front. Mech. Eng.*, vol. 5, no. 30, pp. 1–9, 2019.

[52] R. Rojas, *Neural Networks: A Systematic Introduction.* Springer, 1996.

[53] V. Ćirović and D. Aleksendrić, "Development of neural network model of disc brake operation," *FME Trans.*, vol. 38, pp. 29–38, 2010.

[54] D. Aleksendrić and C. Duboka, "Prediction of automotive friction material characteristics using artificial neural networks-cold performance," *Wear*, vol. 261, pp. 269–282, 2006.

[55] A. Senatore, V. D'Agostino, R. D. Giuda, and V. Petrone, "Experimental investigation and neural network prediction of brakes and clutch material frictional behaviour considering the sliding acceleration influence," *Tribology in Industry*, vol. 44, no. 10, pp. 1199–1207, 2011.

[56] Y. Yin, J. Bao, and L. Yang, "Tribological properties prediction of brake lining for automobiles based on bp neural network," in *Control and Decision Conference (CCDC 2010)*, 2010.

[57] I. Mutlu, "Artificial neural network modelling of non-asbestos brake lining performance boric acid in brake pad," *Inf. Tech. J.*, vol. 8, pp. 389–402, 2009.

[58] D. Aleksendrić and D. C. Barton, "Neural network prediction of disc brake performance," *Tribology international*, vol. 42, no. 7, pp. 1074–1080, 2009.

[59] V. Ćirović and D. Aleksendrić, "Dynamic modeling of disc brake contact phenomena," *FME Trans.*, vol. 39, pp. 177–183, 2011.

[60] G. Ostermeyer and M. Müller, "New insights into the tribology of brake systems," *Proc. Inst. Mech. Eng. Part D J. Automob. Eng.*, vol. 7, pp. 1167–1200, 2008.

[61] K. Han, S. Choi, J. Lee, D. Hyun, and J. Lee, "Accurate brake torque estimation with adaptive uncertainty compensation using a brake force distribution characteristic," *IEEE transactions on vehicular technology*, vol. 66, no. 12, pp. 10 830–10 840, 2017.

[62] M. Acosta and S. Kanarachos, "Tire force estimation and road grip recognition using extended kalman filter, neural networks and recursive least squares," *Neural Computing and Applications*, vol. 2017, pp. 1–21, 2017.

[63] F. Bergman, M. Eriksson, and S. Jacobson, "The effect of reduced contact area on the occurrance of brake squeals for an automotive brake pad," *Proceedings of the Institution of Mechanical Engineers, Part D: Journal of Automobile Engineering*, vol. 214, pp. 561–568, 2000.

[64] M. K. A. Ali, M. M. Makrahy, and H. Xianjun, "Role of the friction layer formed on the brake lining surface in friction stabilization for automotive brakes," *Surface Topography: Metrology and Properties*, vol. 7, no. 1, 2019.

[65] M. Kim, "Development of the braking performance evaluation technology for high speed brake dynamometer," *International Journal of Systems Applications, Engineering and Development*, vol. 6, pp. 122–129, 2012.

[66] R. Nisonger, C. Yen, and D. Antanaitis, "High temperature brake cooling-characterization for brake system modeling in race track and high energy driving conditions," *SAE International Journal of Passenger Cars-Mechanical Systems*, vol. 4, no. 2011-01-0566, pp. 384–398, 2011.

[67] A. Bejan and A. Kraus, *Heat transfer handbook.* John Wiley & Sons, 2003, vol. 1.

[68] J. Gao, W. D. Luedtke, D. Gourdon, M. Ruths, J. N. Israelachvili, and U. Landman, "Frictional forces and amontons' law: From the molecular to the macroscopic scale," *J. Phys. Chem. B*, vol. 108, no. 11, pp. 3410–3425, 2004.

[69] Z. Wan, X. Liu, H. Wang, and Y. Shan, "Research on the time-varying properties of brake friction," *IEEE Access*, vol. 6, pp. 69 742–69 749, 2018.

[70] J. C. Lagarias, J. A. Reeds, M. H. Wright, and P. E. Wright, "Convergence properties of the nelder-mead simplex method in low dimensions," *SIAM Journal of Optimization*, vol. 9, no. 1, pp. 112–147, 1998.

[71] G. P. Fernandes, P. S. Zanotto, and A. Sinatora, "Contribution on understanding the friction film development in the performance of a dry automotive clutch system," *Wear*, vol. 342, no. 11, pp. 364–376, 2015.

[72] M. Kchaou, A. Sellami, R. Elleuch, and H. Singh, “Friction characteristics of a brake friction material under different braking conditions,” *Materials and Design*, vol. 52, pp. 533–540, 2013.

[73] “Uniform provisions concerning the approval of vehicles of categories M, N and O with regard to braking. Addendum 12: Regulation No. 13. 2008,” Economic Commission for Europe, Tech. Rep.

[74] V. Ricciardi, V. Ivanov, and K. Augsburg, “Estimation of power dissipation in disc brakes and tires for motion control applications in electric vehicles,” in *IECON 2018-44th Annual Conference of the IEEE Industrial Electronics Society*, 2018, pp. 4531–4536.

[75] A. Pennycott, L. D. Novellis, P. Gruber, and A. Sorniotti, “Optimal braking force allocation for a four-wheel drive fully electric vehicle,” *Proceedings of the Institution of Mechanical Engineers, Part I: Journal of Systems and Control Engineering*, vol. 228, no. 8, pp. 621–628, 2014.

[76] M. Acosta, “Vehicle dynamics virtual sensing and advanced motion control for highly skilled autonomous vehicles,” Ph.D. dissertation, Technische Universität Ilmenau, 2020.

[77] C. C. de Wit, H. Olsson, K. Aström, and P. Lischinsky, “A new model for control of system with friction,” *IEEE Transactions on Automatic Control*, vol. 40, no. 3, pp. 419–425, 1995.

[78] Kistler. Roadyn wheel force sensor. [Online]. Available: http://www.kistler.com

[79] D. Savitski, K. Augsburg, and V. Ivanov, “Svm classification and kalman filter based estimation of the tire-road friction curve,” in *The 20th World Congress of the International Federation of Automatic Control (IFAC 2017)*, 2017.

[80] D. Savitski, V. Ivanov, L. Heidrich, K. Augsburg, and T. Pütz, “Experimental investigation of braking dynamics of electric vehicles,” in *EuroBrake*, 2013.

[81] U. Kiencke and L. Nielsen, *Automotive control systems: for engine, driveline, and vehicle.* Springer, 2000, vol. 2nd edition.

[82] S. Schneider, “Detaillierte Analyse der Restbremsmomente von Radbremsen,” Master’s thesis, Technische Universität Ilmenau, 2011.

[83] B. Böhme, “Grundlagenuntersuchungen zu niederfrequenten Geräuschphänomenen,” Master’s thesis, Technische Universität Ilmenau, 2017.

[84] S. Savaresi and M. Tanelli, *Active braking control systems design for vehicles.* Springer Science & Business Media, 2010.

[85] M. Doumiati, A. Charara, A. Victorino, and D. Lechner, *Vehicle Dynamics Estimation using Kalman Filtering: Experimental Validation.* WILEY, 2012.

[86] B. Ganzel, "Slip control boost braking system," Patent US9 221 443, 2015.

[87] B. Shyrokau, D. Wang, D. Savitski, K. Hoepping, and V. Ivanov, "Vehicle motion control with subsystem prioritization," *Int. J. of Mechatronics*, vol. 30, pp. 297–315, 2015.

[88] T. Agliullin, V. Ivanov, M. S. Kaddari, V. Ricciardi, D. Savitski, and K. Augsburg, "Sliding mode methods in electric vehicle stability control," in *2019 IEEE International Conference on Connected Vehicles and Expo*, 2019.

[89] A. Aksjonov, V. Ricciardi, K. Augsburg, V. Vodovozov, and E. Petlenkov, "Hardware-in-the-loop test of an open loop fuzzy control method for decoupled electro-hydraulic antilock braking system," *IEEE Transactions on Fuzzy Systems*, 2020.

[90] Y. Oshman and I. Shaviv, "Optimal tuning of a kalman filter using genetic algorithms," *AIAA Guidance, Navigation, and Control Conference and Exhibit*, p. 4558, 2000.

[91] J. F. Archard, "Contact and rubbing of flat surfaces," *J. Appl. Phys.*, vol. 24, pp. 981–988, 1953.

[92] A. Hatam and A. Khalkhali, "Simulation and sensitivity analysis of wear on the automotive brake pad," *Simulation Modelling Practice and Theory*, vol. 84, pp. 106–123, 2018.

[93] H. Ren and G. P. Ostermeyer, "On the wear of brake pads," in *Proc. Appl. Math. Mech.*, vol. 13, 2013, pp. 165–166.

[94] Ž. Arsenić, C. Duboka, and J. Todorović, "Prediction of brake pad life - further development of lwh," *SAE transactions*, pp. 936–944, 1986.

[95] A. Ramalhoa and J. C. Miranda, "The relationshipbetweenwear and dissipatedenergy in sliding systems," *Wear*, vol. 260, pp. 361–367, 2006.

[96] D. Aleksendrić, "Neural network prediction of brake friction materials wear," *Wear*, vol. 268, pp. 117–125, 2010.

[97] D. B. Antanaitis and M. T. Riefe, "Method of estimating brake pad wear and vehicle having a controller that implements the method," Patent US9 416 835B2, 2016.

[98] N. Medinei, D. B. Antanaitis, and S. J. Weber, “Brake pad wear estimation,” Patent US20 190 107 163A1, 2019.

[99] S. K. Rhee, “Wear equation for polymers sliding against metal surfaces,” *Wear*, vol. 16, pp. 431–445, 1970.

[100] G. L. Larson, “Vehicle onboard brake pad/lining wear estimators with temperature estimations,” Patent US7 244 003B2, 2007.

[101] M. N. Howell, J. P. Whaite, P. Amatyakul, Y. Chin, M. A. Salman, C. Yen, and M. Riefe, “Brake pad prognosis system,” Patent US20 080 236 269A1, 2008.

[102] A. Mamakos, M. Arndt, D. Hesse, C. Hamatschek, and K. Augsburg, “Comparison of particulate matter and number emissions from a floating and a fixed caliper brake system of the same lining formulation,” *SAE Technical Paper*, no. 2020-01-1633, 2020.

[103] K. Augsburg and D. Hesse, “Comparative study of brake particle emissions,” in *Internationales AVL Forum Abgas- und PartikelemissionenAt*, 2020.

[104] ——, “Stand und entwicklungstendenzen bei der minderung von non- exhaust-emissionen,” in *FAD-Konferenz "Herausforderung - Abgasnachbehandlung"*, 2019.

[105] K. Augsburg, D. Hesse, U. Kuhn, and R. Leicht, “Comparison of the run-in and emission behavior of different disc concepts,” in *PMP-47-20 rev1*, 2018.

[106] B. R. Denby, I. Sundvor, C. Johansson, L. Pirjola, M. Ketzel, M. Norman, and G. Omstedt, “A coupled road dust and surface moisture model to predict non-exhaust road traffic induced particle emissions (nortrip). part 1: Road dust loading and suspension modelling,” *Atmospheric Environment*, vol. 77, pp. 283–300, 2013.

[107] F. Amato, O. Favez, M. Pandolfi, A. Alastuey, X. Querol, S. Moukhtar, and T. L. Priol, “Traffic induced particle resuspension in paris: Emission factors and source contributions,” *Atmospheric Environment*, vol. 129, pp. 114–124, 2016.

[108] G. Perricone, M. Alemani, I. Metinöz, V. Matějka, J. Wahlström, and U. Olofsson, “Towards the ranking of airborne particle emissions from car brakes - a system approach,” *Proceedings of the Institution of Mechanical Engineers, Part D: Journal of Automobile Engineering*, vol. 231, no. 6, pp. 781–797, 2017.

[109] J. Grochowicz, C. Agudelo, A. Reich, K. H. Wollenweber, and H. Abendroth, “Brake dynamometer test variability part 2-description of the influencing factors,” *SAE International Journal of Passenger Cars-Mechanical Systems*, vol. 4, pp. 1394–1421, 2011.

[110] L. Chasapidis, T. Grigoratos, A. Zygogianni, A. Tsakis, and A. G. Konstandopoulos, "Study of brake wear particle emissions of a minivan on a chassis dynamometer," *Emission Control Science and Technology*, vol. 4, no. 4, pp. 271–278, 2018.

[111] V. Ricciardi, M. Schiele, D. Hesse, P. Hauschild, and K. Augsburg, "Artificial neural networks regression models for the prediction of brake-related emissions," in *EuroBrake FISITA*, 2020.

[112] D. Savitski, "Robust control of brake systems with decoupled architecture," Ph.D. dissertation, Technische Universität Ilmenau, 2019.

[113] H. Pacejka and I. Basselink, "Magic formula tyre model with transient properties," *Veh. Syst. Dyn.*, vol. 27, pp. 234–249, 1997.

[114] F. Bottiglione, A. Sorniotti, and L. Shead, "The effect of half-shaft torsion dynamics on the performance of a traction control system for electric vehicles," *Proceedings of the Institution of Mechanical Engineers, Part D: Journal of Automobile Engineering*, vol. 226, no. 9, pp. 1145–1159, 2012.

[115] D. Savitski, V. Ivanov, K. Augsburg, B. Shyrokau, R. Wragge-Morley, T. Pütz, and P. Barber, "The new paradigm of an anti-lock braking system for a full electric vehicle: experimental investigation and benchmarking," *Journal of Automobile Engineering*, Oct. 2015.

[116] D. P. Bertsekas, *Constrained optimization and Lagrange multiplier methods.* Academic press, 2014.

[117] K. Baba, R. Shibata, and M. Sibuya, "Partial correlation and conditional correlation as measures of conditional independence," *Australian & New Zealand Journal of Statistics*, vol. 46, no. 4, pp. 657–664, 2004.

[118] S. H. Rudy, S. L. Brunton, J. L. Proctor, and J. N. Kutz, "Data-driven discovery of partial differential equations," *Science Advances*, vol. 3, no. 4, 2017.

[119] J. E. Dennis and R. B. Schnabel, *Numerical methods for unconstrained optimization and nonlinear equations.* Siam, 1996, vol. 16.